Advances in Sensitivity and Resolution of Solid State Nuclear Magnetic Resonance and Dynamic Nuclear Polarization

by

Natalie C. Golota

B.A. Chemistry

Washington University in St. Louis, 2018

Submitted to the Department of Chemistry
in Partial Fulfillment of the Requirements for the Degree of

DOCTOR OF PHILOSOPHY IN CHEMISTRY

at the

MASSACHUSETTS INSTITUTE OF TECHNOLOGY

June 2023

Signature of Author:………………………………………………………………..…
Department of Chemistry
May 4, 2023

Certified by:………………………………………………………………………....
Robert G. Griffin
Arthur Amos Noyes Professor of Chemistry
Thesis Supervisor

Accepted by:………………………………………………………………………...
Adam P. Willard
Associate Professor of Chemistry
Graduate Officer

This doctoral thesis has been examined by a Committee of the Department of

Chemistry as follows:

……………………………………………………………………………………………

Professor Keith A. Nelson
Thesis Committee Chair
Haslam and Dewey Professor of Chemistry

……………………………………………………………………………………………

Professor Robert G. Griffin
Thesis Supervisor
Arthur Amos Noyes Professor of Chemistry

……………………………………………………………………………………………

Professor Mei Hong
Thesis Committee Member
Professor of Chemistry

Advances in Sensitivity and Resolution of Solid State Nuclear Magnetic Resonance and Dynamic Nuclear Polarization

By

Natalie C. Golota

Submitted to the Department of Chemistry on May 12, 2023 in partial fulfillment of the requirements for the degree of Doctor of Philosophy in Chemistry

Abstract

Traditional structural biology methods such as x-ray crystallography and solution-state nuclear magnetic resonance (NMR) cannot provide atomic level resolution of insoluble, noncrystalline proteins. Such proteins include amyloid fibrils implicated in numerous neurodegenerative diseases. While solid state NMR using magic angle spinning (MAS) has yielded high resolution structures of amyloid fibrils, including polymorphs of amyloid-β (Aβ), its sensitivity is inherently limited, requiring undesirable time and resource commitments. Dynamic nuclear polarization (DNP) is a powerful method of enhancing solid state NMR sensitivity. However, this sensitivity gain comes at a significant loss of spectral resolution due to sample conformational heterogeneity at the cryogenic temperatures required for efficient electron-nuclear polarization transfers. This hinders acquisition of site-specific structural assignments in complex systems. Thus, it is critical to improve DNP resolution by advancing to higher magnetic fields and faster MAS frequencies. Unfortunately, at high fields, the efficiency of the most widely applied DNP polarization mechanisms decreases, along with the availability of high-power microwave sources. The work presented in this thesis seeks to address instrumentation limitations and improve DNP methods that presently limit the utility and power of MAS DNP at high fields.

This thesis first describes the mechanism of Overhauser Effect (OE) sensitivity enhancements in insulating solids. We demonstrate the generation of strong positive OE with less than 200 mW of microwave power. We also employ selective deuteration to elucidate the role of individual hyperfine-coupled protons on the BDPA radical. This work provides a basis for the improved development of high field DNP radicals with fluctuating hyperfine interactions.

The continued expansion of MAS DNP at high field and with fast MAS rotors requires improvement in the efficiency of coupling microwave irradiation into the sample. We provide a comprehensive discussion of the effect of the radio frequency (RF) coil on the transverse microwave coupling efficiency in 1.3 mm and 0.7 mm rotor systems. When the ratio of the pitch to microwave wavelength is ~ 0.5, the coupling efficiency is significantly reduced, as is the case for a typical 1.3 mm or 0.7 mm RF coil at fields between 460-593 GHz. To address this, we introduce axial microwave coupling schemes for 3.2, 1.3-, and 0.7-mm rotors and demonstrate theoretical improvements in the electron Rabi field of > 60% in 3.2 mm rotor systems and up to a factor of 8 improvement in 0.7 mm rotor systems. We further provide experimental results of MAS spinning stability in 3.2 mm rotors at 95 K using the modified axial bearing required for axial irradiation schemes.

While the first two sections describe sensitivity enhancements under DNP, the later chapters are focused on sensitivity enhancements leveraged via MAS frequencies > 90 kHz and ^{1}H detected MAS NMR. We demonstrate the first ^{1}H detected MAS NMR study of the arctic mutant of Aβ_{1-42}, which is implicated in the pathogenesis of early onset familial AD. Despite resolution limitations in the sample as a result of limited MAS frequency and sample heterogeneity, we determine that the core fibril structure of E22G Aβ_{1-42} is monomorphic with suggested conserved structure relative to that of the wild type fibril.

To further reduce homogenous contributions to the solid-state linewidth, we introduce the fabrication and use of 0.7 mm diameter diamond rotors. The superior material strength, thermal conductivity, and microwave transparency make diamond the optimal MAS rotor material. First, we describe the mechanism of material ablation and characterize the effects of pulse energy, irradiation scheme and pulse number on the achievable taper angle in high aspect ratio holes. We then apply a dual-sided axial machining strategy to fabricate 0.7 mm diamond rotors, and further demonstrate stable operation up to 124 kHz in addition to ^{1}H detected MAS NMR results. Overall, the areas of focus in this thesis describe several resolution and sensitivity advancements that when combined in the future could provide sufficient sensitivity and resolution with which to study ex-vivo amyloid plaque samples and other exogenous biomedically relevant samples.

Thesis Supervisor: Robert G. Griffin
Title: Arthur Amos Noyes Professor of Chemistry
                          Director, Francis Bitter Magnet Laboratory

Acknowledgements

I would first like to thank my advisor, Robert Griffin, for the opportunity to study at MIT and the Francis Bitter Magnet Laboratory. I am sincerely appreciative of the freedom to explore and study a diverse range of topics, in addition the support he has provided for all aspects of my research at MIT. I am very grateful for both the academic and personal growth that has been fostered in his laboratory over the past 5 years. This has been a defining experience in my personal and professional life that would not have been possible without his support, encouragement, and intense lab environment.

I would also like to thank Professor Neil Gershenfeld for welcoming me into his lab at the Center for Bits and Atoms to work on the diamond rotor project. The entire group at the CBA has had a profound and positive impact on me as a researcher and individual. I am incredibly grateful to have had this opportunity. I always looked forward to going to the CBA to talk with CBA members about the work they were doing or work on a new fabrication. I found these experiences to re-invigorate and motivate me to keep pushing the limits of what is possible in science and engineering.

I would not be where I am today without Professor Alexander Barnes who was a fantastic undergraduate research advisor and sparked my interest in solid state NMR and DNP while at Washington University in St. Louis. His passion and excitement for all things physical chemistry and instrumentation inspired me to come to MIT with the goal of designing new instrumentation for MAS DNP. His guidance and the strong foundations I learned as an undergraduate in his lab enabled my success in graduate school and I am grateful for the experience as an undergraduate at Washington University in The Barnes Lab. To that end, I would also like to thank Dr. Erika Sesti who was the best female role model I could have imagined as an undergraduate and who supported me on some of the most difficult days as a graduate student at MIT. Thank you is not enough to express my appreciation to both of you.

I am sincerely grateful to all members of the group including past and present members of Daniel Banks, Brian Michael, Salima Bahri, Christy George, Michael Mardini, and Choon Boon Cheung for all of the mentorship and assistance. Kong Ooi Tan has played a fundamental mentorship role throughout my PhD and I am so grateful for all of the support, guidance and reality checks during my time in the Bitter Lab. Thank you to Eddie Saliba for always being a supportive friend, lab mate, and someone I could count on when the Bitter Lab became overwhelming. Thank you for teaching me so much about physics and always being there to answer my stupidest NMR questions. Thank you to Ravi Shankar Palani for pushing me to be a better scientist and researcher. Your dedication and excitement for research inspired me a lot during our work on the Overhauser effect and I am so appreciative for all the help, camaraderie, and encouragement especially when everything seemed to be breaking in the lab. Finally, thank you to Lauren Schaffer who has been such a positive force in the lab in the last year.

The magnet lab would have been a very hard place without our technicians who always helped bail me out of some of my most precarious equipment problems. Thank you to Stephen Thompson and Dave Ruben for always being so helpful and resourceful in the lab, in addition to Ajay Thakkar and Mike Mullins. Thank you also to Wanda Hernandez and Jillian Haggerty for being so helpful and kind to me during my time in the lab.

I am also very grateful for the collaboration with Richard Temkin's lab. Sudheer Jawla has been an essential collaborator and mentor in this PhD and taught me so much about gyrotrons, microwave coupling and CST. I am extremely grateful for the help provided by Ivan Mastovsky on the 460 and 527 GHz systems. Thank you for all the support you have provided, and I sincerely appreciate always having been able to count on your help, and importantly sense of humor when things where not going well.

The time spent at the CBA changed my PhD for the better and has made me a better scientist, engineer, and collaborator. I have had the absolute pleasure of working with some of the most exceptional students there and going to the CBA was often the highlight of my day. To Zach Fredin, your passion for making and incredible ability to teach and inspire has had such a positive impact on me, especially at some of the hardest times in my PhD. The diamond rotor bender is one of the most vivid memories and in some ways exactly as I thought my PhD would be at MIT. After so many fraught and chaotic hours before Christmas break, delaying travel plans, and working crazy hours, the joy of making the first diamond rotor to spin to 120 kHz is one of the highlights of my PhD. I am incredibly grateful for your level-headed and down to earth advice and friendship, thank you. To Dave Preiss, working with you has also been one of the highlights of my time at MIT. I have learned so much about precision engineering from you, and most importantly how to grow as a communicator and collaborator. I am so grateful for all the work we have done together, and I have really enjoyed it. I cannot thank all the members of the CBA enough for all the fun basement conversations about your own work, helping me become so much better at explaining NMR, and pushing me to think beyond how I was trained as a chemist. Many times, conversations with CBA members helped me to solve a problem that felt intractable back at the magnet lab. Thank you to Joe Murphy, Kara Pendelbury, and Tom Lutz for help and support of the diamond rotor project.

To my friends in the physical chemistry cohort, I couldn't have gotten this far without you. Through all the chaos of first year quantum mechanics and in some of the hardest times at MIT, Jet Lem, Mikaila Hoffmann, Cliff Allington, Vyshnavi Vennelakanti, Maria Castellanso, Ardavan Farahvash, and Daniel Harper were always there. Thank you to all the incredible friends without whom I couldn't have completed this process and certainly would not have laughed as much along the way. To Charlie Farquhar and Gino Occhialini, our wine nights were always much appreciated and needed time to vent and blow off steam, thank you for your friendship and always having my back. To all my other incredible friends in the Chemistry program, I am so grateful for all the

memories and enjoyable times that pulled me out of the lab and made me into a more balanced rounded person.

Getting outside of Cambridge was the most important part of maintaining my sanity and emotional wellbeing during my PhD and I cannot thank all my barn families for their love, support and encouragement. Thank you to Katie Mair and Meredith Lazar for shaping me into who I am today and teaching me so much about determination, hard work and to never give up. To my entire Sterling family, I love you all so much and being with you always gave me something to look forward to, particularly during the first years of my PhD. To David Rand, thank you for welcoming me to your barn and as part of the Rand barn family. Saturdays at the barn many weeks were the absolute happiest and most regenerative time of my week. To the Rand barn family, I cannot thank you enough for always being the best supporters of me each weekend as I finished this thesis. I am also so grateful to Perry and Gabe, in addition to Riley, Skeeter and Hank for being the best equine friends I could have asked for. Knowing that on the hard days I could come and spend time with Perry or Gabe gave me an invaluable break, mental reset, and moments of peace that were so needed during this PhD. Perry, you have been the best four-legged friend throughout most of my teenage and adult life, thank you. Thank you to all at High Tail Acres for caring so well for Perry.

To my grandmothers Stella and Clair, this thesis is dedicated to you both. I wish you were here to see it. I hope you know how much your lasting memories and values you instilled in me motivated and guided me throughout my education.

Finally, to my parents, I couldn't have done any of this without you. You are my biggest supporters and words are not enough to say how grateful I am for you both and how much I love you. To my mom, you modeled how strong and independent women can be growing up and that has been invaluable as I have gone on my own journey of growth and development in my education, particularly at MIT. You have supported me through some of the most painful days at MIT and I am so grateful for our relationship. To my dad, you have taught me so much and I am so grateful for your support of me in all that I do. I am grateful this journey has brought us closer, and I will always love our Saturday calls and reflections of the week that seemed to help me leave tough weeks behind. Seeing your persistence, dedication and ingenuity in both engineering and business has inspired a lot of the approaches that led to my successful PhD.

Table of Contents

List of Figures

List of Tables

17

Chapter 1 : Introduction

1.1 Introduction to Magnetic Resonance

Magnetic resonance spectroscopy, including magnetic resonance imaging (MRI) and nuclear magnetic resonance (NMR), has evolved into a widely applied technique for medical, structural biology, and materials science applications. The technique was discovered simultaneously by Felix Bloch and Edward Purcell in 1946. Over the past several decades advancements in superconducting magnet technology, radio frequency transmitter and receiver technology, sample preparation methods, Magic Angle Spinning (MAS) technology, and the advent of Dynamic Nuclear Polarization (DNP) have made NMR a fundamental and powerful spectroscopic tool. Much of the utility of solid-state NMR is derived from coherent manipulation of the internal spin Hamiltonian. Use of dipolar recoupling techniques can yield intra and inter-molecular distances and orientational constraints in molecules of interest at atomic resolution. Herein, we discuss the nuclear interactions of spin ½ nuclei including ^{13}C, ^{15}N, and ^{1}H. Discussion of the inherent low sensitivity of NMR is also provided and is followed by an introduction into the generation of sensitivity enhancements under DNP. While only a brief review of nuclear and electron spin interactions are offered in this introduction, we direct the reader to complete reviews in the literature [1-5].

1.1.1 Zeeman Hamiltonian and Spin Polarization

In the absence of a magnetic field, the energy levels of nuclear and electron spin states are degenerate. However, when placed into a magnetic field, the state

degeneracy is broken, and the energy levels are split according to the Zeeman interaction as described by the Zeeman Hamiltonian in (1-1).

$$\hat{H} = -\gamma \hbar \vec{I} \cdot \vec{B}$$

(1-1)

In (1-1), the gyromagnetic ratio of the spin is given by γ and describes the strength of the interaction of the spin with the magnetic field. Spin is given as I in (1-1), and in this thesis, we are limited to the discussion of systems where $I = {}^1/_2$. The external magnetic field vector is given by $\vec{B}$. The energy levels of a spin ½ system can be solved for and are given in (1-2).

$$E\left(I = \frac{1}{2}\right) = -\frac{\gamma \hbar B_0}{2}$$

$$E\left(I = -\frac{1}{2}\right) = +\frac{\gamma \hbar B_0}{2}$$

(1-2)

For a spin ½ system, the spin state aligned with the external magnetic field is at a lower energy. The energy difference between the two spin states is given by (1-3), where the Larmor frequency is given by ω_0.

$$\Delta E = \hbar \gamma B_0 = \hbar \omega_0$$

(1-3)

In (1-3) it becomes clear that the gyromagnetic ratio of the spin determines the energy level splitting of a particular spin. The population differences between spin states of an $I = {}^1/_2$ system can be calculated following a Boltzmann distribution and is provided in (1-4).

$$P = \frac{e^{\frac{\gamma \hbar B_0}{2k_B T}} - e^{\frac{-\gamma \hbar B_0}{2k_B T}}}{e^{\frac{\gamma \hbar B_0}{2k_B T}} + e^{\frac{-\gamma \hbar B_0}{2k_B T}}} \tag{1-4}$$

This expression can be simplified at high field and high temperatures > 20 K by expansion and truncation of the exponential terms to yield an expression describing the polarization of a spin system as given in (1-5).

$$P = \frac{\gamma \hbar B_0}{2k_B T} \tag{1-5}$$

The detection and sensitivity of an electron or nuclear spin signal depends on a population difference between spin states, and as such, spins with large energy level differences result in enhanced sensitivity. This is the case for the detection of electron spins in electron paramagnetic resonance (EPR) and serves as the basis for DNP, as described later in this chapter. Spin polarizations can be coherently controlled in NMR and low field EPR via high power radio frequency or microwave pulses on resonance with the nuclear or electron Larmor frequency. While the Zeeman interaction is responsible for the splitting of spin energy levels in a magnetic field, the internal interactions of spin ½ systems are responsible for the valuable information content NMR can yield and are discussed in Section 1.1.2. These interactions are described in detail in the next section. However, at high fields, electron spin polarizations are not coherently controlled due to insufficient microwave Rabi fields. As such, all high field DNP mechanisms to date rely upon continuous wave mechanisms and are discussed in Section 1.2.1.

1.1.2 Internal Interactions

The Hamiltonian describing an interaction, *i*, can be written in spherical tensor form as the scalar product between the qth component of the rank ℓ spatial tensor, A, and spin space tensor, $\Im$ as given in (1-6).

$$\widehat{H} = \sum_i \sum_{l=0}^{2} \sum_{q=-l}^{l} (-1)^q A_{l,q}^i \Im_{l,-q}^i \qquad (1-6)$$

The dominant NMR interactions in the rotating frame for spin ½ nuclei include the chemical shift, dipolar coupling, and scalar couplings. These interactions contain anisotropic, or orientationally dependent, contributions represented by second rank tensors. However, the scalar anisotropy typically cannot be distinguished from the stronger dipolar anisotropy and is typically neglected leaving only the isotropic component. Discussion and presentation of the interaction Hamiltonian for chemical shift, dipolar coupling and scalar couplings are discussed herein.

1.1.2.1. Chemical Shift

The chemical shift interaction describes the perturbation of the magnetic field felt by a nuclear spin due to shielding of local electron spins. The chemical shift has isotropic and anisotropic contributions due to the orientationally asymmetric electronic environment surrounding nuclear spins in external field. The secular chemical shift Hamiltonian in the rotating frame is given in (1-7) in terms of the isotropic chemical shift tensor, σ_{iso}, the anisotropy parameter, δ, and the asymmetry parameter, η. Under magic angle spinning, the chemical shift anisotropy can be attenuated returning only the isotropic chemical shift to yield high resolution spectra.

$$\widehat{H}_{cs} = \sum_k \hat{I}_{kz} \left[\omega_0 \sigma^k + \frac{\omega_{0,k} \delta_\sigma^k}{2} [(3 \cos^2 \beta^k - 1) - \eta_\sigma^k \sin^2(\beta^k) \cos(2\alpha^k)] \right]$$

Where

$$\sigma_{iso}^{(k)} = \frac{1}{3}(\sigma_{xx} + \sigma_{yy} + \sigma_{zz}) \qquad (1\text{-}7)$$

$$\delta^{(k)} = \sigma_{zz} - \sigma_{iso}$$

$$\eta^{(k)} = \frac{(\sigma_{yy} - \sigma_{xx})}{\delta}$$

1.1.2.2. Scalar Interaction

Under fast MAS, such as $\omega_r/2\pi \sim 90 - 111$ kHz as in Chapters 4 and 6, the solid-state spin system begins to have sufficiently long coherence lifetimes such that scalar based, through bond couplings can be used for polarization transfers in multidimensional correlation experiments. The anisotropic contribution to scalar couplings cannot be distinguished easily from the dipolar anisotropy, and so in this description the isotropic Hamiltonian will be given. The general form of the scalar Hamiltonian is given in spherical tensor notation in (1-8).

$$\widehat{H}_J = A_{0,0}^{(k,n)} \mathfrak{J}_{0,0}^{(k,n)} \qquad (1\text{-}8)$$

The isotropic Hamiltonian for a homonuclear spin pair is given by (1-9).

$$\widehat{H}_{J,II} = 2\pi J_{kn}(\vec{I_k} \cdot \vec{I_n}) \qquad (1\text{-}9)$$

For a heteronuclear spin pair under the secular approximation, the Hamiltonian is given by (1-10).

$$\widehat{H}_{J,IS} = 2\pi J_{kn} \hat{I}_{kz} \hat{S}_{nz} \qquad (1\text{-}10)$$

These couplings are isotropic and unaveraged by internal dynamics. This allows correlation spectroscopy to be performed on dynamic regions where dipolar transfers are inefficient.

1.1.3.3. Dipolar Interaction

The dipolar coupling interaction is an anisotropic, through space interaction described by a traceless and axially symmetric second rank tensor. The general form of the interaction Hamiltonian can be written in the lab frame as (1-11).

$$\widehat{H}_D = \sum_q^2 (-1)^q \, A_{2,q}^{(k,n)} \mathfrak{T}_{2,-q}^{(k,n)} \tag{1-11}$$

For a homonuclear interaction between like spins with similar resonance frequencies, the homonuclear dipolar Hamiltonian takes the form of (1-12) in the rotating frame under the secular approximation.

$$\widehat{H}_{D,II} = A_{2,0}^{(k,n)} \, \widehat{T}_{2,0}^{k,n} \tag{1-12}$$

The homonuclear dipolar Hamiltonian between like-spins n and k is given in (1-13). shown in (1-13).

$$\widehat{H}_{D,II} = \frac{\delta_D^{k,n}}{2} \frac{3\cos^2\beta - 1}{2} \left[3\,\hat{I}_{kz}\hat{I}_{nz} - \hat{I}_k \cdot \hat{I}_n \right] \tag{1-13}$$

$$\widehat{H}_{D,II} = \frac{\delta_D^{k,n}}{2} \frac{3\cos^2\beta - 1}{2} \left[2\,\hat{I}_{kz}\hat{I}_{nz} - \hat{I}_{kx}\hat{I}_{nx} - \hat{I}_{ky}\hat{I}_{ky} \right]$$

Upon expansion into raising and lowering operators, it is clear the homonuclear dipolar Hamiltonian allows for "flip flop" zero quantum transitions in addition to manipulation by the single transition operator, I_z., as shown in (1-14).

$$\widehat{H}_{D,II} = \frac{\delta_D^{k,n}}{2} \frac{3\cos^2\beta - 1}{2} \left[2\hat{I}_{kz}\hat{I}_{nz} - \hat{I}_k^+\hat{I}_n^- - \hat{I}_k^-\hat{I}_n^+ \right] \qquad (1\text{-}14)$$

The heteronuclear dipolar Hamiltonian is given in (1-15), where the Hamiltonian has been truncated as the resonant frequency between unlike spins becomes large and renders the ZQ flip flop terms non-secular.

$$\widehat{H}_{D,IS} = A_{2,0}^{(k,n)} \, \widehat{T}_{1,0}^k \, \widehat{T}_{1,0}^n \qquad (1\text{-}15)$$

$$= \frac{\delta_D^{k,n}}{2} \frac{3\cos^2\beta - 1}{2} [2\,\hat{I}_{kz}\hat{I}_{nz}]$$

Under both homo and heteronuclear couplings, the dipolar coupling constant can be extracted from the anisotropy parameter, δ_D and allows for determination of inter and intra-molecular distances with its form given in (1-16).

$$\delta_D^{(k,n)} = -\frac{2\mu_0}{4\pi} \frac{\gamma_k\gamma_n\hbar}{r_{(k,n)}^3} \qquad (1\text{-}16)$$

Importantly, the strength of the dipolar coupling is dependent on the gyromagnetic ratio of the coupled nuclei, γ, and the distance between the nuclei, $r_{k,n}$. While the dipolar interaction is averaged by magic angle spinning, as described in 1.1.3, the reintroduction or recoupling of dipolar interactions permits determination of inter and intramolecular distance constraints.

1.1.3 Magic Angle Spinning

The chemical shift and dipolar coupling interactions contain anisotropic contributions from second rank spatial tensors with eigenvalues that are dependent on orientation, and thus result in significant line broadening in the solid state under static conditions. In solution state NMR, these anisotropic interactions are averaged through

rapid molecular tumbling to yield narrow linewidths. In solids motional averaging and modulation of the second rank spatial tensor can be achieved by mechanical modulation using MAS. Under MAS the orientational dependence of the spatial tensor becomes time dependent with rapid rotation of the rotor at an angle $\beta = arccos(1/\sqrt{3}) \sim 54.74°$ with respect to the external field. At this angle, referred to as the magic angle, the term $(3\cos^2\beta - 1)$ contained in both the dipolar and anisotropic chemical shift Hamiltonians is zero. However, to fully describe the effect of MAS on the anisotropic Hamiltonian, average Hamiltonian theory (AHT) can be used.

The effective modulation of the NMR linewidth by MAS is dependent on the type of interaction present. The NMR linewidth is composed of inhomogeneous and homogenous contributions which are dependent on whether the interaction Hamiltonian for the spin system is self-commuting for all times [6].

If the Hamiltonian is self-commuting, then AHT indicates that all higher order terms containing commutators will vanish. The first three AHT terms are given in (1-17).

$$\overline{H^{(0)}} = \frac{\omega_r}{2\pi} \int_0^{\frac{2\pi}{\omega_r}} \hat{H}(t_1)dt_1$$

$$\overline{H^{(1)}} = -i\frac{\omega_r}{4\pi} \int_0^{\frac{2\pi}{\omega_r}} dt_2 \int_0^{t_2} \left[\hat{H}(t_2), \hat{H}(t_1)\right]dt_1$$

$$\overline{H^{(2)}} = -\frac{1}{6}\frac{\omega_r}{2\pi} \int_0^{\frac{2\pi}{\omega_r}} dt_3 \int_0^{t_3} dt_2 \int_0^{t_1} dt_1 \left\{\left[\hat{H}(t_3), \left[\hat{H}(t_2), \hat{H}(t_1)\right]\right]\right.$$

$$\left. + \left[\left[\hat{H}(t_3), \hat{H}(t_2)\right], \hat{H}(t_1)\right]\right\}$$

(1-17)

If higher order terms are vanishing under MAS, the interaction is deemed to be inhomogeneous. Such interactions include chemical shift anisotropy and heteronuclear dipolar couplings. Even at MAS frequencies less than the strength of the coupling interaction, MAS will result in spectral narrowing and generation of rotational sidebands. These systems are susceptible to "hole burning" upon irradiation and are single spin interactions which are uncoupled throughout the static powder line shape and contain Hamiltonian terms such as $\hat{I}_z$ and $\hat{I}_z\hat{S}_z$ [7].

Interactions for which the higher order average Hamiltonian terms are non-zero are termed homogenous interactions. These include homonuclear dipolar coupling networks which contain zero quantum (ZQ) "flip flop" terms that mediate spin diffusion and mediate thermal equilibration [8]. To narrow homogeneously broadened linewidths using MAS, the magnitude of the applied MAS frequency must be significantly greater than the coupling strength. For this reason, to effectively modulate [1]H-^{1}H dipolar coupling strengths on the order of 30 kHz, MAS frequencies greater than 100 kHz are required. In practice, most systems contain a mixture of homogenous and inhomogeneous broadening requiring MAS and use of homonuclear proton decoupling. The overall linewidth is narrowed linearly or quadratically with increased MAS frequency, as predicted by AHT when considering the inclusion of first order or higher order terms. While in the limit of infinitely fast spinning, all the higher order terms vanish, under finite MAS frequencies, higher order terms remain and contribute to the homogenous linewidth.

1.1.3 Proton-Detected MAS NMR

Previously, application of ^{1}H detection was limited in solid state NMR by poor resolution under conventionally applied MAS frequencies on the order of 20 kHz and achievable with 3.2 mm diameter rotors. While the CSA interaction of ^{1}H will be averaged at MAS frequencies in excess of 50 kHz at high fields, at minimum MAS frequencies of 100 kHz are typically used to attenuate homonuclear dipolar couplings in fully protonated samples. Such interactions are homogeneous under AHT theory and require MAS frequencies significantly higher than the interaction strength for efficient averaging. At ultrafast MAS frequencies, the higher order AHT terms discussed previously will be reduced and result in decreased linewidth. However, in fully protonated samples it has been estimated that MAS frequencies of least 300 kHz and up to 1200 kHz will be required to achieve coherence lifetimes and resolution comparable to that in solution [9-11]. Overcoming the instrumentation limitations currently restricting achievable MAS frequency is advantageous given the higher gyromagnetic ratio of protons yielding a sensitivity enhancement of 8 times for ^{1}H detection over ^{13}C. Importantly, extended coherence lifetime will enable high dimensionality experiments for improved resolution of proton detected spectra.

1.1.4 Dipolar Recoupling

While MAS allows for the acquisition of high-resolution spectra by averaging chemical shift anisotropies, it also attenuates dipolar couplings. The determination of inter and intra-molecular distances and orientations is the basis of structural techniques that have become critical in determining biomolecular structures. Dipolar couplings must be selectively reintroduced by interfering with the averaging process of MAS through

manipulation of the spin terms described in (1-11) and shown in Figure 1.1.This can be accomplished through a multitude of methods, such as rotor synchronized radio frequency (RFDR) pulses or rotational resonance (R^2) techniques in which the chemical shift difference between homonuclear spins is matched to a multiple of the MAS frequency. The case of RFDR in addition to second order recoupling sequences is discussed further in 1.1.4.1

1.1.4.1 Homonuclear Recoupling

Homonuclear dipolar recoupling can be achieved through zero quantum and double quantum techniques in which the effective

A $\bar{\omega}_D = 0$

B

C $\bar{\omega}_D = s\,\omega_D$

Figure 1.1. Dipolar Recoupling. (A) Modulation of spatial tensor to isotropic value by MAS. (B) RF pulses to modulate spin component of Hamiltonian. (C) RF pulses recouple dipolar coupling with a scaling factor s dependent on recoupling scheme used.

Hamiltonian contains terms of $\hat{I}_1^+\hat{I}_2^- + \hat{I}_1^-\hat{I}_2^+$ or $\hat{I}_1^+\hat{I}_2^+ + \hat{I}_1^-\hat{I}_2^-$, respectively. A common method of achieving homonuclear recoupling using a train of 180° pulses is radiofrequency driven recoupling (RFDR). RFDR employs a single π-pulse per rotor period to recouple the ZQ homonuclear "flip flop" terms, with the average Hamiltonian becoming cyclic over two rotor periods [12,13]. The 180° pulse in the middle of the rotor period inverts the chemical shift Hamiltonian and over the 2 rotor periods per cycle does not recouple chemical shift interactions.

Figure 1.2. Homonuclear Dipolar Recoupling. (A). Common homonuclear recoupling sequences of RFDR, DARR, and CORD. (B). Homonuclear dipolar correlation spectra of U-^{13}C isoleucine crystals at a MAS frequency of 40 kHz and external magnetic field of 18.8 T using RFDR (black), DARR (red), and CORD (blue). The CORD and DARR spectra were nearly identical in 2D correlation spectra, however, the relative signal intensities varied.

Importantly, the recoupling efficiency is strongly modulated by the isotropic chemical shift difference between the two homonuclear dipole coupled spins. The broad-banded nature of RFDR makes it subject to dipolar truncation under which the strong dipolar couplings between short range spin pairs interferes with the detection of weaker, long-range couplings. As such, in uniformly labeled ^{13}C samples, RFDR is primarily used for 1 bond correlations yielding spectral assignments. Other broad-banded homonuclear recoupling methods include dipolar assisted recoupling (DARR) and Combined R2$_n^v$-Driven Spin Diffusion (CORD) [14,15]. The pulse sequences for RFDR, CORD, and DARR are provided in Figure 1.2.

DARR and CORD are 2nd order sequences with recoupling dependent on second order AHT terms. These sequences are less sensitive to dipolar truncation effects and are useful in establishing long range correlations. DARR is achieved using a continuous wave (CW) mixing period where the RF field is applied to the proton spins and matched in amplitude to the rotary resonance condition of $\omega_r = \omega_{RF}$, where the MAS frequency is matched to the RF amplitude. CORD is often performed as a super cycled-composite pulse sequence composed of $R2_1^1$, $R2_1^2$, $R2_2^1$, and $R2_2^2$ blocks where the RF power onto the carbon spins is applied at $\omega_r = \omega_{RF}$ or $\frac{\omega_r}{2} = \omega_{RF}$. These mixing sequences can be used to provide two dimensional correlations, or used as building blocks for high dimensionality experiments, as discussed in Chapter 4.

1.1.4.2 Heteronuclear Recoupling

Most heteronuclear dipolar recoupling methods developed for biomolecules have focused on reintroduction of ^{13}C-^{15}N dipolar couplings using a train of 180° pulses with simultaneous strong proton homonuclear decoupling under moderate MAS frequencies. This is the case for rotation double echo resonance (REDOR) [16,17]. Heteronuclear recoupling is accomplished by applying two 180° pulses per rotor period which results in a sign change of the heteronuclear Hamiltonian between *I-S* spin pair. For REDOR between ^{13}C-^{15}N spin pair, ^{13}C spins are first polarized under cross polarization. Application of 2 180° pulses per rotor period on ^{15}N spins reintroduces ^{13}C-^{15}N dipolar couplings, while a 180° pulse in the middle of the rotor period applied to ^{13}C refocuses the isotropic chemical shift. REDOR is carried out as a difference experiment to reduce the effect of relaxation by observing a dephasing curve as a function of mixing time and
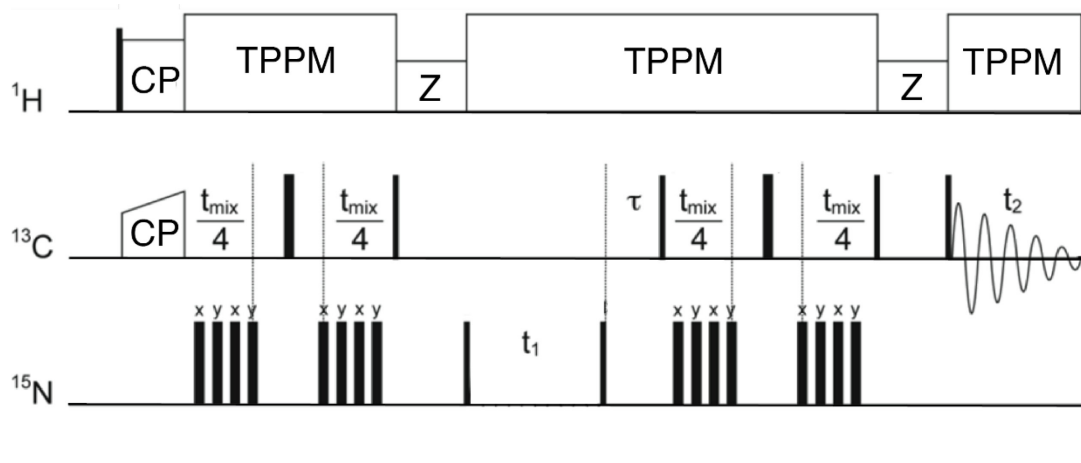
Figure 1.3. TEDOR Heteronuclear Dipolar Recoupling.

compared to an experiment in the absence of ^{15}N recoupling pulses. In practice, REDOR

is often performed as a frequency selective experiment (FS-REDOR) to selectively excite

and recouple a single ^{13}C-^{15}N pair using gaussian pulses placed at the midpoint of the

selective irradiation period at an even number of rotor cycles [17].

To selectively recouple several heteronuclear dipolar coupled spin pairs

simultaneously, z-filtered transferred echo double resonance (ZF-TEDOR) can be utilized

in which coherence transfers select dipolar coupled spins from a background of

uncoupled spins [18]. The addition of a z-filter suppresses the effect of homonuclear ^{13}C-

^{13}C J couplings which contribute to antiphase and multiple quantum coherences

generated during the REDOR mixing periods, which create phase twists and distorted

cross peaks. During the 3D ZF-TEDOR experiment, first *I* spin magnetization is generated

in the transverse plane via CP and is followed by reintroduction of the *I-S* dipolar coupling

using a REDOR period applied to the *S* spins which generates an antiphase coherence.

A pulse is then applied to the *I* spin to generate longitudinal I_zS_z magnetization, while the

antiphase coherence is dephased in the transverse plane under application of weak

proton homonuclear decoupling. A 90° pulse on the *S* channel generates *S* spin coherence in the transverse plane which is evolved under t_1 with *S* spin frequency encoding. Another 90° pulse at the end of the t_1 evolution period generates antiphase coherence on *I* spins. This is followed by a second REDOR period which converts the antiphase coherence to observable *I* spin magnetization, which evolves under a second evolution period during FID acquisition under the *I* spin chemical shift. The third dimension in a pseudo 3D ZF-TEDOR experiment is the incremented recoupling time.

REDOR and TEDOR variants have become the most used heteronuclear recoupling techniques under moderate MAS frequencies. However, recent application of [1]H-detected FS-REDOR has improved the sensitivity of detection, in addition to demonstrating an increase in the effective distances that can be measured afforded by the strength of [1]H-X heteronuclear dipolar couplings, relative to that of [13]C-^{15}N dipolar couplings [19]. However, application of REDOR and TEDOR as described will require very high RF demands as the rotor period is shortened. New methods such as deferred echo doubled resonance (DEDOR) have removed this limitation by extending the basic REDOR block of π-pulses over several rotor periods enabling low power RF pulses instead, with moderate signal to noise losses [20].
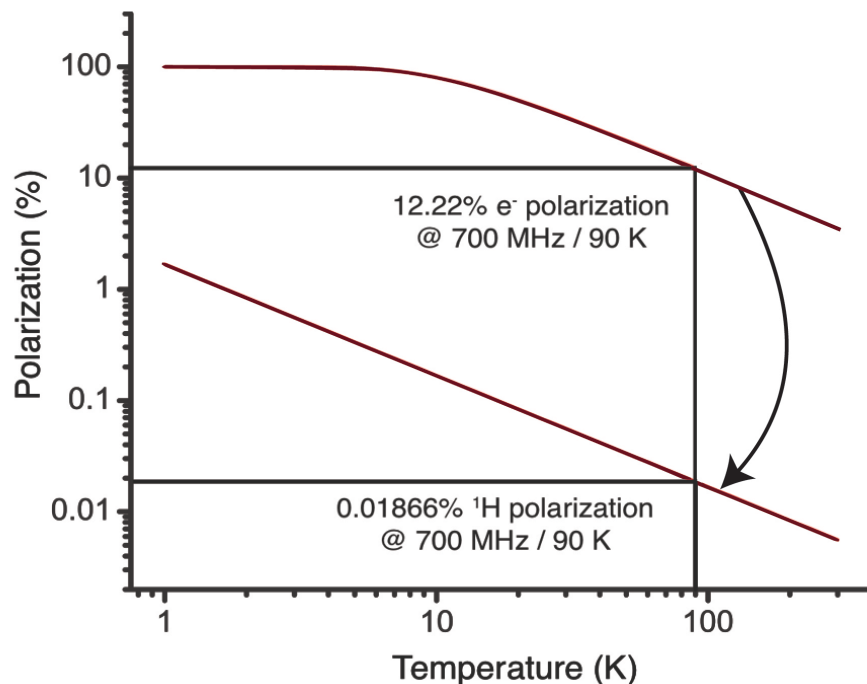
Figure 1.4. Spin polarization at 16.4 T. The larger 12.2% electron spin polarization at 16.4 T (700 MHz) and 90 K can be transferred to the nuclear spin, which has a ~660 times less polarization. This transfer of electron to nuclear spin polarization is the basis for the DNP process.

1.2 Dynamic Nuclear Polarization

NMR is inherently insensitive as the energy splitting between nuclear spin states is small and with low Boltzmann polarization at room temperature, on the order of 0.01866% at 16.4 T, as shown in Figure 1.4. The insensitivity of NMR requires significant signal averaging to achieve sufficient signal to noise in most experiments. A method of overcoming NMR insensitivity is to transfer the larger Boltzmann polarization of electron spins to nuclear spins using dynamic nuclear polarization (DNP), as shown in . Under DNP, stable free radicals are used as a polarizing agent, and electron-nuclear transitions are irradiated with high frequency microwaves (100-600 GHz) at cryogenic temperatures resulting in polarization transfer and enhancement of detected

NMR signal. Theoretical sensitivity enhancements of $\varepsilon \sim 660$ (γ_e / γ_{1H}) for ^{1}H could result in a time savings of 400,000, as the time savings goes as the square of the enhancement factor. Leveraging even a small fraction of this enhancement can enable the study of systems otherwise inaccessible without DNP, such as those at natural abundance. Typical enhancements on model samples range from 200-400, while on biologically relevant samples, enhancements on the order of 50-100 are common. Herein, we discuss the polarization transfer mechanisms and required instrumentation for DNP at high magnetic fields.

1.2.1 DNP Mechanisms

1.2.1.1 Cross Effect

The cross effect is a three-spin mechanism between two electron spins and one nuclear spin that is dominant when the EPR spectrum is significantly inhomogeneously broadened by g anisotropy. This results in a broad EPR spectrum with a breadth greater than the nuclear Larmor frequency, typically at high magnetic fields that satisfies the condition $\Delta > \omega_{0I} > \delta$. In such cases, the relevant Hamiltonian for the 3-spin cross effect is given by (1-18).

$$\widehat{H} = \omega_{0S,1}\hat{S}_{1z} + \omega_{0S,2}\hat{S}_z - \omega_{0I}\hat{I}_z + \left(A_1\hat{S}_{1z} + A_2\hat{S}_{2z}\right)I_z$$
$$+ \left(B_1\hat{S}_{1z} + B_2\hat{S}_{2z}\right)I_x + d\left(3\hat{S}_{1z}\hat{S}_{2z} - \vec{S_1}\cdot\vec{S_2}\right) - 2J\vec{S_1}\cdot\vec{S_2} \tag{1-18}$$

The first two terms represent the electron Zeeman interactions, while the third term represents the nuclear Zeeman interaction. The fourth and fifth terms describe the electron-nuclear hyperfine couplings, while the sixth term describes electron-electron
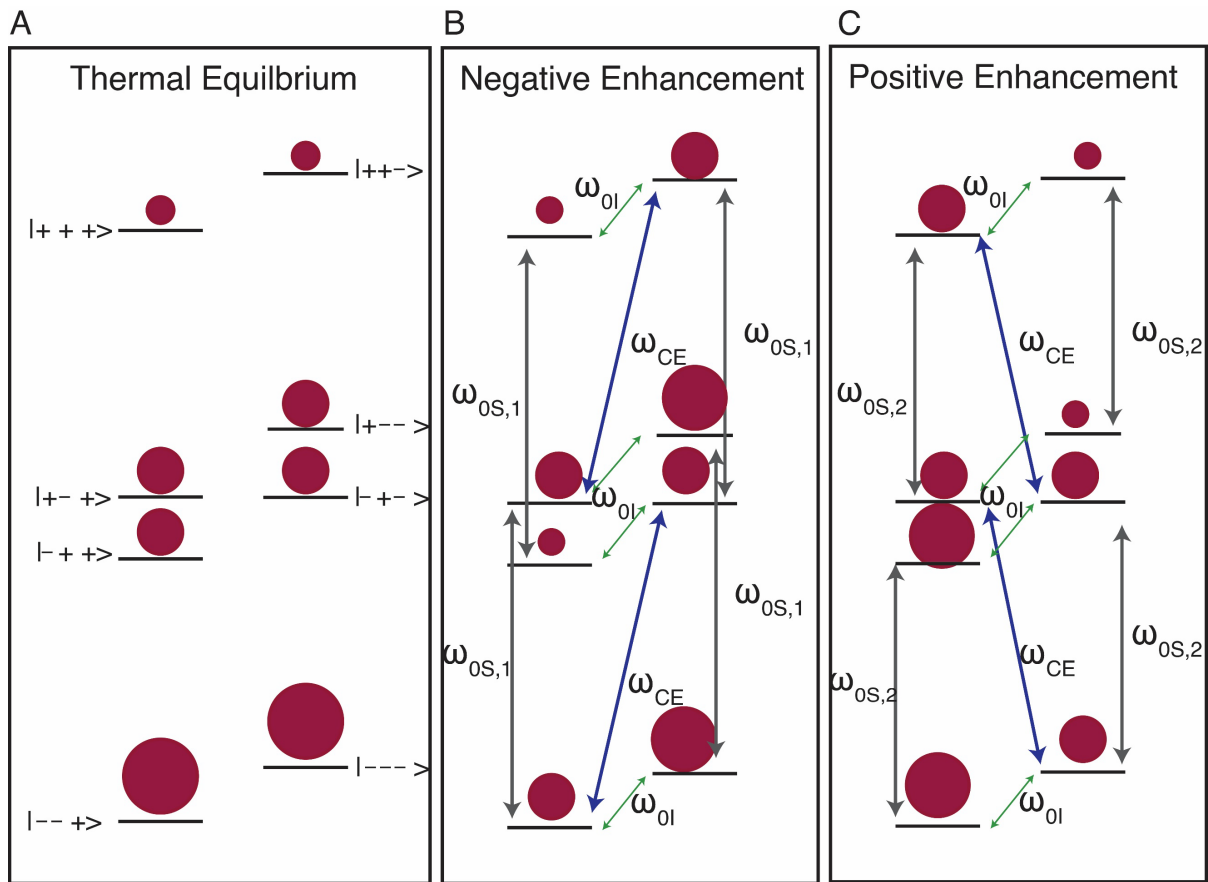
Figure 1.5 Cross Effect DNP. A) Population distribution at thermal equilibrium, degenerate energy levels shown for a rigid biradical at the cross effect matching condition. (B) Negative enhancement shown with microwave irradiation of $\omega_{0S,1}$. (C) Positive enhancement shown with microwave irradiation of $\omega_{0S,2}$

dipolar through space couplings. The final term describes the exchange interaction. This Hamiltonian can be used to solve for the energy level diagram in Figure 1.5. Maximum enhancements for the cross effect are obtained when a rigid biradical polarizing agent is employed, such as in AMUPol [21]. In a rigid biradical, electron spin pairs have a fixed orientation of g tensors, increasing the number of electron spin pairs that satisfy the condition $\left|\omega_{0S,1} - \omega_{0S,2}\right| \sim \omega_{0I}$. This is depicted in Figure 1.5 (A).where the central energy levels $\left|+-+\right>$ and $\left|-+-\right>$ are degenerate in energy, where the state is denoted
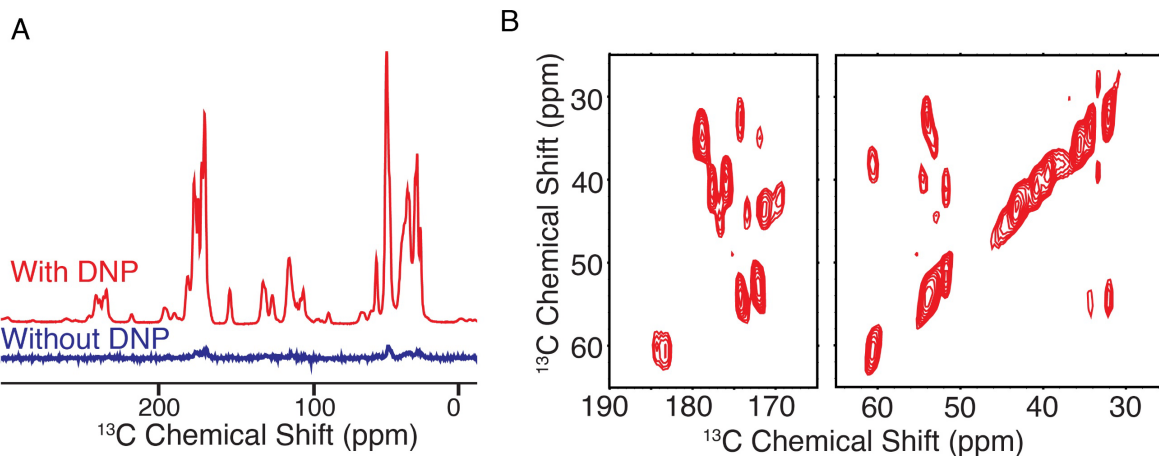
Figure 1.6. DNP of GNNQQNY. DNP of U-^{13}C/^{15}N GNNQQNY monoclinic crystals at ^{1}H Larmor frequency of 500 MHz with 10 mM AMUPol via cross effect mechanism. (A). At 90 K and a MAS frequency of 8 kHz, an enhancement of 110 was obtained via CP MAS. (B). 1.6 ms 1 bond RFDR experiment at a MAS frequency of 10 kHz and a temperature of 108 K. Considerable increase in linewidth is observed relative to room temperature spectra even in the rigid GNNQQNY monoclinic crystal.

$|e_1,e_2,n>$. Microwave irradiation at one electron resonance frequency results in a simultaneous spin flip of the second electron and the nuclear spin, generating a change in nuclear spin polarization. This is shown in Figure 1.5 (B) for the case of irradiation at $\omega_{0S,1}$ where saturation of the electron resonance transition generates increased nuclear spin population in the $|->$ nuclear state, resulting in a negative enhancement in nuclear spin polarization. A positive enhancement is obtained with irradiation at $\omega_{0S,2}$, shown in Figure 1.5 (C).

The probability of the electron spin pair having the required frequency matching to satisfy matching condition is linearly decreased with increasing magnetic field and magnitude of anisotropic g-tensor, as such the cross-effect efficiency scales with ω_{0I}^{-1} [22]. MAS increases cross effect efficiency at low spinning frequencies up to 3-5 kHz and remains approximately constant in temperature-controlled studies for frequencies

up to 40 kHz in the case of biradicals [23]. For a mixed biradical agent of HyTEK2, the CE enhancement however continued to increase with MAS frequencies up to 65 kHz [24]. CE enhancement is dependent on MAS frequency due to a series of avoided level crossings that result in exchange of spin polarization during a rotor period. This follows from the treatment of the time dependent modulation of the CE energy levels under MAS and is described in detail elsewhere [22,25,26].

1.2.1.2 Overhauser Effect

The Overhauser effect (OE) is a two spin DNP mechanism that generates a nuclear spin polarization enhancement when there is a difference in between the double quantum and zero quantum cross relaxation rates of an electron-nuclear spin system [27-31]. The OE is observed in cases where $\Delta \sim \delta < \omega_{0I}$, where Δ is the breadth of the EPR spectrum, δ is the EPR homogenous linewidth, ω_{0I} is the nuclear Larmor frequency. The Hamiltonian for the spin system under MAS is given by (1-19).

$$\hat{H} = [g_{iso} + g(\Omega_t)]\beta_e B_0 \hat{S}_z - g_n \beta_n B_0 \hat{I}_z - [A_{iso} + A_{dipolar}(\Omega_t)]\hat{S}_z I_z$$
$$+ A_{dipolar}^+(\Omega_t)\hat{S}_z \hat{I}_z^+ + A_{dipolar}^-(\Omega_t)\hat{S}_z \hat{I}_z^-$$

(1-19)

The first two terms describe the electron or nuclear Zeeman interaction in terms of the isotropic g value and the time dependent component due to MAS, given by Ω_t. The sources of fluctuating hyperfine couplings that are thought to be a dominant feature in generation of OE enhancement and are described in both the zero quantum and double quantum spaces in (1-19). Upon irradiation of the single quantum (SQ) EPR transition, an imbalance in zero quantum (ZQ) and double quantum (DQ relaxation rates drives
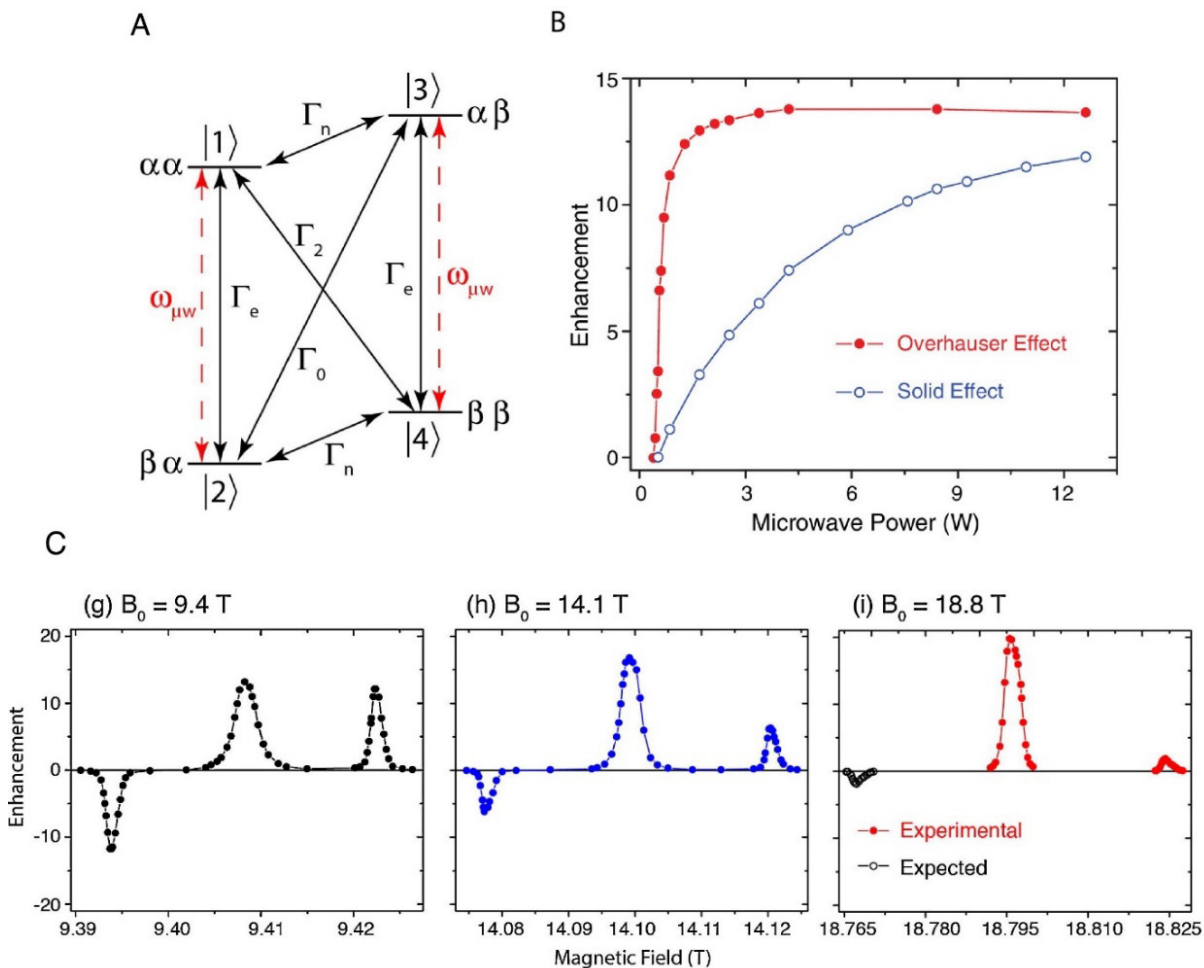
Figure 1.7. Overhauser Effect in insulating solids. Energy level diagram for the Overhauser effect. The imbalance between the zero quantum and double quantum cross relaxation rates, here as Γ_0 and Γ_2, respectively, generates a nuclear spin polarization enhancement. (B). The allowed, single quantum transitions of the OE are saturated at considerably lower microwave powers than the solid effect. (C). The OE is the only DNP mechanism known to scale favorably with the magnetic field. Figure adapted and reproduced from Ref [32] with permission from Elsevier.

population changes mediated by scalar and dipolar hyperfine couplings, respectively. In liquids and conducting solids the DQ transition is dominant, resulting in a negative OE enhancement. In insulating solids, the OE mechanism is thought to proceed through ZQ pathways as a positive enhancement was initially observed.

The OE is the only known DNP mechanism whose efficiency increases with increasing field strength. However, known polarizing agents that mediate OE enhancements are limited to narrow line radicals of 1,3-bisphenylene-2-phenylallyl (BDPA), sulfonated BDPA (SA-BDPA), and in limited mixed valence compounds. Availability of polarizing agents currently restricts the application of OE primarily to organic solids and samples with mobile electrons. New polarizing agents and continued work into theoretical pathways of OE in insulating solids are required for full realization of OE at high field in aqueous systems.

1.2.1.3 Solid Effect

The dominant enhancements for the solid effect are derived from a weakly allowed 2 spin transition through ZQ and DQ pathways [32,33]. However, recent studies have described a three spin solid effect (TSSE) with the largest enhancements to date under SE conditions, although this is effect is unlikely to be significant at high magnetic fields [34]. Herein, we will discuss the traditional two spin solid effect process which occurs when the homogenous linewidth and breadth of the EPR spectrum is less than the nuclear Larmor frequency $(\Delta, \delta < \omega_{0I})$. The relevant Hamiltonians are shown in (1-20) and can be written using perturbation theory with the perturbing Hamiltonian given by the pseudo secular term H_1, where ω_{0S} is the electron Larmor frequency, ω_{0I} is the nuclear Larmor frequency, A is the secular hyperfine coupling and B is the pseudo secular hyperfine coupling.

$$\widehat{H}_{SE} = \widehat{H}_0 + \widehat{H}_1$$

(1-20)

$$\hat{H}_0 = \omega_{0S}\hat{S}_z - \omega_{0I}\hat{I}_z + A\hat{S}_z\hat{I}_z$$

$$\hat{H}_1 = B\hat{S}_z\hat{I}_x = \frac{1}{2}B\hat{S}_z(\hat{I}_+ + \hat{I}_-)$$

H_0 is a diagonal Hamiltonian connecting pure states and does not lead to polarization transfer upon microwave irradiation. However, the perturbing Hamiltonian upon microwave irradiation at $\omega_m = \omega_{0S} \pm \omega_{0I}$ results in state mixing via ZQ and DQ transitions with a state mixing coefficient given by $q = \dfrac{B}{2\omega_{0I}}$. A zero quantum transition with microwave irradiation at $\omega_m = \omega_{0S} + \omega_{0I}$ results in a negative enhancement, while a double quantum transition with microwave irradiation at $\omega_m = \omega_{0S} - \omega_{0I}$ results in a positive enhancement, for nuclear spins with $\gamma > 0$.

The state mixing coefficient indicates that the efficiency of polarization transfer decreases with increasing Larmor frequency and the transition probability scales with
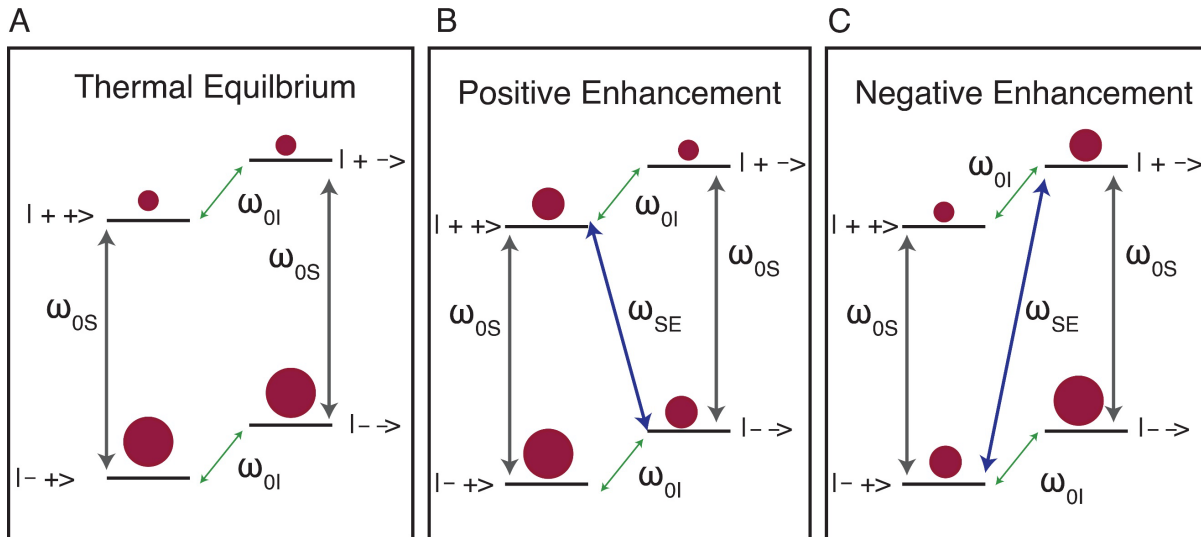
Figure 1.8. Solid Effect Mechanism. Energy level diagrams for (A) thermal equilibrium for an electron-nuclear spin pair. (B). Upon irradiation at $\omega_m = \omega_{0S} - \omega_{0I}$, the positive enhancement via DQ spin transition is generated. (C). Irradiation at $\omega_m = \omega_{0S} + \omega_{0I}$ yields a negative enhancement via ZQ spin transitions.

ω_{0I}^{-2} . Therefore, at the high fields required for study of biomolecules and available

microwave power of ~ 10 W, the solid effect is not an efficient DNP mechanism.

1.2.2 DNP Instrumentation

The typical DNP experiment requires three fundamental components: (1)

microwave source with corrugated or overloaded waveguide to connect to the (2) NMR

probe with electron and nuclear spin channels, and (3) a sample containing polarizing

agent. For high field DNP, a high power gyrotron is used to generate microwave power

usually in the range of ~ 10-50 W to the sample. However, recent advancements in solid

state sources have yielded ~ 250-500 mW of power at 250-263 GHz and will be

discussed in Chapter 3. In a gyrotron, electrons are accelerated from an electron gun

through a strong magnetic field in which they resonate at their cyclotron resonance

frequency. The electrons then encounter an interaction cavity in which the helical or

transverse component of their cyclotron motion is converted to microwave energy. This

microwave beam is directed to a mode converter which outputs the coherent microwave

beam with a desired gaussian-like beam that will efficiently propagate through a

corrugated waveguide to the sample chamber with low power losses. The waveguide

mates with the NMR probe to deliver microwaves to the sample chamber.

The NMR probe generally consists of transmission lines that couple RF

irradiation from the transmitter to the NMR sample coil allowing for high power RF

pulses to be delivered for excitation of specific nuclei. The probe contains the sample

chamber which is composed of a stator enabling MAS frequencies dictated by the rotor

size and spinning gas used. The NMR probe also integrates vacuum jacketed cryogenic

transfer lines to deliver the spinning gases to the bearings and drive plate. The transfer lines typically deliver nitrogen gas that has been cooled using a heat exchanger to temperatures < 100 K, required to extend electron T_1 for efficient polarization transfers. Finally, the sample contained in the NMR rotor must be doped with an efficient polarizing agent typically suspended in a glassy matrix composed of deuterated glycerol, deuterated water and water in a 60:30:10 by volume ratio. At high magnetic fields, these polarizing agents are typically nitroxide biradicals such as AMUPol or TOTAPOL. However, new biradicals containing both a narrow line radical, such as trityl, and a radical with large inhomogeneous broadening such as TEMPO, termed TEMTriPols [25] have become popular. This new class of polarizing agents have been shown to yield larger enhancements with decreased depolarization at high magnetic fields and offer an exciting new radical source for high field DNP [35].

1.3 Overview of Thesis

This thesis is focused on the development of methods for both sensitivity and resolution enhancements. In the first two chapters, sensitivity enhancements via DNP are discussed. The first chapter describes the mechanism of Overhauser Effect (OE) sensitivity enhancements in insulating solids. Importantly, this is the only DNP mechanism that exhibits a favorable scaling factor with applied magnetic field, and as such is the most promising high field DNP mechanism. We demonstrate the generation of strong positive Overhauser enhancements (OE) with less than 200 mW of microwave irradiation and use selective deuteration to elucidate the role of individual hyperfine-

coupled protons on the BDPA radical. This work provides a basis for the improved development of high field DNP radicals with fluctuating hyperfine interactions.

The continued expansion of MAS DNP toward biological samples requires adoption of rotors with diameters < 1.3 mm at high magnetic fields. While such systems have been realized in limited quantities the typical enhancement obtained in such systems remains considerably lower than the theoretical maximum enhancements. To address this, we introduce improved microwave coupling schemes via axial irradiation and demonstrate theoretical improvements in the electron Rabi field of > 60% in 3.2 mm rotor systems and > 100% improvements in 0.7 mm and 1.3 mm rotor systems. We provide experimental results of MAS spinning stability in 3.2 mm rotors at 95 K using the modified axial bearing required for axial irradiation schemes, in addition to introducing a method to measure the Bernoulli displacement of MAS rotors. In the case of the 0.7 mm and 1.3 mm rotor systems at 460-593 GHz, the microwave wavelength becomes ~0.5 times the pitch of the NMR coil, resulting in reduced transverse coupling efficiency. In contrast, the short sample length is subject to reduced dielectric losses in the sample, which promotes generation of electron Rabi fields in the 0.7 mm and 1.3 mm rotors. The sample length is also less than or on the order of Rayleigh length of the microwave beam at high fields with minimal associated divergence of the microwave beam. These combined factors make the use of axial coupling schemes important in the adoption of small diameter MAS rotors at high field for DNP.

While these two sections describe sensitivity enhancements under DNP, the later chapters are focused on ^{1}H detected MAS NMR. We demonstrate the first ^{1}H detected MAS NMR study on the arctic mutant of A$\beta_{1\text{-}42}$, which is implicated in the pathogenesis

of early onset familial AD. Despite resolution limitations in the sample as a function of MAS frequency and sample heterogeneity, we determine the core fibril structure of E22G Aβ_{1-42}, is conserved relative to that of the wild type fibril and is monomorphic in nature. The E22G Aβ_{1-42} sample was only available in limited quantities and underscores the importance of proton detected methods for such critical biological samples. However, a full structural study requires further spectroscopic methods development, improved sensitivity, and improved spectral resolution.

To address the remaining resolution limitations under both ambient NMR and cryogenic MAS DNP, we developed a novel laser micromachining strategy to realize 0.7 mm diameter diamond rotors with the potential to achieve MAS frequencies > 200 kHz when combined with helium gas and helium compatible bearings. First, we describe the mechanism of material ablation and characterize the effects of pulse energy, irradiation scheme and pulse number on the achievable taper angle in high aspect ratio holes. During this study, we measured the laser induced strain from diamond laser machining We then apply a dual-sided axial machining strategy to fabricate 0.7 mm diamond rotors, and further demonstrate stable operation up to 124 kHz in addition to ^{1}H detected MAS NMR results.

In the final chapter, discussion is focused on the use of digital fabrication and 3D printing methods to advance instrumentation needs beyond that of magnetic resonance. The use of such methods is highlighted and reviewed for use in UV/VIS spectrophotometry, Fourier Transform Infrared and Raman spectroscopy, Mass spectrometry, and NMR. Overall, the chapter discusses the specific cases of 3D printing

for molecular and atomic scale analytical techniques and the improvement in accessible and affordable instrumentation for physical chemistry labs at large.

Overall, the areas of focus in this thesis describe several resolution and sensitivity advancements that when combined in the future could provide sufficient sensitivity and resolution with which to study ex-vivo amyloid plaque samples and other exogenous biomedically relevant samples.

1.4 References

1   Abragam, A. *The principles of nuclear magnetism*. (Oxford university press, 1983).

2   Ernst, M. & Meier, B. H. *Lecture Notes High-Resolution Solid State NMR: Principles and Applications*. (2014).

3   Levitt, M. H. *Spin dynamics: basics of nuclear magnetic resonance*. (John Wiley & Sons, 2013).

4   Mueller, L. J. Tensors and rotations in NMR. *Concepts in Magnetic Resonance Part A* **38A**, 221-235 (2011). https://doi.org:https://doi.org/10.1002/cmr.a.20224

5   Rovnyak, D. Tutorial on analytic theory for cross-polarization in solid state NMR. *Concepts in Magnetic Resonance Part A* **32A**, 254-276 (2008). https://doi.org:https://doi.org/10.1002/cmr.a.20115

6   Haeberlen, U. & Waugh, J. S. Coherent Averaging Effects in Magnetic Resonance. *Physical Review* **175**, 453-467 (1968). https://doi.org:10.1103/PhysRev.175.453

7   Portis, A. M. Electronic Structure of F Centers: Saturation of the Electron Spin Resonance. *Physical Review* **91**, 1071-1078 (1953). https://doi.org:10.1103/PhysRev.91.1071

8   Maricq, M. M. & Waugh, J. S. NMR in rotating solids. *The Journal of Chemical Physics* **70**, 3300-3316 (1979). https://doi.org:10.1063/1.437915

9   Böckmann, A., Ernst, M. & Meier, B. H. Spinning proteins, the faster, the better? *Journal of Magnetic Resonance* **253**, 71-79 (2015). https://doi.org:https://doi.org/10.1016/j.jmr.2015.01.012

10   Penzel, S. *et al.* Spinning faster: protein NMR at MAS frequencies up to 126 kHz. *Journal of Biomolecular NMR* **73**, 19-29 (2019). https://doi.org:10.1007/s10858-018-0219-9

11   Xue, K. *et al.* Magic-Angle Spinning Frequencies beyond 300 kHz Are Necessary To Yield Maximum Sensitivity in Selectively Methyl Protonated Protein Samples in Solid-State NMR. *The Journal of Physical Chemistry C* **122**, 16437-16442 (2018). https://doi.org:10.1021/acs.jpcc.8b05600

12   Bennett, A. E., Griffin, R. G., Ok, J. H. & Vega, S. Chemical shift correlation spectroscopy in rotating solids: Radio frequency‐driven dipolar recoupling and longitudinal exchange. *The Journal of Chemical Physics* **96**, 8624-8627 (1992). https://doi.org:10.1063/1.462267

13   Bennett, A. E. *et al.* Homonuclear radio frequency-driven recoupling in rotating solids. *The Journal of Chemical Physics* **108**, 9463-9479 (1998). https://doi.org:10.1063/1.476420

14   Takegoshi, K., Nakamura, S. & Terao, T. 13C–1H dipolar-assisted rotational resonance in magic-angle spinning NMR. *Chemical Physics Letters* **344**, 631-637 (2001). https://doi.org:https://doi.org/10.1016/S0009-2614(01)00791-6

15   Hou, G., Yan S Fau - Trébosc, J., Trébosc J Fau - Amoureux, J.-P., Amoureux Jp Fau - Polenova, T. & Polenova, T. Broadband homonuclear correlation spectroscopy driven by combined R2(n)(v) sequences under fast magic angle

spinning for NMR structural analysis of organic and biological solids. *Journal of Magnetic Resonance* (2013).

16 Pan, Y., Gullion, T. & Schaefer, J. Determination of C☐N internuclear distances by rotational-echo double-resonance NMR of solids. *Journal of Magnetic Resonance (1969)* **90**, 330-340 (1990). https://doi.org:https://doi.org/10.1016/0022-2364(90)90138-Y

17 Jaroniec, C. P., Tounge, B. A., Herzfeld, J. & Griffin, R. G. Frequency Selective Heteronuclear Dipolar Recoupling in Rotating Solids: Accurate 13C−15N Distance Measurements in Uniformly 13C,15N-labeled Peptides. *Journal of the American Chemical Society* **123**, 3507-3519 (2001). https://doi.org:10.1021/ja003266e

18 Jaroniec, C. P., Filip, C. & Griffin, R. G. 3D TEDOR NMR Experiments for the Simultaneous Measurement of Multiple Carbon−Nitrogen Distances in Uniformly 13C,15N-Labeled Solids. *Journal of the American Chemical Society* **124**, 10728-10742 (2002). https://doi.org:10.1021/ja026385y

19 Ghosh, M. & Rienstra, C. M. 1H-Detected REDOR with Fast Magic-Angle Spinning of a Deuterated Protein. *The Journal of Physical Chemistry B* **121**, 8503-8511 (2017). https://doi.org:10.1021/acs.jpcb.7b07313

20 Jain, M. A.-O., Rajalakshmi, G., Madhu, P. K., Agarwal, V. A.-O. & Mote, K. A.-O. Overcoming Prohibitively Large Radiofrequency Demands for the Measurement of Internuclear Distances with Solid-State NMR under Fast Magic-Angle Spinning. (2020).

21 Sauvée, C. *et al.* Highly Efficient, Water-Soluble Polarizing Agents for Dynamic Nuclear Polarization at High Frequency. *Angewandte Chemie International Edition* **52**, 10858-10861 (2013). https://doi.org:https://doi.org/10.1002/anie.201304657

22 Mentink-Vigier, F. *et al.* Fast passage dynamic nuclear polarization on rotating solids. *Journal of Magnetic Resonance* **224**, 13-21 (2012). https://doi.org:https://doi.org/10.1016/j.jmr.2012.08.013

23 Mentink-Vigier, F., Akbey, Ü., Oschkinat, H., Vega, S. & Feintuch, A. Theoretical aspects of Magic Angle Spinning - Dynamic Nuclear Polarization. (2015).

24 Berruyer, P. *et al.* Dynamic nuclear polarization enhancement of 200 at 21.15 T enabled by 65 kHz magic angle spinning. *The Journal of Physical Chemistry Letters* **11**, 8386-8391 (2020).

25 Mentink-Vigier, F. *et al.* Efficient cross-effect dynamic nuclear polarization without depolarization in high-resolution MAS NMR. *Chemical Science* **8**, 8150-8163 (2017). https://doi.org:10.1039/C7SC02199B

26 Thurber, K. R. & Tycko, R. Theory for cross effect dynamic nuclear polarization under magic-angle spinning in solid state nuclear magnetic resonance: The importance of level crossings. *The Journal of chemical physics* **137**, 084508 (2012).

27 Abragam, A. & Goldman, M. Principles of Dynamic Nuclear Polarization. *Reports on Progress in Physics* **41**, 395-467 (1978). https://doi.org:10.1088/0034-4885/41/3/002

28   Can, T. V. *et al.* Overhauser effects in insulating solids. *The Journal of Chemical Physics* **141**, 064202 (2014). https://doi.org:10.1063/1.4891866

29   Carver, T. R. & Slichter, C. P. Polarization of Nuclear Spins in Metals. *Physical Review* **92**, 212-213 (1953). https://doi.org:DOI 10.1103/PhysRev.92.212.2

30   Carver, T. R. & Slichter, C. P. Experimental Verification of the Overhauser Nuclear Polarization Effect. *Physical Review* **102**, 975-980 (1956). https://doi.org:DOI 10.1103/PhysRev.102.975

31   Overhauser, A. W. Polarization of Nuclei in Metals. *Physical Review* **92**, 411-415 (1953). https://doi.org:10.1103/PhysRev.92.411

32   Corzilius, B., Smith, A. A. & Griffin, R. G. Solid effect in magic angle spinning dynamic nuclear polarization. *The Journal of Chemical Physics* **137**, 054201 (2012). https://doi.org:10.1063/1.4738761

33   Smith, A. A., Corzilius, B., Barnes, A. B., Maly, T. & Griffin, R. G. Solid effect dynamic nuclear polarization and polarization pathways. *The Journal of chemical physics* **136**, 01B602 (2012).

34   Tan, K. O., Mardini, M., Yang, C., Ardenkjær-Larsen, J. H. & Griffin, R. G. Three-spin solid effect and the spin diffusion barrier in amorphous solids. *Science Advances* **5**, eaax2743 (2019). https://doi.org:10.1126/sciadv.aax2743

35   Hediger, S., Lee, D., Mentink-Vigier, F. & De Paëpe, G. in *eMagRes*   105-116 (2018).

Chapter 2 : Overhauser Dynamic Nuclear Polarization in Selectively Deuterated BDPA Radicals

2.1 Introduction

Dynamic nuclear polarization (DNP) has emerged as a powerful method to overcome the inherent low sensitivity of nuclear magnetic resonance (NMR) spectroscopy by transferring the large polarization of unpaired electron spins to the nuclei of interest, typically ^1H [1-3]. DNP provides sensitivity enhancements of 2-3 orders of magnitude, enabling the study of biomolecules and materials that are sensitivity limited [4-13] and where structural studies using dipole recoupling are difficult [14-18]. The success of these experiments has stimulated the sustained development of continuous-wave (CW) solid-state devices and gyrotrons that generate microwave powers ranging from several hundred milliwatts to tens of watts, respectively. In turn, these sources provide microwave irradiation to drive electron or electron-nuclear spin transitions that facilitate CW-DNP, enabling experiments at magnetic fields up to 21.1 T [19-26].

There are four known CW-DNP mechanisms–the solid effect (SE), cross effect (CE), thermal mixing (TM), and the Overhauser Effect (OE). The SE involves microwave excitation of weakly allowed *forbidden* zero-quantum (ZQ) or double-quantum (DQ) transitions in coupled electron-nuclear spin systems [27-29]. The CE involves coupled electron-electron-nuclear spin systems where microwave irradiation at the resonance frequency of one of the two participating electron spins alters the equilibrium

polarization difference between the electrons. A fraction of the polarization difference is subsequently transferred to the nucleus via three-spin transitions when the difference between the electron resonance frequencies matches the nuclear resonance frequency [30-34]. TM is similar to CE, except the dipolar interaction between electron spins is homogeneous, and the consequent fast electron spectral diffusion holds the electron spin system in local equilibrium [35-37]. In contrast to other CW-DNP mechanisms that can all be described by time-independent electron-nuclear and electron-electron interactions, the OE relies on the time-dependence of the electron-nuclear couplings to drive the electron-nuclear cross-relaxation. Microwave irradiation of the allowed single quantum (SQ) electron transition results in ZQ and DQ cross-relaxation processes that occur at unequal rates and drive the buildup of nuclear polarization. The positive or negative sign of the observed nuclear enhancement is determined by the relative sizes of the ZQ and DQ cross-relaxation rates, respectively.

In the early 1950s the OE was the initial DNP mechanism proposed for studies of conducting solids, [2] and it was experimentally verified shortly thereafter by Carver and Slichter [38,39]. Much more recently, the OE in insulators was observed using the narrow line radicals SA-BDPA [40] and BDPA [41], which were under investigation initially as polarizing agents for SE-DNP. These recent experiments demonstrated that among the CW-DNP mechanisms in solids, the OE has three crucial advantages. First, the allowed SQ transition is saturated at modest microwave powers, enabling low-power microwave sources for DNP [41]. Second, unlike the other CW-DNP techniques, the enhancement factor of the OE is proportional to the external magnetic field strength making it an attractive choice among DNP methods to pursue at high magnetic fields

[41,42]. Third, the OE enhancement factor is observed to be proportional to the magic angle spinning (MAS) frequency. The observation is rationalized by a source-sink diffusion model with paramagnetic impurities or dissolved oxygen serving as polarization sinks [43]. Furthermore, the OE in insulating solids doped with BDPA has been observed at temperatures ranging from 1.2 K to room temperature [42,44] The source of the time-dependence in the electron-nuclear hyperfine couplings that drives cross-relaxation in insulating solids remains unknown. Recently, Pylaeva *et al.* proposed intra-molecular charge transfer mediated by the mixed-valence nature of BDPA as the source of electron-nuclear hyperfine fluctuations. They computationally predicted the oscillation of hyperfine couplings in the spin system was a consequence of electron hopping between the fluorene moieties and suggested that the rate of oscillation falls in the range required for the OE [45,46]. Guided by this insight, they recently synthesized two new mixed-valence radicals, namely tetrakis(4-methoxyphenyl)benzene-1,4-diamine radical, and tetrakis(4-methoxyphenyl)benzene-1,3-diamine radical, and, in the solvent tetrachloroethylene (TCE), demonstrated higher OE enhancements with these radicals than in samples doped with BDPA [47].

Although DNP experiments were initially reported in 1953 and BDPA has been used for 50 years as a polarizing agent, the details of the polarization transfer mechanism from the radical to the bulk nuclei via either the SE, CE or OE-DNP have only recently been investigated. The three-spin solid effect was used to shed light on the mechanism of polarization transfer in trityl radicals showing that the spin diffusion barrier is < 6 Å, and the first polarization transfer step is to ^{1}H spins on the trityl molecule itself [48]. In H_2O-glycerol matrices polarization is then transferred to glycerol

molecules clustered near trityl radicals and is furthered relayed to the bulk solvent via spin diffusion. Note that trityl spectra do not display resolved hyperfine structure. In a second set of experiments, Stern *et al.* developed microwave gated hyperpolarization resurgence (HypRes) as an approach that allows separation of the contribution of nuclear spin diffusion from the efficiency of the core DNP mechanism [49]. These experiments were applied in the context of CE-DNP in bis-nitroxides and determined the spin diffusion barrier to be < 3 Å.

In this paper we discuss the roles of electron-nuclear hyperfine interactions in the BDPA radicals responsible for the OE-DNP transfer by performing EPR and DNP experiments on selectively deuterated BDPA. Selective deuteration attenuates the specific isotropic couplings and consequently modulates the difference between ZQ and DQ cross-relaxation rates active in the electron-nuclear spin systems. Synthetic routes were developed to synthesize three BDPA radicals, with ^{2}H labels on entire fluorene moieties, or selectively on positions 1,3,6,8 (alternatively labeled α and γ) on the fluorene moieties and the orthogonal positions 2,4,5,7 (alternatively labeled β and δ). We show that the protons with a_{iso}~5.4 MHz isotropic hyperfine couplings at positions 1,3,6,8 in the fluorene moieties are crucial in obtaining positive DNP enhancements via the OE in BDPA. Furthermore, we present preliminary evidence that the protons with weaker isotropic couplings at positions 2,4,5,7 on the fluorene moieties aid substantially in the efficient relay of polarization from the strongly coupled protons in the radical to the bulk ^{1}H in the surrounding matrix.

2.2 Experimental

2.2.1 Synthesis and Sample Preparation

Investigation of the OE in 1,3-bisdiphenylene-2-phenylallyl (BDPA) radicals required the development of synthetic routes that would enable selective ^{2}H labelling of orthogonal positions on the fluorene moieties, i.e., 1,3,6,8 and 2,4,5,7. Conventionally, the deuteration of aromatic compounds requires harsh reaction conditions, costly
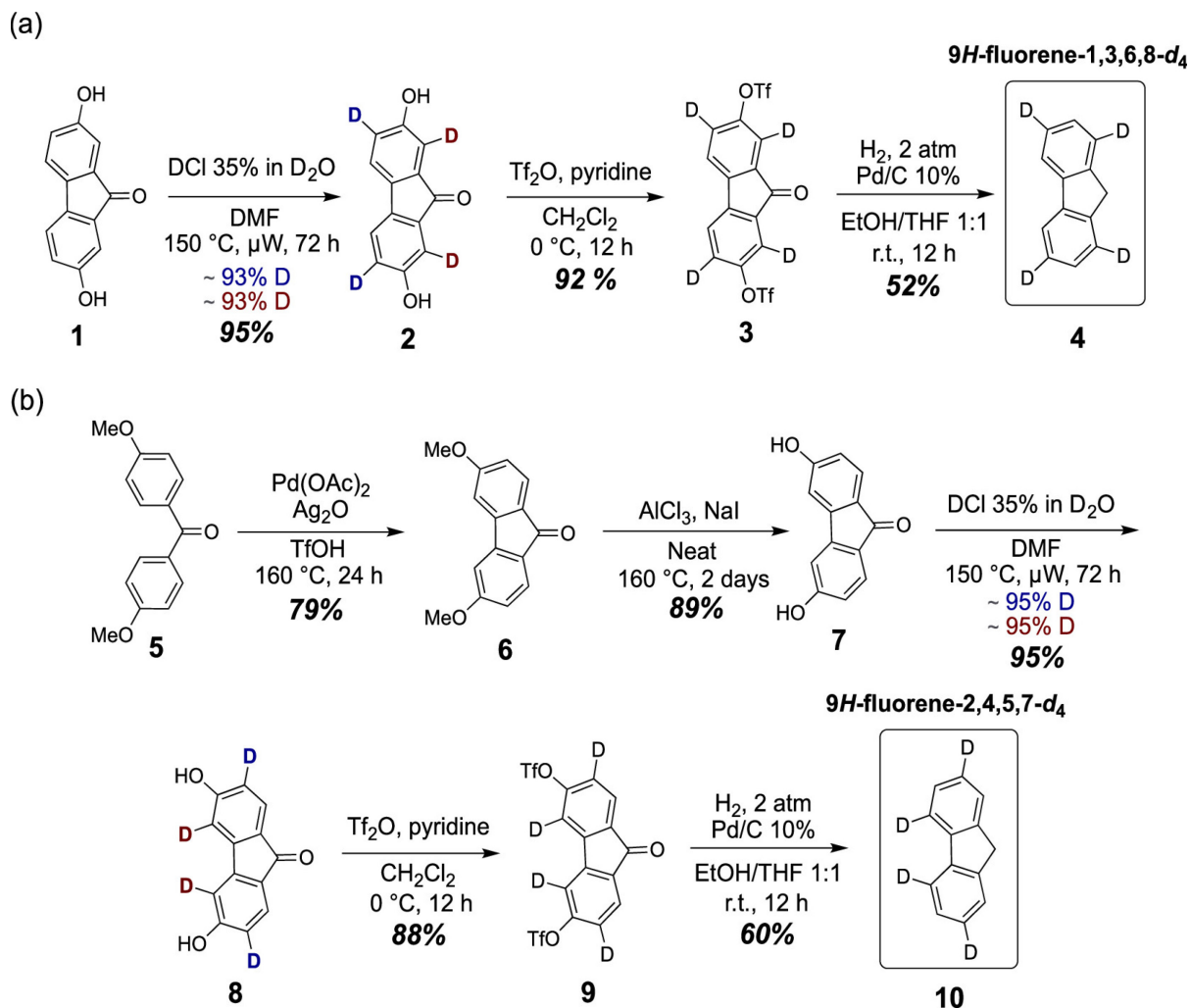
Figure 2.1 Synthetic Routes to Selectively Deuterated Fluorenes (a) 9*H*-Fluorene-1,3,6,8-*d*₄ and (b) 9*H*-Fluorene-2,4,5,7-*d*₄

catalysts and/or extended reaction times as aromatic hydrogens are not labile and often lead to poor deuterium incorporation [50-55]. Efficient direct H/D exchange at alternating positions on arenes is typically achieved using activating groups, specifically ortho/para directors such as phenols and anilines [56-58].

Several deuteration techniques were attempted and were ultimately unsuccessful, including selective bromination and nitration of fluorene followed by deuterium substitution and synthesis of fluorene moieties from commercial deuterated arenes. None of these methods either yielded the desired products or deuteration patterns. Instead, deuterium incorporation into arenes was achieved through an acid-catalyzed electrophilic aromatic hydrogen exchange of phenolic systems, which was rationalized to be efficient for fluorene derivatives **1** and **7** (Figure 2.1). This method allows deuteration at the positions ortho to the hydroxyl groups, which is desirable for the deuteration patterns targeted in this study. Note that the para positions are blocked in both substrates. The starting materials used in these synthetic routes are dihydroxy fluorenone derivatives, and so the resulting products contain hydroxyl and carbonyl groups that will have to be removed. Lastly, this type of reaction is performed in acidic aqueous media, in which all fluorene derivatives suited for the synthesis of targeted substrates are not soluble, and therefore the use of non-aqueous solvents was required.

Figure 2.1 shows the synthetic route developed for the key synthetic intermediates 9*H*-fluorene-1,3,6,8-d_4 and 9*H*-fluorene-2,4,5,7-d_4. Fluorenone derivatives were used primarily as a result of compound **1** being inexpensive and commercially available. Compound **7** was synthesized through modified literature procedures [59,60] . Fluorenone derivative **6** was obtained from diaryl ketone **5** through a Pd-catalyzed
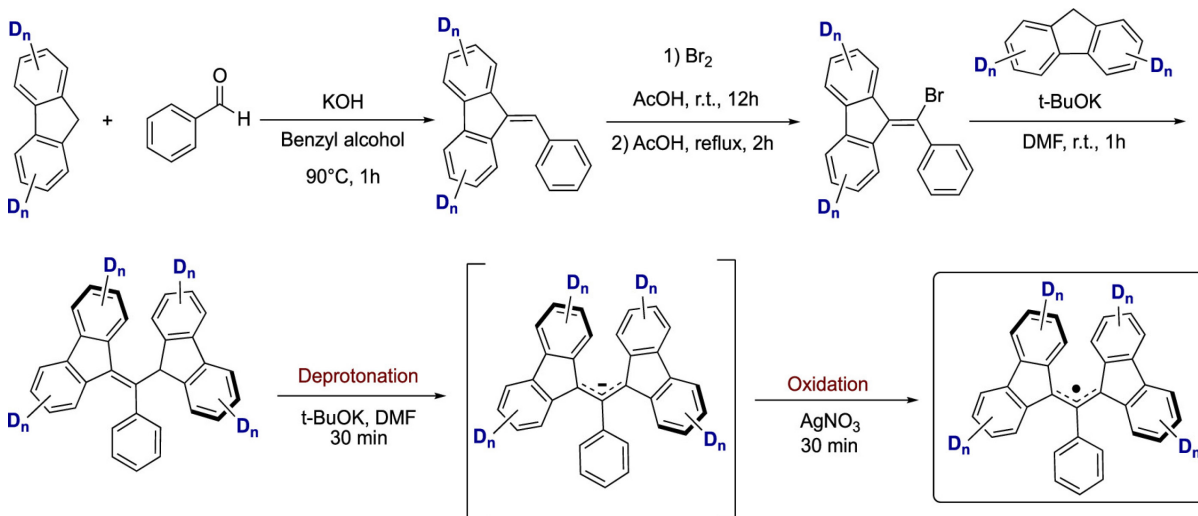
Figure 2.2. General Synthetic Route to Selectively Deuterated BDPA Radicals

oxidative cyclization in a 79% yield. The aryl methoxy groups were subsequently cleaved

using aluminum chloride and sodium iodide to give compound **7** in an 89% yield. The

solubility of starting materials **1** and **7** in acidic aqueous media was

insufficient for synthesis even at elevated temperatures, so a 35% DCl in a 1:1 D_2O/DMF

mixture was used. Microwave assisted methods also proved to integral in our synthesis.

Reactions were initially conducted with conventional heating, and minimal conversion was

observed after 3 days at 140 °C. High boiling, polar solvents DMSO, DMAc, and NMP

yielded no conversion. Deuterium incorporation was monitored by NMR every 12 h and

reached >93% and >95% after 72 h through microwave assistance using a power of 75

W to reach a reaction temperature of 150 °C for compounds **2** and **8**, respectively. Both

compounds were ultimately obtained in a yield of 95%. Decomposition of the DMF

resulted in pressure buildup inside the microwave vial, which had to be released

periodically for a total of 5 times. The hydroxyl groups were subsequently converted into

triflates using triflic anhydride to give compounds **3** and **9** in 92% and 88% yields,

respectively. Removal of the triflate groups was accomplished by palladium-catalyzed hydrogenolysis using hydrogen gas. During the characterization of the latter reaction, a minor product was isolated and was identified as final compound **4**. This led to the conclusion that the carbonyl group of the fluorenone could be removed as well through reductive hydrogenation. By increasing the temperature of reaction from room temperature to 50 °C, complete reduction of respective carbonyls gave key intermediates **4** and **10** as the major products in 52% and 60% yield, respectively. Figure 2.2 details the general synthetic route to BDPA radicals once selectively deuterated fluorene moieties were obtained, which was based on a previous report [61]. Condensation of selectively deuterated fluorene moieties with benzaldehyde yielded 9-benzylidene-9*H*-fluorene derivatives, which subjected to a two-step process by alkene bromination followed by dehydrobromination to yield 9-(bromo(phenyl)methylene)-9*H*-fluorene derivatives. These derivatives were then condensed with deuterated fluorene derivatives via a nucleophilic addition-elimination sequence to form the neutral precursor to BDPA radicals (BDPA-H). Finally, the radical formation was carried out by deprotonation of BDPA-H intermediates, followed by one-electron oxidation of the resulting anion using silver nitrate. For further experimental details on the synthesis of selectively deuterated BDPA radicals, we refer the reader to the supporting information.

2.2.2 EPR Experiments at 0.34 T / 9.6 GHz / X-Band

The EPR samples were prepared by dissolving the BDPA in anhydrous toluene at 50 µM concentrations. h_{21}-BDPA (1,3-bisdiphenylene-2-phenylallyl 1:1 benzene complex) was purchased from Millipore-Sigma (St. Louis, MO), and dissolved

	α	β	γ	δ	o-, p-	m-
h_{21}-BDPA	-5.54	1.38	-5.29	1.09	-0.5	-0.15
1,3-[d_{16}]-BDPA	-0.85	0.21	-0.81	0.17	-0.5	-0.15
1,3-[α,γ-d_8]-BDPA	-0.85	1.38	-0.81	1.09	-0.5	-0.15
1,3-[β,δ-d_8]-BDPA	-5.54	0.21	-5.29	0.17	-0.5	-0.15
Number of spins	4	4	4	4	3	2

Table 2.1. [1]H and [2]H Hyperfine Couplings (in MHz) Used in the EasySpin Simulations of the EPR Spectra Shown in Figure 2.3.

[a]The positions on the fluorene ring are indicated in the first row, and the coupling constants of the ^{1}H or ^{2}H at those positions are listed in the following rows for the four radicals. The total number of spins of each type is listed in the bottom row. Values and assignment of HFCs for h_{21} BDPA were taken from Dalal et al.

paramagnetic oxygen in the solvent was removed by using five freeze–pump–thaw cycles. Continuous-wave, room temperature EPR spectra were recorded using a 5 mm OD Suprasil gastight EPR tube (Wilmad, Buena, NJ) and a Bruker Elexsys E580 spectrometer at 0.34 T/9.6 GHz (X-band). We note that the repeated freeze–pump–thaw cycles were essential to obtain a high-resolution EPR spectra. Similar results were not obtained with repeated freeze–thaw cycles, without pumping.

2.2.3. MAS DNP Experiments at 8.9 T / 380 MHz / 250 GHz

2.5 wt % of h_{21}-BDPA in complex with benzene, 1,3-[α,β,γ,δ-d_{16}]-BDPA, 1,3-[α,γ-d_8]-BDPA, or 1,3-[β,δ-d_8]-BDPA was doped into a mixture of 95/5 mol % d_{14} and h_{14}-o-terphenyl (oTP). In molar concentrations, this corresponds to ~57 mM of h_{21}-BDPA, ~65 mM of 1,3-[α,β,γ,δ-d_{16}]-BDPA, and ~66 mM of 1,3-[α,γ-d_8]-BDPA and 1,3-[β,δ-d_8]-BDPA in the oTP mixture. The doped mixture was then codissolved in deuterated chloroform, which was later removed by evaporation under vacuum. The resulting thin film was finely ground and packed in a 4 mm sapphire rotor (with an ID of 2.45 mm), between a

Kel-F spacer and a top-cap (Revolution NMR). The packed sample was subsequently degassed with five freeze–pump–thaw cycles by using a home-built 3D-printed adapter. Samples were heated to ~58 °C during thaw cycles and rapidly freeze-quenched to promote oTP glass formation [62]. Additional details on home-built adapter are provided in the supporting information.

DNP experiments were performed on a 8.92 T/380 MHz/250 GHz DNP spectrometer [63] at a MAS frequency of $\omega_r/2\pi$ = 5 kHz and at 90 K (calibrated by using KBr) [64]. The microwave pulses were first generated by a 10 GHz local oscillator (LO) source, which is then frequency-multiplied ×2 and ×3 to 60 GHz, before being mixed with a ~2.5 GHz signal from an arbitrary waveform generator (Keysight AWG M8190A). The resultant 62.5 GHz signal is filtered, amplified, and fed into two frequency doublers in an amplifier-multiplier chain (VDI AMC 691) yielding a 160 mW, 250 GHz microwave beam. The DNP frequency profiles were obtained by varying the frequency of the signal from the AWG. Further details of this instrumentation will be discussed in a future publication.

The NMR experiment involved a train of 48 ^{1}H saturation pulses with Rabi frequency of $\omega_{1H}/2\pi$ = 83 kHz and 3 µs pulse width, with interpulse delays of 220 µs. This was followed by a recovery period before the signal was acquired by using a solid echo sequence. The spin–lattice relaxation time T_1 and the DNP buildup time T_B were estimated by fitting a monoexponential to the signal intensities with varying recovery periods. The DNP enhancement was determined by using $\frac{I-I_0}{I_0}$, where I denotes the microwave on NMR signal at a recovery period of $5T_{B,OE}$ and I_0 is the microwave off signal at a recovery period of $5T_1$.

2.3 Results

The strong coupling network of the fully protonated BDPA (h_{21}-BDPA) is verified from the excellent agreement between the EPR spectra and the numerical simulations, as shown in

Figure 2.3. A similar study was repeated on the selectively deuterated BDPA, where the introduction of ^{2}H reduces the magnitude of the hyperfine coupling by a factor of $\gamma_{^1H}/\gamma_{^2H}$ ~6.51. The deuteration at the α and γ positions of the fluorene moieties (1,3-[α,γ-d_8]-BDPA) with a_{iso}~-5.54 and -5.29 MHz couplings, respectively, causes the EPR spectrum to collapse to a single broad line, Figure 2.3. Similarly, introduction of ^{2}H at the β and δ positions which removes the 1.38 and 1.09 MHz couplings from those ^{1}H
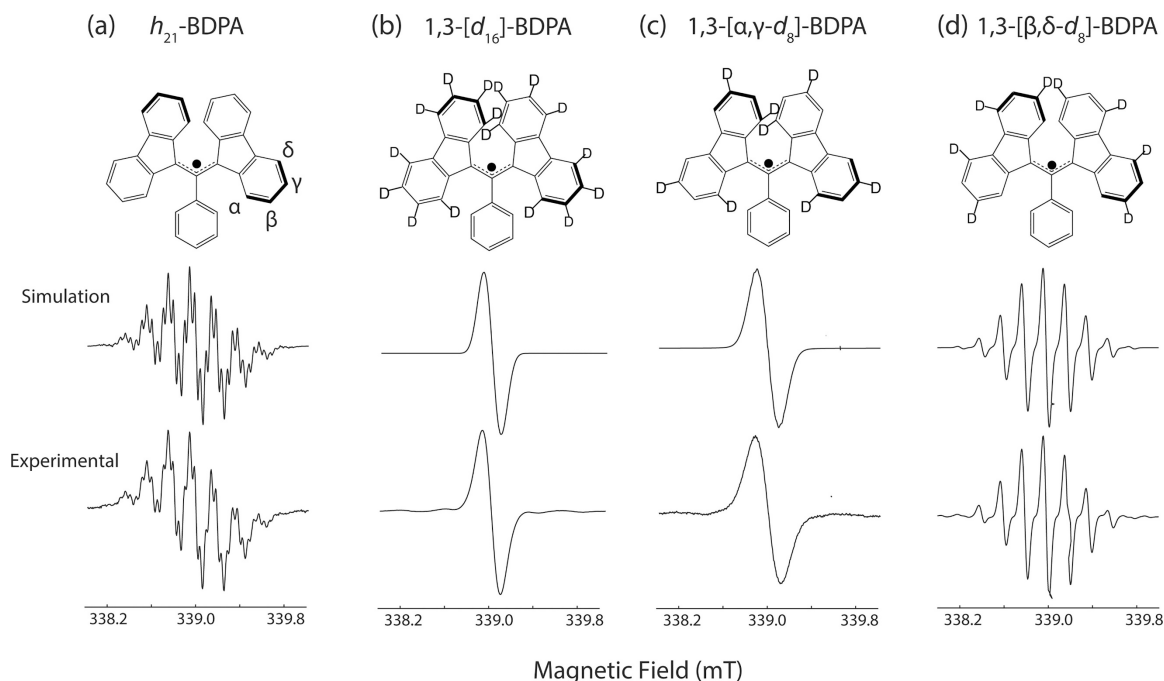
Figure 2.3. 9.5 GHz solution EPR. Simulated and experimental spectra of (a) h21-BDPA, (b) 1,3-[α,β,γ,δ-d16]-BDPA, (c) 1,3-[α,γ-d8]-BDPA, and (d) 1,3-[β,δ-d8]-BDPA with molecular structures given in the top row. Middle row: simulated 9.5 GHz spectra using EasySpin and ^{1}H couplings from Dalal et al. Bottom row: experimental solution state, CW EPR spectra recorded in degassed toluene samples.

Radical	T_1 /s	$T_{B,OE}$ /s	$T_{B,SE}$ /s	ε_{OE}	ε_{SE}	ε_{OE} (normalized)
h_{21}-BDPA	42.7 ± 3.3	43.6 ± 2.3	42.4 ± 2.2	70 ± 3	5.8	70
1,3-[d_{16}]-BDPA	66.4 ± 4.0	74.0 ± 5.8	74.7 ± 5.0	-13 ± 1	1.9	-10
1,3-[α,γ-d_8]-BDPA	66.7 ± 4.9	71.6 ± 6.4	70.4 ± 5.7	-1 ± 0.2	0.5	-3
1,3-[β,δ-d_8]-BDPA	36.8 ± 1.2	41.3 ± 2.0	39.6 ± 1.6	36 ± 4	1.8	23

Table 2.2. Overhauser DNP Enhancements and Build up times. Experimentally Measured Spin–Lattice Relaxation Times (T_1), DNP Buildup Times with the Microwaves at the OE Frequency ($T_{B,OE}$), and the Positive SE Frequency ($T_{B,SE}$) as well as Enhancement Values Calculated for the OE (ε_{OE}) and the Positive SE (ε_{SE}). The errors were estimated from intensities obtained following 180 s of microwave radiation. The last column has the OE enhancement values normalized by their relative radical concentrations.

spins and yields a 9-line pattern. We note the weak feature at 339 ± 0.8 mT present in the experimental trace is likely due to the remaining ~5% protonation of β and δ positions of the fluorene moieties. Finally, complete deuteration of all fluorene moiety protons to yield 1,3-[α,β,γ,δ-d16]-BDPA, results in a single EPR line that is reduced in breadth relative to that of 1,3-[α,γ-d_8]-BDPA. Nevertheless, in all four cases, the simulations are well matched to the main experimental features, verifying that the introduction of specific ^{2}H labels modified the hyperfine structure of the EPR spectrum in the expected manner, and confirming the chemical structure of the target radicals.

Figure 2.4 shows ^{1}H DNP enhancement as a function of microwave irradiation frequency obtained for *o*TP doped with the polarizing agents h_{21}-BDPA, 1,3-[α,β,γ,δ

d_{16}]-BDPA, 1,3-[α,γ-d_8]-BDPA, and 1,3-[β,δ-d_8]-BDPA. A large OE enhancement of ε = 70.2 was observed at 250.02 GHz for h_{21}-BDPA. Note that the SE effect enhancements obtained for h_{21}-BDPA with the diode source are small (ε = 5.8) because of the low power. Deuteration of all the positions on the fluorene moieties resulted in a negative enhancement of ε = -12.7, while deuteration of only the strongly hyperfine coupled protons (-5.54 and -5.29 MHz) at positions 1,3,6,8 on the fluorene moieties to yield 1,3-[α,γ-d_8]-BDPA, also resulted in a very weak, negative OE enhancement ε = -1.2. This result clearly demonstrates that these large hyperfine couplings are primarily responsible for mediating the OE in h_{21}-BDPA. Deuteration of the weakly HF coupled proton at positions 2,4,5,7 on the fluorene moieties, as in 1,3-[β,δ-d_8]-BDPA, results in an attenuated positive OE enhancement of ~36. Additionally, DNP enhancements were observed at 249.64 GHz and 250.40 GHz for the positive and negative SE conditions.
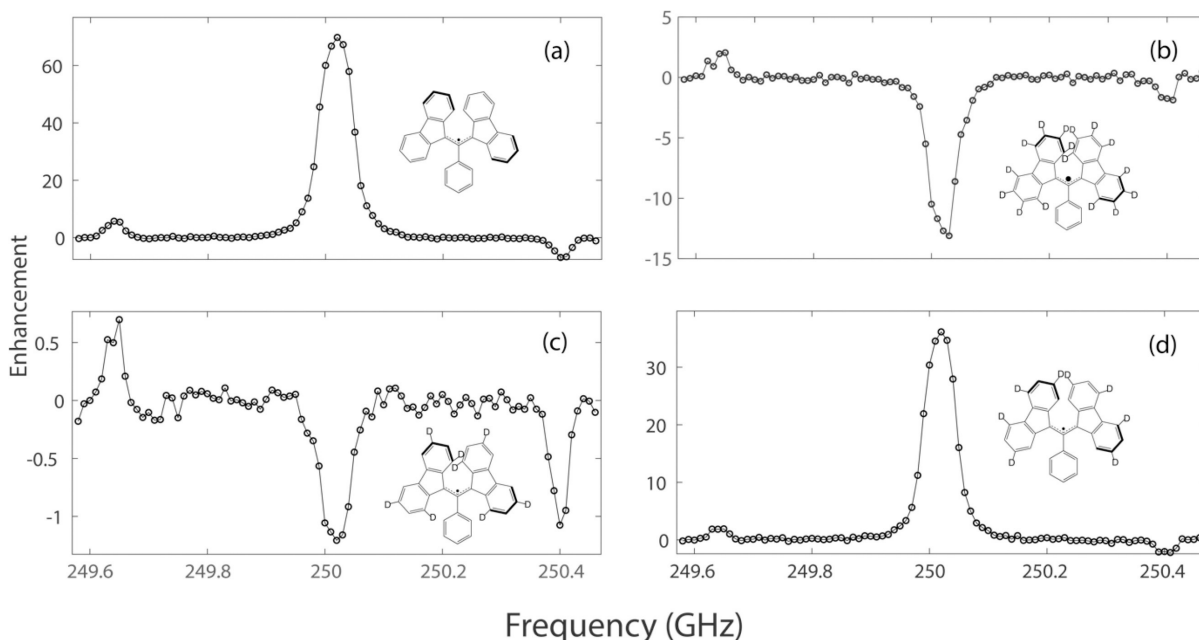
Figure 2.4. DNP Zeeman frequency profiles for selectively deuterated BDPA. Samples containing (a) h_{21}-BDPA, ε = 70, (b) 1,3-[α,β,γ,δ-d_{16}]-BDPA, ε = −13, (c) 1,3-[α,γ-d_8]-BDPA, ε = −1, and (d) 1,3-[β,δ-d_8]-BDPA, ε = 36.

However, the magnitudes of the observed SE enhancements were an order of

magnitude lower than that of the OE enhancements for all three radicals.

Table 2.2 shows the spin-lattice relaxation times (T_1), the DNP buildup times

measured at the OE condition ($T_{B,OE}$) and the positive SE condition ($T_{B,SE}$), and the

observed enhancement values for the four polarizing agents. The enhancement values

reported here are extracted from the frequency profile data depicted in Figure 2.4.

Please refer to Table 2.2 and Table 2.4 for the enhancement values with error estimates

which are generally ±10%. The T_1 for h_{21}-BDPA and The T_1 for h_{21}-BDPA and 1,3-[β,δ-

d_8]-BDPA were found to be comparable at ~43 s and ~37 s respectively. The T_1 for 1,3-

[α,β,γ,δ-d_{16}]-BDPA and 1,3-[α,γ-d_8]-BDPA were found to be much longer and

comparable at ~66 and ~67 s respectively, consistent with the absence of the strongly

coupled ^{1}H spins at α,γ positions. A similar trend was observed with the DNP buildup

times. The table also shows the calculated enhancement values for the OE DNP and

the positive SE DNP.

2.4 Discussion

The observed enhancement of ~70 for 2.5 wt % h_{21} -BDPA in 95/5 mol % d_{14} and

5 h_{14}-oTP matrix is, to our knowledge, the highest reported in the literature normalized

for the field and spinning frequency. Chaudhari *et al.* have reported an enhancement of

~60 for 2.5 wt % BDPA in 95/5 wt % d_{14} and h_{14}-oTP spinning at 5 kHz, but at a higher

field of 18.8 T, a temperature of ~128 K and in a ZrO_2 1.3 mm rotor [43]. We note the

electron Rabi field in a ZrO_2 1.3 mm rotor system was calculated to be 19 μT/W$^{1/2}$[65],

whereas the reported experimental value for the 4 mm system used in this study is 13

$\mu T/W^{1/2}$[66], indicating that the standard 1.3 mm system may have superior excitation efficiency for the electron spin transitions for the same incident microwave power. Moreover, the currently reported enhancement was obtained using a solid-state microwave source with an output power of only 160 mW. Thus, we attribute the improved DNP enhancements obtained in this study to the efficiency of freeze-pump-thaw degassing cycles. This hypothesis is supported by noting that the enhancement factor improves by 75% for the degassed sample compared to the non-degassed h_{21}-BDPA sample (See SI). Our experimental observation here is in good agreement with similar observations reported in literature, where removal of paramagnetic oxygen using freeze-thaw cycles on a BDPA doped 1,1,2,2-tetrachloroethane (TCE) sample also demonstrated improved enhancement factors, and the observation was rationalized using a source-sink model [43].

We note the concentration of active h_{21}-BDPA radical in commercial samples was only 50% of the anticipated value, as determined by measuring the extinction coefficient via UV-vis experiments (see Supporting Information) [67]. Using matrix assisted laser desorption ionization-time of light mass spectrometry (MALDI-TOF-MS), a significant fraction of the sample was determined to be hydroxylated BDPA (HO-BDPA) and hydroperoxylated BDPA (HO-O-BDPA). These impurities were readily removed from the sample using silica gel chromatography and the purity of the radical was verified by further UV-vis experiments (see SI); however, subsequent exposure of purified BDPA radical to air resulted in rapid formation of the hydroxylated species, as suggested in a previous publication [61]. Further details on h_{21}-BDPA purity and determination of sample concentration are provided in the supplementary information.

Relative radical concentrations between each BDPA sample were determined using EPR to compare the magnitude of the enhancements among BDPA derivatives. The relative ratio of electron spins among the four samples — h_{21}-BDPA, 1,3-[α, β, γ ,δ -d_{16}]-BDPA, 1,3-[α,γ-d_8]-BDPA, and 1,3-[β,δ-d_8]-BDPA — was determined to be ~2.2:3.1:1:3.4, respectively. Further details on DNP sample concentration determination are provided in the supporting information.

As mentioned earlier, the OE involves a two-spin system of one electron and one nucleus. Here, the nucleus is ^{1}H and the observed NMR signal is primarily that of the bulk ^{1}H spins in the oTP matrix, after the spins equilibrate with the hyperpolarized ^{1}H spins in and immediately around the radical. The overall DNP enhancement observed in the bulk ^{1}H spins thus results from the cumulative contribution of both positive and negative hyperpolarization originating in the protons coupled to the electron. Deuteration of all the sites on the fluorene moieties in 1,3-[α, β, γ ,δ -d_{16}]-BDPA results in an OE enhancement $ε$ = -12.7, and suggests that the dipolar couplings between the electron and the ^{1}H spins on the phenyl ring of the BDPA radical and the ^{1}H spins on h_{14}-oTP in the vicinity of the radical drive the observed negative enhancement. The dominance of the dipolar hyperfine couplings results in a DQ cross-relaxation rate that is larger than the ZQ cross-relaxation rate, and this difference generates a negative enhancement of nuclear polarization. It is noted here that this DNP result in consistent with prior DNP data on d_{21}-BDPA in polystyrene (PS) presented by Can et al., in which a weak negative enhancement was obtained [68].

Deuteration of only the most strongly coupled sites on the fluorenes in 1,3-[α,γ-d_8]-BDPA also results in a negative enhancement, but of a smaller magnitude, $ε$ = -1.

This establishes the role of the strong α,γ couplings for efficient, positive OE-DNP enhancement observed in h_{21}-BDPA. The smaller magnitudes of the negative enhancements observed in 1,3-[α,β,γ,δ-d_{16}]-BDPA and 1,3-[α,γ-d_8]-BDPA are consistent with the fact that the dominant hyperfine couplings present in these samples are smaller relative to the couplings in samples with protonated α,γ positions on the fluorene moieties. Second, the change in the observed enhancement from -13 in 1,3-[α,β,γ,δ-d_{16}]-BDPA to -1 in 1,3-[α,γ-d_8]-BDPA suggests that weakly coupled protons in the β,δ positions also help mediate ZQ OE DNP, albeit at a lesser extent compared to the α,γ protons. The argument holds true even upon considering a factor of ~3.1 in radical concentrations between the two samples as measured by EPR. We note that the magnitude of the OE-DNP enhancement measured in the bulk ^{1}H is expected to be directly proportional to the BDPA radical concentration, while the sign of the observed OE-DNP enhancement to be independent of the radical concentration. The sign depends only on the relative strengths of the isotropic and dipolar couplings and consequently on the relative dominance between the ZQ and DQ cross-relaxation pathways in the contributing electron-nuclear spin systems. This assumes the relaxation parameters remain reasonably constant and are insensitive to deuteration.

Deuteration of the weakly hyperfine coupled sites of the fluorene moieties in 1,3-[β,δ-d_8]-BDPA yields a positive enhancement of 36. The result when contrasted with the observation of a negative enhancement of -13 in 1,3-[α, β, γ ,δ -d_{16}]-BDPA, provides additional evidence for the importance of the strongly HF coupled ^{1}H spins on the α,γ positions in obtaining a strong positive OE enhancement. Moreover, if we normalize the signal by relative radical concentration, the relative enhancement obtained for 1,3-[β,δ-

d_8]-BDPA is roughly 33% to that of h_{21}-BDPA. As we have deduced earlier from the DNP results of 1,3-[α,β,γ,δ-d_{16}]-BDPA and 1,3-[α,γ-d_8]-BDPA the positive enhancement of the ^{1}H spins on the β,δ positions in h_{21}-BDPA are modest and by themselves, cannot account for the attenuation in the enhancement of 1,3-[β,δ-d_8]-BDPA relative to that of h_{21}-BDPA. This suggests that the protons at positions β,δ on the fluorenes may play a significant role in the process of spin diffusion in h_{21}-BDPA, facilitating the transfer of polarization from the protons at positions α,γ to the bulk ^{1}H spins in the oTP matrix. The absence of these protons in 1,3-[β,δ-d_8]-BDPA may simply be contributing to the attenuation of the DNP enhancement in the bulk ^{1}H. It is noted here that any potential differences in electron spin-lattice relaxation times, T_{1e}, could also contribute to the observed difference in enhancements between the two radicals. However, the absence of eight coupled protons in 1,3-[β,δ-d_8]-BDPA compared to h_{21}-BDPA is expected to result in longer T_{1e} for 1,3-[β,δ-d_8]-BDPA, which, in theory, should enable more efficient OE for electron-nuclear subsystems involving the protons at positions α,γ on the fluorene moieties.

As listed in Table 2.2 the nuclear relaxation times, T_{1n}, are found to be about ~43 and ~37 s for samples doped with h_{21}-BDPA and 1,3-[β,δ-d_8]-BDPA, respectively. They are measured to be longer at ~66 and ~67 s for samples doped with 1,3-[α,β,γ,δ-d_{16}]-BDPA and 1,3-[α,γ-d_8]-BDPA, respectively. These observations are consistent with the presence or absence of the strong isotropic HF couplings of the electron with the proton spins at α,γ-positions in the BDPA radicals.

The observed solid effect enhancement was an order of magnitude lower than the OE enhancement due to the low microwave power (160 mW) available from the

AMC source. The OE utilizes microwave excitation of allowed SQ electron spin transitions, in contrast to the SE which relies upon the weakly allowed *forbidden* spin transitions and requires significantly greater microwave power to induce DNP enhancements. The solid effect enhancement was observed to be attenuated in all three deuterated BDPA radicals relative to h_{21}-BDPA.

2.5 Conclusion

In conclusion, we present a synthetic methodology to generate deuterated BDPA radicals with ^{2}H at all the positions on the fluorene moieties, and selectively at positions 1,3,6,8 and 2,4,5,7 on the fluorene moieties. The synthesis of these radicals enabled the first experimental observations into the role of specific hyperfine coupled protons at these positions in generating both OE and SE DNP enhancements. Perdeuteration of the fluorene moieties entirely results in a moderate negative enhancement, while in the case of 1,3-[α,γ-d_8]-BDPA, where the strong hyperfine coupled protons are deuterated, a weak negative OE enhancement was observed. This highlights the primary role of the protons at 1,3,6,8 positions in the fluorene moieties in generating a strong positive OE enhancement as observed in insulating solids doped with h_{21}-BDPA radicals. Second, deuteration of the weakly coupled protons in 1,3-[β,δ-d_8]-BDPA resulted in a positive OE enhancement that was attenuated in magnitude relative to h_{21}-BDPA. We argue that in h_{21}-BDPA, the weakly hyperfine coupled protons at 2,4,5,7 positions of the fluorene moieties may aid in efficient spin diffusion to the bulk ^{1}H, thereby enabling a larger positive OE enhancement. Finally, the OE enhancement of 70 obtained with only 160 mW of microwave power in a fully degassed BDPA-*o*TP sample emphasizes the

relevance of the OE as a DNP method of choice and the possibility for a wider application using low-cost solid-state microwave sources. The results presented offer insights into the mechanisms of OE-DNP and may allow for the rational design of further OE-DNP polarizing agents for use under high field DNP.

2.6 Supporting Information

Unless otherwise stated, all reactions were carried out under an atmosphere of nitrogen using the standard Schlenk technique. All solvents and reagents were obtained from commercial sources and were purified following standard procedures before use if necessary. NMR spectra were measured on Bruker Avance III HD 600 MHz, spectrometer. Proton chemical shifts are expressed in parts per million (ppm, δ scale) and are referenced to the residual proton in the NMR solvents $CDCl_3$ at δ 7.26 or DMSO-d_6 at 2.50 ppm. ^{1}H NMR spectroscopic data are reported as follows: Chemical shift in ppm (multiplicity, coupling constants J (Hz), integration intensity, assigned proton). The multiplicities are abbreviated with s (singlet), d (doublet), t (triplet), m (multiplet). All ^{13}C spectra recorded are proton-decoupled. The carbon chemical shifts are expressed in parts per million (ppm, δ scale) and are referenced to the carbon resonance of the NMR solvents $CDCl_3$ at δ 77.16 or DMSO at 39.52 ppm. ^{13}C NMR spectroscopic data are reported as follows: Chemical shift in ppm (multiplicity, coupling constants J (Hz), assigned carbon). All raw fid files were processed and the spectra analyzed using the program MestReNOVA 14.2 from Mestrelab Supporting Information SI4 Research S. L.

Deuterium incorporation <100 % at specific positions will result in non-deuterated analogs of targeted compounds. These impurities will appear on NMR spectra and therefore need to be distinguished from the desired selectively deuterated compounds. Hence, for ^{1}H NMR, two set of signals are reported, one corresponding to the desired product, labelled Deuterated Product (**DP**), and the other corresponding to the non-deuterated impurity, labelled Non-Deuterated Impurity (**NDI**). Overlap between both products signals occurred, and the reported signals are from the peaks that could be

resolved. Deuterium incorporation was calculated from the integrated ratio of well-defined ^{1}H NMR signals that are known to be associated with both compounds. For clarity purposes, ^{13}C NMR signals were only reported for the main product, but the signals from non-deuterated impurities can be observed in spectra with high signal-to-noise ratio (**SNR**). The chemical shifts of the deuterated products and non-deuterated impurities singlet differ due to the ^{1}H/^{2}H isotope effect. Signals from carbon atoms directly attached to deuterium atoms are triplet or multiplet due to deuterium coupling. Due to low SNR or the complexity of the molecules further down the synthetic route, some signals could or should not be assigned as triplets, and were assigned as multiplets.

High-resolution mass spectra were recorded on a JEOL AccuTOF LC-Plus 46 with an ionSense DART system.

Synthesis of Selectively Deuterated Fluorene Moieties
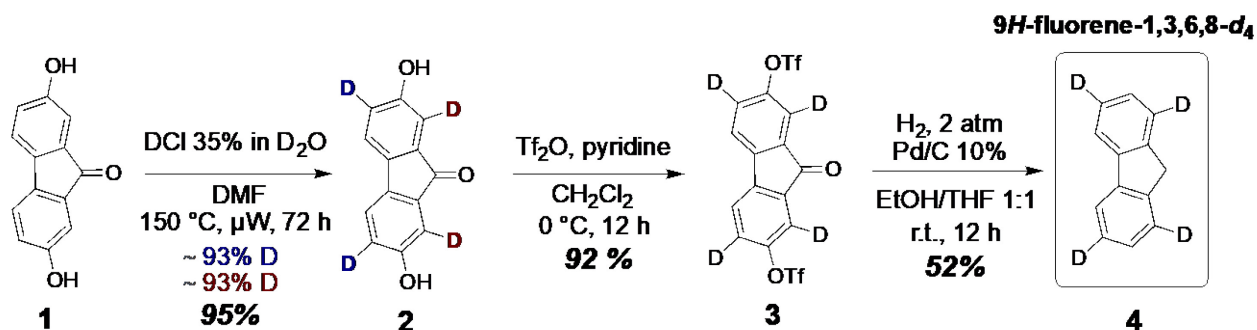
Figure 2.5. General synthetic route for 9*H*-fluorene-1,3,6,8-*d*$_4$
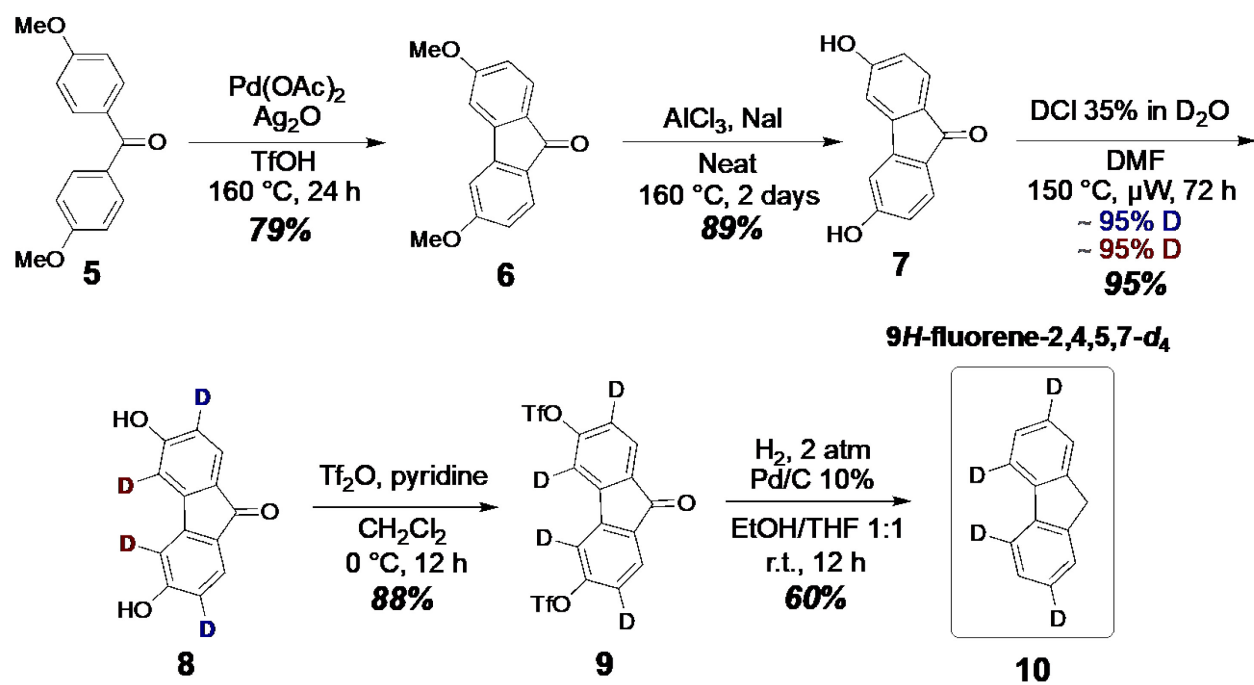
Figure 2.6. General synthetic route for 9*H*-fluorene-2,4,5,7-*d*₄

Synthesis of 9*H*-fluorene-1,3,6,8-*d*₄
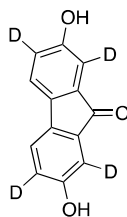
2,7-dihydroxy-9*H*-fluoren-9-one-1,3,6,8-*d*₄ (2)

In a 20 mL microwave reaction vial with a magnetic stirrer bar, 2,7-di(hydroxy-*d*)-9*H*-fluoren-9-one (600 mg, 2.83 mmol) was added, followed by 35 wt.% DCl solution in D_2O (5 mL) and DMF (5 mL) under an argon atmosphere. The vial was sealed and heated in the microwave synthesis apparatus for 24h at 150 °C. The mixture was cooled to room temperature and an additional 3 mL of 35 wt.% DCl solution in D_2O was added. The reaction was suggested again to microwave irradiation at 150°C for 12h to reach a higher deuterium incorporation. Reaction follow-up was done by ^{1}H-NMR. Then, the mixture was cooled to room temperature and was added to of ice-cold H_2O (20 mL), forming a reddish precipitate. The precipitate was filtered on a fritted funnel and, washed with hexanes (3x10 mL), saturated aqueous sodium bicarbonate solution (3x20 mL) and water (3x20 mL). The solid residue was dried over $MgSO_4$ and then dried overnight in a vacuum oven at 100°C to yield 2,7-dihydroxy-9*H*-fluoren-9-one-1,3,6,8-*d*₄ as a red solid (580 mg, 95%). The total incorporation yield for both positions was determined by ^{1}H NMR spectroscopy relative to the intensity of a nonexchangeable proton in the molecule, and was further confirmed by LC-MS analysis. Deuterium incorporation (Position 1 and 8: ~93%; Position 3 and 6: ~93%).

DP:

^{1}H NMR (600 MHz, DMSO-d_6) δ 9.83 (s, 2H), 7.37 (s, 2H).

^{13}C NMR (151 MHz, DMSO-d_6) δ 193.40, 157.47, 135.68, 135.06, 120.96, 120.70 (m), 110.83 (m).

HRMS (DART/AccuTOF) m/z: [M]$^+$ Calcd for $C_{13}H_4D_4O_3$ 217.0758; Found 217.0769.

NDI:

^{1}H NMR (600 MHz, DMSO-d_6) δ 6.88 (d, J = 2.6 Hz, 0.14H), 6.86 (dd, J = 8.0, 2.3 Hz, 0.14H).
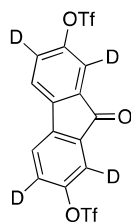
9-oxo-9*H*-fluorene-2,7-diyl-1,3,6,8-*d*₄ bis(trifluoromethanesulfonate) (3)

To a solution of 2,7-di(hydroxy-*d*)-9*H*-fluoren-9-one-1,3,6,8-*d*₄ (550 mg, 2.54 mmol) and pyridine (1 mL) in dichloromethane (8 mL) was added a 1M solution of Tf₂O in DCM (6.35 mL, 6.35 mmol) at 0°C. The stirring was continued overnight at room temperature before it was poured into water and the organic phase was extracted with dichloromethane (3x10 mL). The combined organic phases were washed subsequently with 3% aqueous HCl solution (2x10 mL), saturated aqueous sodium bicarbonate solution (1x10 mL) and brine

(2x10 mL) and then dried over MgSO₄. The reaction mixture was concentrated in vacuo and the purple residue was directly purified by flash chromatography on silica gel (hexanes/ethyl acetate, 90:10) to yield 9-oxo-9*H*-fluorene-2,7-diyl-1,3,6,8-*d₄* bis(trifluoromethanesulfonate**)** as a purple solid (1.12 g, 92%).

DP:

^{1}H NMR (600 MHz, CDCl₃) δ 7.66 (s, 2H).

^{13}C NMR (151 MHz, CDCl₃) δ 189.26, 150.46, 142.72, 136.32, 127.73 (t, *J* = 25.5 Hz,) 122.41, 119.89, 118.36, 118.12 (t, *J* = 25.5 Hz), 117.76, 115.64.

HRMS (DART/AccuTOF) m/z: [M]⁺ Calcd for $C_{15}H_2D_4F_6O_7S_2$ 480.9744; Found 480.9774.

NDI:

^{1}H NMR (600 MHz, CDCl₃) δ 7.61 (d, *J* = 1.8 Hz, 0.13H), 7.46 (dd, *J* = 8.1, 1.9 Hz, 0.13H).
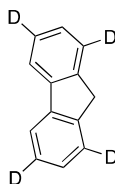
9*H*-fluorene-1,3,6,8-*d₄* (4)

To a round-bottom flask under an argon atmosphere, 10 wt.% palladium on carbon (300 mg, 0.28 mmol) was added, then a 1:1 mixture of THF/MeOH (10 mL) was added slowly and the reaction was degassed with argon for 20 min. Then, 9-oxo-9*H*-fluorene-2,7-diyl-1,3,6,8-*d₄* bis(trifluoromethanesulfonate) (1.0 g, 2.08 mmol) was added and the reaction

was bubbled with 2 atmosphere of hydrogen gas for 20 min. The reaction was sealed and left to stir for 24h or until complete consumption of starting material. The reaction was followed by TLC using fluorene as co-spot. The reaction was then filtered on Celite and the reaction mixture was concentrated in vacuo to afford a beige residue. Further purification by flash chromatography on silica gel (hexanes/ethyl acetate, 95:5) yielded 9*H*-fluorene-1,3,6,8-*d*₄ as a white solid (184 mg, 52%).

DP:

^{1}H NMR (600 MHz, CDCl₃) δ 7.82 (s, 2H), 7.33 (s, 2H), 3.93 (s, 2H).

^{13}C NMR (151 MHz, CDCl₃) δ 143.26, 141.84, 126.61, 126.56 (t, 24.5 Hz), 124.86 (t, 24.5 Hz), 119.89, 36.97.

HRMS (DART/AccuTOF) m/z: [M]$^+$ Calcd for $C_{13}H_6D_4$ 171.1067; Found 171.0933.

NDI:

^{1}H NMR (600 MHz, CDCl₃) δ 7.57 (dd, *J* = 7.4, 1.0 Hz, 0.14H), 7.40 (t, *J* = 7.5 Hz, 0.14H).

Synthesis of 9*H*-fluorene-2,4,5,7-*d*₄
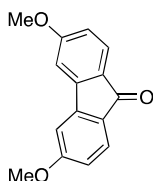
3,6-dimethoxy-9*H*-fluoren-9-one (6)

Synthesized following a modified literature procedure[60]. In a microwave reaction vial with a magnetic stirrer bar, 4,4'-dimethoxybenzophenone (5.0 g, 20.6 mmol), palladium(II) acetate (463 mg, 2.06 mmol), and silver(I) oxide (7.05 g, 30.45 mmol) was added, followed by trifluoroacetic acid (15 mL) under an argon atmosphere. The vial was sealed and heated in the microwave synthesis apparatus for 12h at 160 °C. After completion of the reaction, the reaction mixture was cooled to room temperature, filtered through a short Celite pad and was washed several times with dichloromethane. The combined filtrate was concentrated in vacuo and purified by flash chromatography on silica gel (hexanes/ethyl acetate, 70:30) to yield 3,6-dimethoxy-9*H*-fluoren-9-one as a pale-yellow solid (3.92 g, 79%).

^{1}H NMR (400 MHz, CDCl$_3$) δ 7.58 (d, *J* = 8.2 Hz, 2H), 7.00 (d, *J* = 2.2 Hz, 2H), 6.75 (dd, *J* = 8.2, 2.2 Hz, 2H), 3.90 (s, 6H).
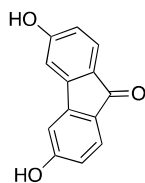
3,6-dihydroxy-9*H*-fluoren-9-one (7)

Synthesized following a modified literature procedure[69]. In an unsealed 50 mL pressure vial, 3,6-dimethoxy-9*H*-fluoren-9-one (2.0 g, 8.32 mmol), AlCl$_3$ (3.33 g, 24.97 mmol) and NaI (6.24 g, 41.6 mmol) were heated at 160 °C for 12 h under neat conditions. The crude was cooled to room temperature and deionized H$_2$O (50 mL) was added. The mixture was extracted with 3 x 20 mL of ethyl acetate and the organic phase was dried over

MgSO$_4$, concentrated in vacuo and purified by flash chromatography on silica gel (dichloromethane/ethyl acetate, 95:5) to yield 3,6-dihydroxy-9*H*-fluoren-9-one as a white solid (1.57 g, 89%).

^{1}H NMR (400 MHz, Acetone) δ 9.40 (s, 2H), 7.42 (d, *J* = 8.1 Hz, 2H), 7.18 (d, *J* = 2.3 Hz, 2H), 6.81 (dd, *J* = 8.1, 2.2 Hz, 2H).
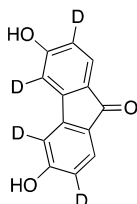
3,6-dihydroxy-9*H*-fluoren-9-one-2,4,5,7-*d*$_4$ (8)

In a 20 mL microwave reaction vial with a magnetic stirrer bar, 3,6-di(hydroxy-*d*)-9*H*-fluoren-9-one (600 mg, 2.83 mmol) was added, followed by 35 wt.% DCl solution in D$_2$O (5 mL) and DMF (5 mL) under an argon atmosphere. The vial was sealed and heated in the microwave synthesis apparatus for 24h at 150 °C. The mixture was cooled to room temperature and was added to of ice-cold H$_2$O (20 mL), forming a yellow precipitate. The precipitate was filtered on a fritted funnel and, washed with hexanes (3x10 mL), saturated aqueous sodium bicarbonate solution (1x10 mL) and water (3x20 mL). The solid residue was dried overnight in a vacuum oven at 100°C to yield 3,6-dihydroxy-9*H*-fluoren-9-one-2,4,5,7-*d*$_4$ as a yellow solid (580 mg, 95%). The total incorporation yield for both positions was determined by ^{1}H NMR spectroscopy relative to the intensity of a nonexchangeable proton in the molecule, and was further confirmed by LC-MS analysis. Deuterium incorporation (Position 2 and 7: ~95%; Position 4 and 5: ~95%)

DP:

^{1}H NMR (600 MHz, DMSO) δ 10.51 (s, 2H), 7.38 (s, 2H).
^{13}C NMR (151 MHz, DMSO) δ 190.31, 163.59, 145.70, 126.01, 125.33, 114.72 (m), 108.27 (t, 23.5 Hz)
HRMS (DART/AccuTOF) m/z: [M]$^+$ Calcd for $C_{13}H_4D_4O_3$ 217.0758; Found 217.0742.

NDI:
^{1}H NMR (600 MHz, DMSO) δ 7.04 (s, 0.09H), 6.67 (d, J = 8.1 Hz, 0.10H).
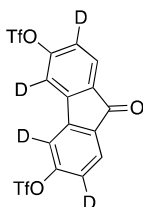
9-oxo-9*H*-fluorene-3,6-diyl-2,4,5,7-*d*$_4$ bis(trifluoromethanesulfonate) (9)

Prepared according to the general procedure used for compound **2**, 2,7-di(hydroxy-*d*)-9*H*-fluoren-9-one-1,3,6,8-*d*$_4$ (500 mg, 2.36 mmol), pyridine (1 mL), dichloromethane (7.5 mL), and 1M solution of Tf$_2$O in DCM (5.90 mL, 5.90 mmol) were used. Yielding 9-oxo-9*H*-fluorene-3,6-diyl-2,4,5,7-*d*$_4$ bis(trifluoromethanesulfonate) as a yellow solid (1.07 g, 88%).

DP:

^{1}H NMR (600 MHz, CDCl$_3$) δ 7.81 (s, 2H).

^{13}C NMR (151 MHz, CDCl$_3$) δ 189.47, 154.02, 145.01, 133.67, 126.57, 122.87 (t, 25.0 Hz), 119.88, 117.76, 114.68 (t, 25.0 Hz).

HRMS (DART/AccuTOF) m/z: [M]$^+$ Calcd for $C_{15}H_2D_4F_6O_7S_2$ 480.9844; Found 480.9842.

NDI:

^{1}H NMR (600 MHz, CDCl$_3$) δ 7.48 (s, 0.08H), 7.30 (d, J = 8.1 Hz, 0.09H).
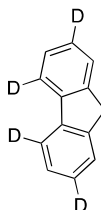
9H-fluorene-2,4,5,7-d_4 (10)

Prepared according to the general procedure used for compound **3**, 10 wt.% palladium on carbon (240 mg, 0.22 mmol), 1:1 mixture of THF/MeOH (8 mL), 9-oxo-9*H*-fluorene-2,7-diyl-1,3,6,8-d_4 bis(trifluoromethanesulfonate) (800 mg, 1.66 mmol) was used. Yielding 9H-fluorene-2,4,5,7-d_4 as a white solid (170 mg, 60%).

DP:

^{1}H NMR (600 MHz, CDCl$_3$) δ 7.56 (s, 1H), 7.39 (s, 1H), 3.92 (s, 1H).

^{13}C NMR (151 MHz, CDCl$_3$) δ 143.34, 141.75, 126.68, 126.53 (t, 24.5 Hz), 125.05, 119.74 (t, 24.5 Hz), 37.06.

HRMS (DART/AccuTOF) m/z: [M]$^+$ Calcd for $C_{13}H_6D_4$ 171.1067; Found 171.0934.

NDI:

^{1}H NMR (600 MHz, CDCl$_3$) δ 7.81 (d, J = 7.6 Hz, 0.10H), 7.32 (t, J = 7.4 Hz, 0.11H).

Synthesis of Selectively Deuterated BDPA Radicals
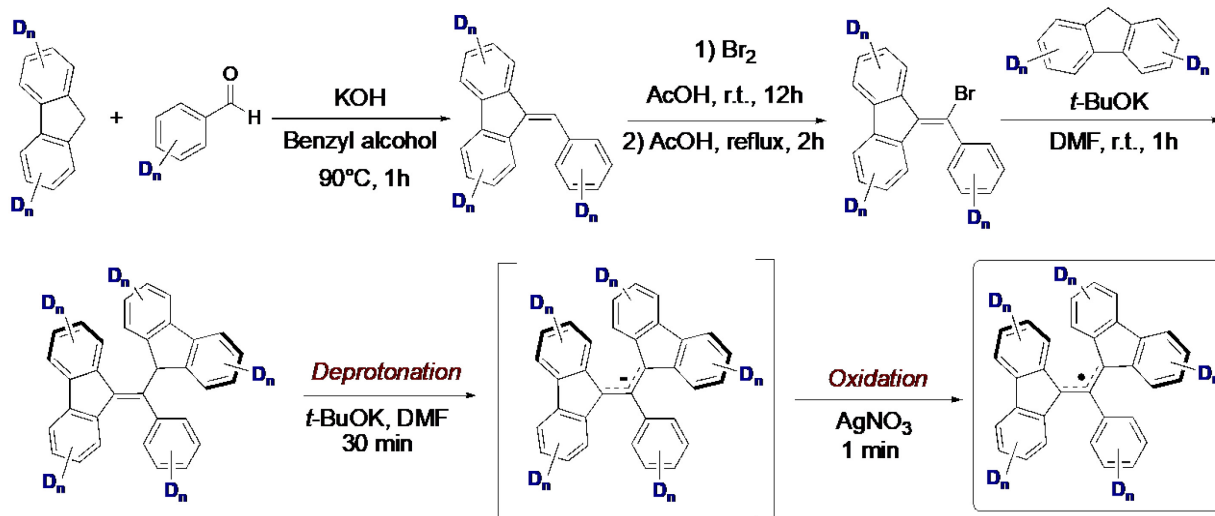
Figure 2.7. General synthetic route to 1,3-[α,γ-d_8]-BDPA and 1,3-[β,δ-d_8]-BDPA

Synthesis of 1,3-[α,γ-d_8]-BDPA
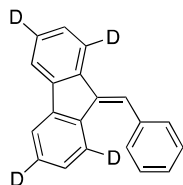
9-benzylidene-9H-fluorene-1,3,6,8-d_4 (11)

Synthesized following a modified literature procedure[70]. Benzaldehyde (60 μL, 0.587 mmol) was added dropwise to a solution of 9H-fluorene-1,3,6,8-d_4 (100 mg, 0.587 mmol) and CsOH·H$_2$O (40 mg, 0.235 mmol) in EtOH (1.2 mL) and the mixture was stirred at 25 °C for 2h. Complete consumption of the starting materials was observed by TLC and the reaction mixture was concentrated in vacuo. The crude reaction mixture was purified by

flash chromatography on silica gel (hexanes/ethyl acetate, 80:20) to yield 9-benzylidene-9H-fluorene-1,3,6,8-d_4 as a pale-yellow solid (131 mg, 86%).

DP:

^{1}H NMR (600 MHz, CDCl$_3$) δ 7.77 – 7.69 (m, 3H), 7.60 (d, J = 7.2 Hz, 2H), 7.47 (t, J = 7.6 Hz, 2H), 7.40 (t, J = 7.6 Hz, 1H), 7.34 (s, 1H), 7.06 (s, 1H).

^{13}C NMR (151 MHz, CDCl$_3$) δ 146.88, 141.39, 139.56, 139.33, 137.04, 136.60, 129.40, 128.67, 128.17, 127.42, 126.91, 126.58, 124.99 – 124.07 (m), 120.39 – 119.79 (m), 119.74, 119.61.

HRMS (DART/AccuTOF) m/z: [M]$^+$ Calcd for C$_{20}$H$_{10}$D$_4$ 259.1180; Found 259.1158.

NDI:

^{1}H NMR (600 MHz, CDCl$_3$) δ 7.80 (d, J = 7.6 Hz, 0.16H), 7.56 (d, J = 7.8 Hz, 0.16H), 7.31 (d, J = 7.4 Hz, 0.23H), 7.25 – 7.21 (m, 0.48H).
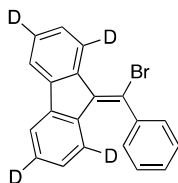
9-(bromo(phenyl)methylene)-9H-fluorene-1,3,6,8-d_4 (12)

Synthesized following a modified literature procedure[70]. To a flask covered with aluminum foil was suspended 9-benzylidene-9H-fluorene-1,3,6,8-d_4 (70 mg, 0.27 mmol) in acetic acid (1 mL). The reaction was cooled to 0°C, then Br$_2$ (13 µL, 0.26 mmol) was added dropwise while stirring heavily. The reaction mixture was warmed at room

temperature and stir overnight. Then, 50 mL of water was added to precipitate the product. The mixture was extracted with dichloromethane (3 x 5 mL) and the organic phases were washed with saturated aqueous sodium bicarbonate solution (3x20 mL) and water (3 x 20 mL). The organic phase was concentrated in vacuo and the intermediate product 9-bromo-9-[bromo(phenyl)methyl]-9*H*-fluorene was dried for 2h before being suspended in acetic acid (2 ml) and heated at reflux for 2 h. The reaction mixture was left to cool at room temperature overnight and the product was collected by filtration and dried under vacuum to give the crude desired product with a 90% purity. The crude mixture was further purified by flash chromatography on silica gel (hexanes/ethyl acetate, 85:15) to yield 9-(bromo(phenyl)methylene)-9*H*-fluorene-1,3,6,8-*d₄* as a yellow solid (54 mg, 59%).

DP:

^{1}H NMR (600 MHz, CDCl$_3$) δ 7.74 (s, 1H), 7.65 (s, 1H), 7.56 – 7.44 (m, 5H), 7.40 (s, 1H), 6.85 (s, 1H).

^{13}C NMR (151 MHz, CDCl$_3$) δ 142.96, 141.35, 139.95, 138.24, 137.99, 136.17, 129.40, 129.38, 129.30 – 128.73 (m), 128.69, 128.55 – 127.76 (m), 127.01, 126.75, 126.20 – 125.67 (m), 124.8 – 124.35 (m), 121.04 – 120.38 (m), 119.56, 119.28.

HRMS (DART/AccuTOF) m/z: [M]$^+$ Calcd for C$_{20}$H$_9$D$_4$Br 337.0412; Found 337.0382.

NDI:

¹H NMR (600 MHz, CDCl₃) δ 8.88 (d, *J* = 8.0 Hz, 0.07H), 7.70 (s, 0.08H), 7.62 – 7.58 (m, 0.17H), 7.34 (s, 0.07H), 7.23 (t, *J* = 7.5 Hz, 0.08H), 7.06 (s, 0.06H), 6.21 (d, *J* = 8.0 Hz, 0.07H).
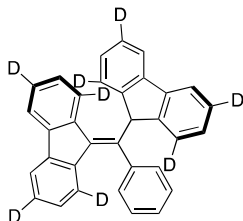
9-((9*H*-fluoren-9-yl-1,3,6,8-*d₄*)(phenyl)methylene)-9*H*-fluorene-1,3,6,8-*d₄* (13)

Synthesized following a modified literature procedure[70]. ᵗBuOK (27 mg, 0.24 mmol) was added in portions to a stirred solution of 9-(bromo(phenyl)methylene)-9*H*-fluorene-1,3,6,8-*d₄* (20 mg, 0.059 mmol) and 9*H*-fluorene-1,3,6,8-*d₄* (11 mg, 0.065 mmol) in DMF (0.5 mL) under N₂. The reaction mixture was stirred 3h at room temperature, then hydrochloric acid (1 M, 1 mL was added and the reaction mixture followed by water (2 ml) to give an orange precipitate. The crude mixture was collected by filtration, washed with water (10 ml) and methanol (10 ml) and dried overnight. Purification by flash chromatography on silica gel (hexanes/ethyl acetate, 80:20) gave the 9-((9*H*-fluoren-9-yl-1,3,6,8-*d₄*)(phenyl)methylene)-9*H*-fluorene-1,3,6,8-*d₄* as an orange solid (20 mg, 78%).

DP:

¹H NMR (600 MHz, CDCl₃) δ 7.89 (s, 1H), 7.75 (s, 1H), 7.66 (s, 2H), 7.36 (s, 1H), 7.26 (s, 2H), 7.07 (t, *J* = 7.4 Hz, 1H), 6.99 (t, *J* = 7.6 Hz, 2H), 6.81 (s, 1H), 6.67 (d, *J* = 7.1 Hz, 2H), 6.48 (s, 1H).

^{13}C NMR (151 MHz, CDCl$_3$) δ 145.27, 144.22, 142.11, 141.44, 139.89, 139.00, 138.78, 138.71, 136.06, 128.48, 127.86, 127.36, 127.20, 126.83, 126.48, 126.09 – 125.63 (m), 125.21 – 124.69 (m), 119.99, 119.95, 119.08, 52.79.

HRMS (DART/AccuTOF) m/z: [M]$^+$ Calcd for C$_{33}$H$_{14}$D$_8$ 427.2257; Found 427.2345.

NDI:

^{1}H NMR (600 MHz, CDCl$_3$) δ 8.44 (d, J = 8.0 Hz, 0.07H), 7.60 (d, J = 7.6 Hz, 0.14H), 7.47 (t, J = 7.5 Hz, 0.08H), 7.34 (t, J = 7.6 Hz, 0.14H), 7.22 (t, J = 7.3 Hz, 0.15H), 6.49 (s, 0.08H), 5.90 (d, J = 8.0 Hz, 0.07H).
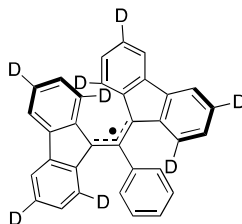
1,3-[α,γ-d_8]-BDPA radical (14)

Synthesized following a modified literature procedure[71]. ^{t}BuOK (24 mg, 0.21 mmol) was added in portions to a stirred solution of compound 9-((9*H*-fluoren-9-yl-1,3,6,8-d_4)(phenyl)methylene)-9*H*-fluorene-1,3,6,8-d_4 (15 mg, 0.035 mmol) in DMF (0.3 ml) under N$_2$ at room temperature which resulted in a colour change from orange to dark blue. After 30 min, a solution of AgNO$_3$ (35 mg, 0.21 mmol) in DMF (0.1 mL) was added. The solution immediately became red-brown and was diluted after 30 min of stirring with 2 mL of 0.01 M HCl and extracted with diethyl ether (3x2 mL). The combined organic layers were washed with water (3x10 mL) and dried under vacuum. Purification by flash

chromatography on silica gel (hexanes/ethyl acetate, 80:20) gave the 9-((9*H*-fluoren-9-yl-1,3,6,8-*d₄*)(phenyl)methylene)-9*H*-fluorene-1,3,6,8-*d₄* radical as a deep red glassy solid (10 mg, 66%).

Synthesis of 1,3-[β,δ-*d₈*]-BDPA
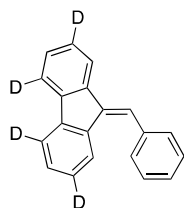
9-benzylidene-9*H*-fluorene-2,4,5,7-*d₄* (15)

Prepared according to the general procedure used for compound **11**. Benzaldehyde (60 µL, 0.587 mmol), 9*H*-fluorene-2,4,5,7-*d₄* (100 mg, 0.587 mmol) and CsOH·H₂O (40 mg, 0.235 mmol), and EtOH (1.2 mL) was used. Yielding 9-benzylidene-9*H*-fluorene-2,4,5,7-*d₄* as a pale-yellow solid (136 mg, 90%).

DP:

^{1}H NMR (600 MHz, CDCl₃) δ 7.80 (s, 1H), 7.71 (s, 1H), 7.59 (d, *J* = 8.1 Hz, 2H), 7.56 (s, 1H), 7.47 (t, *J* = 7.5 Hz, 2H), 7.43 – 7.36 (m, 2H), 7.31 (s, 1H).

^{13}C NMR (151 MHz, CDCl₃) δ 141.29, 139.61, 139.24, 137.04, 136.67, 136.62, 129.40, 128.67, 128.46, 128.16, 128.13, 127.40, 127.14 – 126.30 (m), 124.44, 120.26, 119.90 – 119.25 (m).

HRMS (DART/AccuTOF) m/z: [M]$^+$ Calcd for $C_{20}H_{10}D_4$ 259.1180; Found 259.1168.

NDI:

^{1}H NMR (600 MHz, CDCl$_3$) δ 7.75 – 7.71 (m, 0.06H), 7.35 – 7.32 (m, 0.06H), 7.06 (td, J = 7.6, 1.3 Hz, 0.06H).
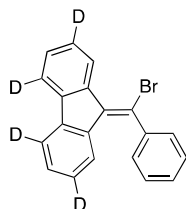
9-(bromo(phenyl)methylene)-9*H*-fluorene-2,4,5,7-*d*$_4$ (16)

Prepared according to the general procedure used for compound **12**. 9-Benzylidene-9*H*-fluorene-2,4,5,7-*d*$_4$ (70 mg, 0.27 mmol), Br$_2$ (13 µL, 0.26 mmol) and acetic acid (1 +2 mL) was used. Yielding 9-(bromo(phenyl)methylene)-9*H*-fluorene-2,4,5,7-*d*$_4$ as a pale-yellow solid (49 mg, 54%).

DP:

^{1}H NMR (600 MHz, CDCl$_3$) δ 8.87 (s, 1H), 7.60 – 7.38 (m, 6H), 7.23 (s, 1H), 6.21 (s, 1H).

^{13}C NMR (151 MHz, CDCl$_3$) δ 142.98, 141.27, 139.87, 138.32, 138.07, 136.20, 129.40, 129.39, 129.06, 128.70, 128.05, 127.25 –126.46 (m), 126.08, 124.76, 124.65, 124.44, 120.26, 119.71 – 118.91 (m).

HRMS (DART/AccuTOF) m/z: [M]$^+$ Calcd for C$_{20}$H$_9$D$_4$Br 337.0412; Found 337.0399.

NDI:

^{1}H NMR (600 MHz, CDCl$_3$) δ 7.80 (s, 0.12H), 7.74 (d, *J* = 7.5 Hz, 0.06H), 7.71 (s, 0.11H), 7.65 (d, *J* = 7.5 Hz, 0.06H), 7.56 (s, 0.07H), 7.41 (s, 0.06H). 7.31 (s, 0.06H), 6.85 (t, *J* = 7.7 Hz, 0.07H).
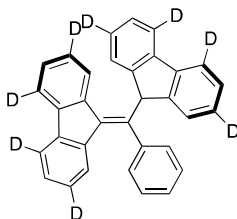
9-((9*H*-fluoren-9-yl-2,4,5,7-*d₄*)(phenyl)methylene)-9*H*-fluorene-2,4,5,7-*d₄* (17)

Prepared according to the general procedure used for compound **13**. ^{t}BuOK (27 mg, 0.24 mmol), 9-(bromo(phenyl)methylene)-9*H*-fluorene-2,4,5,7-*d₄* (20 mg, 0.059 mmol), 9*H*-fluorene-1,3,6,8-*d₄* (11 mg, 0.065 mmol), and DMF (0.5 ml) was used. Yielding 9-((9*H*-fluoren-9-yl-2,4,5,7-*d₄*)(phenyl)methylene)-9*H*-fluorene-2,4,5,7- *d₄* as an orange solid (17 mg, 68%).

DP:

^{1}H NMR (600 MHz, CDCl$_3$) δ 8.45 (s, 1H), 7.60 (s, 2H), 7.47 (s, 1H), 7.34 (s, 2H), 7.23 (s, 1H), 7.08 (t, *J* = 7.5 Hz, 1H), 7.00 (t, *J* = 7.7 Hz, 2H), 6.67 (d, *J* = 7.5 Hz, 2H), 6.50 (s, 1H), 5.90 (s, 1H).

^{13}C NMR (151 MHz, CDCl$_3$) δ 145.27, 144.30, 142.03, 141.36, 139.81, 139.07, 138.86, 138.71, 136.11, 128.50, 127.85, 127.37, 127.36, 127.32, 126.20 – 126.92 (m), 126.04, 125.51, 125.14, 119.55 – 120.09 (m), 118.66 – 119.15 (m), 52.84.

HRMS (DART/AccuTOF) m/z: [M]$^+$ Calcd for C$_{33}$H$_{14}$D$_8$ 427.2257; Found 427.2242.

NDI:

^{1}H NMR (600 MHz, CDCl$_3$) δ 7.89 (d, *J* = 7.6 Hz, 0.06H), 7.75 (d, *J* = 7.6 Hz, 0.06H), 7.66 (d, *J* = 7.6 Hz, 0.12H), 7.37 (d, *J* = 7.7 Hz, 0.06H), 6.82 (t, *J* = 7.7 Hz, 0.10H).
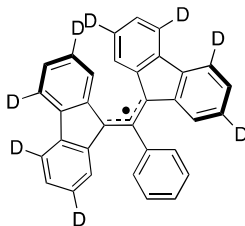
1,3-[β,δ-*d*$_8$]-BDPA (18)

Prepared according to the general procedure used for compound **14**. ^{t}BuOK (24 mg, 0.21 mmol) was added in portions to a stirred solution of compound 9-((9*H*-fluoren-9-yl-2,4,5,7-*d*$_4$)(phenyl)methylene)-9*H*-fluorene-2,4,5,7-*d*$_4$ (15 mg, 0.035 mmol), AgNO$_3$ (35 mg, 0.21 mmol), DMF (0.3 mL) was used. Yielding 9-((9*H*-fluoren-9-yl-1,3,6,8-*d*$_4$)(phenyl)methylene)-9*H*-fluorene-2,4,5,7-*d*$_4$ radical as a deep red glassy solid (11 mg, 73%).

NMR Spectra
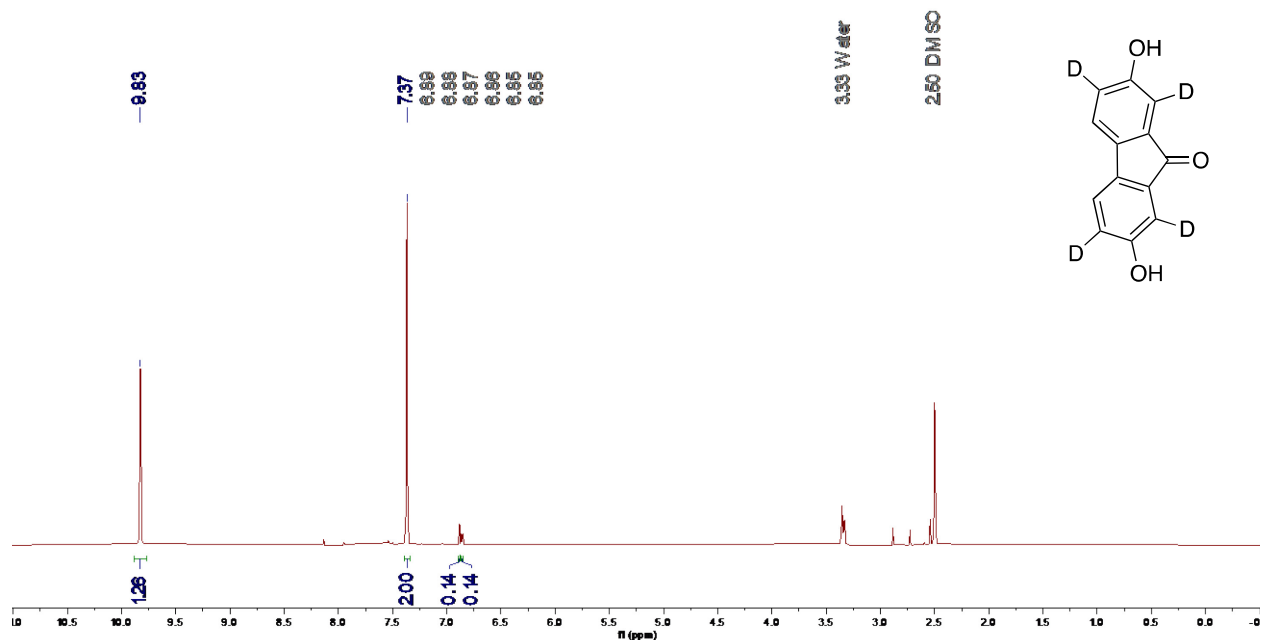
Figure 2.8. ^{1}H NMR spectrum (600 MHz, DMSO-d_6) of 2,7-dihydroxy-9*H*-fluoren-9-one-1,3,6,8-d_4 (2)
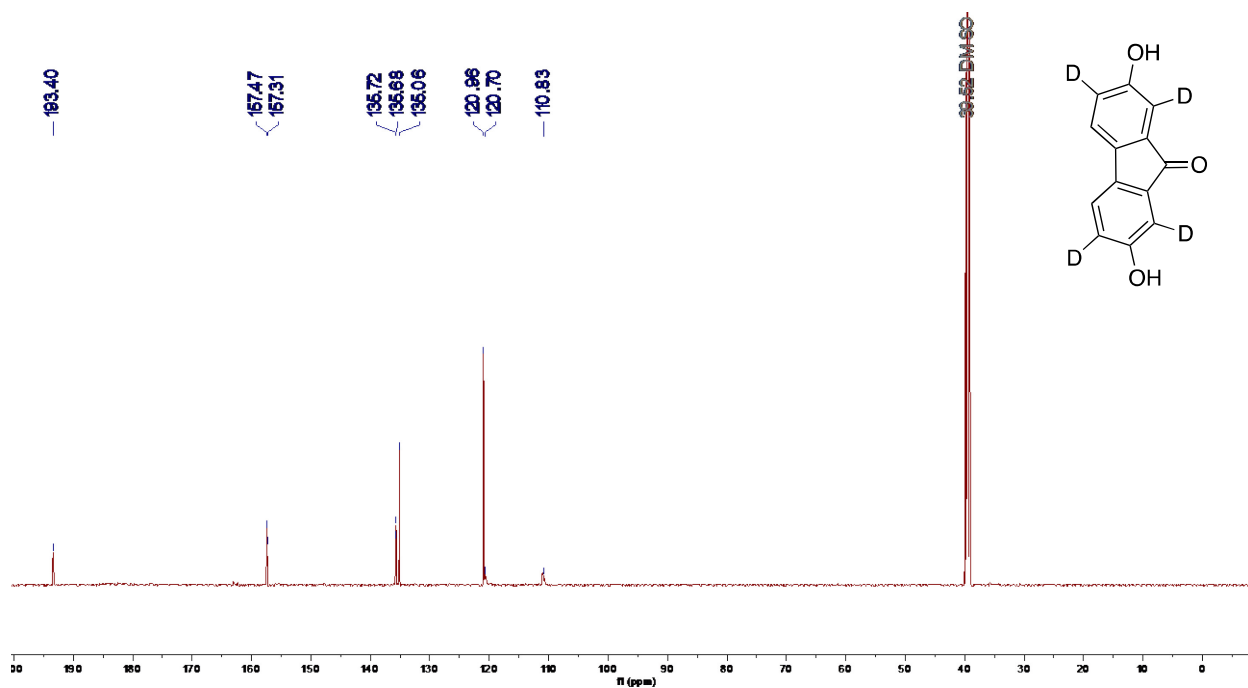
Figure 2.9. ^{13}C NMR spectrum (600 MHz, DMSO-d$_6$) of 2,7-dihydroxy-9H-fluoren-9-one-1,3,6,8-d$_4$ (2)
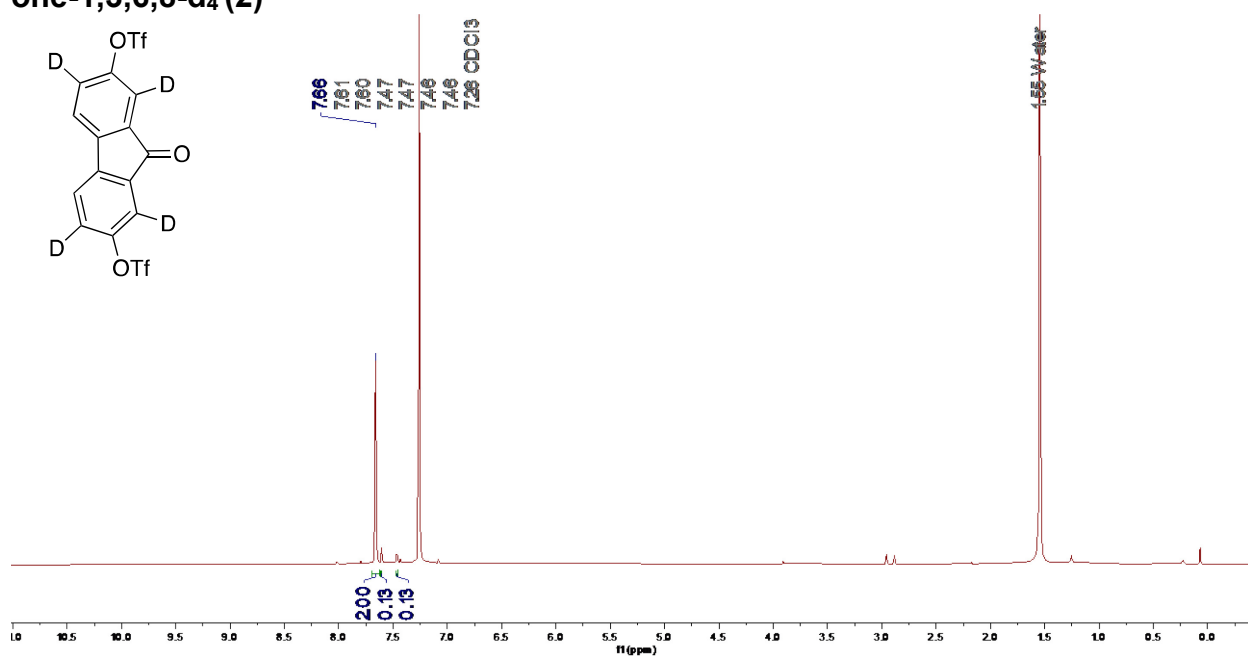
Figure 2.10. ^{1}H NMR spectrum (600 MHz, CDCl$_3$) of 9-oxo-9*H*-fluorene-2,7-diyl-1,3,6,8-*d*$_4$ bis(trifluoromethanesulfonate) (3)
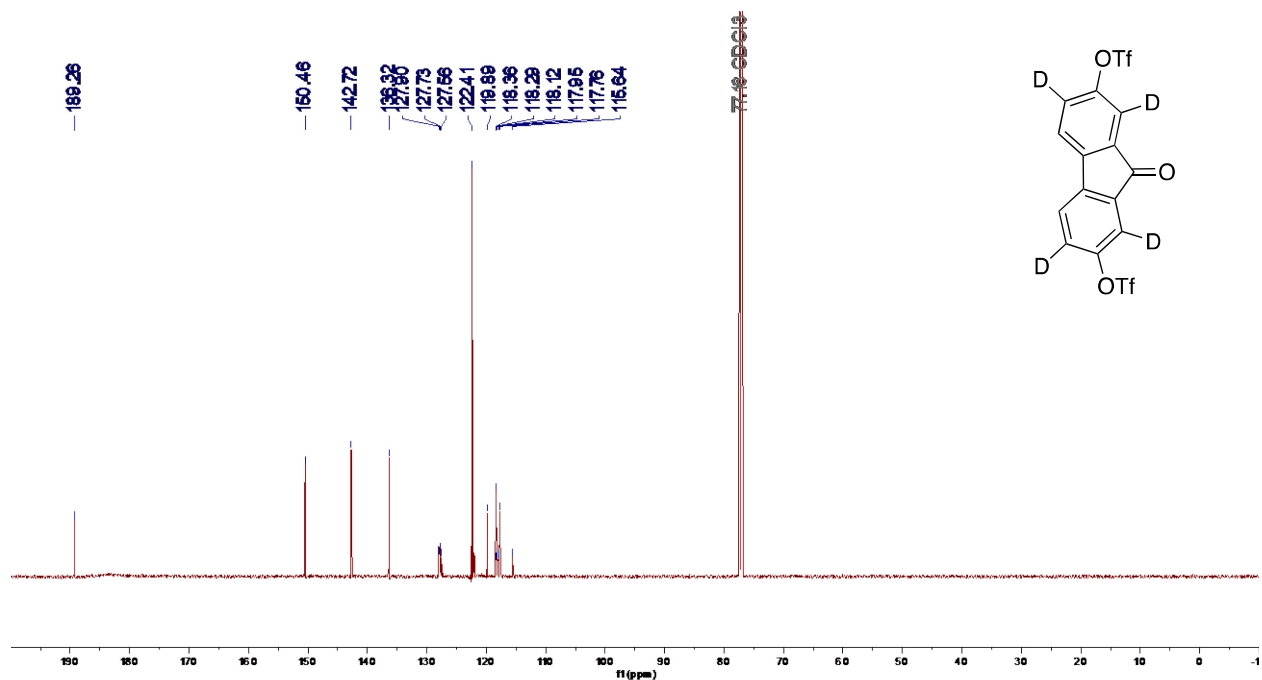
Figure 2.11. ^{13}C NMR spectrum (600 MHz, CDCl$_3$) of 9-oxo-9*H*-fluorene-2,7-diyl-1,3,6,8-*d*$_4$ bis(trifluoromethanesulfonate) (3)
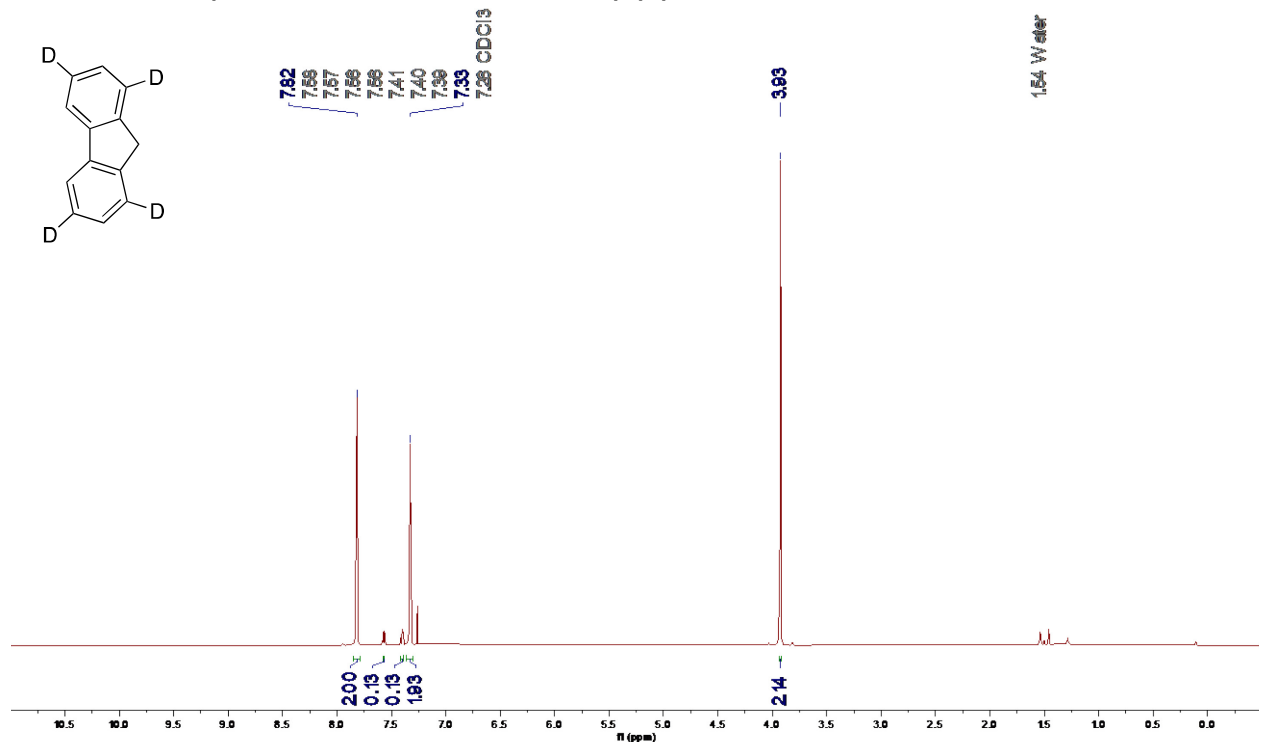
Figure 2.12. ^1H NMR spectrum (600 MHz, CDCl$_3$) of 9*H*-fluorene-1,3,6,8-*d*$_4$ (4)

143.26
141.84
126.61
126.56
124.86
119.89
77.16 CDCl3
36.97
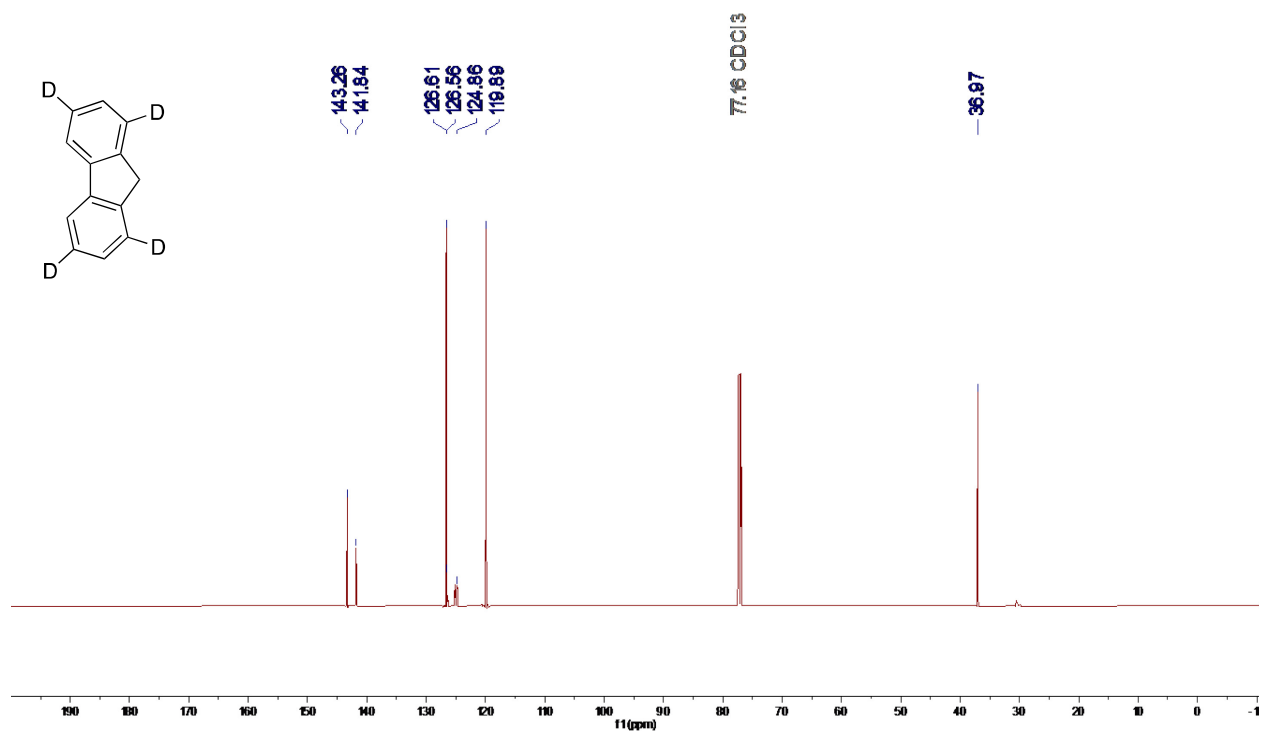
Figure 2.13. ^{13}C NMR spectrum (600 MHz, CDCl$_3$) of 9*H*-fluorene-1,3,6,8-*d*$_4$ (4)

10.51
7.38
7.04
6.67
3.35 Water
2.50 DMSO
2.08 Acetone

2.14

2.00
0.09
0.10
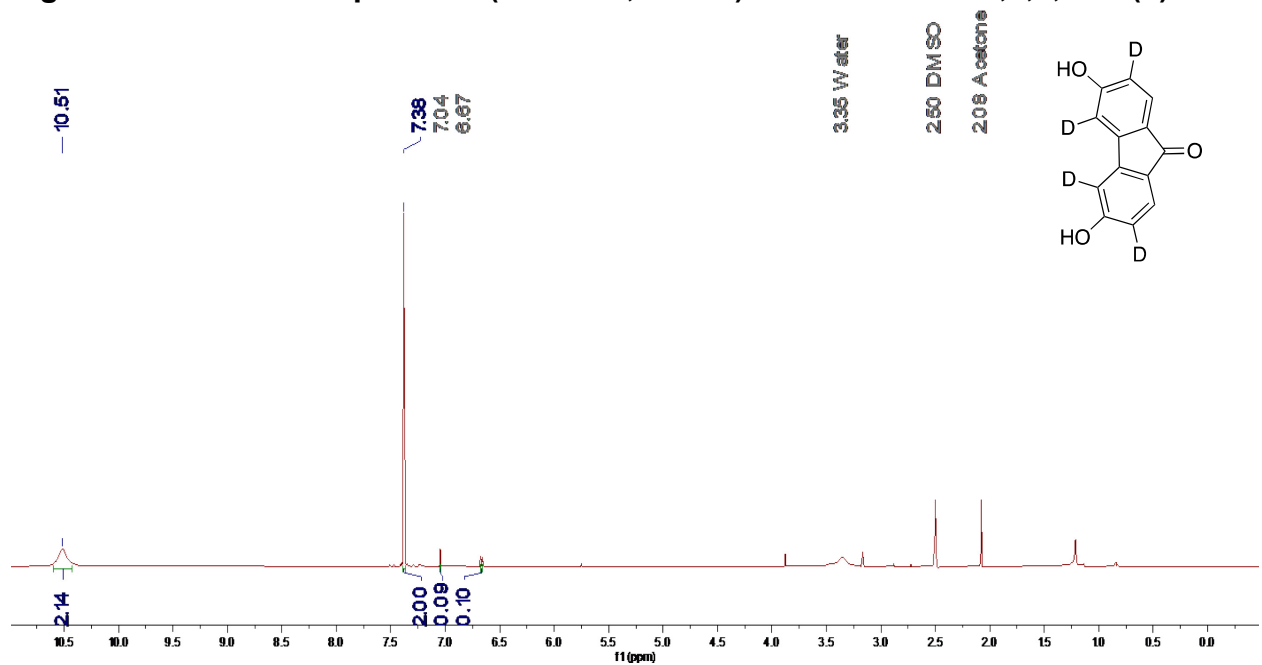
Figure 2.14. ^{1}H NMR spectrum (600 MHz, DMSO-d_6) of 3,6-dihydroxy-9H-fluoren-9-one-2,4,5,7-d_4 (8)
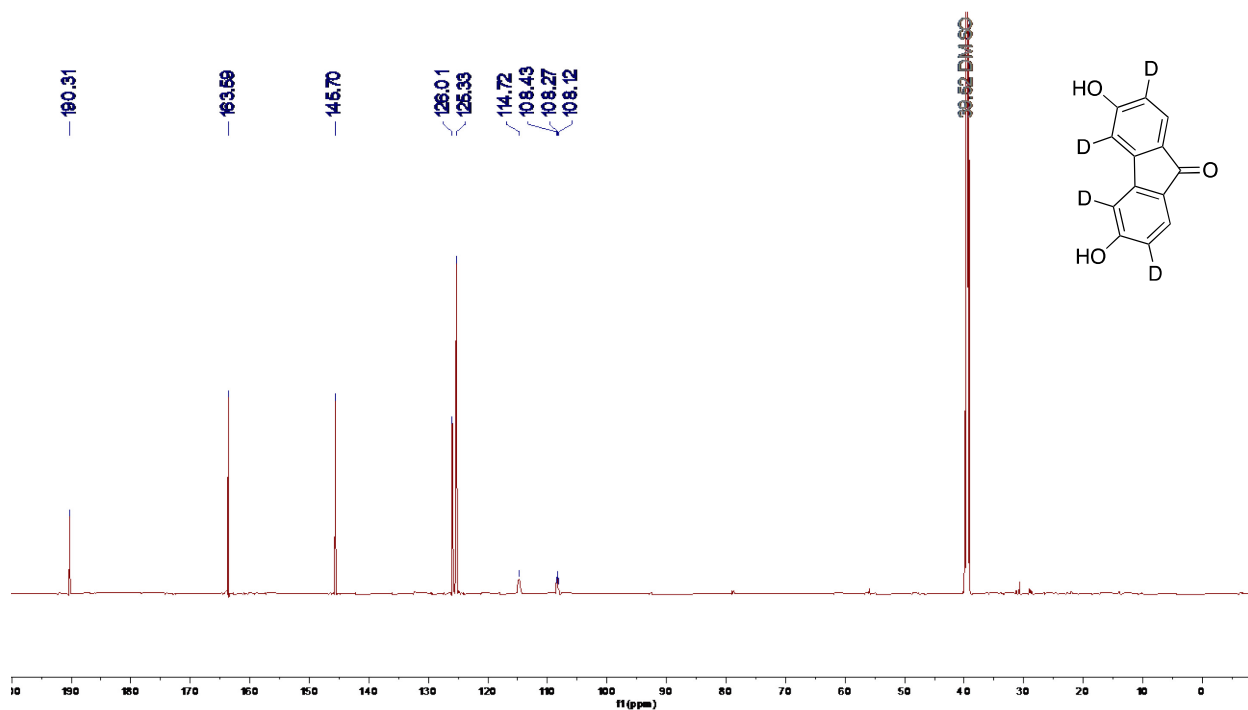
Figure 2.15. ^{13}C NMR spectrum (600 MHz, DMSO-d_6) of 3,6-dihydroxy-9H-fluoren-9-one-2,4,5,7-d_4 (8)
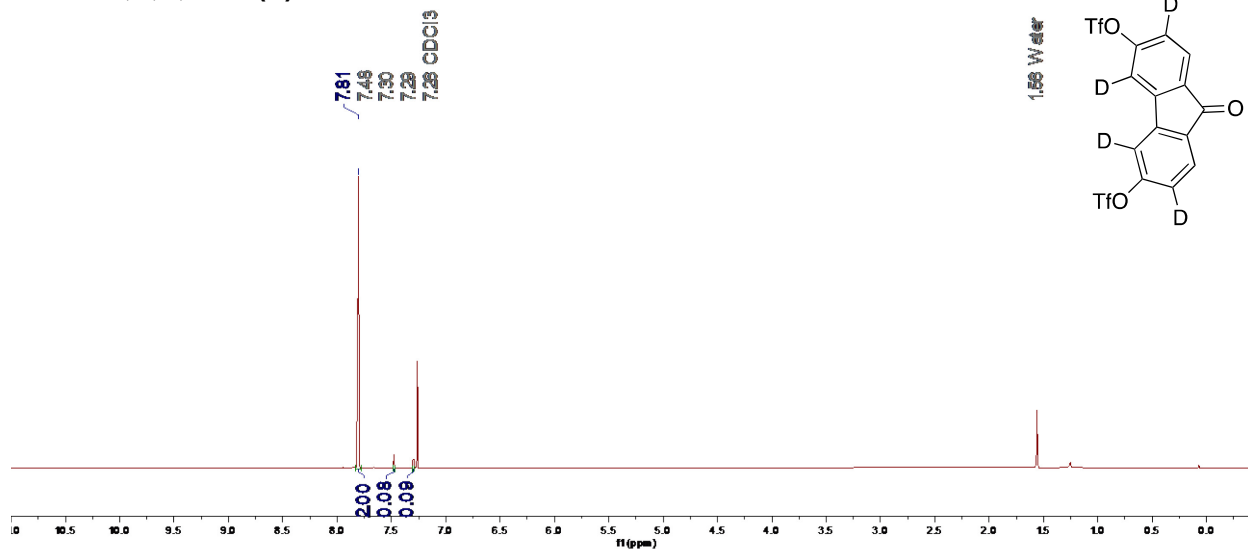
Figure 2.16. ^{1}H NMR spectrum (600 MHz, CDCl$_3$) of 9-oxo-9H-fluorene-3,6-diyl-2,4,5,7-d_4 bis(trifluoromethanesulfonate) (9)
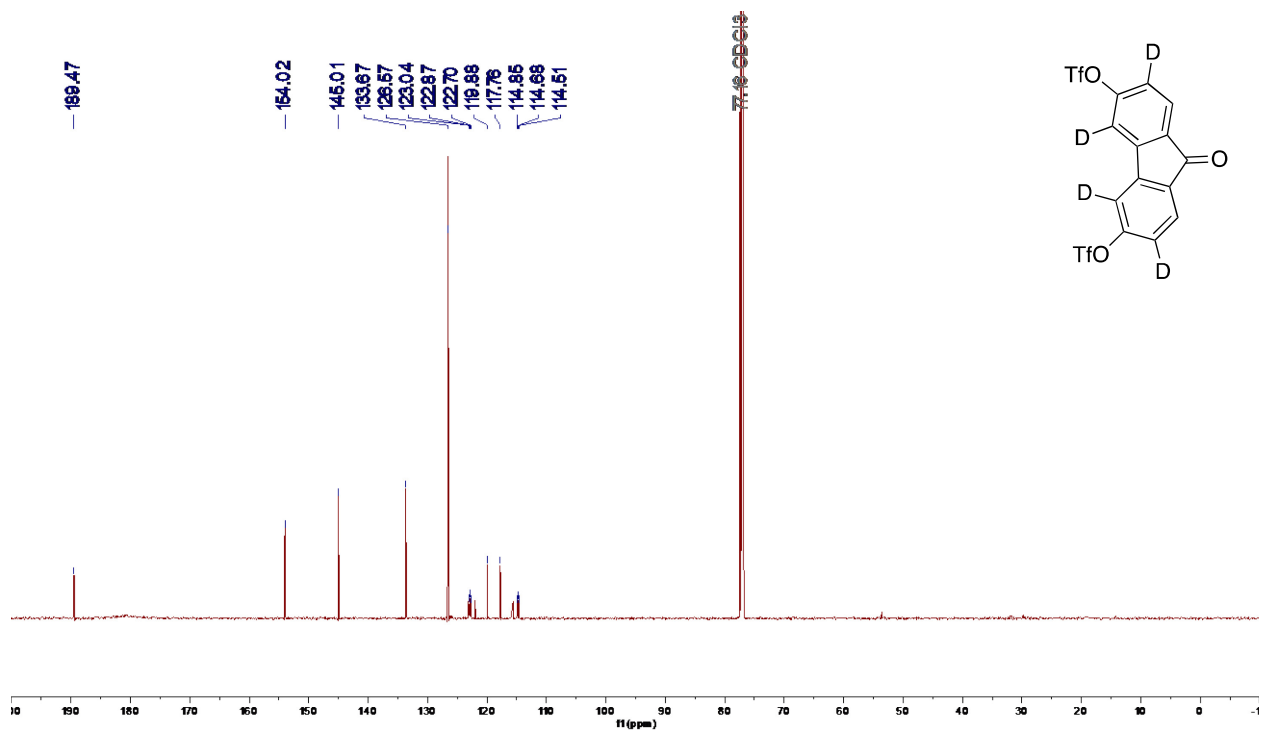
Figure 2.17. ^{13}C NMR spectrum (600 MHz, CDCl$_3$) of 9-oxo-9*H*-fluorene-3,6-diyl-2,4,5,7-*d*$_4$ bis(trifluoromethanesulfonate) (9)
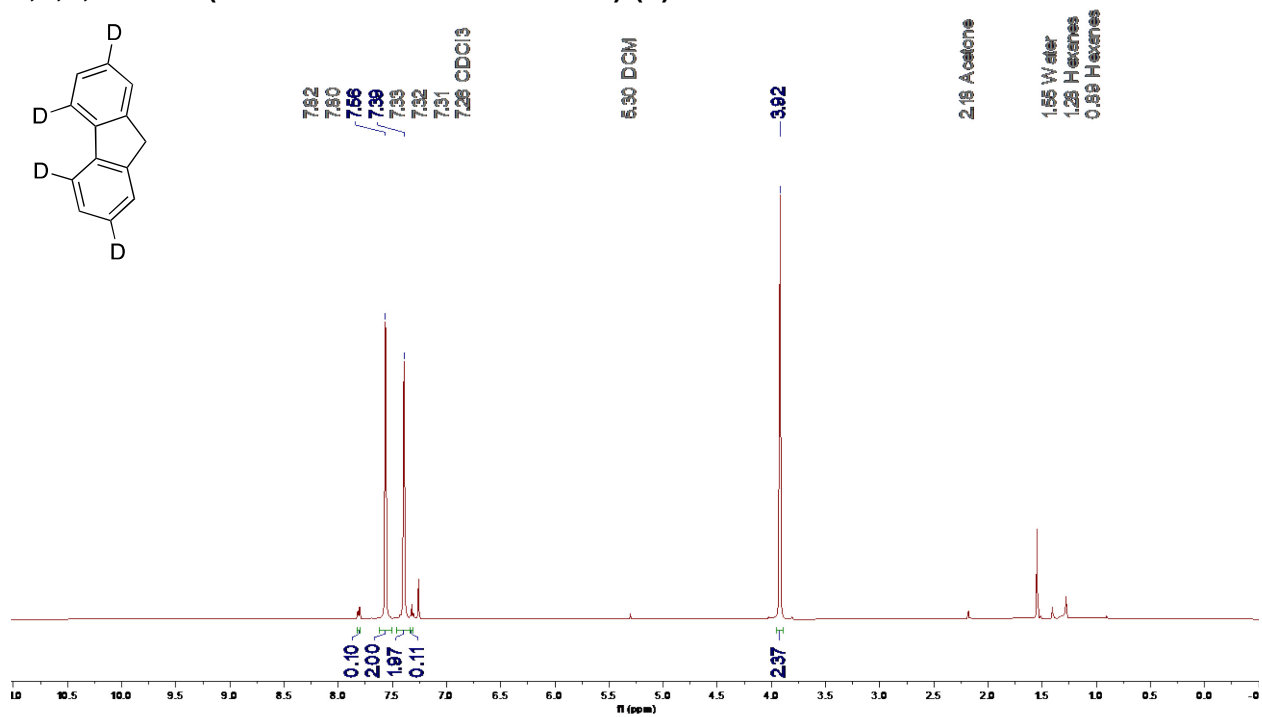
Figure 2.18. ^{1}H NMR spectrum (600 MHz, CDCl$_3$) of 9H-fluorene-2,4,5,7-*d*$_4$ (10)
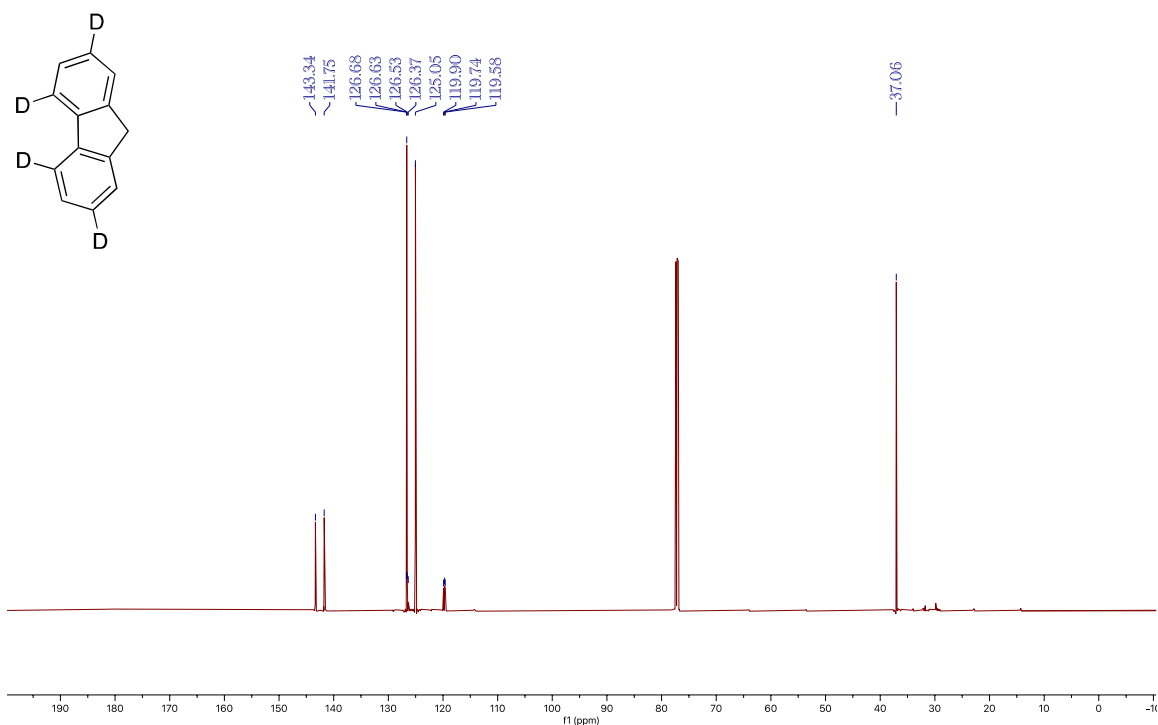
Figure 2.19. ^{13}C NMR spectrum (600 MHz, CDCl$_3$) of 9H-fluorene-2,4,5,7-d_4 (10)
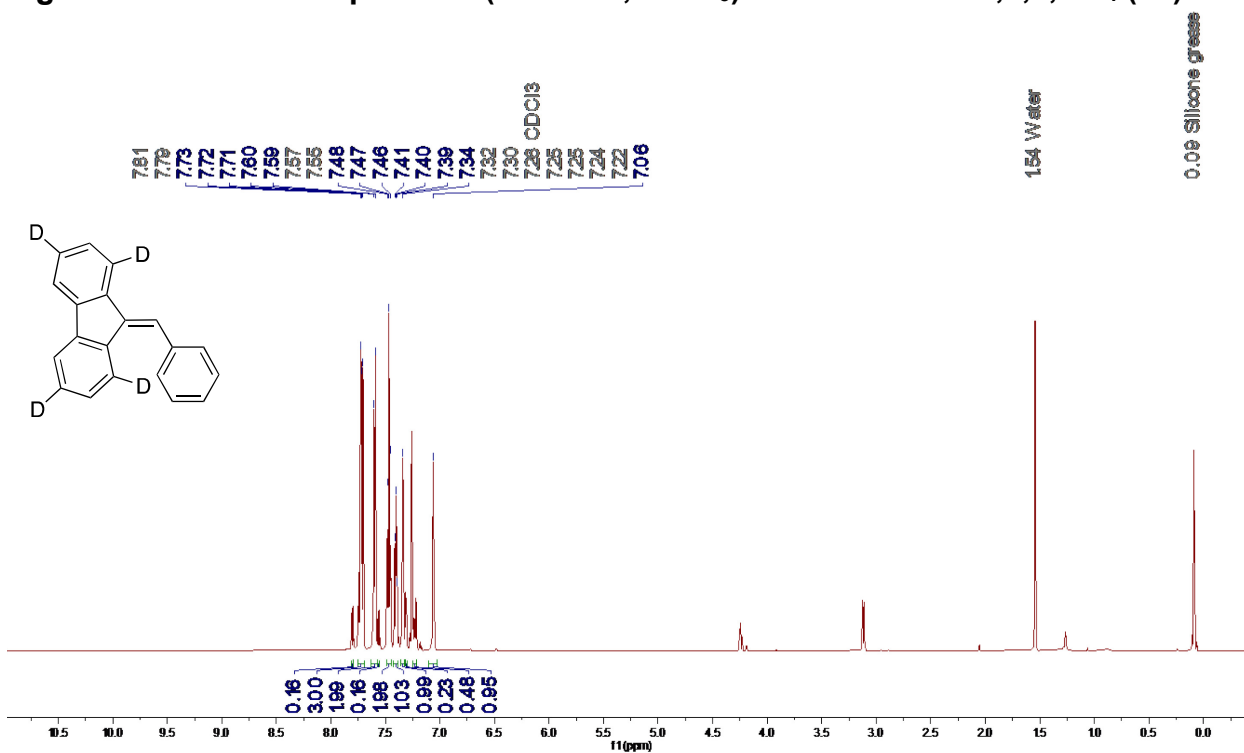
Figure 2.20. ^1H NMR spectrum (600 MHz, CDCl$_3$) of 9-benzylidene-9*H*-fluorene-1,3,6,8-*d$_4$* (11)

95
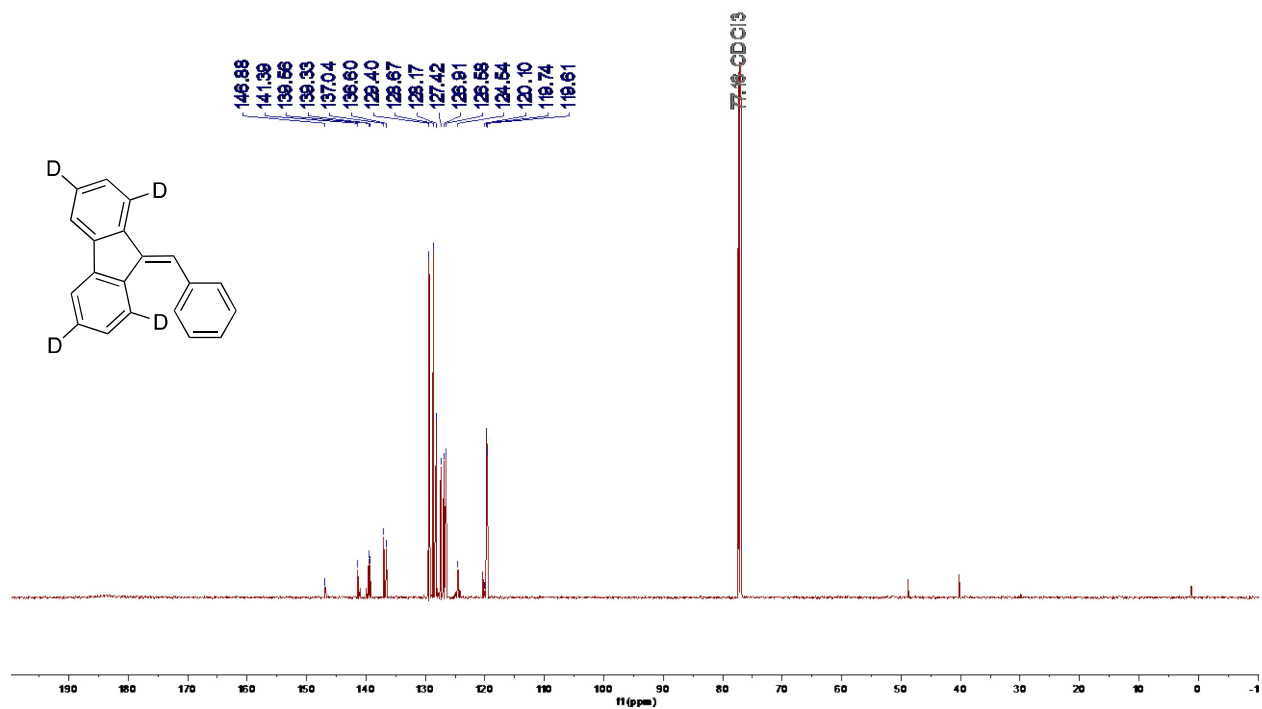
Figure 2.21. ¹³C NMR spectrum (600 MHz, CDCl₃) of 9-benzylidene-9*H*-fluorene-1,3,6,8-*d*₄ (11)
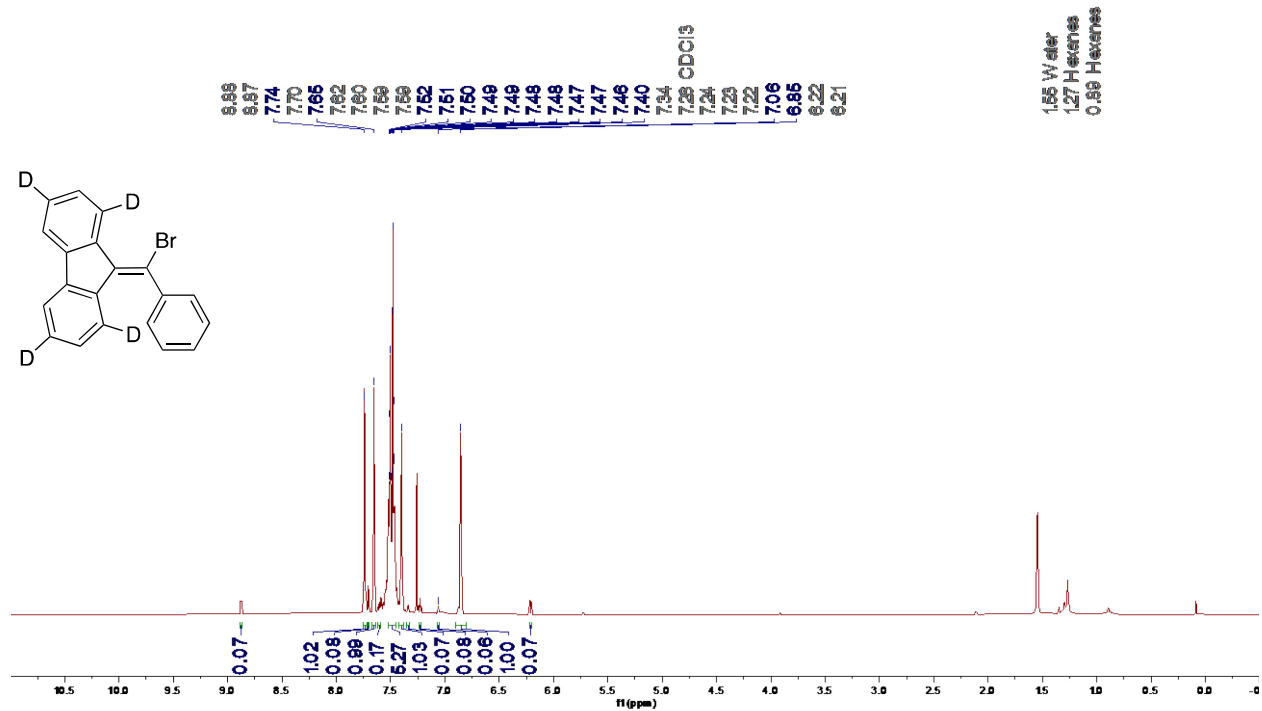
Figure 2.22. ¹H NMR spectrum (600 MHz, CDCl₃) of 9-(bromo(phenyl)methylene)-9*H*-fluorene-1,3,6,8-*d*₄ (12)
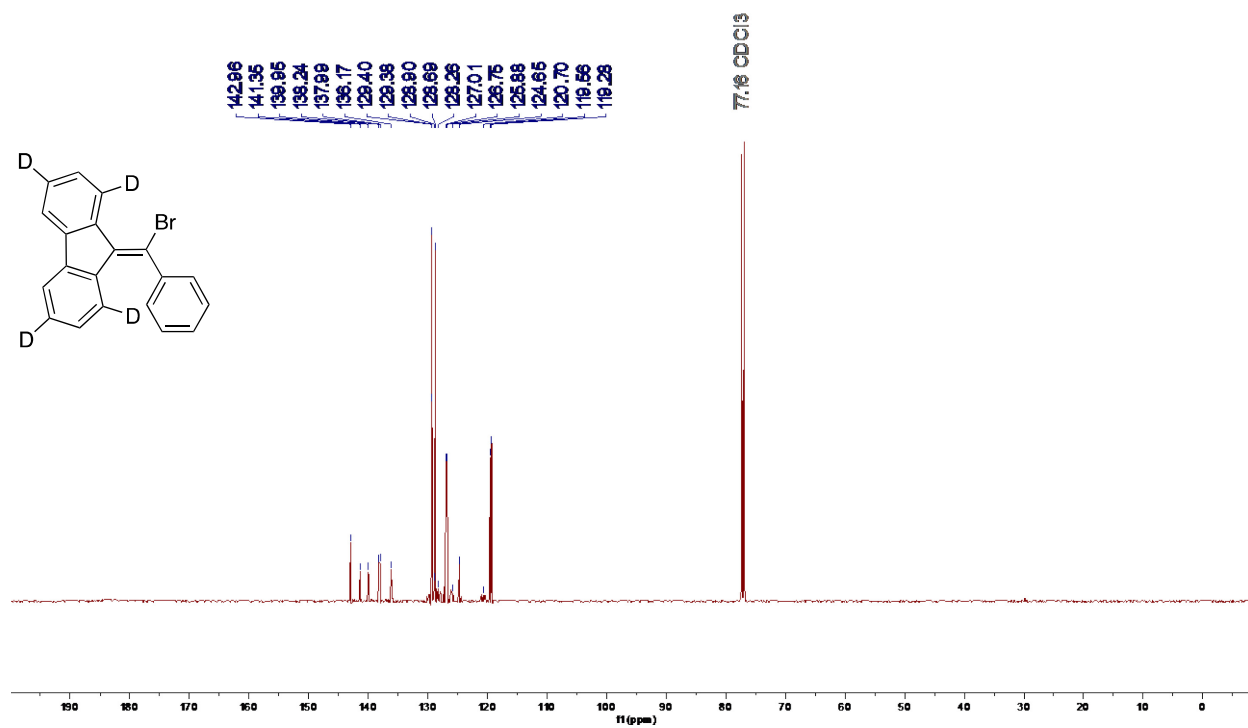
Figure 2.23. ^{13}C NMR spectrum (600 MHz, CDCl$_3$) of 9-(bromo(phenyl)methylene)-9*H*-fluorene-1,3,6,8-*d*$_4$ (12)
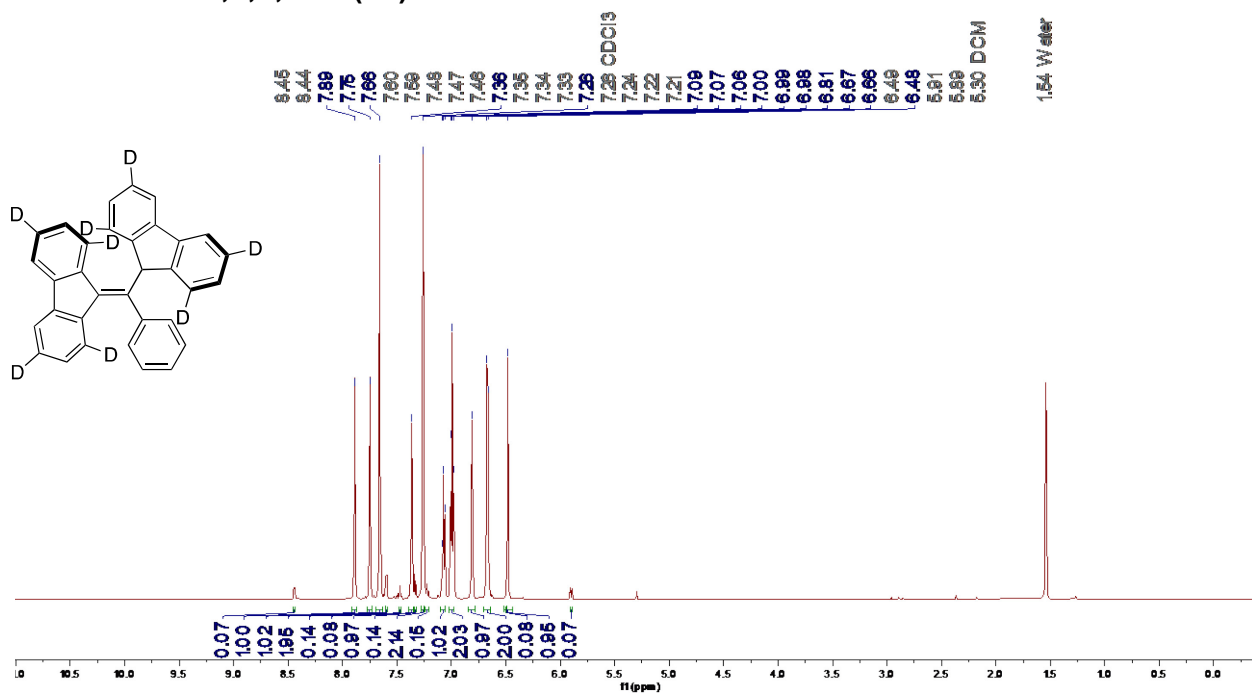
Figure 2.24. ^{1}H NMR spectrum (600 MHz, CDCl$_3$) of 9-((9*H*-fluoren-9-yl-1,3,6,8-*d*$_4$)(phenyl)methylene)-9*H*-fluorene-1,3,6,8-*d*$_4$ (13)
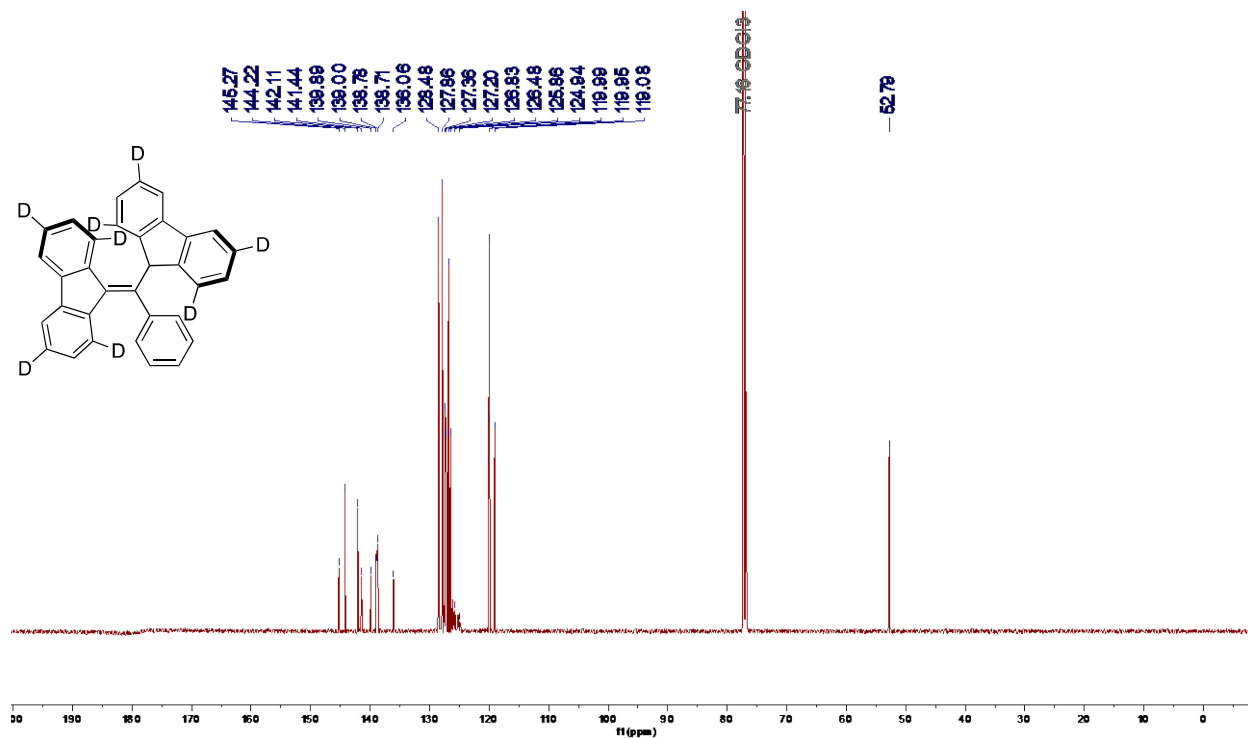
Figure 2.25. ^{13}C NMR spectrum (600 MHz, CDCl$_3$) of 9-((9*H*-fluoren-9-yl-1,3,6,8-*d$_4$*)(phenyl)methylene)-9*H*-fluorene-1,3,6,8-*d$_4$* (13)
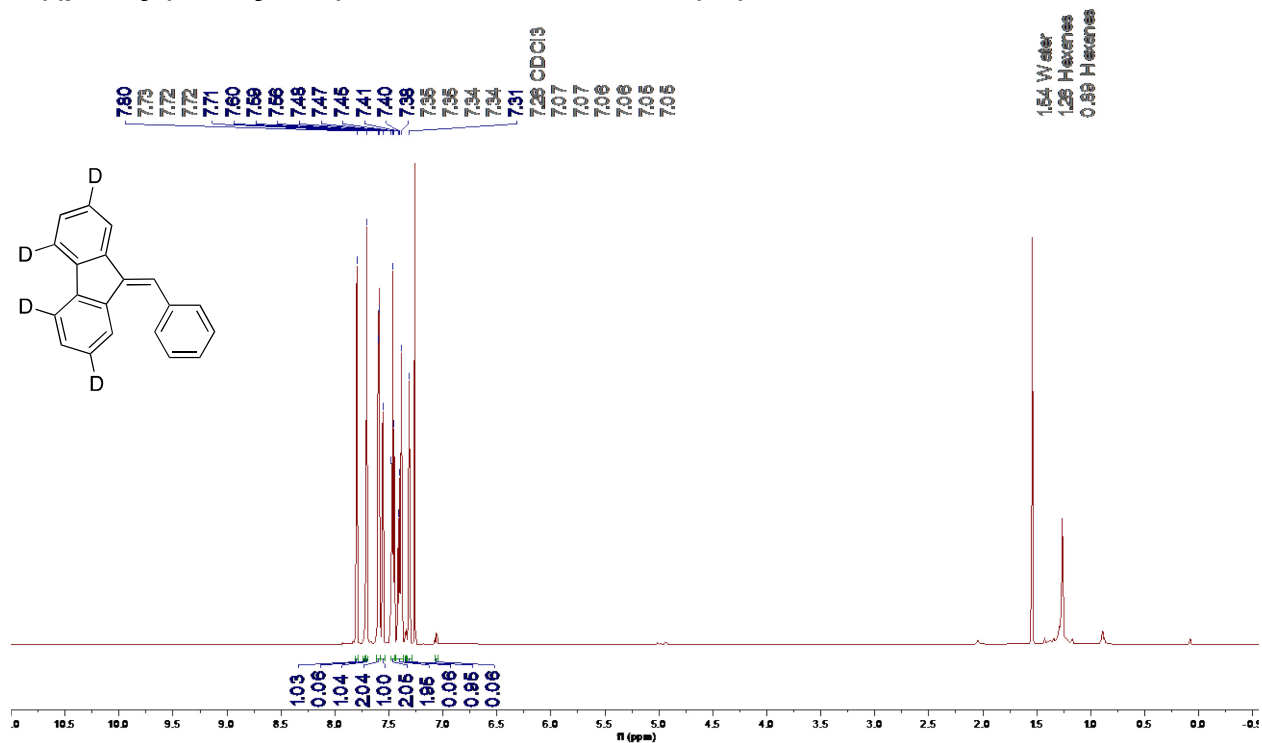
Figure 2.26. ^{1}H NMR spectrum (600 MHz, CDCl$_3$) of 9-benzylidene-9*H*-fluorene-2,4,5,7-*d$_4$* (15)
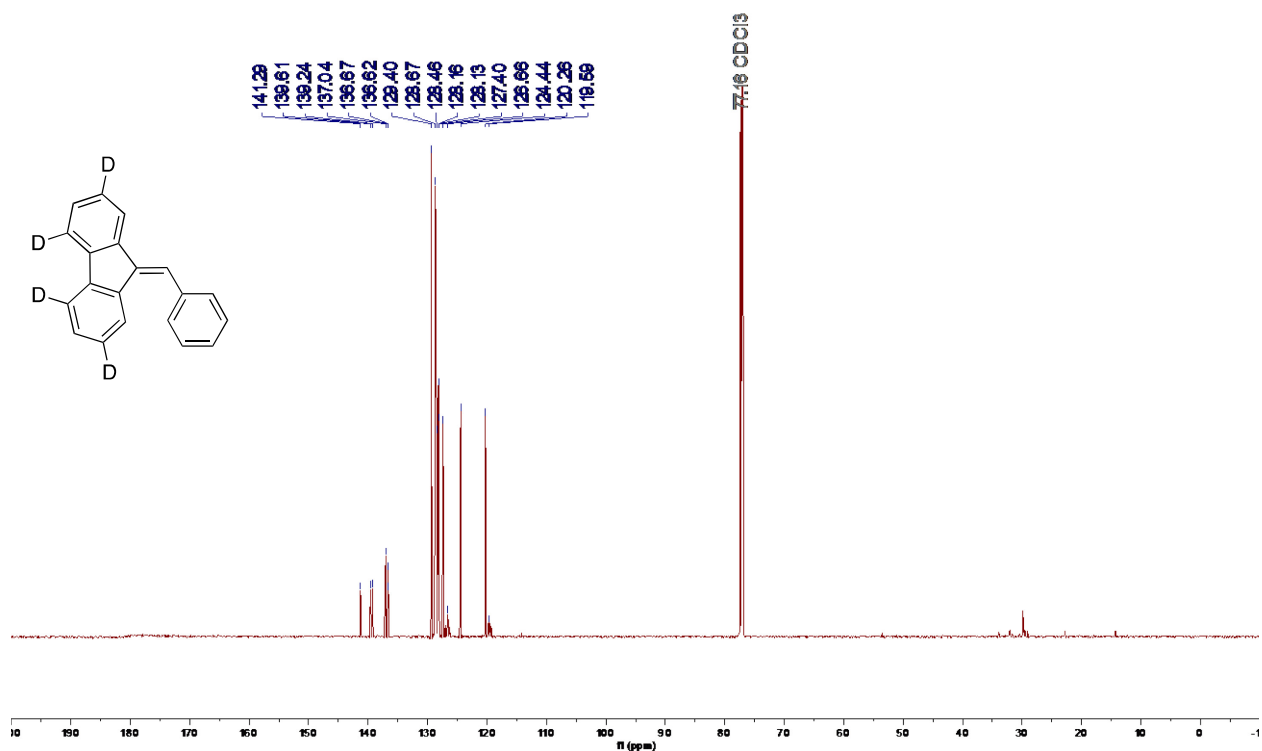
Figure 2.27. ^{13}C NMR spectrum (600 MHz, CDCl$_3$) of 9-benzylidene-9*H*-fluorene-2,4,5,7-*d*$_4$ (15)
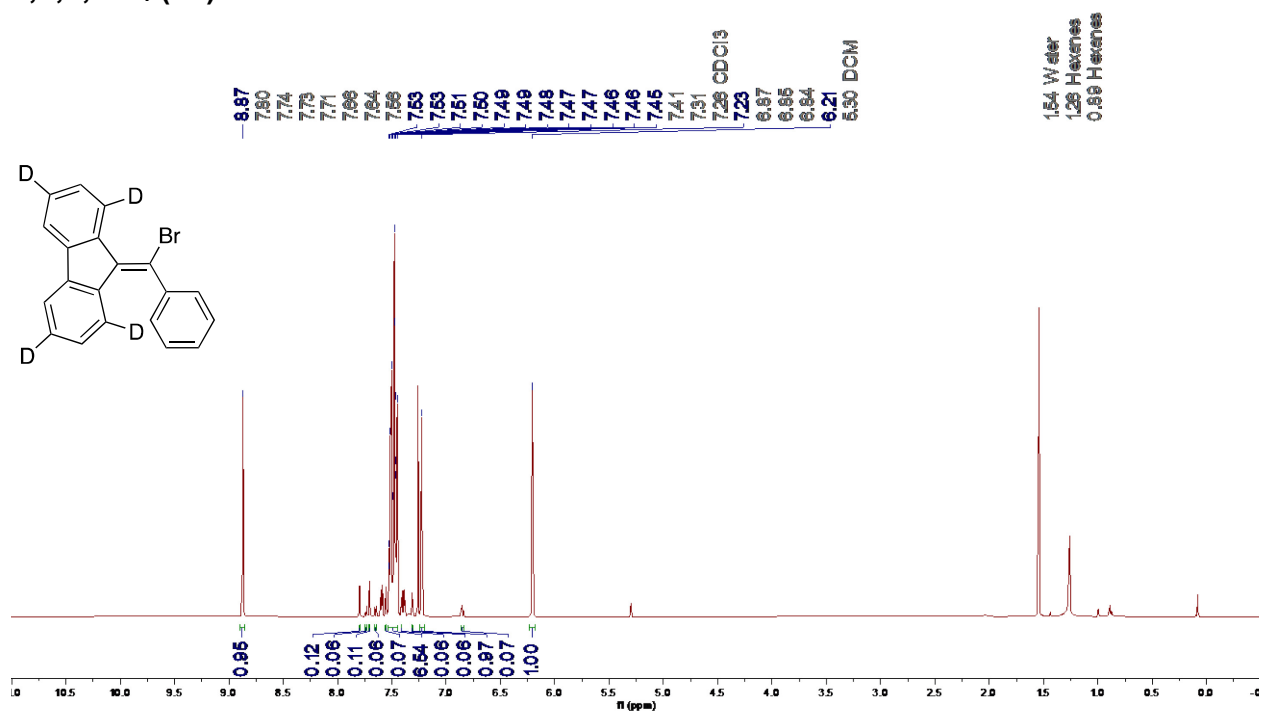
Figure 2.28. ^{1}H NMR spectrum (600 MHz, CDCl$_3$) of 9-(bromo(phenyl)methylene)-9*H*-fluorene-2,4,5,7-*d*$_4$ (16)
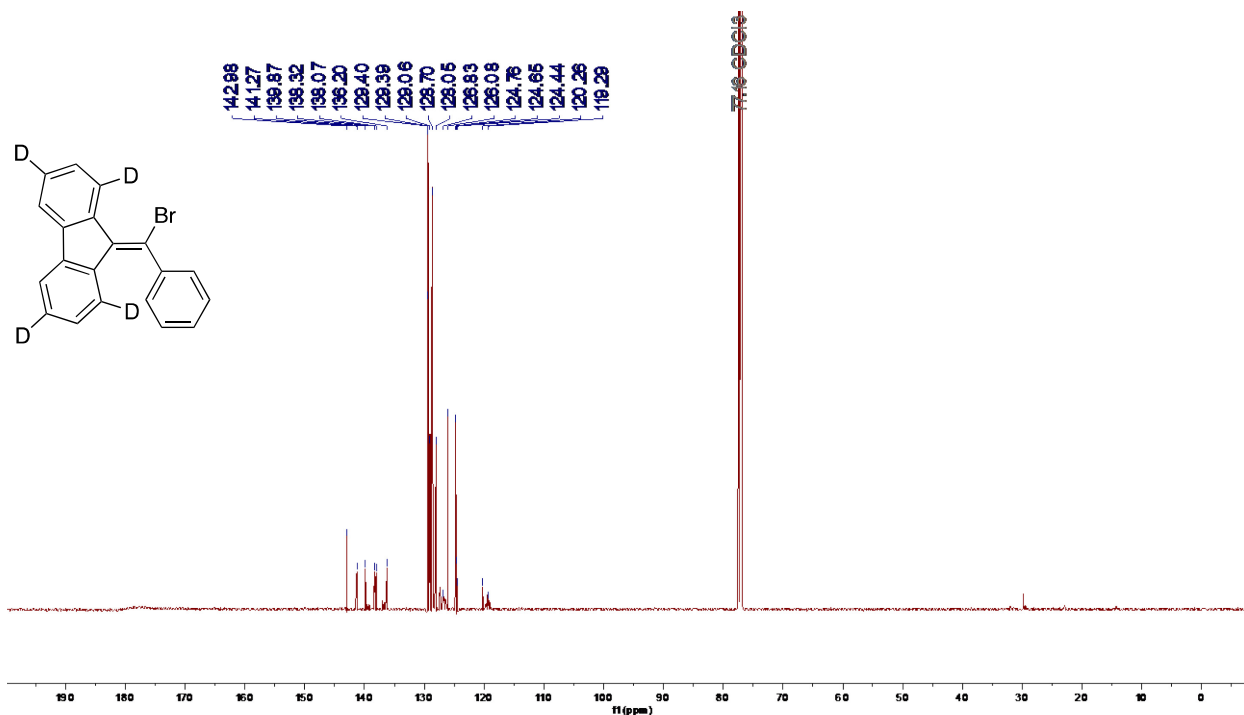
Figure 2.29. ^{13}C NMR spectrum (600 MHz, CDCl$_3$) of 9-(bromo(phenyl)methylene)-9*H*-fluorene-2,4,5,7-*d*$_4$ (16)
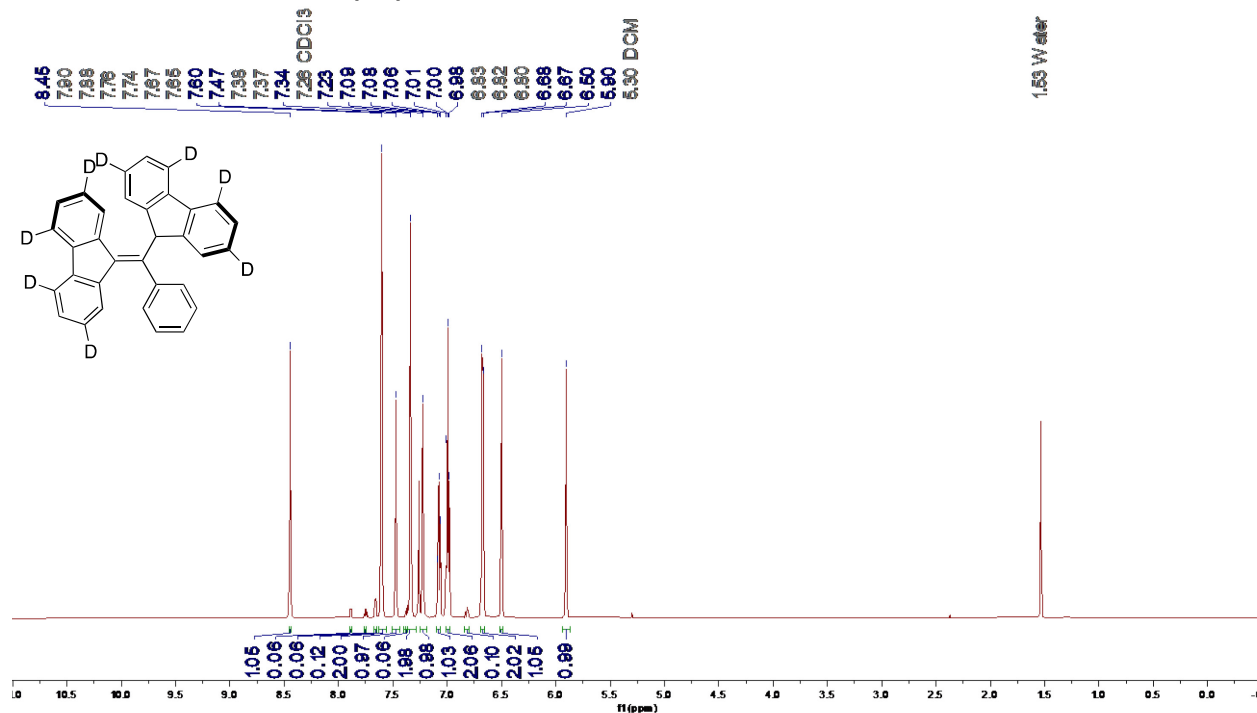
Figure 2.30. ^{1}H NMR spectrum (600 MHz, CDCl$_3$) of 9-((9*H*-fluoren-9-yl-2,4,5,7-*d*$_4$)(phenyl)methylene)-9*H*-fluorene-2,4,5,7-*d*$_4$ (17)
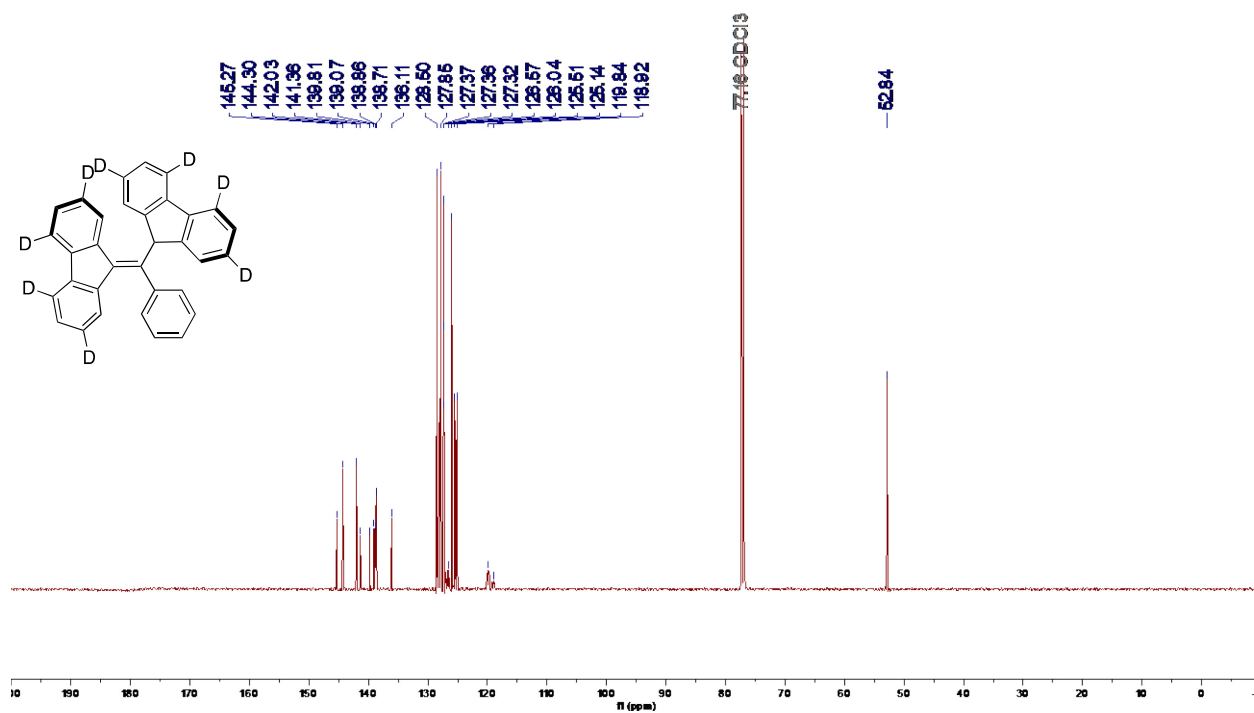
Figure 2.31. ^{13}C NMR spectrum (600 MHz, CDCl$_3$) of 9-((9*H*-fluoren-9-yl-2,4,5,7-*d*$_4$)(phenyl)methylene)-9*H*-fluorene-2,4,5,7-*d*$_4$ (17)

Sample Purity

(a) stock BDPA from Sigma-Aldrich   (b) "purified" BDPA   (c) "purified" BDPA + 10 days
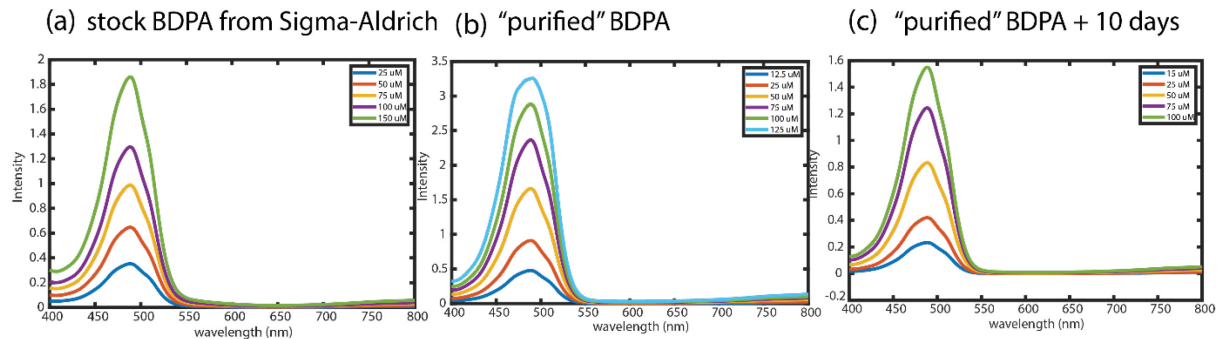
Figure 2.32. BDPA UV-VIS Measurements. UV-vis measurements at different concentrations for (a) stock h_{21}-BDPA (complex with benzene) as purchased from Sigma-Aldrich and used in the presented work, (b) h_{21}-BDPA purified via silica gel chromatography, and (c) the same as (b) only measured 10 days later.

Sample	Extinction coefficient
Stock h_{21}-BDPA from Sigma-Aldrich	12930 ± 650
"Purified" h_{21}-BDPA	28770 ± 3300
"Purified" h_{21}-BDPA after 10 days	16360 ± 920

Table 2.3. Calculated extinction coefficients Extinction coefficients for h_{21}-BDPA based on measurements given in Figure 2.32. The stock h_{21}-BDPA used in this work is found to possess only about 50% of active radicals.

(a)

(b)

(c)
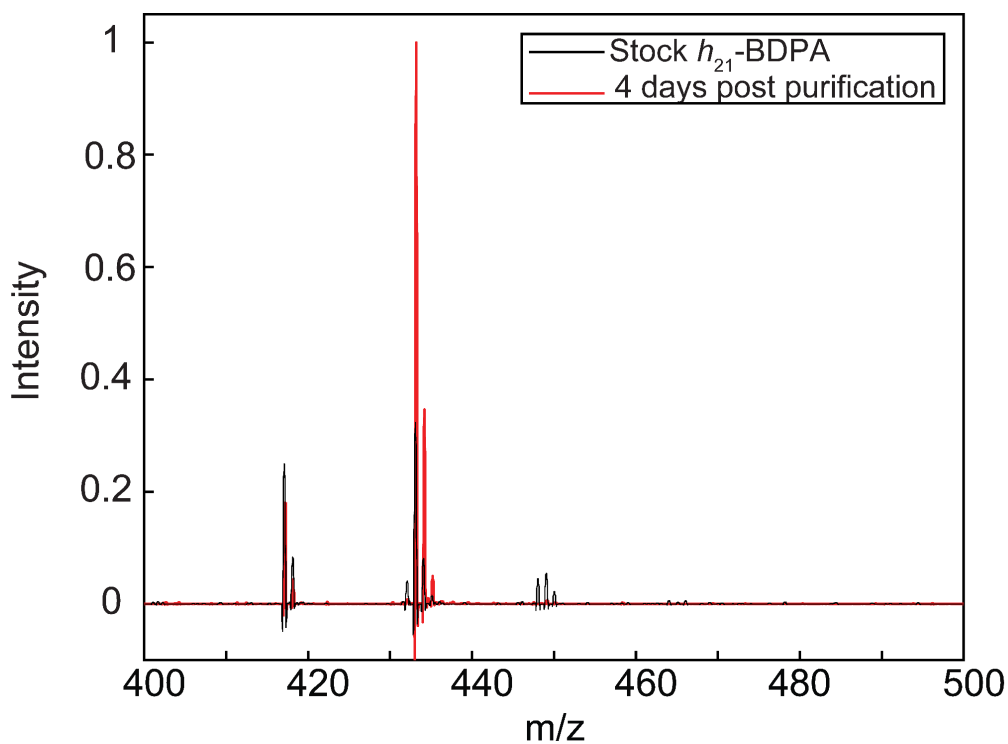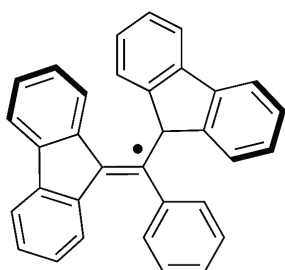
Molecular Weight: 418.54   Molecular Weight: 434.54   Molecular Weight: 450.54
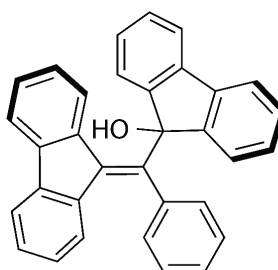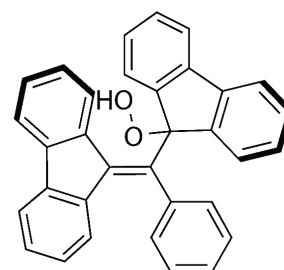
Figure 2.33. MALDI-TOF-MS. Matrix assisted laser desorption ionization-time of light mass spectrometry (MALDI-TOF-MS) of Sigma Aldrich of h_{21}-BDPA 1:1 in complex with benzene (black) and 4 days after silica gel chromatography purification (red). MALDI-TOF-MS samples were prepared by dissolving h_{21}-BDPA into chloroform and spotting onto sample plate. Major species in the MALDI-TOF-MS spectrum are (a) h_{21}-BDPA radical, (b) hydroxylated BDPA, and (c) hydroperoxylated BDPA. Following purification of the sample and removal of benzene, h_{21}-BDPA is prone to hydroxylation.

Radical Concentrations

EPR signal intensity of DNP samples in a 4 mm sapphire rotor was determined using a Magnettch ESR5000 spectrometer and double integral (DI) signal intensities were calculated using MATLAB[72]. The quantity of electron spins in h_{21}-BDPA, 1,3-[α,γ-d_8]-BDPA, and 1,3-[β,δ-d_8]-BDPA were determined relative to a standard sample whose concentration and number of electron spins was determined using absolute spin quantification methods on a EMXnano spectrometer. The number of electron spins, n, in each DNP sample were determined as $n_{DNP} = \dfrac{DI_{DNP} \times n_{Standard}}{DI_{Standard}}$. In Figure S28, the standard deviation of three EPR measurements is shown in the shaded region. The concentration was then calculated by measuring the length of sample in the rotor, the uncertainty in length measurement is reflected in the minimum and maximum concentration values in Figure 2.35.
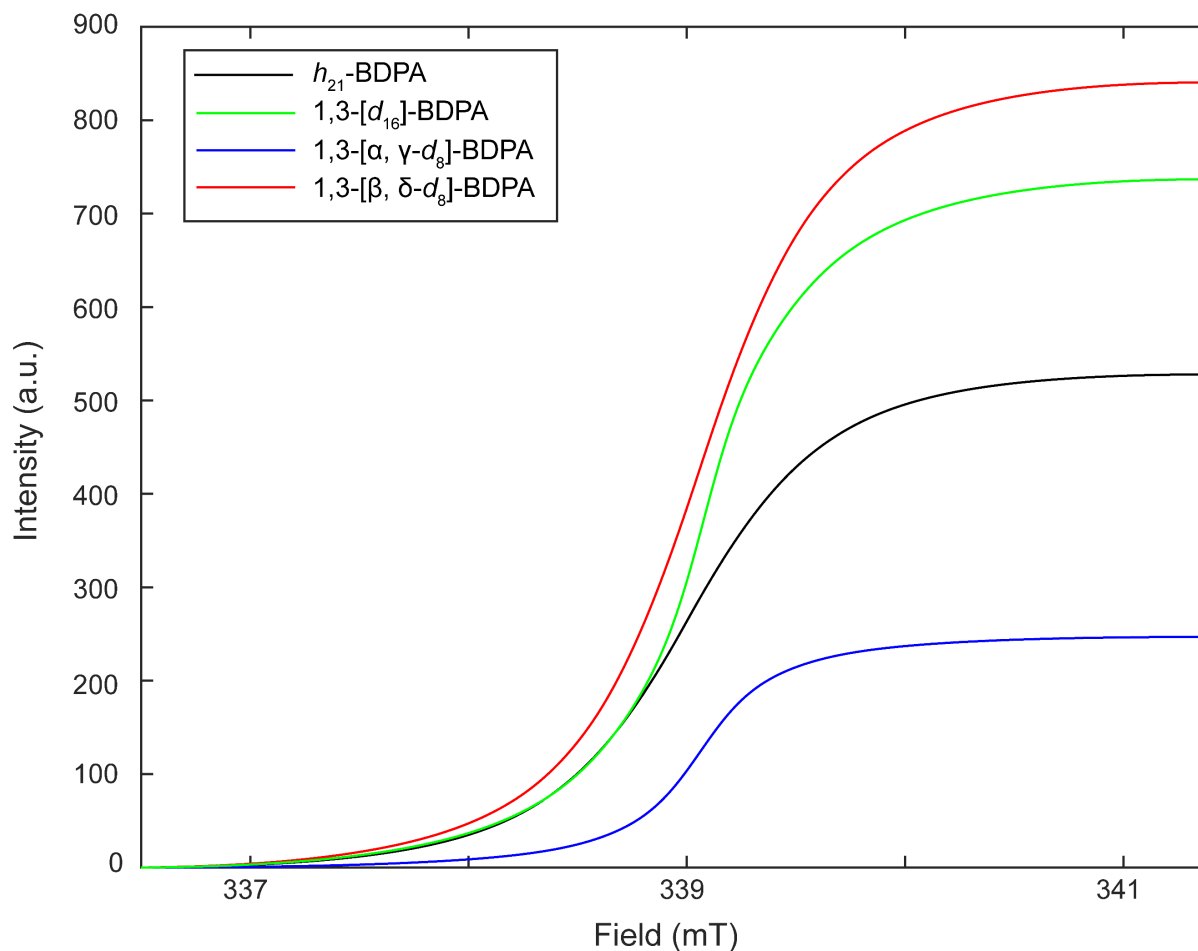
Figure 2.34. Quantitative EPR of BDPA Radicals. Double Integral of X-Band EPR derivative spectra for h_{21}-BDPA, 1,3-[d_{16}]-BDPA, 1,3-[α,γ-d_8]-BDPA, and 1,3-[β,δ-d_8]-BDPA.
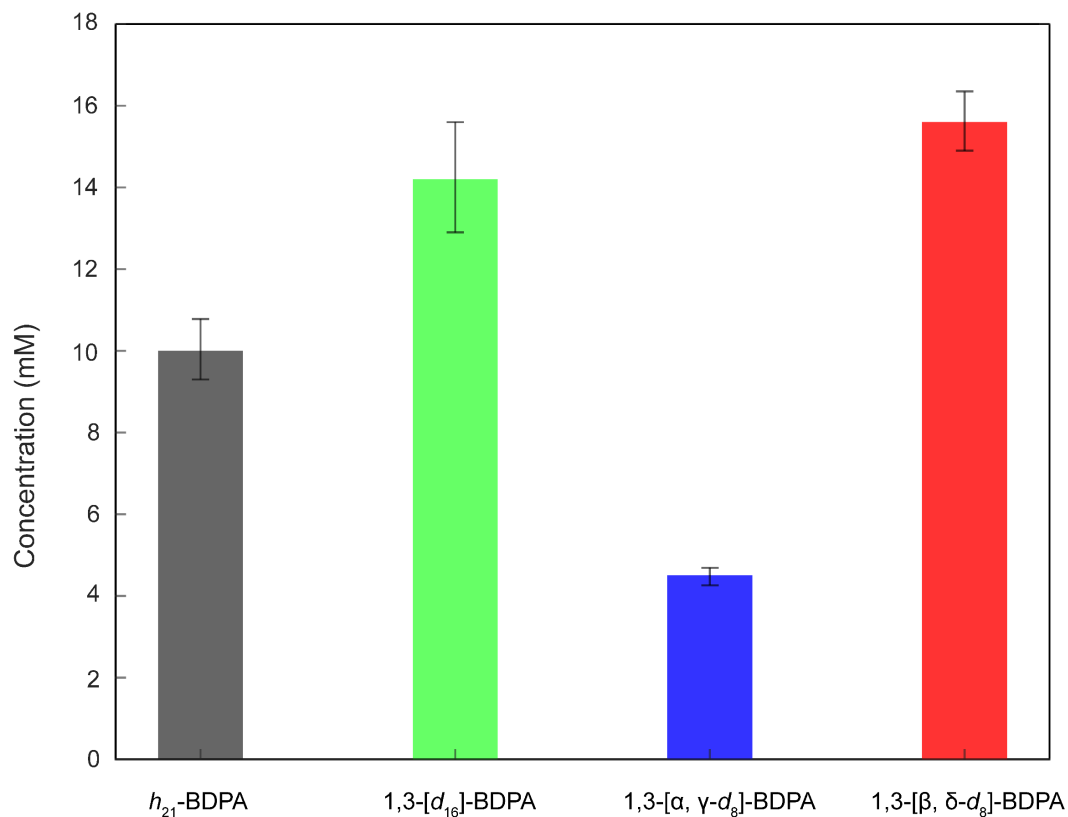
Figure 2.35. Radical Concentrations. Radical concentrations from X-Band EPR for h_{21}-BDPA, 1,3-[d_{16}]-BDPA, 1,3-[α,γ-d_8]-BDPA, and 1,3-[β,δ-d_8]-BDPA. Determined concentrations by EPR were 10 mM, 14.2 mM, 4.5 mM, and 15.6 mM for h_{21}-BDPA, 1,3-[d_{16}]-BDPA, 1,3-[α,γ-d_8]-BDPA, and 1,3-[β,δ-d_8]-BDPA, respectively.

DNP Supporting information

All DNP samples were degassed using a freeze-pump-thaw procedure using the

homebuilt adapter shown in Figure 2.36(a). The adapter was 3D printed using a Form3

3D printer using Rigid 4K resin (Formlabs Somerville, MA). The adapter was then

epoxied to a 3-way valve, as shown in Figure 2.36(b), through which vacuum was

applied to the rotor directly. The sample was kept immersed in liquid nitrogen while

being transferred to a glove bag following 5 freeze-pump-thaw cycles. The rotor was

removed from degassing apparatus and endcap inserted in the glove bag and

immediately inserted into spectrometer.

(a)   (b)
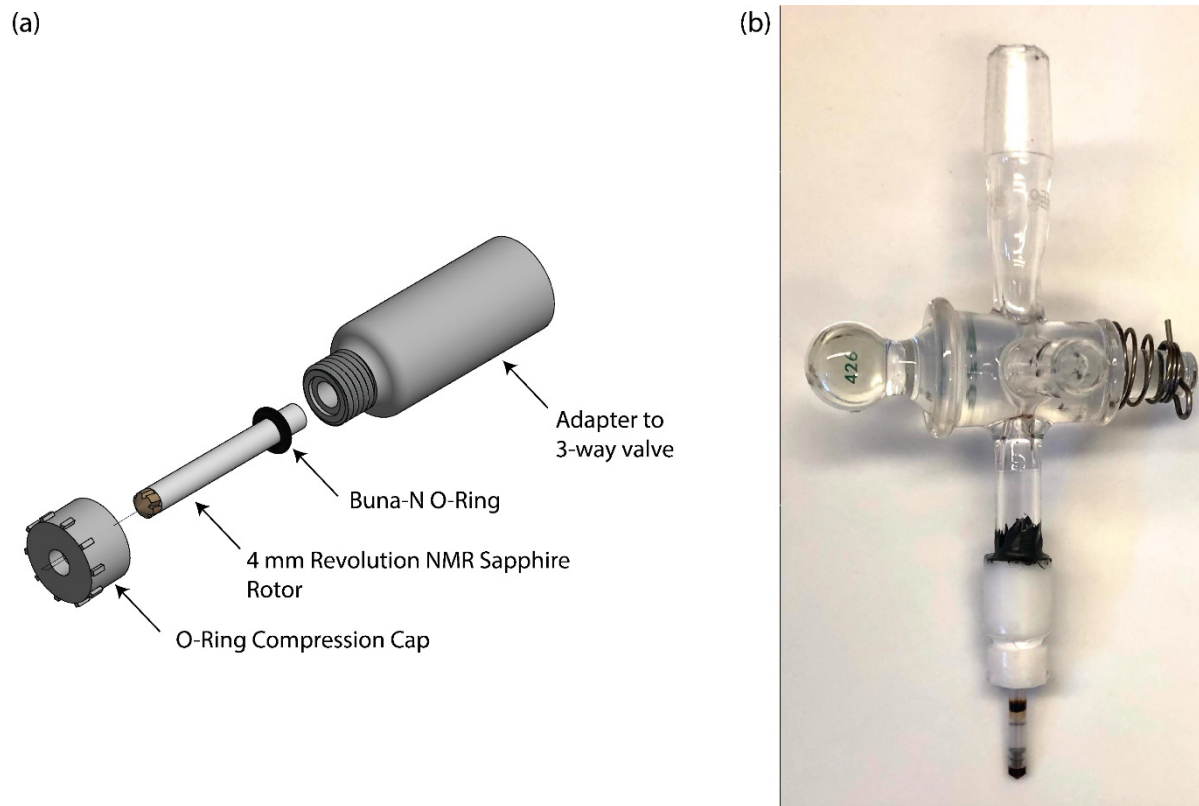
Figure 2.36. Degassing Apparatus. Homebuilt degassing apparatus used for DNP
sample preparation. (a) CAD rendering of 3D printed adapter. Sample rotor was sealed
against atmosphere using Buna-N O-ring which was observed to maintain sufficient
sealing while sample was immersed into liquid nitrogen during freezing and pumping
steps. (b) Photograph of assembled adapter epoxied on 3-way valve which enabled
connection to vacuum pump in addition to nitrogen gas purge line.

Sample	T_1 /s	$T_{B,OE}$ /s	$T_{B,SE}$ /s	Enh. (OE)	Enh. (SE)
Non-degassed	32.1 ± 2.2	37.5 ± 1.5	38.4 ± 1.9	70.2	5.8
Degassed	42.6 ± 3.3	43.6 ± 2.3	42.4 ± 2.1	39.7	3.3

Table 2.4. Summary of Degassing of DNP Samples. Experimentally observed spin-lattice relaxation times (T_1), DNP buildup times with the microwave irradiation at the OE frequency ($T_{B,OE}$) or at the positive SE frequency ($T_{B,SE}$) are expressed in seconds for 2.5 wt% h_{21}-BDPA in 5 mol% h_{14}- and 95 mol% d_{14}-oTP matrix with the sample subjected to freeze-pump-thaw degassing or not. The enhancement values calculated for the OE and the positive SE are also mentioned. The NMR magnetic field strength was 8.92 T (380 MHz [1]H Larmor frequency), the sample temperature was 90 K, and the MAS frequency was 5 kHz.
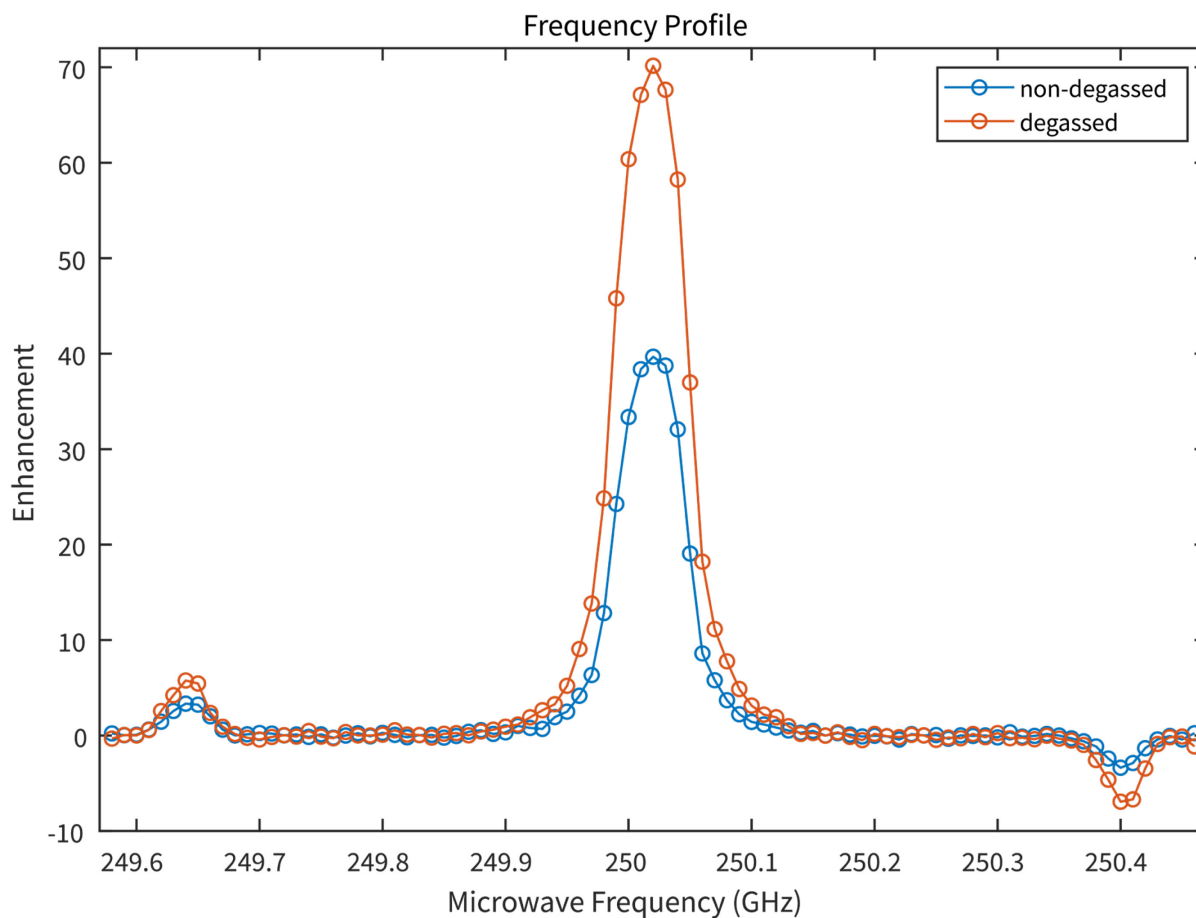
Figure 2.37. [1]H DNP enhancement frequency profiles. [1]H DNP enhancement frequency profiles for 2.5 wt% h_{21}-BDPA in 5 mol% h_{14}- and 95 mol% d_{14}-oTP matrix with the sample subjected to freeze-pump-thaw degassing (red) or not (blue). The NMR magnetic field strength was 8.92 T (380 MHz [1]H Larmor frequency), the sample temperature was 90 K, and the MAS frequency was 5 kHz.

2.7 Acknowledgements

2.8 References

1   Abragam, A. *The principles of nuclear magnetism*. (Oxford university press, 1983).
2   Overhauser, A. W. Polarization of Nuclei in Metals. *Physical Review* **92**, 411-415 (1953). https://doi.org:10.1103/PhysRev.92.411
3   Slichter, C. P. *Principles of magnetic resonance*. Vol. 1 (Springer Science & Business Media, 2013).
4   Becerra, L. R., Gerfen, G. J., Temkin, R. J., Singel, D. J. & Griffin, R. G. Dynamic nuclear polarization with a cyclotron resonance maser at 5 T. *Physical Review Letters* **71**, 3561-3564 (1993). https://doi.org:10.1103/PhysRevLett.71.3561
5   Gerfen, G. J. *et al.* High frequency (140 GHz) dynamic nuclear polarization: polarization transfer to a solute in frozen aqueous solution. *The Journal of chemical physics* **102**, 9494-9497 (1995).
6   Griffin, R. G., Swager, T. M. & Temkin, R. J. High Frequency, Dynamic Nuclear Polarization: New Directions for the 21st Century. *Journal of magnetic resonance (San Diego, Calif.: 1997)* **306**, 128 (2019).
7   Judge, P. T. *et al.* Dynamic Nuclear Polarization with Electron Decoupling in Intact Human Cells and Cell Lysates. *The Journal of Physical Chemistry B* **124**, 2323-2330 (2020).
8   Lelli, M. *et al.* Fast characterization of functionalized silica materials by silicon-29 surface-enhanced NMR spectroscopy using dynamic nuclear polarization. *Journal of the American Chemical Society* **133**, 2104-2107 (2011).
9   Ni, Q. Z. *et al.* High frequency dynamic nuclear polarization. *Accounts of chemical research* **46**, 1933-1941 (2013).

10   Ni, Q. Z. *et al.* Peptide and protein dynamics and low-temperature/DNP magic angle spinning NMR. *The Journal of Physical Chemistry B* **121**, 4997-5006 (2017).

11   Rossini, A. J. *et al.* Dynamic nuclear polarization enhanced solid‐state NMR spectroscopy of functionalized metal–organic frameworks. *Angewandte Chemie International Edition* **51**, 123-127 (2012).

12   Smith, A. N., Caporini, M. A., Fanucci, G. E. & Long, J. R. A method for dynamic nuclear polarization enhancement of membrane proteins. *Angewandte Chemie* **127**, 1562-1566 (2015).

13   Zhao, L., Pinon, A. C., Emsley, L. & Rossini, A. J. DNP‐enhanced solid‐state NMR spectroscopy of active pharmaceutical ingredients. *Magnetic Resonance in Chemistry* **56**, 583-609 (2018).

14   Smith, S. O. *et al.* Low-temperature solid-state carbon-13 NMR studies of the retinal chromophore in rhodopsin. *Biochemistry* **26**, 1606-1611 (1987).

15   Raleigh, D., Creuzet, F., Das Gupta, S., Levitt, M. & Griffin, R. G. Measurement of internuclear distances in polycrystalline solids. Rotationally enhanced transfer of nuclear spin magnetization. *Journal of the American Chemical Society* **111**, 4502-4503 (1989).

16   Griffiths, J. M. & Griffin, R. G. Nuclear magnetic resonance methods for measuring dipolar couplings in rotating solids. *Analytica chimica acta* **283**, 1081-1101 (1993).

17   Bertini, I. *et al.* High-resolution solid-state NMR structure of a 17.6 kDa protein. *Journal of the American Chemical Society* **132**, 1032-1040 (2010).

18   Ni, Q. Z. *et al.* Primary transfer step in the light-driven ion pump bacteriorhodopsin: An irreversible U-turn revealed by dynamic nuclear polarization-enhanced magic angle spinning NMR. *Journal of the American Chemical Society* **140**, 4085-4091 (2018).

19   Becerra, L. R. *et al.* A Spectrometer for Dynamic Nuclear Polarization and Electron Paramagnetic Resonance at High Frequencies. *Journal of Magnetic Resonance, Series A* **117**, 28-40 (1995). https://doi.org:https://doi.org/10.1006/jmra.1995.9975

20   Berruyer, P. *et al.* Dynamic nuclear polarization enhancement of 200 at 21.15 T enabled by 65 kHz magic angle spinning. *The Journal of Physical Chemistry Letters* **11**, 8386-8391 (2020).

21   Hornstein, M. K. *et al.* Second harmonic operation at 460 GHz and broadband continuous frequency tuning of a gyrotron oscillator. *IEEE Transactions on Electron Devices* **52**, 798-807 (2005).

22   Jawla, S. K., Griffin, R. G., Mastovsky, I. A., Shapiro, M. A. & Temkin, R. J. Second harmonic 527-GHz gyrotron for DNP-NMR: Design and experimental results. *IEEE transactions on electron devices* **67**, 328-334 (2019).

23   Scott, F. J. *et al.* Frequency-agile gyrotron for electron decoupling and pulsed dynamic nuclear polarization. *Journal of Magnetic Resonance* **289**, 45-54 (2018).

24   Siaw, T. A., Leavesley, A., Lund, A., Kaminker, I. & Han, S. A versatile and modular quasi optics-based 200 GHz dual dynamic nuclear polarization and

electron paramagnetic resonance instrument. *Journal of Magnetic Resonance* **264**, 131-153 (2016).

25   Thurber, K. R., Yau, W.-M. & Tycko, R. Low-temperature dynamic nuclear polarization at 9.4 T with a 30 mW microwave source. *Journal of Magnetic Resonance* **204**, 303-313 (2010).

26   Torrezan, A. C. *et al.* Continuous-wave operation of a frequency-tunable 460-GHz second-harmonic gyrotron for enhanced nuclear magnetic resonance. *IEEE Transactions on Plasma Science* **38**, 1150-1159 (2010).

27   Hovav, Y., Feintuch, A. & Vega, S. Theoretical aspects of dynamic nuclear polarization in the solid state–The solid effect. *Journal of Magnetic Resonance* **207**, 176-189 (2010).

28   Smith, A. A., Corzilius, B., Barnes, A. B., Maly, T. & Griffin, R. G. Solid effect dynamic nuclear polarization and polarization pathways. *The Journal of chemical physics* **136**, 01B602 (2012).

29   Wenckebach, W. T. The solid effect. *Applied Magnetic Resonance* **34**, 227 (2008).

30   Hovav, Y., Feintuch, A. & Vega, S. Theoretical aspects of dynamic nuclear polarization in the solid state – The cross effect. *Journal of Magnetic Resonance* **214**, 29-41 (2012). https://doi.org:https://doi.org/10.1016/j.jmr.2011.09.047

31   Hu, K.-N., Song, C., Yu, H.-h., Swager, T. M. & Griffin, R. G. High-frequency dynamic nuclear polarization using biradicals: A multifrequency EPR lineshape analysis. *The Journal of chemical physics* **128**, 052302 (2008).

32   Hwang, C. F. & Hill, D. A. Phenomenological model for the new effect in dynamic polarization. *Physical Review Letters* **19**, 1011 (1967).

33   Thurber, K. R. & Tycko, R. Theory for cross effect dynamic nuclear polarization under magic-angle spinning in solid state nuclear magnetic resonance: The importance of level crossings. *The Journal of chemical physics* **137**, 084508 (2012).

34   Hu, K.-N., Debelouchina, G. T., Smith, A. A. & Griffin, R. G. Quantum mechanical theory of dynamic nuclear polarization in solid dielectrics. *The Journal of chemical physics* **134**, 03B622 (2011).

35   Equbal, A., Li, Y., Tabassum, T. & Han, S. Crossover from a solid effect to thermal mixing 1H dynamic nuclear polarization with trityl-OX063. *The journal of physical chemistry letters* **11**, 3718-3723 (2020).

36   Hovav, Y., Feintuch, A. & Vega, S. Theoretical aspects of dynamic nuclear polarization in the solid state–spin temperature and thermal mixing. *Physical Chemistry Chemical Physics* **15**, 188-203 (2013).

37   Wenckebach, W. T. Dynamic nuclear polarization via thermal mixing: Beyond the high temperature approximation. *Journal of Magnetic Resonance* **277**, 68-78 (2017).

38   Carver, T. R. & Slichter, C. P. Polarization of Nuclear Spins in Metals. *Physical Review* **92**, 212-213 (1953). https://doi.org:DOI 10.1103/PhysRev.92.212.2

39   Carver, T. R. & Slichter, C. P. Experimental Verification of the Overhauser Nuclear Polarization Effect. *Physical Review* **102**, 975-980 (1956). https://doi.org:DOI 10.1103/PhysRev.102.975

40   Haze, O., Corzilius, B. r., Smith, A. A., Griffin, R. G. & Swager, T. M. Water-soluble narrow-line radicals for dynamic nuclear polarization. *Journal of the American Chemical Society* **134**, 14287-14290 (2012).

41   Can, T. V., Ni, Q. Z. & Griffin, R. G. Mechanisms of dynamic nuclear polarization in insulating solids. *Journal of Magnetic Resonance* (2015).

42   Lelli, M. *et al.* Solid-state dynamic nuclear polarization at 9.4 and 18.8 T from 100 K to room temperature. *Journal of the American Chemical Society* **137**, 14558-14561 (2015).

43   Chaudhari, S. R. *et al.* Dynamic nuclear polarization efficiency increased by very fast magic angle spinning. *Journal of the American Chemical Society* **139**, 10609-10612 (2017).

44   Ji, X. *et al.* Overhauser effects in non-conducting solids at 1.2 K. *Journal of Magnetic Resonance* **286**, 138-142 (2018).

45   Pylaeva, S., Ivanov, K. L., Baldus, M., Sebastiani, D. & Elgabarty, H. Molecular Mechanism of Overhauser Dynamic Nuclear Polarization in Insulating Solids. *J Phys Chem Lett* **8**, 2137-2142 (2017). https://doi.org:10.1021/acs.jpclett.7b00561

46   Pylaeva, S. *et al.* Organic Mixed-Valence Compounds and the Overhauser Effect in Insulating Solids. *J Phys Chem A* **125**, 867-874 (2021). https://doi.org:10.1021/acs.jpca.0c11296

47   Gurinov, A. *et al.* Mixed‐valence compounds as polarizing agents for Overhauser dynamic nuclear polarization in solids. *Angewandte Chemie* (2021).

48   Tan, K. O., Mardini, M., Yang, C., Ardenkjær-Larsen, J. H. & Griffin, R. G. Three-spin solid effect and the spin diffusion barrier in amorphous solids. *Science advances* **5**, eaax2743 (2019).

49   Stern, Q. *et al.* Direct observation of hyperpolarization breaking through the spin diffusion barrier. *Science Advances* **7**, eabf5735 (2021).

50   Atzrodt, J., Derdau, V., Fey, T. & Zimmermann, J. The renaissance of H/D exchange. *Angewandte Chemie International Edition* **46**, 7744-7765 (2007).

51   Boix, C. & Poliakoff, M. Efficient HD exchange of aromatic compounds in near-critical D2O catalysed by a polymer-supported sulphonic acid. *Tetrahedron letters* **40**, 4433-4436 (1999).

52   Iluc, V. M., Fedorov, A. & Grubbs, R. H. H/D Exchange processes catalyzed by an iridium-Pincer complex. *Organometallics* **31**, 39-41 (2012).

53   Larsen, J. W. & Chang, L. W. A convenient preparation of deuterated aromatic compounds. *The Journal of Organic Chemistry* **43**, 3602-3602 (1978).

54   Werstiuk, N. H. & Timmins, G. Protium–deuterium exchange of alkylated benzenes in dilute acid at elevated temperatures. *Canadian Journal of Chemistry* **67**, 1744-1747 (1989).

55   Ito, N. *et al.* Efficient and Selective Pt/C-Catalyzed H–D Exchange Reaction of Aromatic Rings. *Bulletin of the Chemical Society of Japan* **81**, 278-286 (2008).

56   Banijamali, A. R., Charalambous, A., van der Schyf, C. J. & Makriyannis, A. Specific deuteration of phenols and aromatic ethers using boron trifluoride and deuterium oxide. *Journal of Labelled Compounds and Radiopharmaceuticals* **24**, 1479-1482 (1987).

57   Okazaki, N. & Okumura, A. The Rearrangement of N-Deuterated Aromatic Amine Hydrochloride into its Ring-deuterated Analogue in the Solid Phase: The Rearrangements of o-and m-Toluidine Hydrochlorides and the Effect of Anions on the Rate of Rearrangement of Anilinium Salts. *Bulletin of the Chemical Society of Japan* **34**, 989-995 (1961).

58   Small, P. & Wolfenden, J. Exchange reactions of heavy water with organic compounds. Part I. Phenol, acetanilide, and the formate ion. *Journal of the Chemical Society (Resumed)*, 1811-1817 (1936).

59   Brunetti, F. G., Gong, X., Tong, M., Heeger, A. & Wudl, F. Strain and Hückel aromaticity: driving forces for a promising new generation of electron acceptors in organic electronics. *Angewandte Chemie International Edition* **49**, 532-536 (2010).

60   Gandeepan, P., Hung, C.-H. & Cheng, C.-H. Pd-catalyzed double C–H bond activation of diaryl ketones for the synthesis of fluorenones. *Chemical Communications* **48**, 9379-9381 (2012).

61   Plater, M. J., Kemp, S. & Lattmann, E. Heterocyclic free radicals. Part 1. 4, 5-Diazafluorene derivatives of Koelsch's free radical: an EPR and metal-ion complexation study. *Journal of the Chemical Society, Perkin Transactions 1*, 971-979 (2000).

62   Ong, T.-C. *et al.* Solvent-free dynamic nuclear polarization of amorphous and crystalline ortho-terphenyl. *The Journal of Physical Chemistry B* **117**, 3040-3046 (2013).

63   Bajaj, V. *et al.* Dynamic nuclear polarization at 9 T using a novel 250 GHz gyrotron microwave source. *Journal of Magnetic Resonance* **213**, 404-409 (2011).

64   Thurber, K. R. & Tycko, R. Measurement of sample temperatures under magic-angle spinning from the chemical shift and spin-lattice relaxation rate of 79Br in KBr powder. *Journal of magnetic resonance* **196**, 84-87 (2009).

65   Purea, A. *et al.* Improved waveguide coupling for 1.3 mm MAS DNP probes at 263 GHz. *Journal of Magnetic Resonance* **302**, 43-49 (2019). https://doi.org:https://doi.org/10.1016/j.jmr.2019.03.009

66   Nanni, E. A. *et al.* Microwave field distribution in a magic angle spinning dynamic nuclear polarization NMR probe. *Journal of Magnetic Resonance* **210**, 16-23 (2011). https://doi.org:https://doi.org/10.1016/j.jmr.2011.02.001

67   Lamb, R. C., Pacifici, J. G. & Ayers, P. W. Organic Peroxides. Iv. Kinetics and Products of Decompositions of Cyclohexaneformyl and Isobutyryl Peroxides. Bdpa as a Free-Radical Scavenger1. *Journal of the American Chemical Society* **87**, 3928-3935 (1965).

68   Can, T. V. *et al.* Overhauser effects in insulating solids. *The Journal of Chemical Physics* **141**, 064202 (2014). https://doi.org/10.1063/1.4891866

69   Brunetti, F. G., Gong, X., Tong, M., Heeger, A. J. & Wudl, F. Strain and Hückel Aromaticity: Driving Forces for a Promising New Generation of Electron Acceptors in Organic Electronics. *Angewandte Chemie International Edition* **49**, 532-536 (2010). https://doi.org:https://doi.org/10.1002/anie.200905117

70   Plater, M. J., Kemp, S. & Lattmann, E. Heterocyclic free radicals. Part 1. 4,5-Diazafluorene derivatives of Koelsch's free radical: an EPR and metal-ion complexation study. *Journal of the Chemical Society, Perkin Transactions 1*, 971-979 (2000). https://doi.org:10.1039/A909109B

71   Haze, O., Corzilius, B., Smith, A. A., Griffin, R. G. & Swager, T. M. Water-Soluble Narrow-Line Radicals for Dynamic Nuclear Polarization. *Journal of the American Chemical Society* **134**, 14287-14290 (2012). https://doi.org:10.1021/ja304918g

72   MATLAB R2020a (The MathWorks, Inc., Natick, Massachusetts, 2020).

Chapter 3 : Axial Microwave Irradiation Strategies in Rotating Solids

Adapted from Golota, N.C[*]., Schaffer, L[*]., Jawla, S., Shankar-Palani, R., Banks. D.P., Mastovsky, I., Temkin, R., Griffin, R.G. To be submitted to Journal of Magnetic Resonance.

* These authors share contributions equally in publication following experimental validation of the work in this chapter.

3.1 Introduction

While nuclear magnetic resonance is a powerful spectroscopic technique, it suffers from inherently low sensitivity requiring sample isotopic enrichment and often long acquisition times. To increase the sensitivity of NMR, the large Boltzmann polarization of electron spins can be transferred to nuclear spins using dynamic nuclear polarization (DNP) [1]. Under DNP, stable free radicals are doped into the sample as a polarizing agent, and electron-nuclear transitions are irradiated with high frequency microwaves (100-800 GHz) at cryogenic temperatures resulting in enhancement of the nuclear spin signal. Over the past 20 years, DNP has facilitated the study of low sensitivity samples ranging from amyloid fibrils, membrane proteins, viral particles, and inorganic materials [2-13]. However, DNP resolution continues to be significantly limited due to homogenous and inhomogeneous broadening at low temperatures, particularly as dynamic residues are frozen into multiple conformations [14,15]. Additionally, instrumentation advances for DNP NMR have lagged that of ambient NMR in terms of achievable MAS frequency and applied external fields. As such, DNP is most often performed with field strengths between 400-800 MHz, MAS frequencies under 15 kHz

using 3.2 mm rotors, and temperatures of 100 K. Recent commercial instrumentation has extended available field strengths to 900 MHz and 65 kHz MAS frequencies, albeit with limited availability thus far [5]

The limited resolution of DNP NMR motivates the development of DNP spectrometers at higher fields, however, continuous wave (CW) DNP mechanisms scale unfavorably with the applied magnetic field. At lower fields such as ~9 T, a record enhancement of 420 was obtained, though this is only about 64% of the theoretical maximum enhancement of 660 [10,16]. As the magnetic field strength is increased the microwave devices used for DNP can be limited in output power and frequency tuning. Despite these limitations, gyrotrons remain the dominant and best available microwave source for DNP, with CW gyrotrons operating across the sub-THz range of 140-592 GHz [3,17-21]. While CW gyrotron oscillators have become the leading THz source for MAS DNP, they require an external magnetic field either matched or at half the field of the NMR magnet for a fundamental or second harmonic gyrotron, respectively. For example, an NMR spectrometer operating at a proton Larmor frequency of 1.2 GHz with a 28.2 T magnet requires a minimum of a 14 T gyrotron magnet, greatly increasing the cost and footprint of the DNP spectrometer.

Alternatively, solid state sources have been used in the 250-263 GHz regime with power outputs up to ~ 500 mW [22-26]. However, the realization of higher frequency solid state sources has been limited and with attenuated output powers. An additional CW microwave source is the extended interaction klystrons (EIK) that have been used at 263 GHz with ~ 5W of output power [27,28]. These devices have the advantage of decreased infrastructures costs and space constraints, however, with

lower powers and decreased instrument lifespan. Toward efficient high field DNP, improvements in (1) polarizing agents, (2) decreased sample temperatures, (3) higher MAS frequencies, (4) high frequency and high-power microwave devices, (5) time domain DNP methods and (6) microwave coupling efficiency into the MAS rotor are all necessary areas of research and development [17,29-38].

Herein, we focus on the optimization of microwave coupling schemes for MAS DNP NMR at high field ($\geq$ 16.4 T) and with smaller diameter rotors. Many microwave coupling strategies have previously been presented for both cylindrical and spherical rotors [35,36,39-41]. Three metrics can be established for evaluating the relative performance and significance for use with DNP NMR. First is the achievable electron Rabi field, $\gamma_e B_{1e}$, which is directly proportional to the microwave driven magnetic field that oscillates in resonance with electron spins, B_{1e}. Overall, with a higher $\gamma_e B_{1e}$, the equivalent enhancement can be obtained at lower microwave irradiation powers, greatly alleviating instrumental demands. The second consideration is the uniformity of the electron Rabi field throughout the sample volume. Electromagnetic simulations of MAS DNP rotors reveal non-uniform propagation of the microwave beam throughout the sample volume. This can lead to non-uniform enhancement and biased detection regions of the sample under study. Additionally, diffractive effects from the RF coil can lead to non-unform Rabi field intensity. Finally, the integration of the microwave components, cryogenic transfer lines, and radiofrequency components in the probe head represents a considerable engineering challenge. The repeated thermal cycling of MAS DNP probes can place large strain and misalignment of non-thermally matched

Rotor diameter	Sample length	Sample volume	Coil inner diameter	Coil length	Coil pitch
3.2 mm	9.4 mm	36 µL	3.9 mm	7.9 mm	1.13-1.2 mm
1.3 mm	3.9 mm	2.5 µL	1.7 mm	2.5 mm	0.25 -0.3 mm
0.7 mm	2.7 mm	0.59 µL	1.1 mm	1.9 mm	0.237 mm

Table 3.1. Sample volume and Coil parameters for MAS rotors. The sample length and volume for 3.2 mm, 1.3 mm and 0.7 mm rotors are provided. Additionally, the coil inner diameter, coil length and pitch are provided for reference and taken from Tošner et. al. The free space microwave wavelengths at 250, 395, 460, 527, 593, and 790 GHz are 1.2, 0.759, 0.652, 0.569, 0.506, and 0.379 mm, respectively.

materials. For these reasons, the ease of use and reliability of the MAS DNP probe is of the utmost importance.

In most MAS DNP probes, including commercially available probes from Bruker BioSpin, the microwave beam is incident transverse to the MAS rotor, requiring transmission through the radiofrequency coil. In these schemes, the polarization of the electric field is perpendicular to the NMR coil. Diffraction and reflection across the RF coil can result in significant transmission losses. At 250 GHz a theoretical maximum transmission value of 84% was reported, while the experimentally validated system had a calculated transmission of ~60% into a 4 mm diameter rotor [35]. Concurrent with the push toward higher magnetic fields for improved resolution, MAS rotors have been continuously miniaturized to achieve faster MAS frequencies and improved spectral resolution. However, in the combined case of high field DNP NMR at commercially available frequencies up to 593 GHz and <1.3 mm diameter MAS rotors, the standard

Bruker RF transmit and receive coil pitch is roughly ~0.5 times the microwave frequency. For these small rotors and associated coils, the wire diameter is typically 100-200 um with coil lengths of < 3 mm [42]. Given these constraints, the construction of an optimized RF coil that minimizes microwave reflection and diffraction becomes nontrivial. We note that as higher frequency microwave sources up to 790 GHz, corresponding to the highest field commercially available NMR magnet, the coil pitch of a 0.7 mm rotor system becomes closer to 0.8 times the microwave frequency. This results in a moderate return in the efficiency of transverse coupling schemes at very high fields such as 28.2 T, as described later in this chapter.

To improve the transverse coupling efficiency for 1.3 mm rotors, a waveguide coupler near the RF coil was introduced and demonstrated up to a factor of 2 improvement in enhancement at low microwave powers, while this improvement dropped to ~ 15% at powers between ~5-8 W for cross effect derived enhancements [36]. In this scheme, the 263 GHz microwave irradiation was focused onto a 2 mm ID copper tube using a plano-convex lens. In conventional designs, a focusing lens is used only at the output of a larger typically 6-8 mm ID corrugated waveguide and does not as effectively focus the microwave beam onto a small sample volume. This design is still subject to coil diffraction and reflection, decreasing the effective transmission of microwaves into the sample. Furthermore, private correspondence with users of this coupling scheme outside of the published work report considerable disruption to the NMR line shape that room temperature shimming was often insufficient to reduce adamantane linewidths to < 10 Hz, as is standard practice. This directly reduces the

value of fast MAS DNP probes when the achievable linewidth is dominated by field inhomogeneity from the copper waveguide.

An alternative strategy has been to axially irradiate down the length of the MAS rotor, entirely avoiding transmission through the RF coil. This approach has been demonstrated in the 1990s at lower fields of 39 GHz and 140 GHz [3,43]. In a more recent example, a quasi-optic transmission system was devised in which the microwaves were directed axially into the MAS stator using two mirrors in the probe head [44]. Finally, in the case of very large 9.5 mm MAS rotors, axial irradiation was proposed but without experimental verification of the DNP enhancement [39,45]. In all schemes, the efficiency of microwave coupling down the axial length of the rotor decreased with distance down the sample due to dielectric losses within the sample volume. To overcome this, the 9.5 mm MAS rotor system offered integration of an in-rotor focusing system which was theorized to generate electron Rabi fields of ~2-3 MHz with 5 W of microwave power within a 2.2 µL sample volume [39]. These designs were incompatible with sample eject systems, which are essential for rapid sample exchange and reduced thermal stresses on the DNP probe. Finally, spherical rotors were also introduced and use axial irradiation without transmission through the RF coil, producing comparably predicted electron Rabi fields but with sample eject capabilities [39,46].

To date there has not been a rigorous comparison between axial and transverse coupling schemes. The previously demonstrated axial irradiation methods are not compatible with the widely used Bruker BioSpin style MAS stators, thus limiting the widespread adoption of these coupling strategies. Herein, we present a rigorous theoretical comparison using CST simulations between axial and transverse coupling

methods in 3.2 mm, 1.3 mm, and 0.7 mm rotors. For 3.2 mm rotors at 460 GHz, axial irradiation results in a theoretical improvement in electron Rabi field of 60% over the optimized transverse coupling scheme. These schemes have been fabricated and stable spinning at 100 K has been demonstrated using a modified axial bearing design that facilitates the improved Rabi fields in 3.2 mm rotors.

For 1.3 mm and 0.7 mm rotors, the design of an optimized RF coil that is both transparent to GHz irradiation and affords efficient detection of NMR signals becomes non-trivial. We compare the simulated electron Rabi fields for 1.3 mm rotors without an RF coil, with a conventional uniform pitch coil, and with optimized non-uniform pitch coils. In all cases, axial irradiation results in considerably improved electron Rabi fields and a typical factor of 2 improvement in electron Rabi field. Finally, we present efficient coupling schemes for 0.7 mm rotors for the first time at both 460 GHz and 790 GHz. Axial coupling schemes outperformed the transverse scheme by at least a factor of 2 and up to a factor of 8 times. Overall, the continued development of improved microwave coupling is essential to maintain efficient DNP at high fields and in small diameter rotors, as required for improved resolution spectra under DNP.

3.2 Experimental

3.2.1 CST Simulations

An existing 700 MHz/460 GHz DNP probe served as the starting point for computer assisted designs of both transverse and axial coupling schemes [47,48]. Initial axial scheme optimizations were performed using a MATLAB script to compute the reflectivity and transmittivity as a function of the length and dielectric constant of

each component of the axial scheme. Final optimizations were performed in CST as described below.

All microwave coupling simulations were performed using CST microwave studio 2019 (Dassault Systèmes, Vélizy-Villacoublay, France). All simulations were performed as time domain simulations with the microwave excitation source provided as a gaussian beam at a single frequency and an excitation power of 1W. In all simulations, the direction of beam propagation was in the -z direction. The beam waist was specified for each simulation according to the waveguide inner diameter from which the beam was launched. The lines per wavelength of the source signal was 8 and a truncation error of 0.001 was used. Hexahedral meshing was used with an accuracy of -30 dB. Typical minimum and maximum mesh cell sizes were 5 and 100 µm, respectively.

The dielectric constants for each material used are provided in Table 3.2. While the dielectric constants of most of the materials are not well characterized at cryogenic temperatures, particularly that of the DNP sample, values were taken from prior work [35,36]. The output of each CST simulation is the magnetic field magnitude in the sample volume given in A/m in the x, y, z cartesian coordinate system. A rotation matrix

Material	Dielectric Constant	Loss Tangent
Fused Quartz	3.85	0.0005
Fused Silica	3.82	--
PTFE (Teflon)	2.1	0.0002
Diamond	5.68	0.00005
Sample	3.5-3.7	0.013
Zirconia	33.75	0.005
Vespel ®	12.5	--

Table 3.2. Material dielectric properties. The real component of the dielectric constant is provided for each material, in addition to the loss tangent.

given in (3-1) is applied to compute the magnetic field in the laboratory frame with axes of x', y', z' where the rotor is orientated at the magic angle of 54.74°.

$$\begin{bmatrix} B'_x \\ B'_y \\ B'_z \end{bmatrix} = \begin{bmatrix} 1 & 0 & 0 \\ 0 & \sin(\theta_m) & \cos(\theta_m) \\ 0 & \cos(\theta_m) & -\sin(\theta_m) \end{bmatrix} \begin{bmatrix} B_x \\ B_y \\ B_z \end{bmatrix}$$ (3-1)

The transverse magnetic field can be computed by decomposing the linearly polarized gyrotron beam into circularly polarized components with two fields rotating in different directions. Only the circularly polarized component rotating with the nutating electron spins contributes to DNP. The average transverse B1 field in the lab frame is computed in (3-2).

$$\langle \gamma_{1e} B_{1e} \rangle = \frac{1}{2}\sqrt{(B'^2_x + B'^2_y)\alpha \, P \, \gamma_{1e}}$$ (3-2)

Where α is a constant to convert 1 A/m to 1.254 μT, P is the incident microwave power in watts, and γ_{1e} is the electron gyromagnetic ratio, 0.28025 MHz/μT.

3.2.2 Bernoulli displacement measurements

To measure the axial displacement and associated air gap generated by the Bernoulli effect in 3.2 mm and 1.3 mm systems, a Micro epsilon opto NCDT 2300 laser displacement sensor (Ortenburg, Germany) was used, as shown in

Figure 3.1. The sampling rate was 20 kHz with a specified accuracy of 0.0001 mm. X,Y,Z stages were integrated into a test stand to align the entire stator assembly to the laser displacement sensor. The stator was fixed at the magic angle using a 3D printed mounting piece. The MAS frequency was monitored using a Bruker BioSpin (Billerica, MA) infrared laser tachometer and controlled using a MAS 3 controller. The
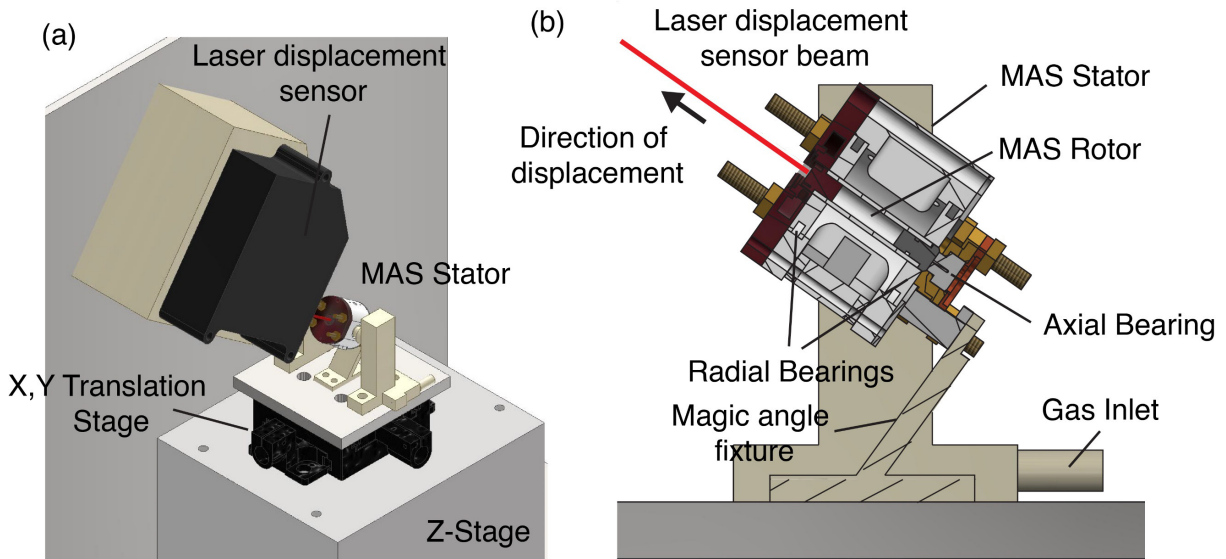
Figure 3.1. Laser Displacement Sensor Setup.(a). Laser displacement setup scheme to measure Bernoulli displacement on 3.2 mm (shown) or 1.3 mm rotor systems. Stator is fixed at the magic angle and X,Y,Z stages are used to align the laser displacement sensor to the center of the drive tip. (b) enlarged cross sectional view down the center of the stator showing the radial and axial bearings. Direction of rotor displacement is toward the laser displacement sensor and shown as a black arrow. A cartoon representation of the laser displacement sensor beam is provided

1.3 mm measurements were identically performed. All measurements were acquired in

triplicate and the entire rotor spin up and spin down process was monitored. Data was

processed using MATLAB.

3.2.3 MAS Stator Design and Spin Testing at 100 K

The MAS stators used in spin testing the modified axial bearing design are

adapted from previous work and were 3D printed from yttria stabilized zirconia [49]. The

performance of the 3D printed microfine drive plate and drive tips described in [49] were

found to be unreliable, particularly at low temperature. As such, vespel® was used for

drive tips and drive plate in this design and were machined by Challenge Machining

(Blaine, MN). The wall thickness of the 3.2 mm diameter rotor was optimized for 460

GHz transverse irradiation and fabricated by O'Keefe Ceramics (Woodland Park, CO).

124

All fused quartz inserts were fabricated from LightFab GmbH (Aachen, Germany). The axial bearing plate was assembled using Hysol EA 9361 epoxy suitable for cryogenic applications. The entire stator assembly for the axial and transverse coupling scheme is provided in Figure 3.3 and Figure 3.17. Rotors were packed with potassium bromide for all spinning stability measurements. MAS rate was controlled using a MAS 1 controller and logged using a custom Python script.

Low temperature spin testing was performed using a 700 MHz/460 GHz DNP probe described previously [47,48]. Spinning gases were precooled using Polycold chillers and were directed into a homebuilt counterflow heat exchanger adapted from [29] and shown in Figure 3.2. The counterflow coil further precools the incoming gas with the cold exhaust from the probe, reducing the evaporation rate of the liquid nitrogen bath. In the homebuilt heat exchanger, a widemouthed ~30 in diameter dewar (CryoFab, Kenilworth, NJ) was used to reduce the effective level change during operation. The heat exchanger was originally fabricated for use with a 1.3 mm DNP probe in which the MAS rate is highly sensitive to level changes in the liquid nitrogen bath of the heat exchanger, including during automatic liquid nitrogen fills. As such, while the volume change may be the same as in a narrow dewar, in the large diameter dewar the effective height change will be minimized resulting in improved MAS stability.
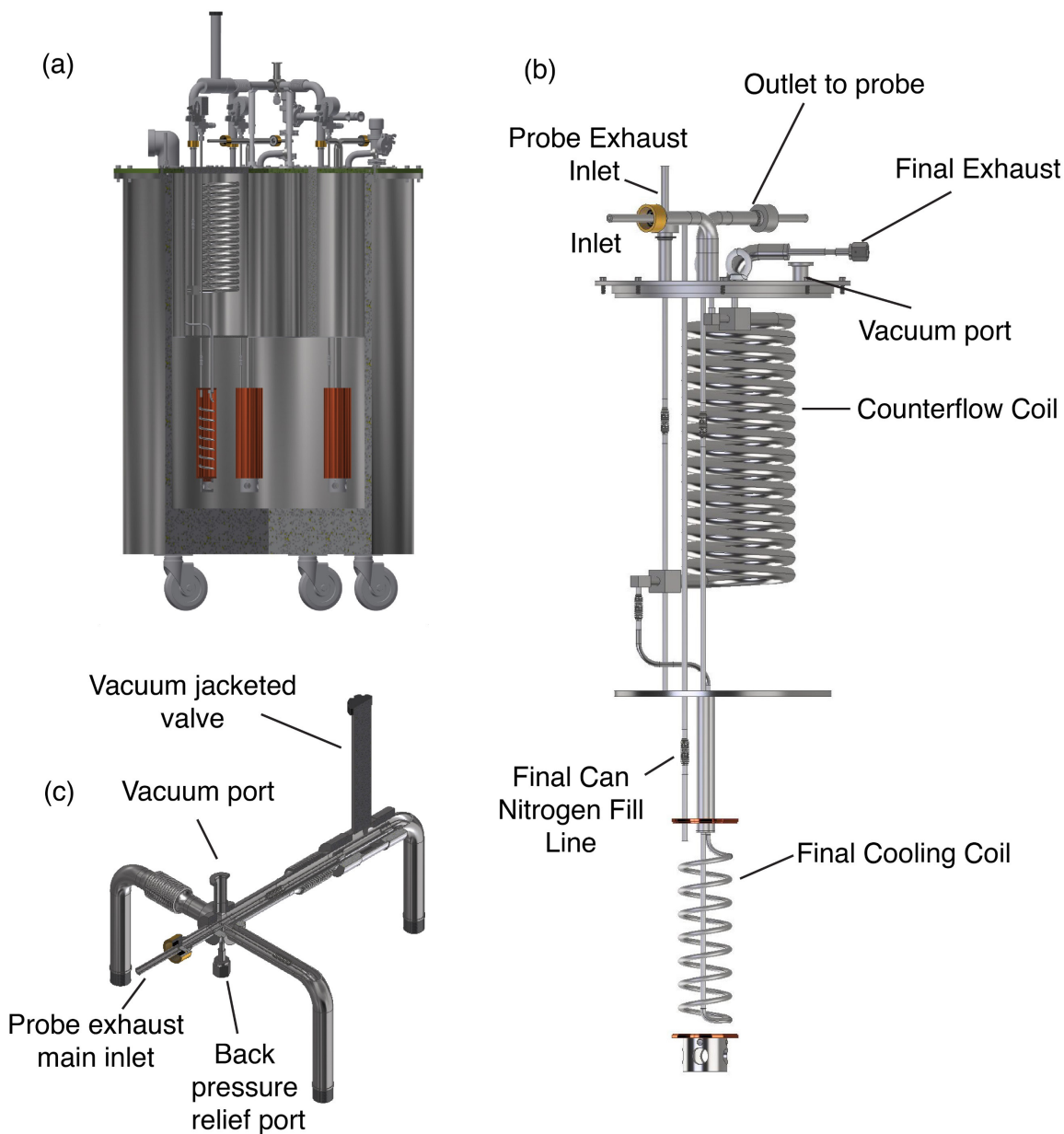
Figure 3.2. Homebuilt Counterflow Heat Exchanger. (a) overview of triple can (for bearing, drive, and variable temperature (VT) gas) counterflow heat exchanger in cryogenic dewar. The dewar is filled with liquid nitrogen which exchanges heat with the copper can and gas in the final cooling coil. The level in the dewar is controlled by an automatic fill module. (b) view of an individual heat exchanger module. The large vacuum chamber around the counterflow coil and the final copper cooling cans are not shown. Gas enters the inlet vacuum jacketed bayonet from the polycold chillers where it is further pre-cooled by the cold return gas from the probe. The gas is cooled to ~90 K in the final cooling can and output to the probe. The final exhaust line is compatible with a helium recirculation system for helium MAS. (c) A return manifold collects and re-distributes the probe exhaust gas back into the individual modules. The vacuum jacketed valve isolates the third heat exchanger from two used for bearing and drive gases when probes without VT are used.

3.3 Results and Discussion

3.3.1 3.2 mm microwave coupling

The 3.2 mm microwave coupling schemes were designed for compatibility with an 89 mm diameter NMR magnet bore and are shown in Figure 3.3. In the axial coupling scheme, Figure 3.3 (A) the waveguide was tapered to 3.2 mm and launched from a miter bend axially aligned to the rotor with the stator fixed at the magic angle. To allow transmission of microwave irradiation into the sample axially, a largely microwave transparent quartz end cap was used, the distance between the quartz end cap and end of waveguide was 4.6 mm. This is on the order of the Rayleigh length of the microwave beam output from the 3.2 mm ID waveguide at 460 GHz, as such, minimal beam divergence is expected over this short distance. The sample is then irradiated via the incident beam and a reflective mirror can be installed on the edge of the drive tip to enable a second microwave pass. The same coil and rotor were to be used in each coupling scheme. In the case of traditional transverse coupling, Figure 3.3 (B), the microwave irradiation is incident from an 8 mm ID corrugated waveguide and focused onto the sample using a plano-convex PTFE lens. The approximate focal length of the lens is 13 mm. The beam is then transmitted through a 5 turn uniform pitch coil with a length of 6.4 mm and wire diameter of 0.64 mm.
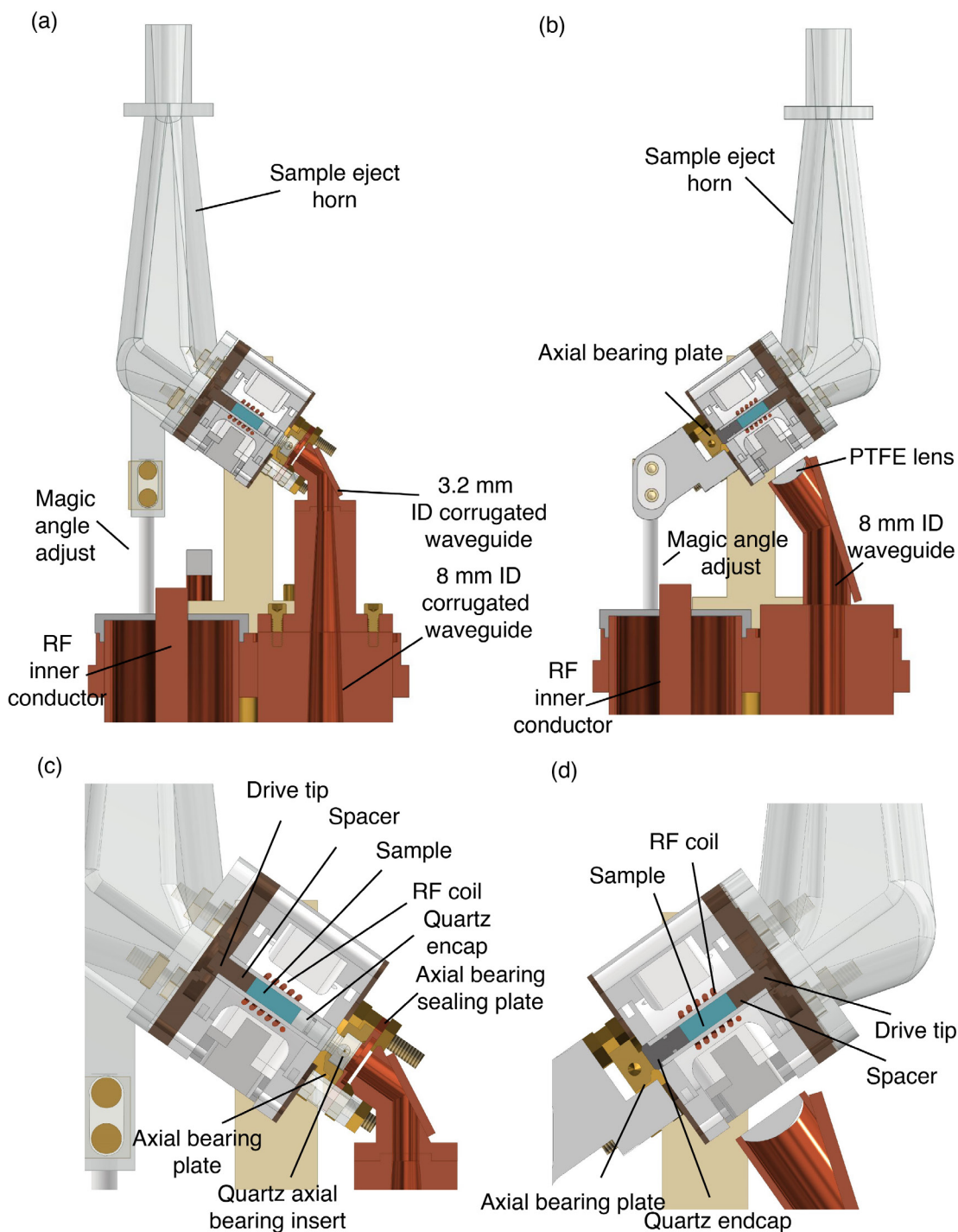
Figure 3.3. 3.2 mm microwave coupling designs. In all views, the orientation of the probe head is the same to illustrate the same probe can easily accommodate both the transverse and axial coupling schemes. (a). Overview of the axial coupling scheme. Microwaves are incident axially to the MAS rotor via a 3.2 mm ID corrugated waveguide (b). Overview of the transverse coupling scheme. Microwaves are incident transverse and perpendicular to the MAS coil at the output of an 8 mm ID waveguide. A PTFE lens focuses the microwaves onto the center of the sample. (c). Enlarged view of the stator for axial microwave coupling. (d). Enlarged view of the stator for transverse coupling.

To accurately simulate each coupling scheme, the dielectric constant, dielectric

loss tangent, and length of each component the beam propagates through must be

known. One of the unknown geometric constraints of the axial coupling scheme was the

air gap generated by the Bernoulli effect during MAS. As initial bearing gas is added at the initiation of spinning, the axial and radial bearings levitate the rotor, with the axial bearing placing a mild upward force on the rotor resulting in an axial displacement as shown in Figure 3.1 (B). As the MAS frequency is increased and higher bearing pressures are used, the speed of the fluid increases and there is a corresponding pressure drop. This results in a mild downward force onto the rotor toward the axial bearing plate, as described by Bernoulli's principle and observed using a laser displacement sensor as shown in Figure 3.4. For the modified 3.2 mm rotor using a

(a)

(b)

Figure 3.4. Bernoulli displacement of 3.2 mm rotor. (a). Displacement from static position. (b). MAS spinning profile during displacement measurement.

quartz end cap and the modified axial bearing, both shown in Figure 3.17, the net

displacement was 23 ± 7 µm and 19 ± 6 µm at 5 kHz and 8 kHz, respectively.

The design of the axial bearing required considerable optimization to achieve

stable magic angle spinning. Previous axial bearing designs used either a monolithic

PTFE axial bearing plate or a brass axial bearing plate fitted with two quartz windows. In

the prior case, thermal contraction of the PTFE plate resulted in rotor failure. In the latter

case, significant turbulence occurred between the two quartz windows that sealed the

axial bearing plate and resulted in rotor failure. Ultimately the use of a monolithic quartz

axial bearing insert reduced turbulence in the Bernoulli channel through which the axial

bearing is fed via the radial air bearings. It was critical to use a single, continuous

Bernoulli channel that is ~280-300 µm in diameter to minimize turbulence and gas leaks

in the axial bearing plate. This design is shown in Figure 3.17 (B). Use of a copper
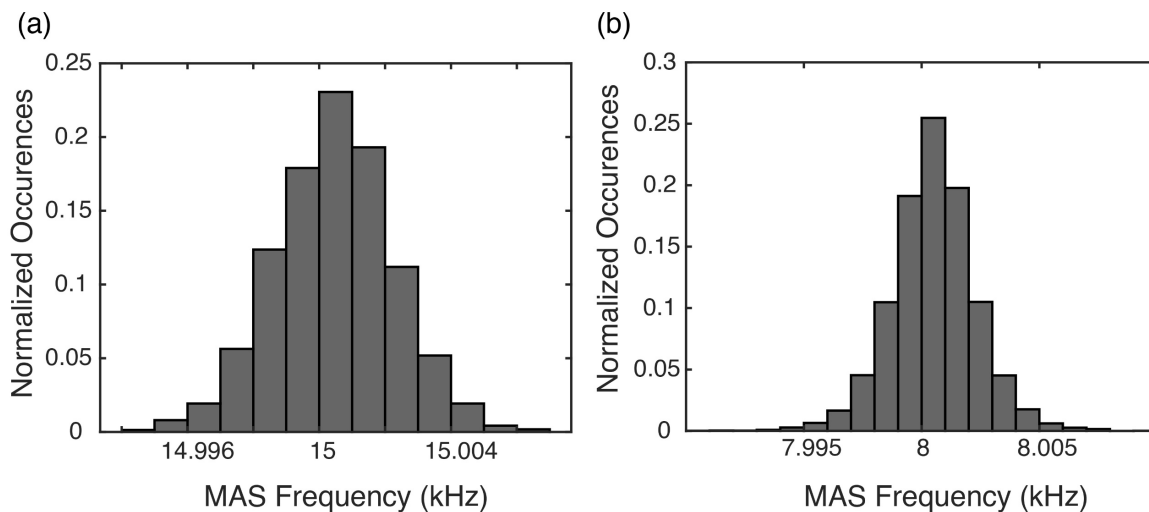
Figure 3.5. MAS stability measurements. In both cases, the quartz insert axial bearing plate was used and the rotor was fitted with the quartz endcap. (a). MAS rate of 15 ± 0.0018 kHz at 298 K. (b). MAS rate of 8 ± 0.0018 kHz at 95 K. In the case of cryogenic spinning the bearing gas was maintained at 94 K while the drive gas was 107 K.

sealing plate against the cryogenic epoxied quartz insert and brass axial bearing plate withstood several thermocycles and remained sufficiently sealed for stable spinning. We note that any leaks in the axial bearing plate typically resulted in rotor ejection and/or rotor crash. At both room temperature and at 95 K, highly stable spinning was observed with the modified axial bearing design. MAS frequencies up to 15 kHz were tested at room temperature and up to 8 kHz at 95 K, in both cases the standard deviation in the spinning frequency was 1.8 Hz as shown in Figure 3.5.

The transverse irradiation scheme resulted in considerable coil diffraction as shown in Figure 3.6(B). Areas of high intensity approaching 50 A/m are observed in the rotor walls with a diffraction pattern matching the spacings in the RF coil. This results in nonuniform electron Rabi field distributions within the sample volume. The average electron Rabi field with 10 W of irradiation power was calculated to be 0.46 MHz, with maximum in the sample and minimum values of 3.5 MHz and 0 MHz, respectively. This corresponds to an average field of 5.2 $\mu T/W^{1/2}$. We note the wall thickness of the zirconia rotor was optimized for transmission of 460 GHz irradiation and was 2.188 mm.

While the average field intensity is lower quantitatively to other publications at 250 GHz or 263 GHz, the field profile is in good agreement [35,36]. We note that the final average field intensity obtained via CST or HFSS simulations is highly dependent on choice of meshing, truncation effects, and dielectric constant used, as reported in [40]. As most dielectric constants have only been measured at low fields, the linearly extrapolated loss tangents may be more detrimental at the higher frequencies simulated herein. Additionally, the transverse coupling simulations described for 3.2 mm at 460 GHz required over 240 M mesh cells at a simulation time of nearly 2.5 days. This was
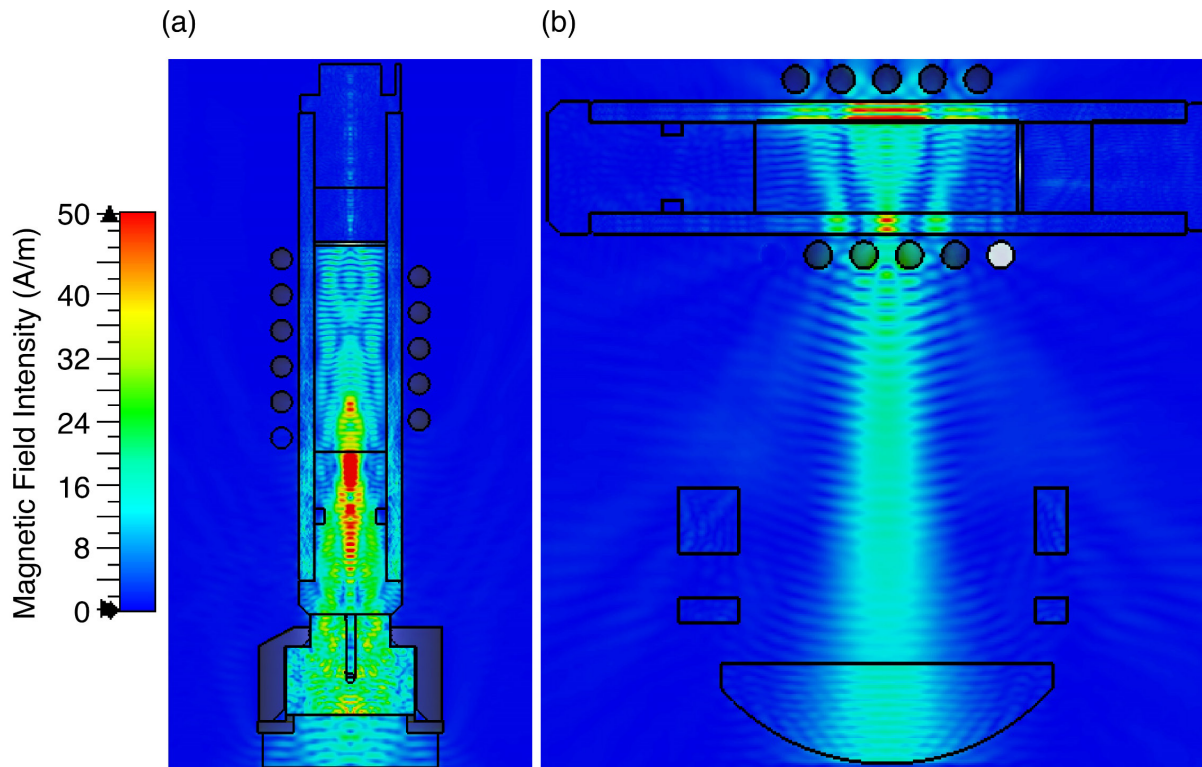
Figure 3.6. 3.2 mm microwave coupling simulations. In both simulations the magnetic field intensity at 460 GHz is shown. (a) Axial coupling simulation. (b). Transverse coupling simulation.

achieved with a minimum mesh size of 7 cells per wavelength and smallest mesh size of 5 μm. Farther from the model a larger mesh cell of 91 μm was used. We treat all simulations herein as comparative within the study, rather than strictly quantitative and focus on the uniformity of Rabi field and the relative field intensity.

In the case of the axial irradiation, as shown in Figure 3.6 (A), the microwave field intensity is more homogeneous than in the transverse coupling scheme where coil diffraction effects significantly degrade the Rabi field homogeneity and average electron Rabi field intensity. While maximum field intensities are observed in the quartz end cap, the average sample Rabi field was calculated to be 0.72 MHz with 10 W of power, as compared to 0.46 MHz in the transverse irradiation scheme. The use of a copper mirror
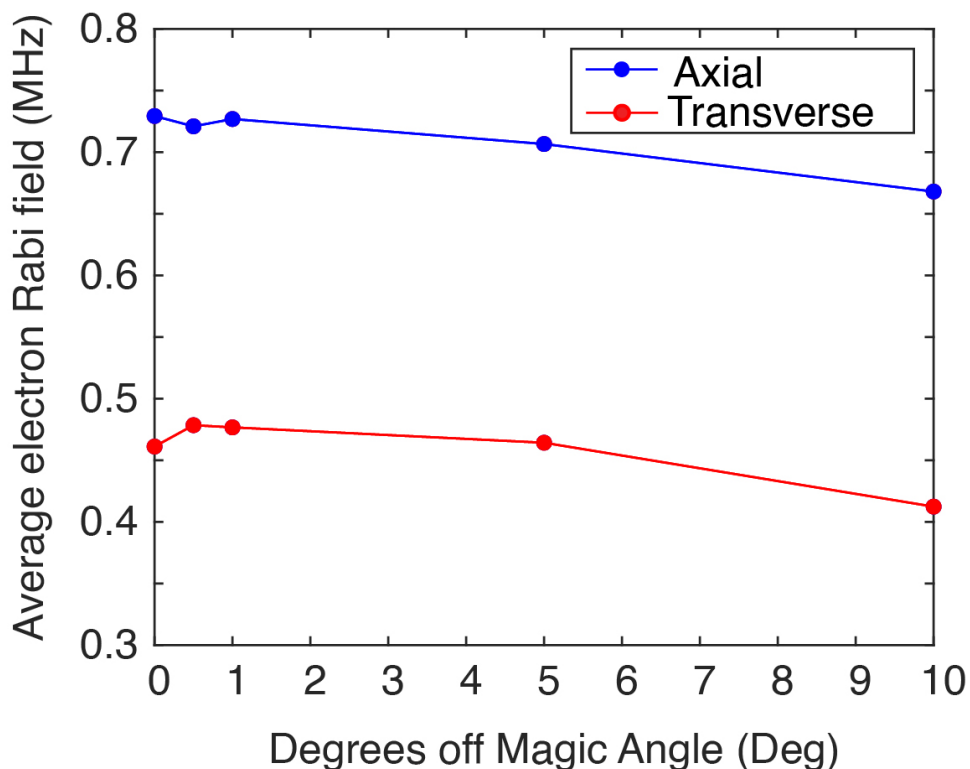
Figure 3.7. Effect of magic angle offset on electron Rabi field. Simulated electron Rabi field as a function of offset in degrees from the magic angle for 3.2 mm coupling schemes.

on the bottom of the drive tip resulted in an improvement of ~ 5%. This could be further improved by modifying the back surface of the drive tip into a parabolic mirror and could be rapidly iterated using a Form3 printer [50], but was not further explored in this study. The use of center packing the sample using a 3D printed spacer, which restricts the sample to the region enclosed only by the RF coil, improved the effective average Rabi field in both cases by ~20%. The effectiveness of the axial coupling strategy could be further improved through inclusion of a focusing lens that would maintain a tightly focused beam until the sample center point, preventing high Rabi field intensities in the quartz end cap. This approach was used for 1.3 mm and 0.7 mm axial coupling

schemes, as described below, but was not implemented for the 3.2 mm rotor system due to space constraints in the existing probe.

The effect of magic angle offset was further simulated in both the axial and transverse coupling schemes. Overall, magic angle offsets of up to 10 ° were simulated and are shown in Figure 3.7. In both axial and transverse schemes, the decrease in Rabi field for a magic angle offset of 10° was roughly 10%. As such, we conclude that both coupling schemes are robust to magic angle offset, which to our knowledge has not been previously considered in the DNP literature. Overall, the axial coupling scheme provides an improvement in the electron Rabi field of ~ 60%, or 1.5 times, over the transverse coupling scheme at 460 GHz in a 3.2 mm rotor. While experimental results remain forthcoming due to hardware restrictions at 460 GHz, they will be reported in a future publication.

3.3.2 1.3 mm microwave coupling

To further improve the resolution of DNP NMR biomolecular samples, it is important to use smaller diameter rotors that are capable of MAS frequencies exceeding 40 kHz at 100 K. This plays a critical role in reducing the homogenous linewidth in biological samples at low temperatures [7]. However, in practice at the high fields currently accessible with commercial instrumentation, and with smaller diameter MAS rotors, efficient transmission through the radio frequency coil becomes increasingly non-trivial.

Previously, to improve 1.3 mm rotor transverse microwave coupling schemes, small waveguides were inserted into the stator to more effectively couple microwaves

into the sample [36]. However, we were unable to quantitively reproduce the exceptionally high electron Rabi fields which were nearly an order of magnitude greater than reported in previous literature [35,51]. The minimum mesh cell size used in the prior work was 22 µm, which is far coarser mesh than what was used in this work. For the identical design, we obtained electron Rabi fields of 0.50 MHz and 1.2 MHz, in the presence or absence of an RF coil (pitch 0.3 mm, 0.13 mm wire diameter) at 263 GHz, respectively. This contrasts with the reported Rabi field of 5.7 MHz, and we note the value we obtained of 0.50 MHz with 10 W of power is in closer agreement with typical literature values.

To optimize the through coil coupling in an upcoming DNP probe at 460 GHz with 1.3 mm rotors, we began simulations comparing the relative effect of various RF coils and stator inserted waveguides, in addition to axial coupling schemes. In the case of 1.3 mm simulations, the real component of the sample dielectric constant was 3.7. For simulations of the RF coil transmission shown in Figure 3.10 and Figure 3.11, the gaussian beam was launched directly onto the sample at 1.1 mm from the sample center. This is the same distance that the beam would be launched from the quartz rod coupler discussed below, however, to reduce simulation mesh sizes the coil block was not included.

First, a comparison between a monolithic fused silica coil block, a quartz rod, and the conventional copper tube was performed. The loss through a solid quartz rod was approximately 4% over a 10.4 mm length, compared to nearly zero loss in the copper tube. All subsequent simulations were performed using a coupler which consisted of a
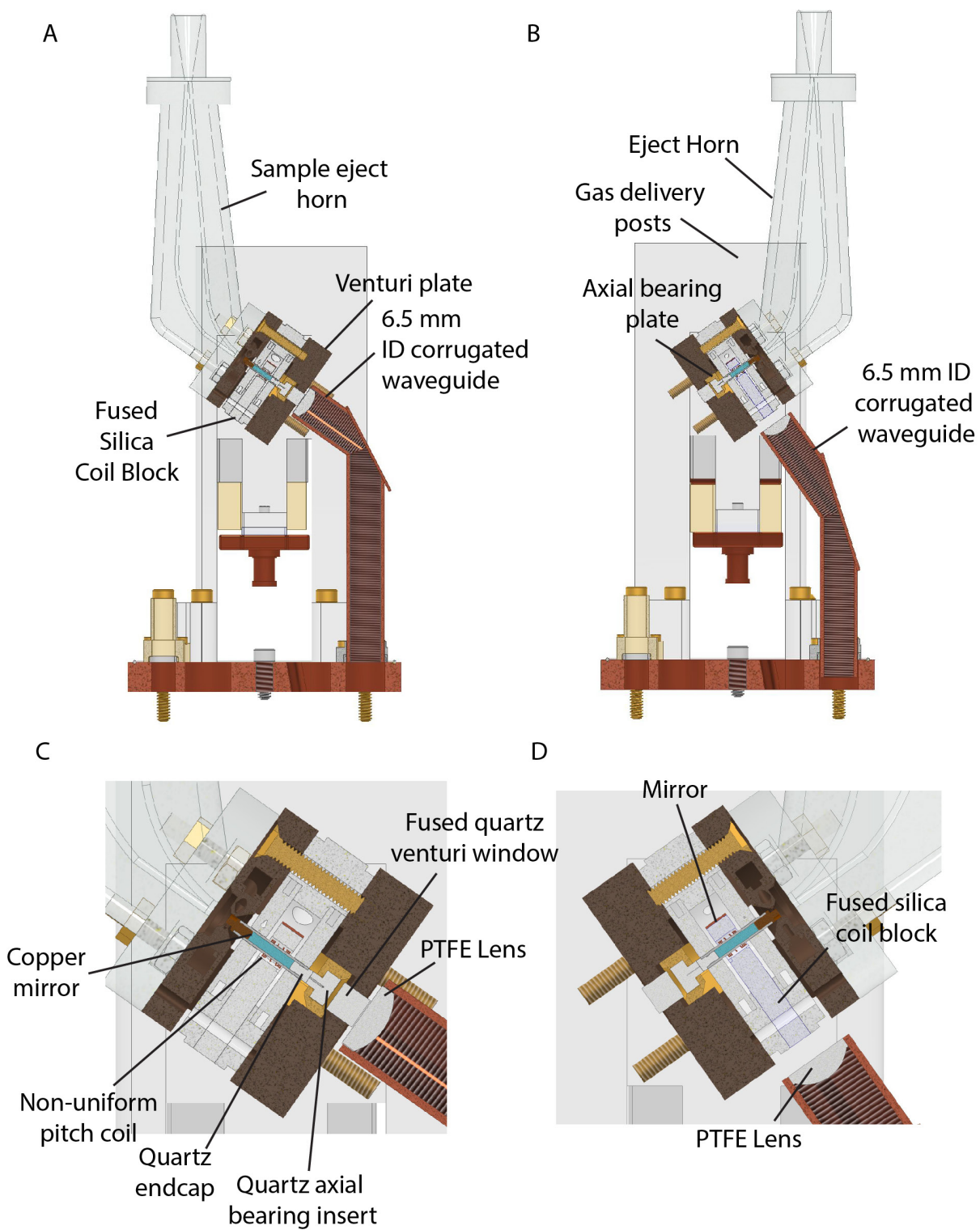
Figure 3.8 1.3 mm rotor microwave coupling (A,C) Axial coupling CAD design for 1.3 mm rotors. (B, D). Transverse coupling scheme for 1.3 mm rotors.
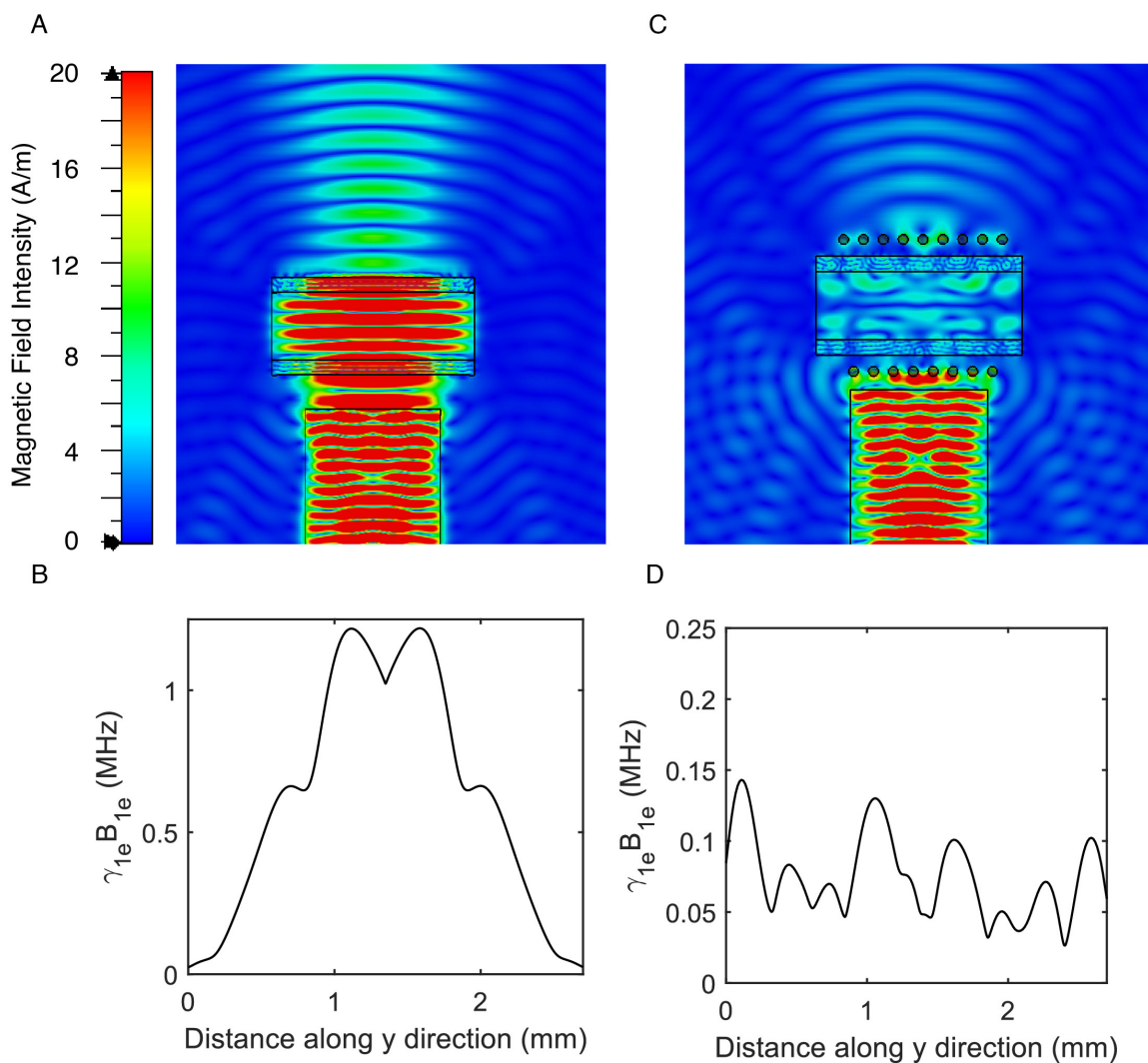
Figure 3.9. 1.3 mm MW field distribution MW field distribution in A/m for a 1.3 mm sample of length ~2.4 mm contained within a zirconia rotor. (A) in the absence of a radio frequency coil (B)Electron Rabi field plot along the center of the sample length. The average Rabi field was 1.13 MHz with 10 W of power at 460 GHz. (C) with a 0.13 mm wire diameter, 0.3 mm pitch and 8.25 turn coil, the average Rabi field was 0.23 MHz. (D) The field profile shows considerable inhomogeneity and diffraction effects from the RF coil.

transparent monolithic quartz or fused silica coil block given concerns over RF coil

arcing and magnetic field homogeneity disturbances with the presence of a copper

waveguide in close proximity to the RF coil. A fused silica plano-convex focusing lens

was used to focus the microwave beam onto the sample at the end of the 10.4 mm long monolithic quartz coil block.

The coupling efficiency through the rotor and into the sample was evaluated in the absence of radio frequency coil, as shown in Figure 3.9 (A,B). This resulted in an average electron Rabi field of 1.13 MHz with homogenous propagation of the microwave beam through the sample volume. We note, in Figure 3.9 (A,B), the sample volume is restricted that only contained by the RF coil and was 1.6 µL, compared to the total 1.3 mm rotor sample volume of 2.5 µL. When considering the entire sample volume with length of 3.9 mm, the average electron Rabi field was reduced by ~30%. Upon introduction of the standard 0.3 mm pitch, 8.25 turn, and 0.13 mm wire diameter coil, the microwave field distribution is significantly perturbed, and considerable refractive and diffractive effects are observed. The electron Rabi field in the sample was reduced by nearly 80% to 0.23 MHz. We note in a rotating solid, the microwave field homogeneity is in effect improved under sample rotation as a time average during the DNP experiment.

To improve microwave transmission through the RF coil, further optimization of coil pitch and wire diameter can be performed. Optimization of the RF coil to GHz irradiation requires a potential tradeoff in the sensitivity of NMR detection at MHz frequencies. The sensitivity of an NMR RF coil is given in (3-3), where the detection sensitivity is proportional to the induced magnetic field. The induced magnetic field from

$$RF\ Detection\ Sensitivity\ \propto\ -\frac{\partial}{\partial t}\left[\frac{\mu_0 N}{r}\frac{1}{\sqrt{1+\left(\frac{l}{2r}\right)^2}}\right] \qquad (3\text{-}3)$$

nuclear spin precession is given in terms of the magnetic permeability, μ_0, the number

of coil turns, N, the length of the coil, l, and the coil inner radius, r. In the 1.3 mm MAS

system, the coil length is constrained by the distance between the radial bearings at ~

2.4 mm. Optimization of the RF coil to transmission of high frequency microwaves is

dependent largely on the wire diameter and the ratio of the coil pitch, d, to the

microwave wavelength, λ. We observed that as the ratio of d/λ was increased the

simulated electron Rabi field concurrently increased, shown in Figure 3.10. Use of
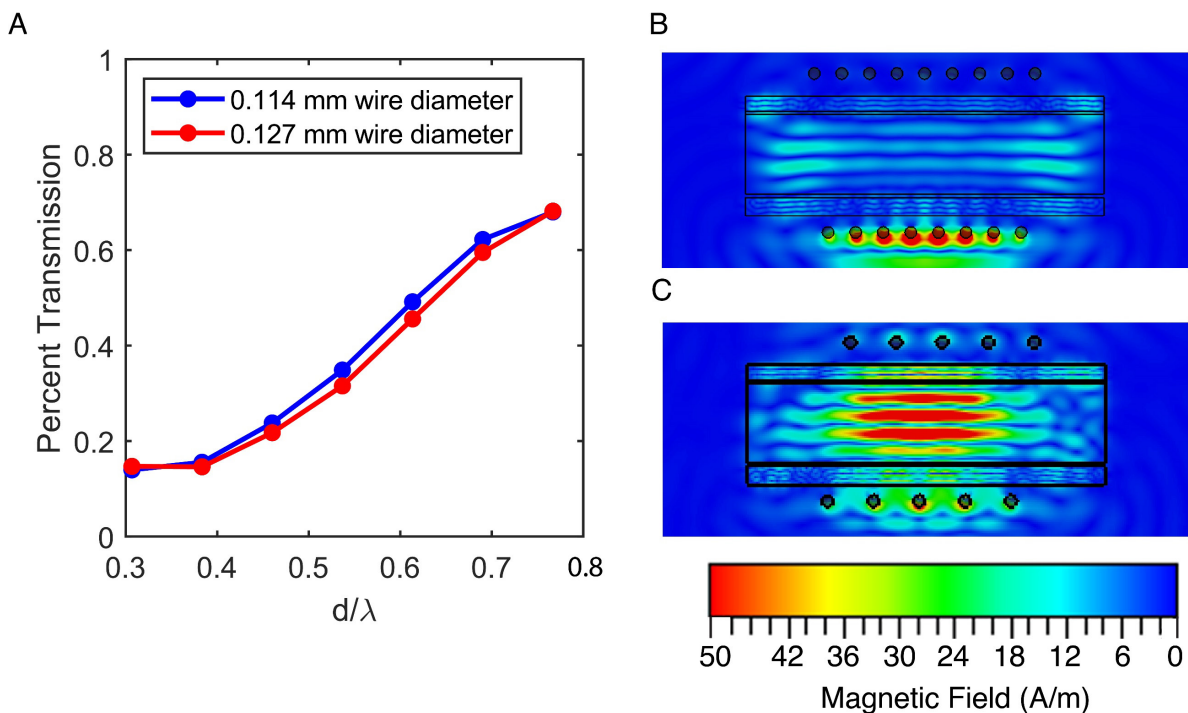
Figure 3.10. Effect of Coil Pitch on Electron Rabi Frequency. (A) The electron Rabi field at 460 GHz as a function of the ratio of the coil pitch and microwave wavelength (0.652 mm at 460 GHz) for 2 wire diameters. The percent transmission is relative to irradiation in the absence of the RF coil. (B). Microwave field distribution for a 0.3 mm pitch coil with 8.25 turns and 0.127 mm diameter wire with resulting average electron Rabi field of 0.26 MHz. (C). Microwave field distribution for a 0.5 mm pitch coil (d/λ ~ 0.8) with 4.95 turns and 0.127 mm diameter wire with resulting average electron Rabi field of 0.82 MHz.

smaller coil wire diameters also improved the coupling efficiency, though this is subject to additional fabrication challenges and reduction in total current that can be carried in the RF coil. The standard RF coil for 1.3 mm systems has a ratio of d/λ of ~ 0.46 at 460 GHz. While a uniform pitch coil with d/λ = 0.8 would result in increased microwave transmission up to ~70%, reducing the number of RF coil turns would be associated with a decrease in the detection sensitivity relative to the standard RF coil with 8.25 turns. Using up to a 0.5 mm pitch coil resulted in an electron Rabi field of 0.82 MHz, however, this would result in only 4.95 turns of the RF coil and reduced RF detection sensitivity relative to that of the original 8.25 turn coil.

To find a balance between efficient irradiation at microwave and radio frequencies, a nonuniform coil can be designed. Non-uniform coils are typically used to improve the RF homogeneity in MAS systems [52] but can be additionally used to improve the transmission of GHz radiation. CST simulations were used to evaluate non-unform pitch coils on the microwave field distribution and intensity in the 1.3 mm rotor sample volume and results are shown in Figure 3.11. A center pitch on the order of the microwave wavelength resulted in average electron Rabi fields of ~1 MHz, Figure 3.11 (B,C). When the center pitch was reduced below the microwave wavelength as in Figure 3.11 (D), the Rabi field was further reduced to 0.78 MHz. Reduced pitch sections at the ends of the coil were used to improve the RF performance and homogeneity. In these cases, the efficiency of microwave transmission is comparable to that in Figure 3.10(C), however, the number of turns was maximized at 8 turns compared to ~4 turns, improving the RF sensitivity.
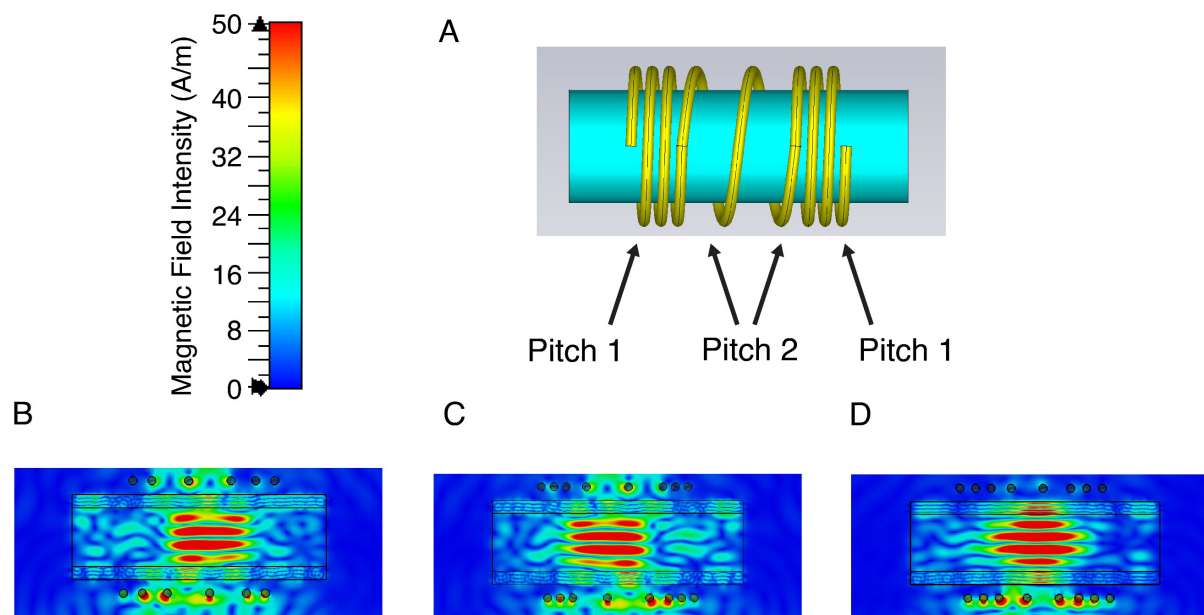
Figure 3.11. Non-uniform pitch coil simulation results (A). Design of the non-uniform pitch coil with two variable pitch sections with 2 turns of pitch 2, and a variable number of turns of pitch 1 and wire diameter of 0.127 mm (B). Average Rabi field of 1.15 MHz using a coil with 4 turns at pitch 1 of 0.292 mm and 2 turns at pitch 2 of 0.652 mm. (C). Average Rabi field of 1.11 MHz using a coil with 6 turns at pitch 1 of 0.1952 mm and 2 turns at pitch 2 of 0.652 mm. (D) Average Rabi field of 0.78 MHz using a coil with 6 turns at pitch 1 of 0.245 mm and 2 turns at pitch 2 of 0.50 mm.

The nuclear Rabi fields were comparably simulated using CST and for the uniform 0.3 mm pitch coil with 8.25 turns, values of 74 kHz, 73 kHz, 52 kHz, and 33 kHz for ^{1}H, ^{13}C, [17]O, and ^{15}N were obtained, respectively. When the number of turns was reduced, as in the uniform 0.5 mm pitch coil with 4.95 turns, the relative [1]H Rabi field was anomalously increased to 99 kHz, however, the lower frequency nuclei saw performance decreases on the order of 20%. The resulting Rabi fields were 58 kHz, 34 kHz, and 26 kHz for ^{13}C, [17]O, and ^{15}N, respectively. In the case of the nonuniform pitch in Figure 3.11 (C) the nuclear Rabi fields were 76 kHz, 80 kHz, 47 kHz, and 27 kHz for ^{1}H, ^{13}C, [17]O, and ^{15}N, respectively. The comparable nuclear Rabi field efficiency in the

optimized non-uniform pitch relative to the standard coil is accompanied by a nearly 3 times increase in the electron Rabi field at 460 GHz. As such, we have demonstrated an optimal coil design for both microwave and radiofrequency irradiation at 460 GHz.

The optimized coil was then incorporated into the overall 1.3 mm coil block and sample chamber design, as shown in Figure 3.8 and Figure 3.12. For transverse coupling, a 6.5 mm waveguide and PTFE focusing lens directed the incident microwave radiation onto either a quartz rod, monolithic fused silica or quartz coil block, or quartz rod contained in an aluminum nitride coil block. Initial optimization used the 1.8 mm diameter quartz rod which was bounded by free space and resulted in a sample electron Rabi field of 0.92 MHz. However, the free rod must be fixtured into the stator and two designs are presented in Figure 3.12 (B,C). In the case of a monolithic fused silica coil block, the electron Rabi field was 0.66 MHz, as shown in Figure 3.12 (B). There is a ~ 1 mm gap through which a fused silica or copper rod is inserted to fixture the coil block in the stator at a fixed height. While the microwave field distribution appears improved using an aluminum nitride coil block to fixture the quartz waveguide coupler, Figure 3.12 (C), the overall electron Rabi field was only minimally improved to 0.69 MHz. Given the added fabrication challenges of fixturing the quartz rod into the aluminum nitride coil block, the monolithic fused silica coil block was chosen for use. In both cases, a copper reflecting mirror can be added onto the top of the coil block to facilitate a second microwave pass, which resulted in ~ 10% increase in the electron Rabi field.
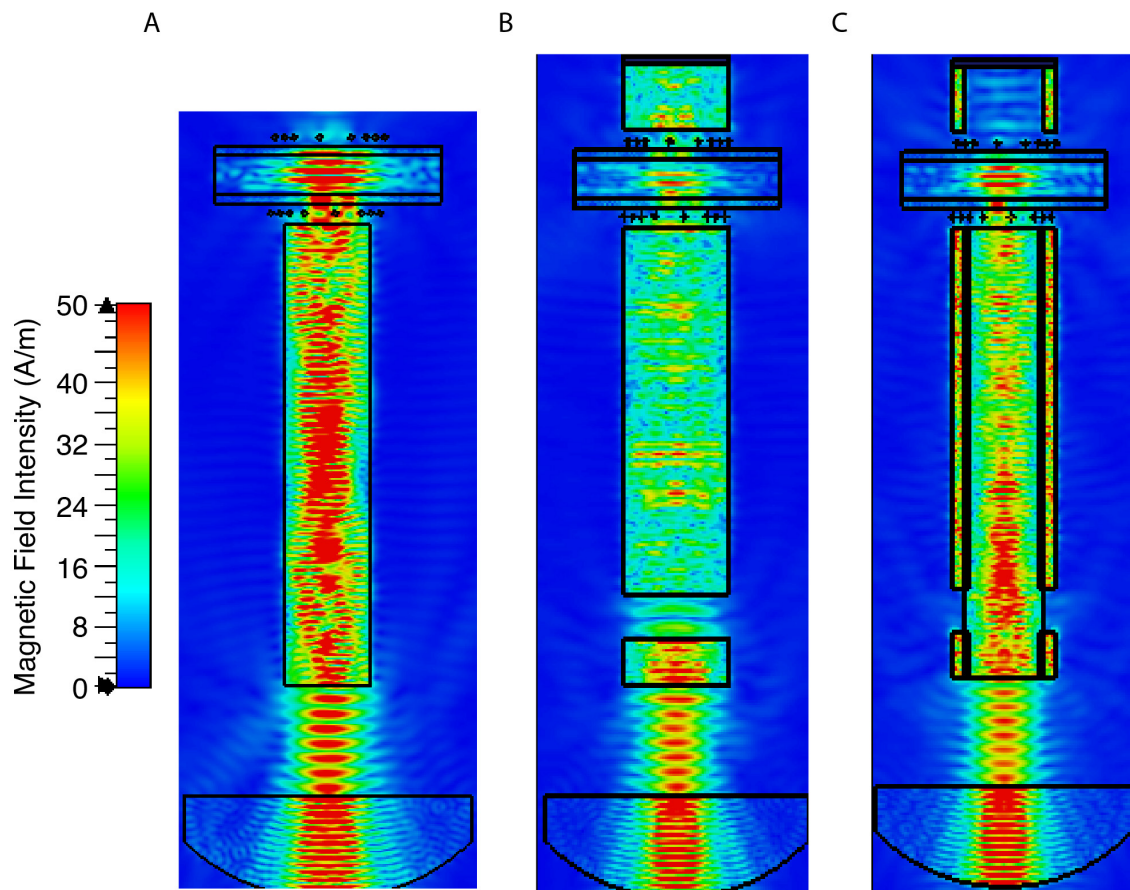
Figure 3.12. 1.3 mm rotor transverse microwave coupling (A) A 1.8 mm quartz coupler bounded by free space with sample electron Rabi field of 0.92 MHz. (B). A monolithic quartz coil block and sample electron Rabi field of 0.66 MHz. (C). An aluminum nitride coil block fixtures a 1.8 mm quartz rod coupler for an electron Rabi field of 0.69 MHz.

The axial coupling scheme was also evaluated for the case of the 1.3 mm rotor system. The small rotor diameter required a tightly focused beam that was achieved using a PTFE plano-convex lens launched from a 6.5 mm ID waveguide, as opposed to the case of the 3.2 mm where no focusing lens was used. In the case of 1.3 mm and 0.7 mm MAS DNP probes, the Bernoulli effect alone is insufficient to prevent rotor ejection during MAS. A passive venturi pump is added and operates under the same principle as the Bernoulli effect, but with increased applied downward force on the rotor. A quartz window was used to seal the venturi space and permit microwave transmission through
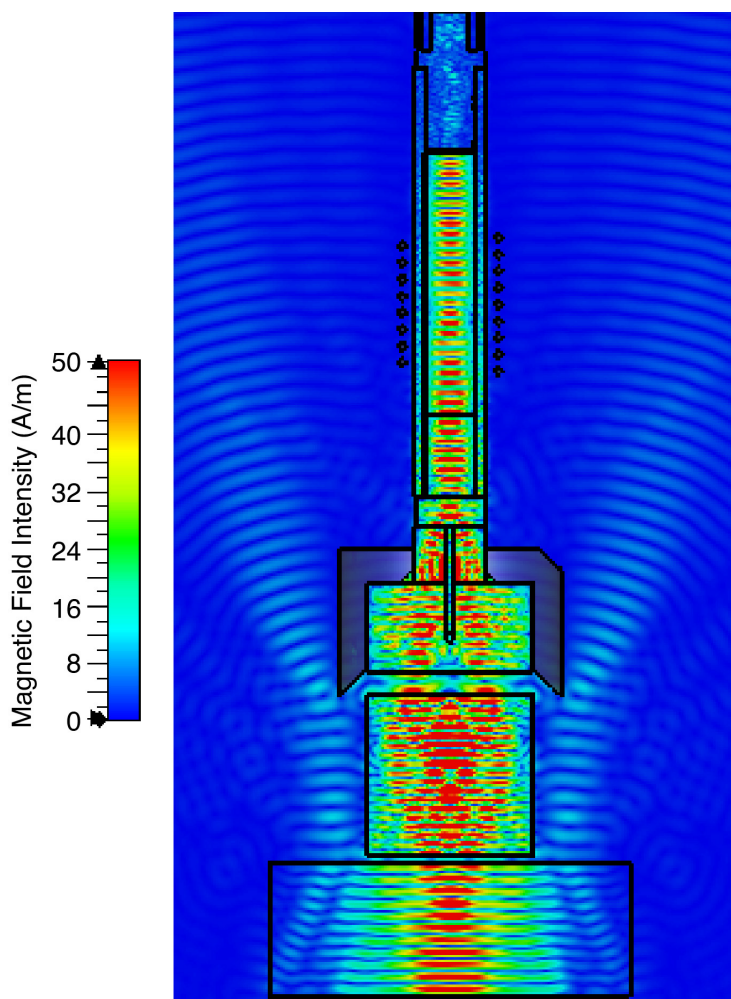
Figure 3.13. 1.3 mm axial coupling. Axial microwave coupling for a 1.3 mm rotor at 460 GHz resulted in an average electron Rabi field of 1.4 MHz with 10 W of power.

the venturi plate. A similar quartz axial bearing insert was used for the 1.3 mm rotor system as in the case of the 3.2 mm system previously discussed. To quantify the Bernoulli air gap in the 1.3 mm system, laser displacement sensor measurements were repeated, and typical displacements were on the order of 10 μm, with the exact measurement dependent on the radial bearing and venturi gas pressures. The results of these measurements are provided in the supplemental information.

The axial coupling scheme was designed for 460 GHz, with optimization of the quartz window and axial bearing insert performed in CST. The overall electron Rabi field generated in the 2.5 μL sample volume was 1.4 MHz with 10 W of microwave power, as shown in Figure 3.13. Overall, this represents an improvement of ~100% over the transverse irradiation scheme. Notably, this value is comparable to the Rabi field generated via transverse irradiation in the absence of a radiofrequency coil. This

suggests the improvement via axial coupling is dominated by the removal of coil

reflection and diffraction in the 1.3 mm MAS system. Importantly, this scheme is

considerably easier to implement across a wide frequency range as the diffractive

effects of the RF coil are frequency dependent and optimizations must be performed at

each desired operating frequency. In the case of the axial scheme, only optimization of

the length of the quartz window, axial bearing insert, and potentially the focusing lens

radius is needed and are simple to fabricate and optimize.

3.3.3 0.7 mm microwave coupling

While the use of 0.7 mm rotors for MAS DNP has to date been limited, the

availability of such systems is expected to increase given the considerable resolution

improvements afforded by 65 kHz MAS frequencies at low temperatures. The case of

transverse coupling can become unfavorable as the parameter space for coil pitch and

wire diameter is restricted by the stator geometry and desired high detection sensitivity

at RF frequencies. On the other hand, the short sample length of 2.7 mm is subject to

reduced dielectric losses relative to the larger MAS rotors which is expected to improve

the relative performance of the axial coupling in 0.7 mm rotors. Microwave coupling into

a 0.7 mm rotor was evaluated at 460 GHz and 790 GHz. 790 GHz corresponds to the

microwave frequency for a 28.2 T / 1.2 GHz NMR magnet which at present represents

the highest commercially available magnet field. While there are no currently available

microwave sources at this frequency, development is underway [53].

First, the optimal RF coil pitch was characterized at 460 GHz and 790 GHz, as

shown in Figure 3.14. For a 0.7 mm rotor, the RF coil is 1.9 mm long and 1.1 mm in

diameter, making even the fabrication of a uniform pitch coil a challenge. As such, we
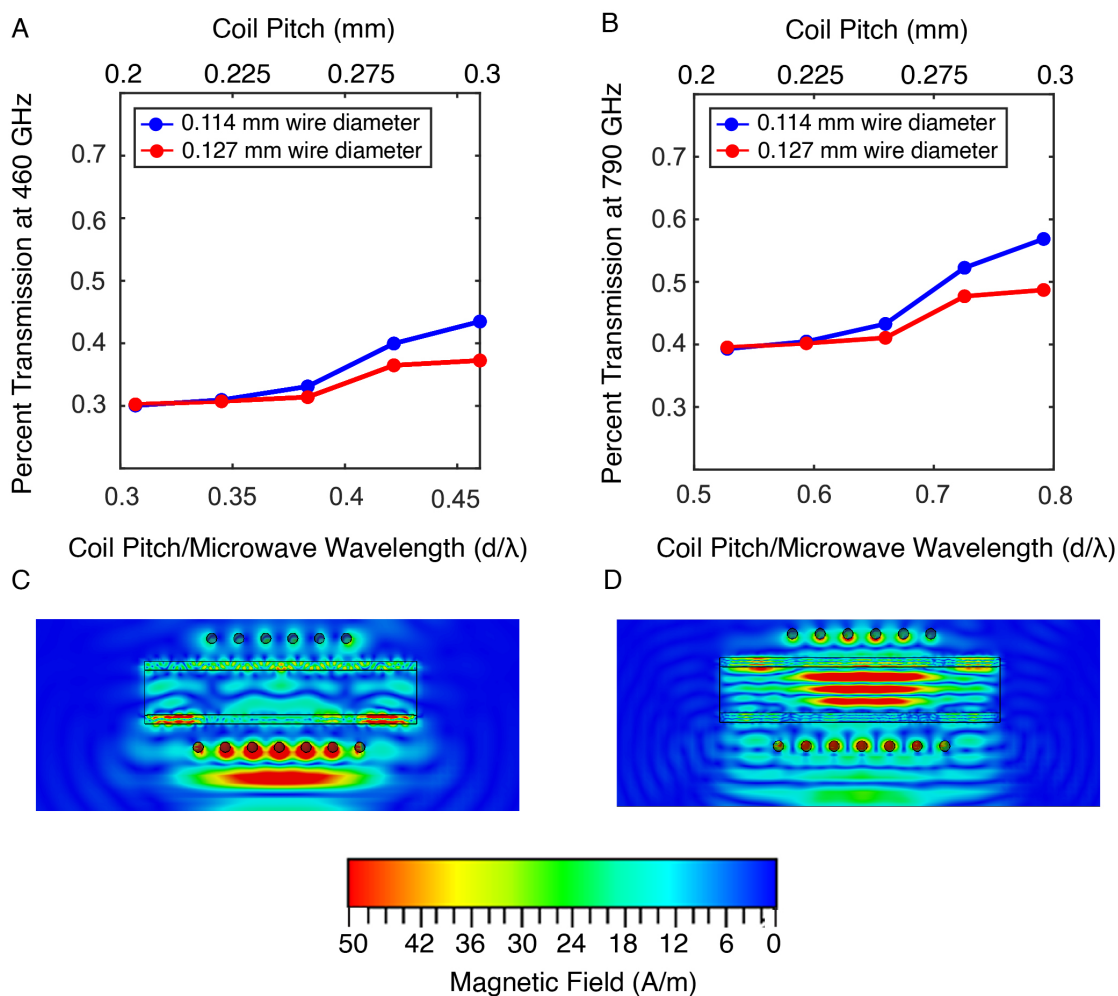
Figure 3.14. Uniform pitch coils for 0.7 mm microwave coupling. Percent transmission of microwaves as a function of varying the RF coil pitch from 0.2 mm to 0.3 mm. Percent transmission was calculated as the ratio between electron Rabi fields in the presence or absence of RF coil for (A) 460 GHz and (B) 790 GHz. The magnetic field distribution is given for a 0.114 mm wire diameter coil with a pitch of 0.3 mm at (C) 460 GHz with 43% microwave transmission and (D) 790 GHz with 57% microwave transmission.

did not consider the fabrication of non-uniform pitch coils. As previously discussed for 1.3 mm rotors at 460 GHz, the ratio of the RF coil pitch to the microwave wavelength (d/λ) is the most critical parameter in determining the effective transmission of microwave irradiation into the sample. In the case of the 0.7 mm rotors, coil pitches varied from 0.2 mm to 0.3 mm, corresponding to RF coils with between 9.5 and 6.33 turns, respectively. At 460 GHz, this corresponds to an unfavorable d/λ ratio between 0.3 and 0.46, with resulting maximum transmission through the RF coil into the sample at ~43%. In contrast, at 790 GHz the d/λ ratio is increased considerably up to 0.8 for a 0.3 mm pitch coil. This results in up to 57% microwave transmission through the RF coil. These results emphasize the frequency dependent nature of microwave coupling schemes. At present, 0.7 mm DNP probes are only available at 527 GHz and 593 GHz. Such probes may use the specified uniform coil pitch of 0.2375 mm, resulting in a d/λ of 0.41 and 0.47 at 527 or 593 GHz, respectively. Based on the results herein, we would expect the microwave transmission to then be less than 50% in these state-of-the art probes.

The entire transverse coupling scheme for 0.7 mm rotors at both 460 GHz and 790 GHz was further evaluated and is shown in Figure 3.15. A fused silica lens focuses the microwave beam onto a monolithic fused silica coil block and through the 0.3 mm pitch coil with a wire diameter of 0.114 mm. The beam is then reflected back onto the rotor via a copper mirror. At 460 GHz the average electron Rabi field with 10 W of microwave power was 0.41 MHz. At 790 GHz, the average electron Rabi field with 10 W
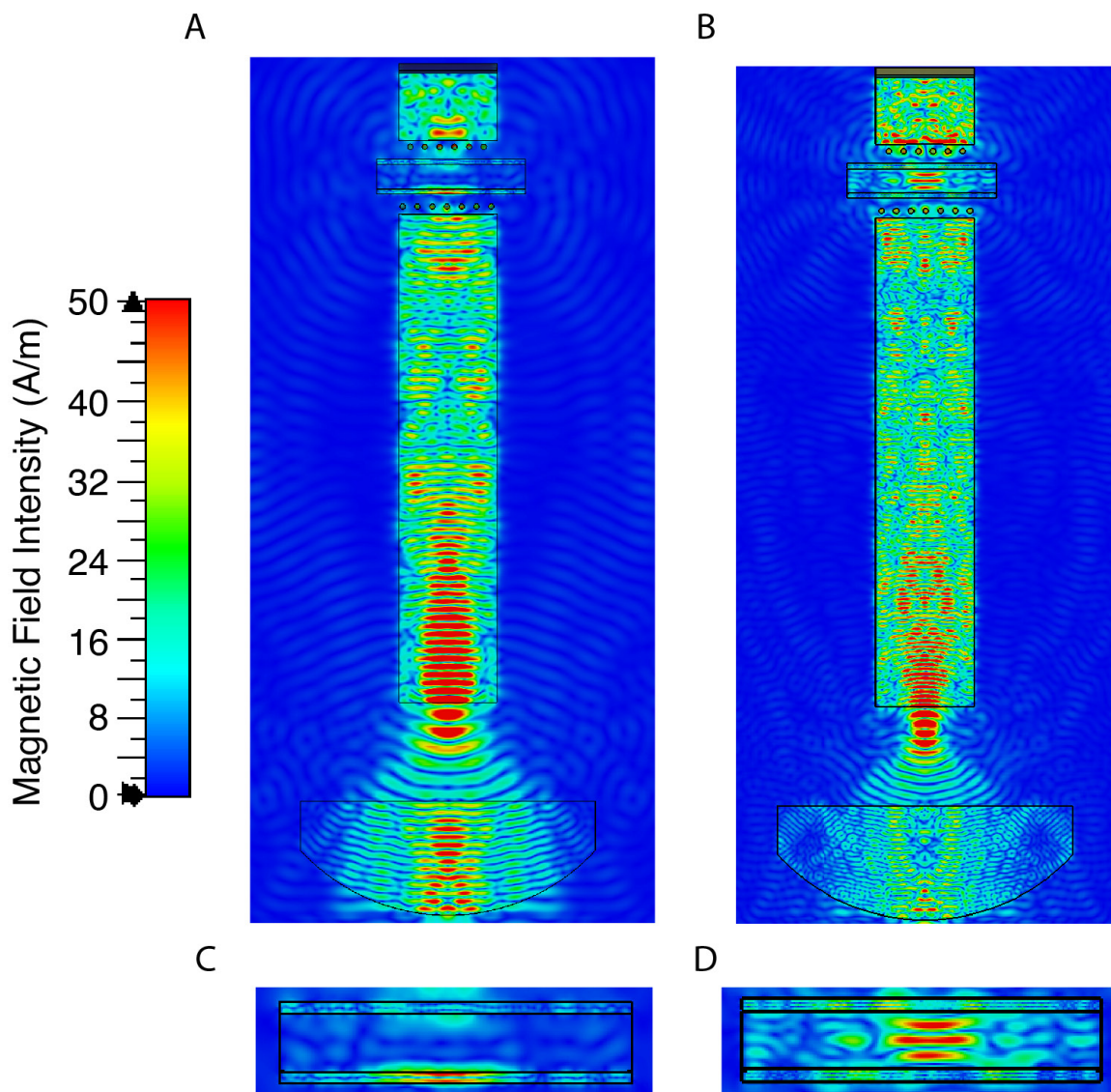
Figure 3.15. Transverse coupling in 0.7 mm rotors. The magnetic field distribution in transverse coupling schemes at (A,C) 460 GHz or (B,D) 790 GHz. (C,D) show enlarged views of the sample and rotor in (A,B). The average electron Rabi field was 0.41 MHz or 0.81 MHz at 460 or 790 GHz, respectively.

of microwave power was 0.81 MHz. At both frequencies, the coupling efficiency in the

absence of the RF coil was comparable. This confirms that reflection and diffraction due

to the RF coil dominates the achievable electron Rabi field in the transverse coupling
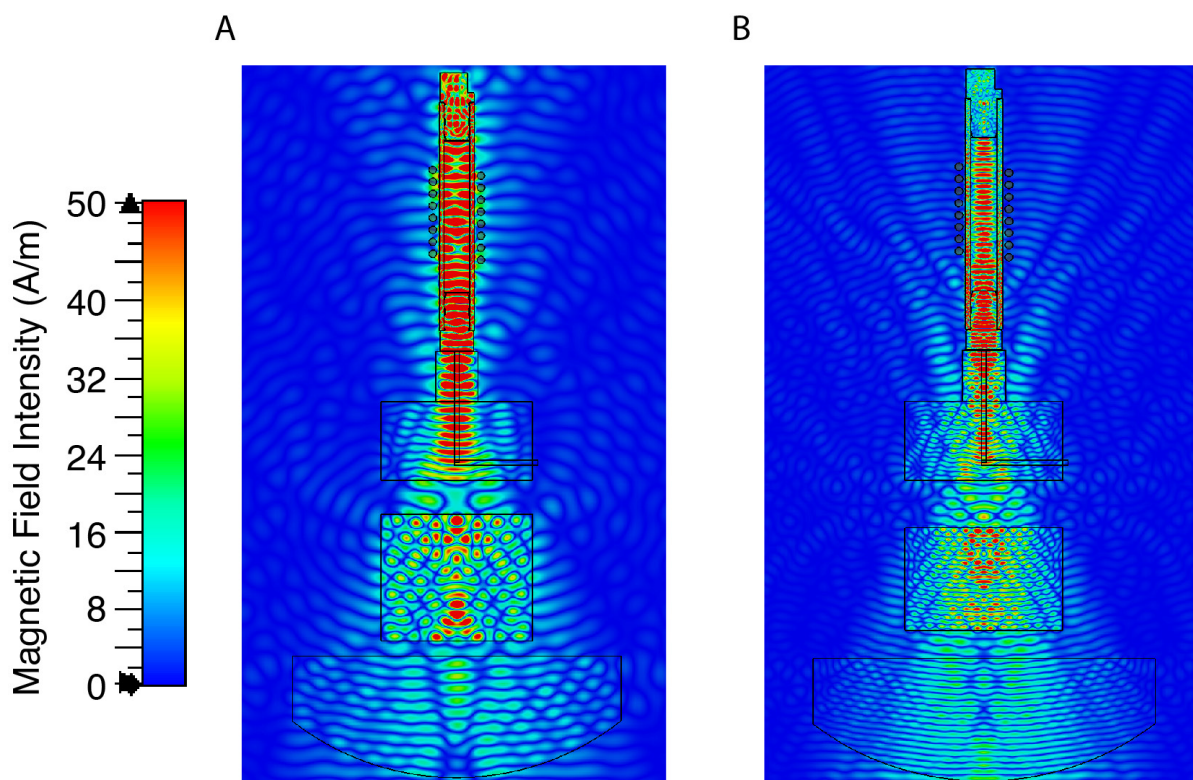
scheme.

Figure 3.16. Axial coupling in 0.7 mm rotors. (A). Axial coupling in a 0.7 mm rotor at 460 GHz with an average electron Rabi field of 3.41 MHz. (B). Axial coupling in 0.7 mm at 790 GHz with an average electron Rabi field of 1.76 MHz.

The axial coupling scheme was also investigated at 460 GHz and 790 GHz for 0.7 mm rotors and is shown in Figure 3.16. For 0.7 mm rotors, we note that simulations were performed using diamond endcaps, shown in Figure 6.15. At 460 GHz, the axial coupling strategy for 0.7 mm rotors significantly outperformed the transverse coupling scheme with an average electron Rabi field of 3.41 MHz after extensive optimization of the length and position of the quartz window, quartz axial bearing, and the depth of the axial bearing air channel. This represents an ~ 8 times improvement in the electron Rabi field over the transverse scheme at 460 GHz. At 790 GHz, the average electron Rabi field was 1.76 MHz, representing a ~2 times improvement over the transverse scheme.

The decreased relative improvement of the axial scheme at 790 GHz is due likely due to a multitude of factors. First, the focusing of the higher frequency beam and the depth of the air bearing channel can be further optimized in the 790 GHz scheme. To preserve functionality between the 460 GHz case and 790 GHz this was unmodified to enable stators to be readily swapped between frequencies. In the future, comprehensive optimization of axial coupling at 460 GHz, 527 GHz, 593 GHz, and 790 GHz could be performed to obtain an optimal axial bearing design across nearly 300 GHz of

microwave frequencies. We note additionally that the shorter wavelength is more favorable to transverse coupling schemes for 0.7 mm rotors as described previously.

At both frequencies in the 0.7 mm diameter rotor, considerable constructive magnetic field intensity was observed in the X,Y components of the magnetic field in the CST frame in contrast to the transverse case. Overall, the use of a tightly focused microwave beam incident onto the short sample length and reduced diameter results in high electron Rabi fields. The high dielectric material of the MAS rotor appears to further confine the focused microwave beam in the rotor. We note that in the case of 100 W of incident power at 460 GHz, an electron Rabi field of > 10 MHz is expected. This represents an important instrumental advance toward performing time domain DNP in rotating solids at high fields.

3.4 Conclusion

The development of efficient microwave coupling schemes at high magnetic fields (> 16 T) and fast MAS (> 40 kHz), is critical for the further application of DNP NMR to biomolecular samples. We have presented a comprehensive investigation into

transverse and axial microwave irradiation strategies for 3.2 mm, 1.3 mm, and 0.7 mm rotors at 460 GHz. For 3.2 mm rotors, an axial microwave coupling scheme compatible with commercially available DNP systems was presented. The design and optimization of this system required measurement of the Bernoulli displacement in the 3.2 mm rotor system and was found to be on the order of 20 μm. A modified axial bearing was designed using an optically transparent quartz axial bearing insert in addition to quartz rotor endcap. Despite these modifications, stable MAS between 8 and 15 kHz was demonstrated at 95 and 300 K, respectively. The axial coupling method was found to improve the effective electron Rabi field by ~60% over transverse irradiation for 3.2 mm rotors. In the case of smaller diameter MAS rotors, the improvement of axial coupling schemes over transverse irradiation was more significant. Despite considerable optimization of transverse irradiation and use of non-uniform pitch coil for a 1.3 mm rotor at 460 GHz, an electron Rabi field of 0.66 MHz was obtained with 10 W of microwave power. Use of an axial coupling scheme improved the effective electron Rabi field by ~100% with a simulated field of 1.4 MHz. Finally, in a 0.7 mm rotor system, electron fields of 3.41 MHz were obtained with 10 W of power, and up to 10 MHz of electron Rabi fields are expected with 100 W of power. At higher frequencies of 790 GHz, beyond what is currently accessible commercially, a maximum electron Rabi field of 1.76 MHz was achieved with 10 W of power in a 0.7 mm rotor under axial irradiation. These findings represent a considerable improvement in microwave coupling at high field and in small diameter MAS rotors. Overall, the presented axial coupling methods may prove highly valuable for the development of time domain DNP methods with high

power gyro amplifiers and gyrotrons, in addition to improving the achievable DNP

enhancements with more accessible low power solid state sources.

3.5 Supporting information

Figure 3.17. 3.2 mm stator CAD view. (a). Expanded view of 3.2 mm stator and rotor used in microwave coupling schemes. (b). Modified axial bearing plate top view. (c). Cross sectional view of modified axial bearing plate.
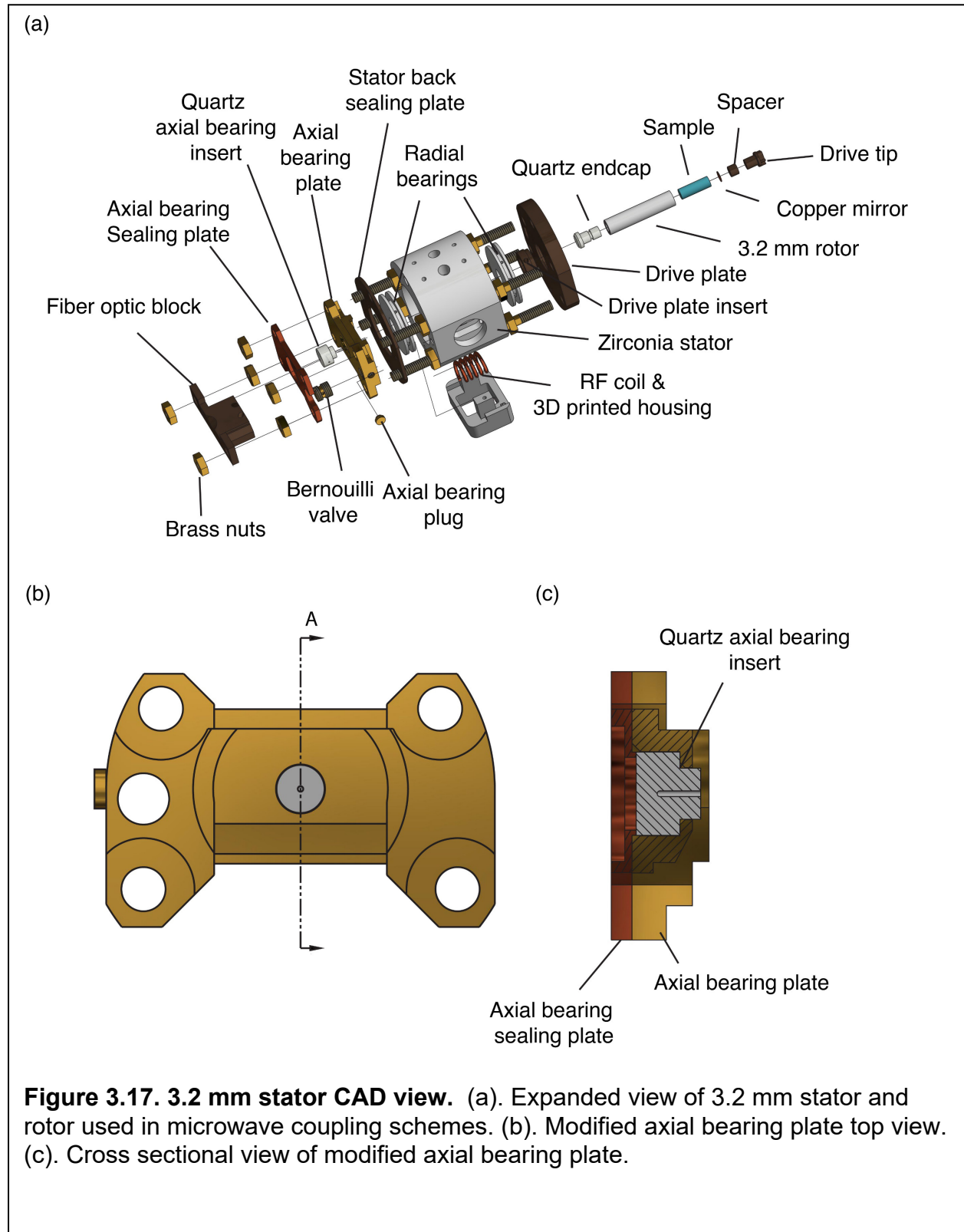
Trial	Displacement (µm)	Peak to Peak Deviation (µm)
1	25	7.3
2	18	5.5
3	27	7.2
Average	23	7

Table 3.3. Bernoulli displacement for 3.2 mm rotor at 5 kHz. Rotor was fitted with a quartz end cap, polymer drive tip and the quartz insert was used in the axial bearing plate.

Trial	Displacement (µm)	Peak to Peak Deviation (µm)
1	23	5.9
2	17	6.9
3	25	5.2
4	20	6.3
Average	19	6

Table 3.4. Bernoulli displacement for 3.2 mm rotor at 8 kHz. Rotor was fitted with a quartz end cap, polymer drive tip and the quartz insert was used in the axial bearing plate.
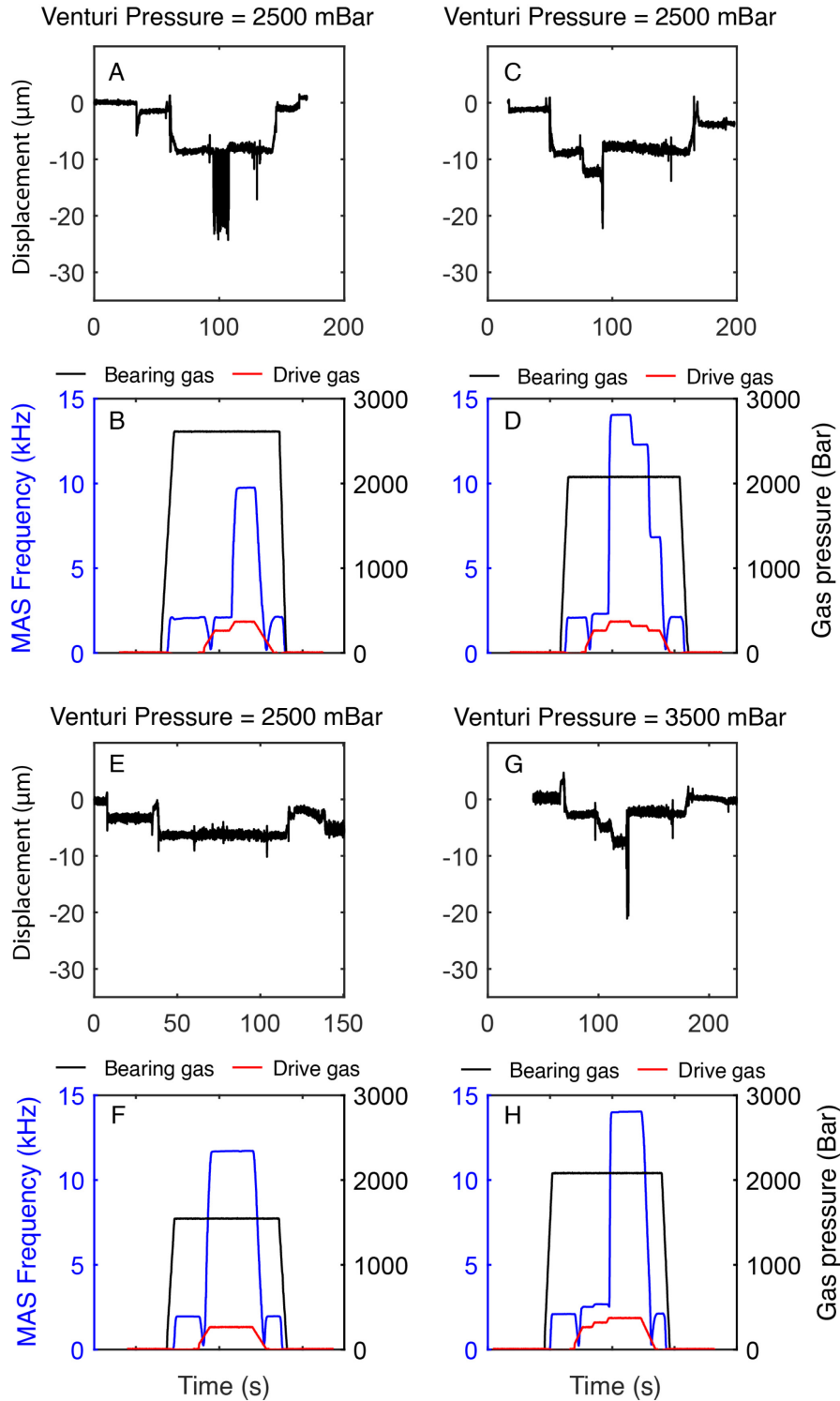
Figure 3.18. Laser displacement measurements for 1.3 mm rotors. Rotor displacement using laser displacement sensor for 1.3 mm rotors at various bearing pressures and venturi pressures.

3.6 Acknowledgements

3.7 References

1   Abragam, A. & Goldman, M. Principles of Dynamic Nuclear Polarization. *Reports on Progress in Physics* **41**, 395-467 (1978). https://doi.org:10.1088/0034-4885/41/3/002

2   Bahri, S. *et al.* 1H detection and dynamic nuclear polarization–enhanced NMR of Aβ1-42 fibrils. *Proceedings of the National Academy of Sciences* **119**, e2114413119 (2022). https://doi.org:10.1073/pnas.2114413119

3   Becerra, L. R. *et al.* A Spectrometer for Dynamic Nuclear Polarization and Electron Paramagnetic Resonance at High Frequencies. *Journal of Magnetic Resonance, Series A* **117**, 28-40 (1995). https://doi.org:https://doi.org/10.1006/jmra.1995.9975

4   Becerra, L. R., Gerfen, G. J., Temkin, R. J., Singel, D. J. & Griffin, R. G. Dynamic nuclear polarization with a cyclotron resonance maser at 5 T. *Physical Review Letters* **71**, 3561-3564 (1993). https://doi.org:10.1103/PhysRevLett.71.3561

5   Berruyer, P. *et al.* Dynamic Nuclear Polarization Enhancement of 200 at 21.15 T Enabled by 65 kHz Magic Angle Spinning. *The Journal of Physical Chemistry Letters* **11**, 8386-8391 (2020). https://doi.org:10.1021/acs.jpclett.0c02493

6   Berruyer, P., Emsley, L. & Lesage, A. in *eMagRes*   93-104 (2018).

7   Jaudzems, K. *et al.* Dynamic Nuclear Polarization-Enhanced Biomolecular NMR Spectroscopy at High Magnetic Field with Fast Magic-Angle Spinning. *Angewandte Chemie International Edition* **57**, 7458-7462 (2018). https://doi.org:https://doi.org/10.1002/anie.201801016

8   Judge, P. T. *et al.* Dynamic Nuclear Polarization with Electron Decoupling in Intact Human Cells and Cell Lysates. *The Journal of Physical Chemistry B* **124**, 2323-2330 (2020).

9   Lelli, M. *et al.* Solid-state dynamic nuclear polarization at 9.4 and 18.8 T from 100 K to room temperature. *Journal of the American Chemical Society* **137**, 14558-14561 (2015).

10   Ni, Q. Z. *et al.* High frequency dynamic nuclear polarization. *Accounts of chemical research* **46**, 1933-1941 (2013).

11   Ni, Q. Z. *et al.* Peptide and protein dynamics and low-temperature/DNP magic angle spinning NMR. *The Journal of Physical Chemistry B* **121**, 4997-5006 (2017).

12   Rossini, A. J. *et al.* Dynamic nuclear polarization enhanced solid‐state NMR spectroscopy of functionalized metal–organic frameworks. *Angewandte Chemie International Edition* **51**, 123-127 (2012).

13   Smith, A. N., Caporini, M. A., Fanucci, G. E. & Long, J. R. A method for dynamic nuclear polarization enhancement of membrane proteins. *Angewandte Chemie* **127**, 1562-1566 (2015).

14   Linden, A. H. *et al.* Cryogenic temperature effects and resolution upon slow cooling of protein preparations in solid state NMR. *Journal of Biomolecular NMR* **51**, 283-292 (2011). https://doi.org:10.1007/s10858-011-9535-z

15   Siemer, A. B., Huang, K.-Y. & McDermott, A. E. Protein Linewidth and Solvent Dynamics in Frozen Solution NMR. *PLOS ONE* **7**, e47242 (2012). https://doi.org:10.1371/journal.pone.0047242

16   Can, T. V., Ni, Q. Z. & Griffin, R. G. Mechanisms of dynamic nuclear polarization in insulating solids. *Journal of Magnetic Resonance* (2015).

17   Blank, M., Borchard, P., Cauffman, S. R. & Felch, K. L. Demonstration of a 593 GHz Gyrotron for DNP. *2018 43rd International Conference on Infrared, Millimeter, and Terahertz Waves (IRMMW-THz)*, 1-2 (2018).

18   Hornstein, M. K. *et al.* Second harmonic operation at 460 GHz and broadband continuous frequency tuning of a gyrotron oscillator. *IEEE Transactions on Electron Devices* **52**, 798-807 (2005).

19   Jawla, S. K., Griffin, R. G., Mastovsky, I. A., Shapiro, M. A. & Temkin, R. J. Second harmonic 527-GHz gyrotron for DNP-NMR: Design and experimental results. *IEEE transactions on electron devices* **67**, 328-334 (2019).

20   Scott, F. J. *et al.* Frequency-agile gyrotron for electron decoupling and pulsed dynamic nuclear polarization. *Journal of Magnetic Resonance* **289**, 45-54 (2018).

21   Torrezan, A. C. *et al.* Continuous-wave operation of a frequency-tunable 460-GHz second-harmonic gyrotron for enhanced nuclear magnetic resonance. *IEEE Transactions on Plasma Science* **38**, 1150-1159 (2010).

22   Delage-Laurin, L. *et al.* Overhauser Dynamic Nuclear Polarization with Selectively Deuterated BDPA Radicals. *Journal of the American Chemical Society* **143**, 20281-20290 (2021). https://doi.org:10.1021/jacs.1c09406

23   Palani, R. S. *et al.* Amplified Overhauser DNP with Selective Deuteration: Attenuation of Double-Quantum Cross-Relaxation. *The Journal of Physical Chemistry Letters* **14**, 95-100 (2023). https://doi.org:10.1021/acs.jpclett.2c03087

24   Shankar Palani, R., Mardini, M., Quan, Y. & Griffin, R. G. Dynamic nuclear polarization with trityl radicals. *Journal of Magnetic Resonance* **349**, 107411 (2023). https://doi.org:https://doi.org/10.1016/j.jmr.2023.107411

25   Siaw, T. A., Leavesley, A., Lund, A., Kaminker, I. & Han, S. A versatile and modular quasi optics-based 200 GHz dual dynamic nuclear polarization and

electron paramagnetic resonance instrument. *Journal of Magnetic Resonance* **264**, 131-153 (2016).

26   Thurber, K. R., Yau, W.-M. & Tycko, R. Low-temperature dynamic nuclear polarization at 9.4 T with a 30 mW microwave source. *Journal of Magnetic Resonance* **204**, 303-313 (2010).

27   Roitman, A. *et al.* in *2017 Eighteenth International Vacuum Electronics Conference (IVEC).* 1-2.

28   Rosay, M. *et al.* in *2018 43rd International Conference on Infrared, Millimeter, and Terahertz Waves (IRMMW-THz).* 1-2.

29   Albert, B. J. *et al.* Instrumentation for cryogenic magic angle spinning dynamic nuclear polarization using 90L of liquid nitrogen per day. *Journal of Magnetic Resonance* **283**, 71-78 (2017). https://doi.org:https://doi.org/10.1016/j.jmr.2017.08.014

30   Berruyer, P. *et al.* Dynamic nuclear polarization enhancement of 200 at 21.15 T enabled by 65 kHz magic angle spinning. *The Journal of Physical Chemistry Letters* **11**, 8386-8391 (2020).

31   Can, T. V. *et al.* Frequency-Swept Integrated and Stretched Solid Effect Dynamic Nuclear Polarization. *The Journal of Physical Chemistry Letters* **9**, 3187-3192 (2018). https://doi.org:10.1021/acs.jpclett.8b01002

32   Can, T. V., Tan, K. O., Yang, C., Weber, R. T. & Griffin, R. G. Time domain DNP at 1.2 T. *Journal of Magnetic Resonance* **329**, 107012 (2021). https://doi.org:https://doi.org/10.1016/j.jmr.2021.107012

33   Judge, P. T. *et al.* Sensitivity analysis of magic angle spinning dynamic nuclear polarization below 6 K. *Journal of Magnetic Resonance* **305**, 51-57 (2019). https://doi.org:https://doi.org/10.1016/j.jmr.2019.05.011

34   Mathies, G. *et al.* Efficient Dynamic Nuclear Polarization at 800 MHz/527 GHz with Trityl-Nitroxide Biradicals. *Angewandte Chemie International Edition* **54**, 11770-11774 (2015). https://doi.org:https://doi.org/10.1002/anie.201504292

35   Nanni, E. A. *et al.* Microwave field distribution in a magic angle spinning dynamic nuclear polarization NMR probe. *Journal of Magnetic Resonance* **210**, 16-23 (2011). https://doi.org:https://doi.org/10.1016/j.jmr.2011.02.001

36   Purea, A. *et al.* Improved waveguide coupling for 1.3 mm MAS DNP probes at 263 GHz. *Journal of Magnetic Resonance* **302**, 43-49 (2019). https://doi.org:https://doi.org/10.1016/j.jmr.2019.03.009

37   Rosay, M. *et al.* Solid-state dynamic nuclear polarization at 263 GHz: spectrometer design and experimental results. *Physical Chemistry Chemical Physics* **12**, 5850-5860 (2010). https://doi.org:10.1039/C003685B

38   Thurber, K. & Tycko, R. Low-temperature dynamic nuclear polarization with helium-cooled samples and nitrogen-driven magic-angle spinning. *Journal of Magnetic Resonance* **264**, 99-106 (2016).

39   Chen, P.-H., Gao, C. & Barnes, A. B. Perspectives on microwave coupling into cylindrical and spherical rotors with dielectric lenses for magic angle spinning dynamic nuclear polarization. *Journal of Magnetic Resonance* **308**, 106518 (2019). https://doi.org:https://doi.org/10.1016/j.jmr.2019.07.005

40   Maly, T. & Sirigiri, J. R. Simplified THz Instrumentation for High-Field DNP-NMR Spectroscopy. (2012).

41   Scott, F. J. *et al.* Magic angle spinning NMR with metallized rotors as cylindrical microwave resonators. *Magnetic Resonance in Chemistry* **56**, 831-835 (2018). https://doi.org:https://doi.org/10.1002/mrc.4744

42   Tošner, Z. *et al.* Radiofrequency fields in MAS solid state NMR probes. *Journal of Magnetic Resonance* **284**, 20-32 (2017). https://doi.org:https://doi.org/10.1016/j.jmr.2017.09.002

43   Afeworki, M., McKay, R. A. & Schaefer, J. Selective observation of the interface of heterogeneous polycarbonate/polystyrene blends by dynamic nuclear polarization carbon-13 NMR spectroscopy. *Macromolecules* **25**, 4084-4091 (1992). https://doi.org:10.1021/ma00042a006

44   Pike, K. J. *et al.* A spectrometer designed for 6.7 and 14.1T DNP-enhanced solid-state MAS NMR using quasi-optical microwave transmission. *Journal of Magnetic Resonance* **215**, 1-9 (2012). https://doi.org:https://doi.org/10.1016/j.jmr.2011.12.006

45   Scott, F. J. *et al.* A versatile custom cryostat for dynamic nuclear polarization supports multiple cryogenic magic angle spinning transmission line probes. *Journal of Magnetic Resonance* **297**, 23-32 (2018). https://doi.org:https://doi.org/10.1016/j.jmr.2018.10.002

46   Chen, P. *et al.* Magic angle spinning spheres. *Science Advances* **4**, eaau1540 (2018). https://doi.org:10.1126/sciadv.aau1540

47   Barnes, A. B. *et al.* Dynamic nuclear polarization at 700 MHz/460 GHz. (2012).

48   Michaelis, V. K. *et al.* Biradical Polarizing Agents at High Fields. *The Journal of Physical Chemistry B* **126**, 7847-7856 (2022). https://doi.org:10.1021/acs.jpcb.2c03985

49   Banks, D., Michael, B., Golota, N. & Griffin, R. G. 3D-printed stators & drive caps for magic-angle spinning NMR. *Journal of Magnetic Resonance* **335**, 107126 (2022). https://doi.org:https://doi.org/10.1016/j.jmr.2021.107126

50   Amerein, C. *et al.* In-house fabrication of 1.3 to 7 mm MAS drive caps using desktop 3D printers. *Journal of Magnetic Resonance* **348**, 107391 (2023). https://doi.org:https://doi.org/10.1016/j.jmr.2023.107391

51   Hoff, D. E. M. *et al.* Frequency swept microwaves for hyperfine decoupling and time domain dynamic nuclear polarization. *Solid State Nuclear Magnetic Resonance* **72**, 79-89 (2015). https://doi.org:https://doi.org/10.1016/j.ssnmr.2015.10.001

52   Kelz, J. I., Kelly, J. E. & Martin, R. W. 3D-printed dissolvable inserts for efficient and customizable fabrication of NMR transceiver coils. *Journal of Magnetic Resonance* (2019).

53   Pagonakis, I. G. *et al.* in *2022 47th International Conference on Infrared, Millimeter and Terahertz Waves (IRMMW-THz).* 1-2.

Chapter 4 : Proton detected RFDR of amyloidogenic peptides and fibrils reveals monomorphic state of E22G Aβ$_{1-42}$ fibrils

Adapted from: Natalie C. Golota, Brian Michael, Edward P. Saliba, Sara Linse, Robert G. Griffin. To be submitted to *Biochemistry.*

4.1 Introduction

Misfolding and aggregation of peptides are implicated in the development of over 40 diseases, including Alzheimer's disease (AD), Parkinson's disease, and dialysis related amyloidosis (DRA). As of 2022, it is estimated that 1 in 9 adults over 65 have AD, which rises to 1 in 3 adults over age 85. This figure is expected to increase as the US population continues to age [1]. The aggregation of amyloid-β (Aβ) in the brain has been correlated with pathogenesis of Alzheimer's Disease (AD), and, although not proven as the cause of AD, it and remains a critical biomarker of the disease [2-4]. Aβ occurs most frequently as a small protein that is 40 or 42 residues in length and is derived by proteolytic cleavage of amyloid precursor protein (APP) [5-7]. While Aβ$_{1-42}$ is expressed at lower levels than Aβ$_{1-40,}$ it is associated with greater cell toxicity and is a major component of plaque found in AD patients [8]. The development of aggressive, early onset forms of AD are the result of alterations to the APP and can result in enhanced aggregation dynamics in a series of mutations at A21G, E22Δ, E22K, E22G, or D23N [7,9-14]. The E22G, or arctic mutant, is characterized by rapid aggregation and fibrillization which is driven by reduced electrostatic repulsive forces and decreased sidechain size [15]. Additionally, most E22G Aβ$_{1-40}$ studies have revealed extensive

polymorphism [16,17], while the characterization of E22G A$\beta_{1\text{-}42}$ has been limited to cryogenic electron microscopy studies [18].

Since amyloid fibrils are insoluble and non-crystalline, they are not amenable to many conventional biomolecular structure determination methods, such as X-Ray crystallography and solution-state NMR. However, because MAS NMR can address structural questions in such systems, it has become a valuable tool for probing dynamics, polymorphism, and determining atomic resolution structures of amyloid fibrils. Development of dipolar recoupling and fast magic angle spinning (MAS) methods have led to marked improvements in the resolution, sensitivity, and utility of biomolecular solid-state NMR [19-22]. MAS NMR studies of A$\beta_{1\text{-}42}$ have revealed a monomorphic, dimeric structure of mirror image S-shaped monomers in which hydrophobic residues were isolated to the interior of the fibril core [23-26]. Cryogenic electron microscopy has also been used to study amyloid fibrils and has been particularly valuable in the study of brain derived samples [18,23,27,28].

Only recently has application of ^{1}H detected MAS methods of amyloid fibrils become more common, and these approaches leverage an absolute sensitivity enhancement over conventional ^{13}C detection, in addition to improved coherence lifetimes [29]. The improved sensitivity of ^{1}H detection has been used to enhance the study of amyloid fibrils and membrane proteins [30-37]. Conventional ^{13}C detected methods have relied upon large sample volumes and moderate MAS frequencies, typically in the interval $\omega_r/2\pi \sim$20-40 kHz. Under such ^{13}C detected schemes, radio frequency driven recoupling (RFDR) is the default starting point for carbon-carbon homonuclear spin correlations and short-range resonance assignments. RFDR is a first

order zero quantum recoupling sequence that uses one 180° pulse centered in the rotor period to recouple homonuclear dipolar couplings as modulated by the chemical shift anisotropy and finite pulse effects [38-40]. This dipolar recoupling method has been instrumental in probing amyloids, membrane proteins and viral particles [41-45]. Homonuclear recoupling has recently been combined with MAS $\geq$ 90 kHz to acquire proton detected multidimensional experiments on a few hundred micrograms of material. However, to date few proton detected studies have been performed on fully protonated amyloid β, demonstrating the need for continued development and application of dipolar recoupling at high spinning frequencies [46,47].

In this paper, we demonstrate the use of proton detected NMR for high-resolution structural characterization of fully protonated GNNQQNY and E22G-Aβ1-42 samples. These spectra are important since they demonstrate the utility of the rigid crystal in optimizing the development of proton detected methods to the study of amyloidogenic proteins. A MAS frequency of $\omega_r/2\pi$ = 90 kHz was sufficient to achieve 1H linewidths of ~0.3 ppm in GNNQQNY using CP-HSQC experiments. Furthermore, the hCCH-RFDR experiment was optimized on GNNQQNY and we determined that mixing times for RFDR at $\omega_r/2\pi$=90 kHz were comparable to those at $\omega_r/2\pi$= 20 kHz. Isotopically enriched expression yields of E22G-Aβ$_{1-42}$ were very limited; thus, proton detected MAS NMR was essential for study of the E22G arctic mutant.1H-13C CP-HSQC spectra reveal a dynamic residue of A42, as previously observed in wild type Aβ1-42 and overall small chemical shift perturbation relative to wild type Aβ1-42. The 1H-15N CP-HSQC spectra indicate significant sample heterogeneity and dynamics that reduce the spectral resolution. Finally, we demonstrate the utility of homonuclear recoupling sequences at

90 kHz to determine that E22G-Aβ1-42 fibrils are largely monomorphic, except for observation of the dynamic doubling of the A42 residue. The hCCH spectra recorded using either RFDR or TOCSY mixing confirms the low chemical shift perturbations observed in hCH spectra. Overall, we use proton detected MAS NMR to conclude E22G Aβ1-42 fibrils are monomorphic and with fibril core structure similar to that of wild type Aβ1-42, in accordance with a recently published cryo-EM study [18].

4.2 Experimental

4.2.1 GNNQQNY Synthesis

Uniformly labeled $^{13}C,^{15}N$ GNNQQNY was synthesized using solid phase peptide synthesis and purified via HPLC courtesy of the Swanson Biotechnology Center at the MIT Koch Institute. Samples were crystallized at protein concentrations < 10 mg/mL as previously described[48,49]. The crystals were then packed into a 3.2 mm or 0.7 mm rotor using ultracentrifugation.

4.2.2 Expression and purification of EDDIE-Aβ$_{1\text{-}42}$ E22G

The toxicity of Aβ(M1-42)E22G to *Escherichia coli* leads to relatively poor yield of tag-free peptide [15]. We therefore expressed Aβ1-42E22G in fusion with the self-cleavable tag nPro in the form of its EDDIE mutant [50], which protects the cells by driving the expressed product to inclusion bodies. This mode of expression enables the isolation of Aβ peptides starting with Asp1 at the N-terminus [51,52], as well as the expression of other toxic peptides such as for example IAPP [53]. The amino acid sequence of the expressed construct is as follows, with the Aβ1-42E22G sequence underlined:

MELNHFELLYKTSKQKPVGVEEPVYDTAGRPLFGNPSEVHPQSTLKLPHDRGEDDIET TLRDLPRKGDCRSGNHLGPVSGIYIKPGPVYYQDYTGPVYHRAPLEFFDETQFEETTK RIGRVTGSDGKLYHIYVEVDGEILLKQAKRGTPRTLKWTRNTTNCPLWVTSC<u>DAEFRH DSGYEVHHQKLVFFAGDVGSNKGAIIGLMVGGVVIA</u>.

The gene construct was designed with *E. coli*-preferred codons in a Pet3a plasmid (purchased from Genscript, Piscataway, New Jersey) and the fusion protein was expressed in *E. coli* BL21 DE3 PlysS star in M9 minimal medium with ^{13}C-glucose and ^{15}NH$_4$Cl as the sole carbon and nitrogen sources.

A cell pelleted from 4 L of solution was sonicated 5 times in 80 mL 10 mM Tris/HCl, 1 mM EDTA, pH 8.5 (buffer A) containing a trace of DNase, with centrifugation at 18,000 g for 7 min between sonications. The inclusion body pellet after the 5th sonication was dissolved in 150 mL buffer A with 10 M urea, 1 mM DTT, by sonication and stirring. The resulting solution (ca. 9.4-9.7 M urea) was diluted with 200 mL buffer A with 1 mM DTT (thus yielding ca. 4 M urea) and loaded onto 2 x 20 mL DEAE-sepharose FF columns (GE Healthcare) in tandem, equilibrated in buffer A with 4 M urea and 1 mM DTT. The columns were washed with 100 mL buffer A with 4 M urea and 1 mM DTT and eluted with a 0-0.4 M NaCl gradient in the same buffer. Fractions containing EDDIE-Aβ1-42E22G were diluted 15 times with 1 M Tris, 1 mM EDTA, 5 mM DTT, pH 7.9 in glass bottles and left at 4°C for 48 h, total volume 1.0 L. During this time EDDIE slowly folded leading to auto-cleavage and release of Aβ1-42E22G. The solution was then dialyzed in 3.5 kDa MW cutoff dialysis bags (boiled 4 times in Millipore water before use) against a total of 30 L of 5 mM Tris/HCl, 0.5 mM EDTA, pH 8.5, in three shifts (10 L per shift). The dialyzed solution was supplemented with 50 g Q-sepharose big beads (GE Healthcare,

equilibrated in buffer A) and incubated for 0.5 h in the cold room with occasional stirring using a glass rod. The beads were collected on a Büchner funnel and washed with 200 mL buffer A. Aβ1-42E22G was eluted in buffer A with 50 mM NaCl, 8 fractions of 50 mL each. The fractions were lyophilized, dissolved 2-by-2 in 10 mL 6 M GuHCl and isolated from any residual *E. coli* proteins, aggregates, and small molecule contaminants by size exclusion chromatography (SEC) in 20 mM sodium phosphate, 0.2 mM EDTA, 0.02% (w/v) NaN$_3$, pH 8.5 using a Superdex 75 26/600 column. The eluted fractions were monitored by UV absorbance and SDS PAGE with Coomassie staining. Fractions corresponding to the center of the Aβ1-42E22G monomer peak were pooled in a glass bottle, pH adjusted to 8.0 by adding NaH$_2$PO$_4$ and the pool was incubated quiescent at 37°C. Monomer from each of the four rounds of SEC were added to the same bottle to propagate the morph formed in the first of the four aliquots.

The formation of fibrils was validated for a small withdrawn sample using thioflavin T fluorescence in a Perkin Elmer LS50B fluorescence spectrometer, in comparison with the thioflavin T fluorescence in buffer. The morphology of the fibrils as revealed by cryo-TEM, is indistinguishable from that of the wild type peptide, displaying a double-filament structure with a short twist distance between the apparent cross-over points [15].

We also purified one aliquot of Aβ1-42E22G after expression of NT*Aβ1-42E22G (synthetic gene with *E. coli*-preferred codons in Pet3a plasmid purchased from Genscript) in *E. coli* BL21 DE3 PlysS star in 1 L M9 minimal medium with ^{13}C-glucose and ^{15}NH$_4$Cl as the sole carbon and nitrogen sources using the published protocol [54], and after the final SEC, this aliquot was mixed into the same solution as described above.

The fibril sample was finally packed into a 0.7 mm rotor using ultracentrifugation. Tryptic digest and intact mass spectrometry were used to confirm the desired sequence and absence of Aβ$_{1\text{-}42}$ wild type fibrils.

4.2.3 MAS NMR

^{1}H detected spectra were acquired at a static field of 18.8 T (800 MHz ^{1}H) with a three channel (HCN) 0.7 mm Bruker MAS probe. The sample was spun at $\omega_r/2\pi$ =111 kHz using a MAS 3 controller and temperature was maintained at 273 K using a Bruker cooling unit. The 90° pulse durations were 133 kHz (1.875 μs), 83 kHz (3 μs), and 83 kHz (3 μs) for ^{1}H, ^{13}C, and ^{15}N, respectively.

Dipolar based CP-HSQC spectra were recorded using the pulse sequence previously described using the zero-quantum cross polarization condition at nutation frequencies near $^5/_4$ ω_r and $^1/_4$ $_{\omega_r}$, for proton with a 10% ramp and ^{15}N or ^{13}C, respectively [36].

For hCCH experiments, the ^{1}H-^{13}C CP was performed using a tangent ramp on the proton RF power and a linear 10% ramp was used for the ^{13}C-^{1}H CP. For hCCH-TOCSY, WALTZ-16 was used with an RF field of ~22.5 kHz corresponding to ω$_r$/4. For hCCH-RFDR experiments, shown in Figure 4.1, the π pulse width was 2.5 μs and a corresponding RF field of 200 kHz. Decoupling was not employed during the RFDR

mixing period. Spectra were apodized using 60° shifted squared sine bells or gaussian apodization and zero filled to at least twice the number of points in the indirect dimension. Additional acquisition parameters are given in Table 4.2.

In all ^{1}H detected experiments, swept-low power TPPM at an RF field amplitude of 24 kHz was used for proton decoupling during t_1 and WALTZ-16 was applied to 13C or 15N at 10 kHz, respectively [55,56]. Water suppression was achieved through the MISSISSIPPI pulse sequence without homospoil gradients [57], using a 24 kHz RF field and 200 ms pulse duration.

hCC-RFDR spectra were acquired at a static field of 18.8 T (800 MHz ^{1}H) with a three channel (HCN) 3.2 mm Bruker MAS probe at a MAS rate of 20 kHz and a temperature of 273 K. For the 3.2 mm probe, 90° pulse durations were 3 μs for ^{1}H and [13]C. RFDR mixing was performed using π pulse width of ~ 6 μs and a CW proton decoupling field of 83 kHz.
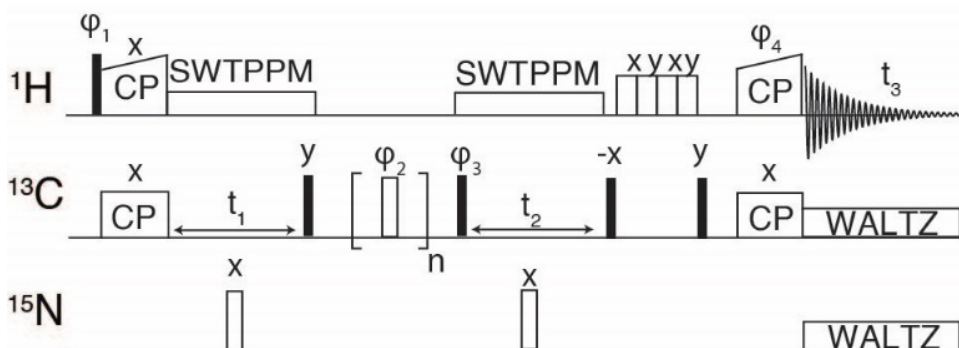
Figure 4.1. hCCH-RFDR pulse sequence. Pulse sequence for 3-dimensional hCCH experiment using RFDR for carbon-carbon mixing. The phase cycle φ_1 was {y, -y}, φ_2 was XY-32, φ_3 was {x, x, -x, -x}, φ_4 was {4*x, 4*-x}. The receiver phase cycle was {x,-x, -x, x, -x, x, x, -x}.
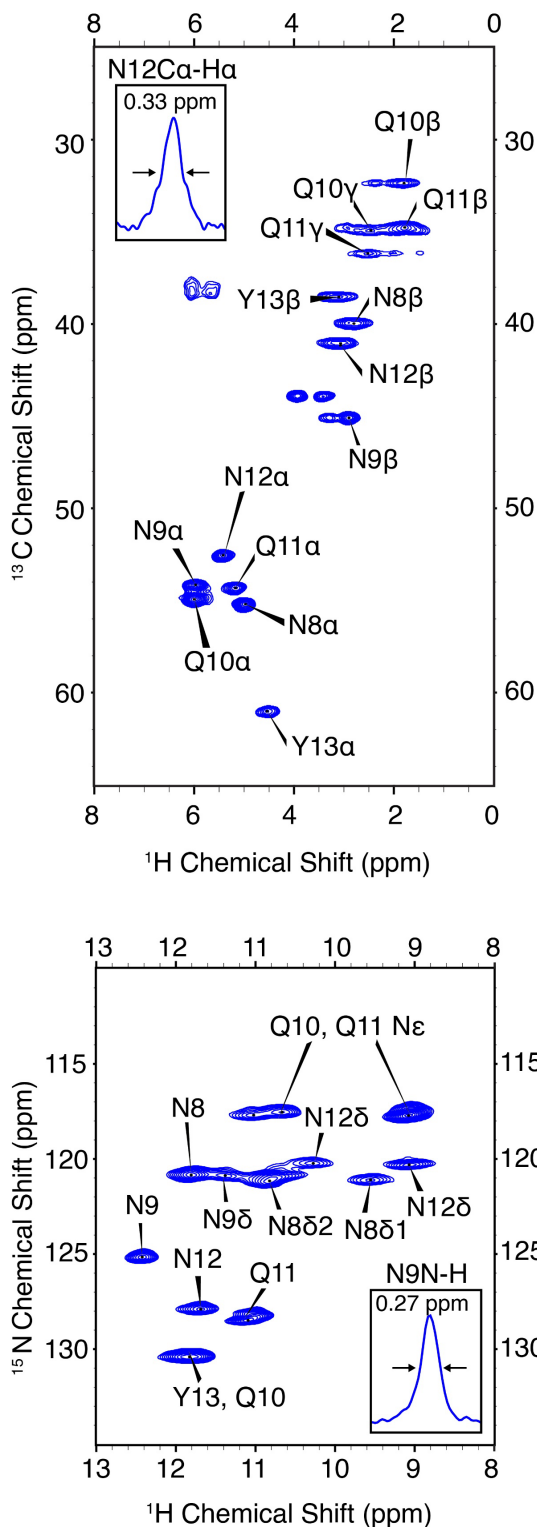
Figure 4.2 ^{1}H detected CP-HSQC of U-^{13}C, ^{15}N GNNQQNY (top) ^{1}H-^{13}C correlations. (bottom) ^{1}H-^{15}N correlations.

4.3 Results and Discussion

4.3.1 1H detected GNNQQNY

GNNQQNY is part of the N terminal domain of Sup35p, an amyloid forming yeast prion protein [48]. Early studies found the monoclinic microcrystals of GNNQQNY, as used herein, have amylogenic properties including binding of Congo red and formation of β-sheets and steric zipper structure. High resolution X-ray crystal structures have been obtained, in addition to carbon and nitrogen assignments via MAS NMR [49,58-61]. The monoclinic crystals are rigid and offer a high resolution amyloidogenic system with which to optimize protein spectroscopic methods. The CP-HSQC heteronuclear correlation spectra of GNNQQNY monoclinic crystals and associated proton assignments are illustrated in Figure

4.2. These are the first initial proton detected experiments on the amyloidogenic peptide GNNQQNY to date. In the fully protonated sample at $\omega_r/2\pi$ =90 kHz and 18.8 T, linewidths of 0.33 ppm and 0.27 ppm were obtained for the alpha carbon proton of N12 and the amide proton of N9, respectively. The degeneracy of amino acids in this sample results in peak overlap, reducing the effective resolution of many resonances. Typically, proton linewidths were less than 0.5 ppm for individual resonances, where all linewidths are reported without apodization. The narrow line shapes in the fully protonated sample are indicative of the highly ordered crystal structure of GNNQQNY, while further reduction in linewidth is expected with application of higher MAS rates.

The CP-HSQC hCH experiment was then used as a building block for the hCCH-RFDR experiment initially implemented on GNNQQNY, using the pulse sequence is shown in Figure 4.1. A MAS frequency of $\omega_r/2\pi$=90 kHz and $\omega_{1C}/2\pi$=200 kHz RFDR pulses was sufficient to recouple ^{13}C-^{13}C and decouple ^{1}H-^{13}C. Thus, the use of conventional ^{1}H decoupling during the RFDR mixing period was not necessary. At a MAS frequency of 90 kHz, the theoretical description of the pulse sequence accounts for the finite pulse length, given the 2.5 μs 180° pulse used occupies a considerable fraction of the 11.11 μs rotor period. Under the description of fast MAS and finite pulses, the dependence of ^{13}C chemical shift differences for efficient homonuclear recoupling is reduced due to dipolar evolution during the 180° pulse which further to longitudinal
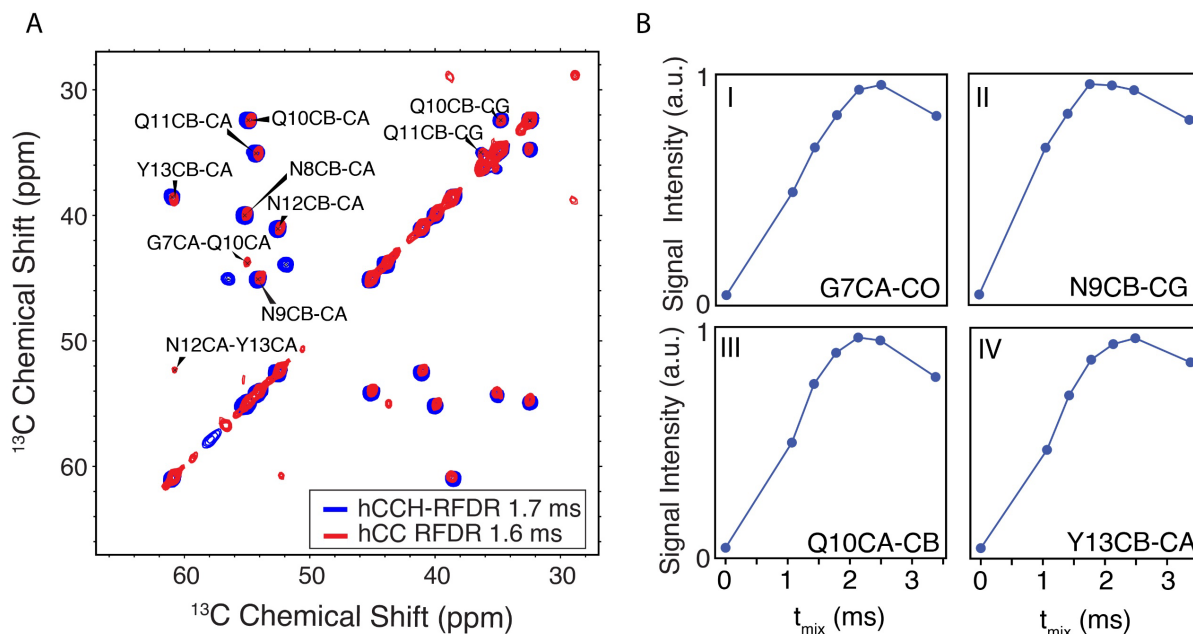
Figure 4.3. hCCH-RFDR of GNNQQNY. A) The carbon-carbon correlations of hCCH-RFDR (red) and hCC RFDR (blue) of U[^{13}C,^{15}N]-GNNQQNY crystals. The hCCH-RFDR was acquired at 90 kHz using a mixing time of 1.7 ms. The conventional 2-dimensional hCC-RFDR was acquired at 20 kHz MAS using a mixing time of 1.6 ms. (B) Signal intensity as a function of RFDR mixing time for hCCH-RFDR. For each contact in I-IV, the normalized signal intensity is plotted.

mixing. For further description of finite pulse RFDR the reader is referred to the original

paper by Bennett, et al. where finite pulses are discussed [62].

As shown in Figure 4.3(A), the hCCH-RFDR at 90 kHz reproduces all intra-

residue correlations that are expected in a 1 bond RFDR. While numerous other

heteronuclear and homonuclear correlation methods have been developed for ^{1}H

detected MAS NMR, the direct comparison of hCCH to hCC spectra acquired at 20 kHz

MAS is a valuable spectroscopic tool for spectral fingerprinting of limited quantity

samples. However, we note that the very weakly detected inter-residue correlations of

N12Cα-Y13Cα and G7Cα-Q10Cα were not observed in the hCCH-RFDR spectrum.

These longer-range correlations may be more effectively probed under fast MAS by

other homonuclear correlation schemes or with additional transients per point. In the present spectrum, 8 scans per point were acquired for the hCCH-RFDR leading to a total experiment time of 2 days and 15 hours.

As shown in Figure 4.3 (B), most residues have reached maximum signal intensity between 1.7 and 2.5 ms, which is comparable to optimal mixing times under reduced MAS frequencies, such as the commonly used MAS frequency of 20 kHz. The longest optimal mixing times are observed for the G7 and Y13 residues, which are excluded from the steric zipper core interface between peptide dimers. Overall, we demonstrate the first proton detected spectra of the amyloidogenic peptide GNNQQNY at high resolution. We additionally use the model peptide to optimize spectral fingerprinting via hCCH-RFDR and determine optimal mixing times comparable to those canonically used at lower MAS frequencies.

4.3.2 ^{1}H detected A$\beta_{1\text{-}42}$ E22G

The proton detected experiments were then applied to yield the first characterization of A$\beta_{1\text{-}42}$ E22G by MAS NMR. The E22G A$\beta_{1\text{-}42}$ mutant was expressed using a fusion construct and an EDDIE mutant expressed in E. Coli for uniform ^{13}C and ^{15}N isotopic enrichment. However, only limited sample quantities could be produced, and as such, proton detected MAS NMR was required for reasons of sensitivity. The expression protocol was previously validated and cryo-TEM revealed the morphology of the E22G A$\beta_{1\text{-}42}$ fibrils to be indistinguishable from the wild type A$\beta_{1\text{-}42}$ fibrils, with both fibrils displaying a double filament structure with short twist distance between apparent cross over points [15].

A

B
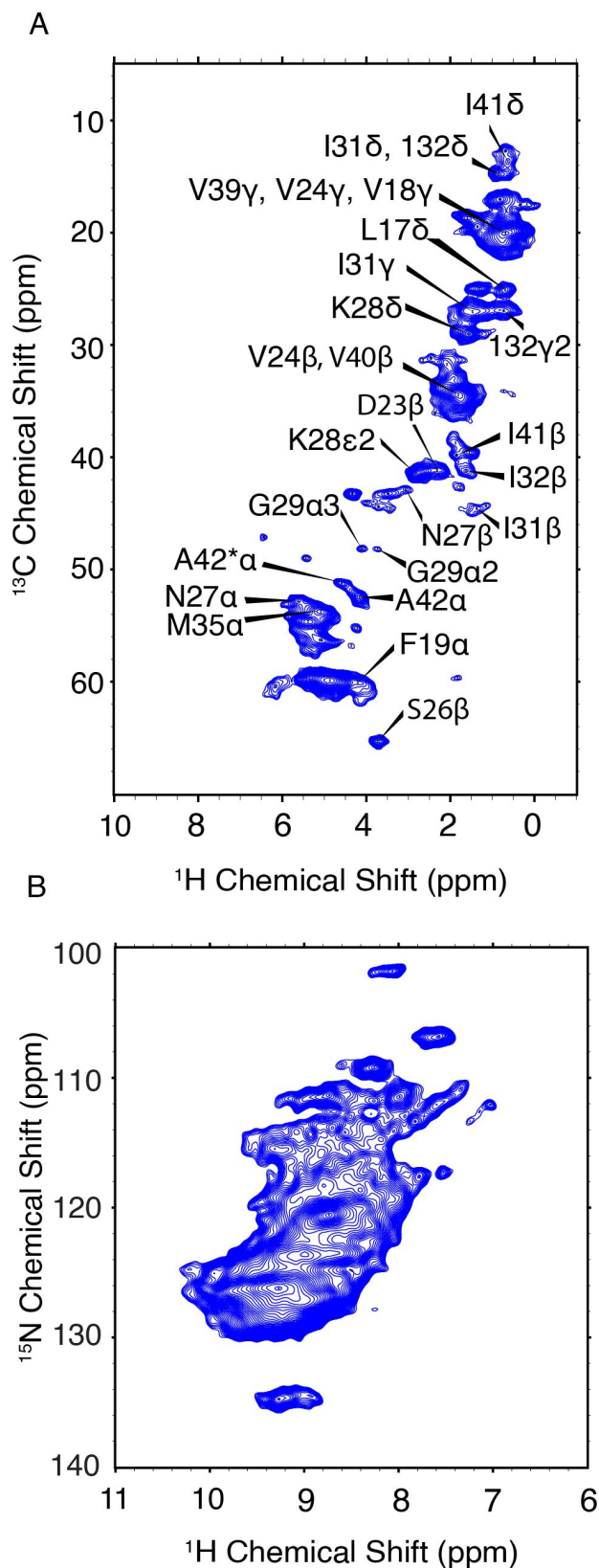
Figure 4.4. ^{1}H detected CP-HSQC of U-^{13}C, ^{15}N E22G Aβ$_{1-42}$. (A) hCH, (B) hNH correlations.

CP HSQC spectra were acquired for E22G Aβ $_{1-42}$ and illustrated in Figure 4.4.The hCH spectra showed only small chemical shift perturbations from the previously published wild type Aβ $_{1-42}$ fibril spectra [46]. We note an overall reduction in the spectral resolution of the E22G sample acquired at $\omega_r/2\pi$= 90 kHz and a proton Lamour frequency of 800 MHz, relative to the wild type sample at $\omega_r/2\pi$= 111 kHz and a proton Larmor frequency of 1 GHz [46]. Two resonances were assigned to the A42 ^{13}Cα in both the E22G spectrum and the previously studied wild type sample. This peak doubling was observed in wild type Aβ$_{1-42}$ only at fast MAS conditions and was not observed at 20 kHz MAS. The twofold doubling of the resonance is attributed to two

172

conformations of the A42 residue that are only detected during high frequency spinning. E22G-Aβ1-42 cross peak assignments were rapidly obtained due to small chemical shift perturbations in the hCH spectra of E22G to previously obtained assignments of wild type samples, as shown in Figure 4.6. The shared presence of dynamics of the C-terminal domain in both wild type and E22G Aβ$_{1-42}$ suggests a conserved C-terminal structural fold. There are several unassigned, narrow resonances that could also be attributable to dynamic residues in the N-terminal domain. These observations underscore the importance of developing fast MAS spectroscopy alone, or in combination with low temperature MAS, to study the N and C-terminal domain dynamics.

The hNH spectrum of E22G-Aβ $_{1-42}$ demonstrates a pronounced reduction in resolution, indicating a high degree of sample and structural heterogeneity. The reduction in resolution of the ^{15}N spectral dimension has been observed previously in Aβ fibrils [47]. The primary contribution to decreased resolution is probably structural heterogeneity, with polymorphism, sample impurities, and dynamics also contributing. To probe the role of potential polymorphism beyond the likely structurally doubling of A42, we employed the hCCH-RFDR and hCCH-TOCSY experiments.

hCCH-RFDR offers a direct spectral comparison to the wealth of previously acquired hCC spectra of Aβ $_{1-42}$ in the literature [23,25,63]. Despite the ubiquity of hCC-RFDR, hCCH-RFDR has to date been sparsely applied in fully protonated samples [47,64] or in selectively deuterated samples [65]. Instead, hCHH or hNHH-RFDR methods are used most often, offering increased sensitivity and the potential for longer range quantitative distance measures [30,37,46,66]. However, in fully protonated samples the continued development of high spinning frequency MAS rotors and pulse
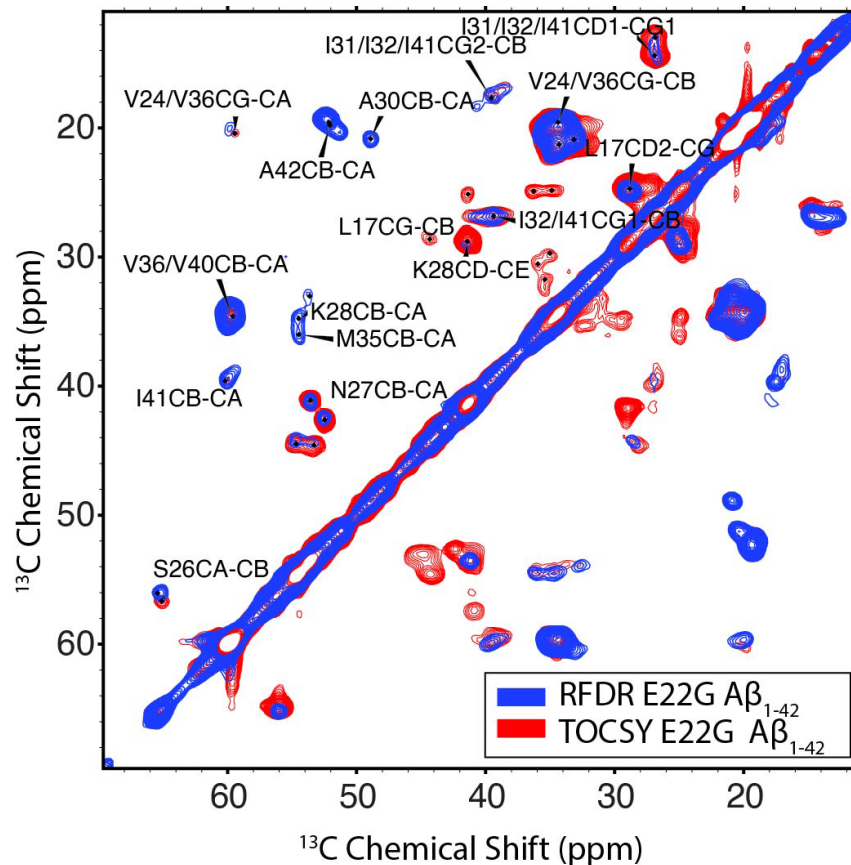
Figure 4.5. hCCH of E22G-Aβ$_{1-42}$. Acquisition using TOCSY (red) or RFDR (blue) for carbon homonuclear mixing.

sequence methodology is required. The comparison between the hCCH-RFDR and hCCH-TOCSY are illustrated in Figure 4.5. The TOCSY based hCCH has been described previously, with mixing largely mediated by C-C scalar couplings[35] and is based on total through bond correlation pulse sequences[67]. As such, increased MAS rates beyond 90 kHz would be expected to improve the performance of the pulse sequence with increased T$_{1\rho}$ during the WALTZ-16 mixing period on a dynamic sample such as the E22G Aβ $_{1-42}$ fibrils. RFDR performance was increased over TOCSY when a large chemical shift difference was present, as expected for the RFDR sequence. For both pulse sequences the C-C projection of the hCCH experiment displays improved
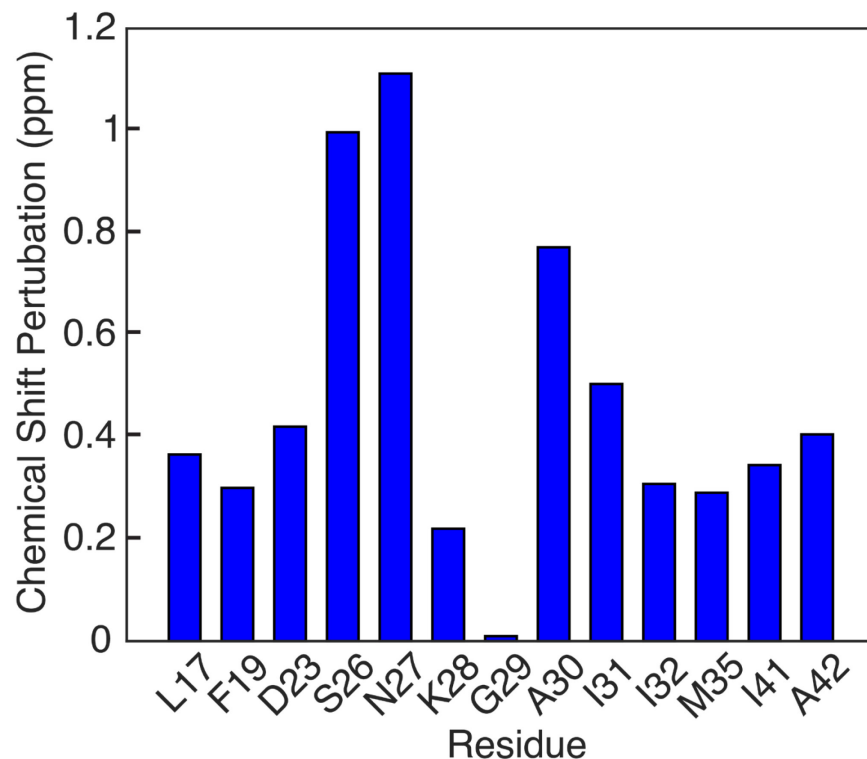
Figure 4.6. Chemical Shift Perturbations of E22G-Aβ$_{1\text{-}42}$. Chemical shift perturbations are relative to wild type Aβ$_{1\text{-}42}$ fibrils as reported in Colvin et. al. and Bahri. et.al.

resolution over the hCH detected experiments, however, site specific resolution is still not achieved in this sample. Higher MAS frequencies and access to higher magnetic fields remains a critical step for the study of pathologically relevant AB fibrils. Despite these limitations, several important preliminary biological conclusions can be drawn using the spectra presented herein.

First, serine residues have previously been used to characterize polymorphism in Aβ$_{1\text{-}42}$ fibrils [23,25] . In the present E22G sample, the S26 Cα-Cβ correlation was observed as a single resonance, with ~ 1 ppm in chemical shift difference relative to wild type Aβ$_{1\text{-}42}$. Aside from the dynamically driven doubling of A42Cα, no further resonance doubling was observed. Compared to wild type Aβ$_{1\text{-}42}$ RFDR fingerprint

spectra, E22G $A\beta_{1-42}$ is similarly monomorphic without fibril seeding. Overall, the core residues of the E22G $A\beta_{1-42}$ fibril display minimal chemical shift perturbations, on the order of 1 ppm, as shown in Figure 4.6.

In previous studies, $A\beta_{1-40}$ E22G and was found to be at least four-fold polymorphic in in most resonances of the selectively isotopically labeled sample [16]. In a separate study, unseeded $A\beta_{1-40}$ E22G fibrils displayed two-fold polymorphism in two of the four selectively labeled sites [17]. Cross-seeding of $A\beta_{1-40}$ E22G with $A\beta_{1-40}$ or $A\beta_{1-42}$ fibrils resulted in a largely monomorphic fibril with minimal chemical shift differences to the wild type $A\beta_{1-42}$. As in other studies, this suggested the dominant form of the arctic mutant may adopt similar β strand confirmation as the wild type $A\beta_{1-42}$ and is further supported by the MAS NMR data presented here.

Another notable feature in the present E22G $A\beta_{1-42}$ is the minimal chemical shift perturbations of the K28 residues, indicating the likely conserved K28-A42 salt bridge observed previously in wild type $A\beta_{1-42}$. This salt bridge serves to stabilize the beta-sheet regions of the fibrils via electrostatic interactions and has been a conserved feature between wild type $A\beta_{1-42}$ and the E22Δ $A\beta_{1-39}$ mutant. The largest observed chemical shift perturbations remained limited to ~ 1 ppm, with the largest shifts being co-localized near the G22 residue. This supports the hypothesis the mutation induces electrostatic perturbations while conserving fibril core features.

Cryo-EM recently has yielded structures of two human brain protofilament extracts consisting of residues V12-V40 and E11-G37 of E22G, in addition to filaments from brains of mice with the artic mutation E22G [18]. While the recently published cryoEM data suggested a common substructure that was shared between E22G and

wild type protofilaments, MAS NMR data has previously and reproducibly demonstrated results that differ from the with cryoEM derived structures. The differences between MAS NMR and cryoEM have not been reconciled, and while the present study does not address this issue, the lack of chemical shift perturbation and monomorphic behavior does support the suggestion that E22G Aβ_{1-42} adopts a similar conformation to wild type fibrils. In combination with the previous studies, this suggests that while both E22G Aβ $_{1-42}$ and Aβ $_{1-40}$ species may adopt conformations more comparable to the wild type Aβ $_{1-42}$ fibril structure, polymorphism plays a more dominant role in the structure of E22G Aβ $_{1-40}$ than in E22G Aβ $_{1-42.}$

4.4 Conclusion

We present the initial ^{1}H detected MAS NMR results on two amyloidogenic systems, GNNQQNY monoclinic crystals and fibrils of E22G Aβ $_{1-42}$. Linewidths typically of 0.2-0.3 ppm were observed in CP-HSQC spectra on the rigid peptide GNNQQNY. This high-resolution model system was employed to optimize hCCH-RFDR experiments, and an optimal mixing period in this system was observed to be ~ 2 ms, on par with mixing periods used at lower MAS frequencies. These methods were then extended to the study of E22G-Aβ $_{1-42}$ fibrils. The spectral resolution was reduced relative to wild type A$\beta_{1-42,}$ indicating an increase in sample heterogeneity perhaps due to the rate at which the fibrils are formed. The use of fast MAS confirmed the observation of dynamics in the A42 residue as observed also in wild type samples, indicating the C-terminus is not strongly modulated by the E22G mutation. hCCH-RFDR demonstrated the sample to be largely monomorphic, in contrast to studies of synthetic

E22G-Aβ_{1-40} in which multiple polymorphs were observed. Overall, < 1 ppm of chemical shift perturbations were observed across numerous residues between the previously reported wild type Aβ_{1-42} and the present E22G-Aβ_{1-42}. This result suggests a conserved core fibril structure, in accordance with recent cryo EM results. Taken as whole, this study presents further evidence that the Arctic mutant has a propensity for adopting Aβ_{1-42} like fibril features as previously observed in Aβ_{1-40} fibrils of E22G mutant. In the future, the use of dynamic nuclear polarization and access to increased MAS rates and higher fields can aid in the determination of the complete three-dimensional structure of the sample quantity limited E22G mutant of Aβ_{1-42}.

4.5 Supporting Information
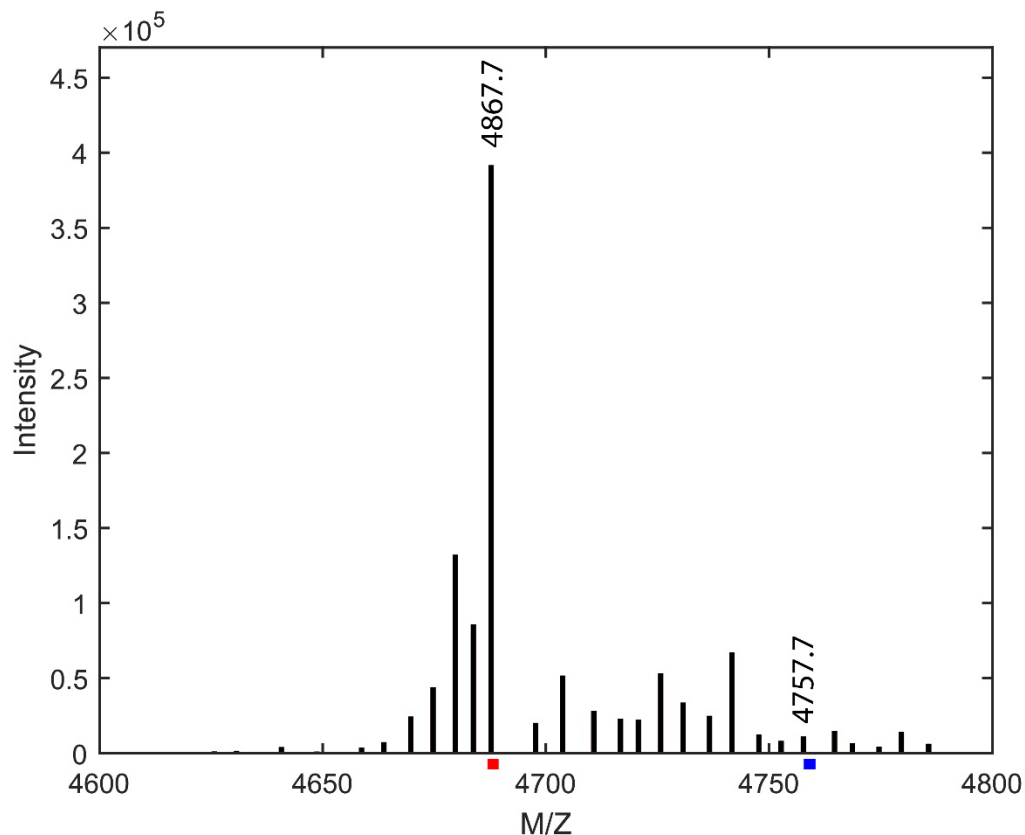
Figure 4.7. Intact MS of Aβ1-42 E22G Sample. The predominant peak corresponding to 4867.7 m/z is the Aβ$_{1-42}$ E22G corresponding to ~ 97.3% isotopic enrichment. The distribution of small peaks can correspond to sample impurities or between 95-100% isotopic enrichment of the sample. The range of 97%-98% isotopic enrichment is provided in the red bar for Aβ$_{1-42}$ E22G or the blue bar for the wild type Aβ$_{1-42}$. Given the presence of a small peak minimally outside the range of 97% isotopic enrichment of Aβ$_{1-42}$, tryptic digestion was performed to further probe the protein sequence. However, the predominant species in the sample corresponds to 97-98% isotopically enriched Aβ$_{1-42}$ E22G

Sequence	Sequence #	B	Y	Sequence #
L	1	120.825-121.088	1322.894-1325.609	12
V	2	225.664-226.154	1203.076-1205.528	11
F	3	382.355-383.219	1098.237-1100.463	10
F	4	539.046-540.284	941.546-943.397	9
A	5	613.929-615.318	784.855-786.332	8
G	6	673.834-675.336	709.972-711.298	7
D	7	793.662-795.361	650.067-651.280	6
V	8	898.502-900.425	530.239-531.256	5
G	9	958.407-960.444	425.400-426.191	4
S	10	1049.281-1051.473	365.494-366.172	3
N	11	1169.092-1171.510	274.621-275.143	2
K	12	1304.884-1307.598	154.809-155.106	1
Total Monoisotopic mass (M)		1321.887-1324.602	1322.662-1325.377	
$(M+2H)^{2+}$		661.951-663.308	662.338-663.696	

Table 4.1. Monoisotopic masses for the tryptic digest fragment LVFFAGDVGSNK of E22G Aβ1-42. In the B column, fragmentation is performed from N to C terminus while for fragmentation in the Y column fragmentation is performed from C to N.
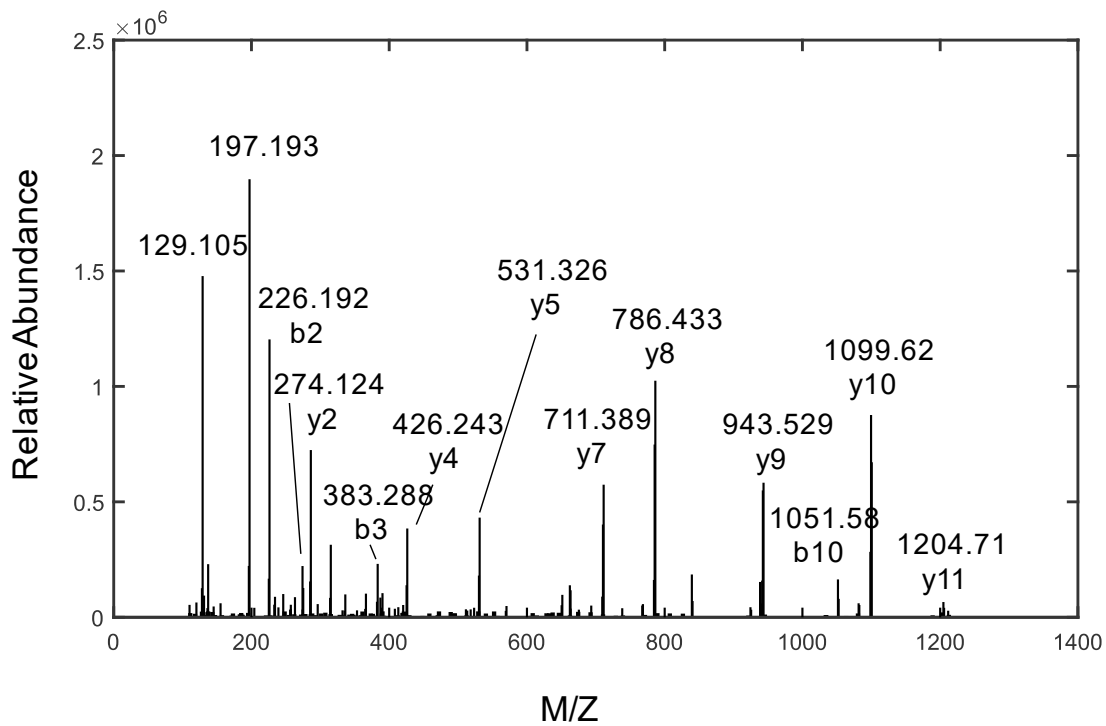
Figure 4.8. MS2 fragment spectrum of the 662.908 m/z peak. Overall, enough fragments are identified to confirm the E22G mutation was adopted and isotopically labeled at 97-100% enrichment. Tryptic digestion and subsequent fragmentation did not detect wild type $A\beta_{1-42}$

Spectrum	Max Evolution Time (ms)			Number of complex points			Spectral Width (Hz/ppm)			Scans per point	Interscan delay (s)	Experiment time
	ω_1	ω_2	ω_3	t_1	t_2	t_3	ω_1	ω_2	ω_3			
(H)NH GNNQQNY	19.7	15.9		160	1024		4050/50	32051/40		32	1.5	2 h 27 min
(H)CH GNNQQNY	16.3	12.56		460	2048		14069/70	81521/102		32	1.5	7 h 25 min
hCCH-RFDR GNNQQNY	5.3	5.3	10.2	128	128	2048	12059/60	12059/60	100,000/125	8	1.5	2d 14 h 57 min
hCC RFDR GNNQQNY	8.5	17.2		1024	2048		60000/298.5	59523/296.1		32	3	1d 3h 34 min
(H)NH E22G AB1-42	19.7	15.9		160	1024		4050/50	32051/40		32	1.5	2 h 27 min
(H)CH E22G AB1-42	16.3	12.56		460	2048		14069/70	81521/102		32	1.5	7 h 25 min
hCCH-RFDR E22G Aβ1-42	5.3	5.3	10.2	128	128	2048	12059/60	12059/60	100,000/125	32	1.5	10d 11 h 47 min
hCCH-TOCSY E22G Aβ1-42	5.3	5.3	10.2	128	128	2048	12059/60	12059/60	100,000/125	32	1.5	10d 12 h 53 min

Table 4.2. NMR spectral acquisition parameters.

Res	Cα	Cβ	Cγ1	Cδ1	Cδ2	Cε
L17		44.68	29.23		25.25	
F19	60.16					
D23		41.3				
S26	56.2	65.3				
N27	53.81	41.4				
K28	54.76	34.84		29.22		41.63
G29	48.21					
A30	49.13	21.03				
I31		44.65	27.14			
I32	59.98	41.29	27.05			
M35	54.75	36.25				
I41	60.137	39.76		13.73		
A42	52.42	19.62				

Table 4.3. Chemical Shifts assigned to E22G Aβ1-42 fibrils.

Res	Cα	Cβ	Cγ1	Cδ1	Cδ2	Cε
L17		44.62	28.6		25.24	
F19	59.86					
D23		40.88				
S26	54.96	65.97				
N27	52.76	42.57				
K28	54.69	34.85		29.62		41.8
G29	48.22					
A30	50.22	20.99				
I31		43.94		27.2		
I32	59.72	40.84	27.17			
M35	54.34	36.28				
I41	59.7	39.57		14.09		
A42	52.3	20.18				

Table 4.4. Chemical Shifts assigned to wild type Aβ1-42 fibrils.

Wild type chemical shifts from [23,46,63]

4.6 Acknowledgements

4.7 References

1   2022 Alzheimer's disease facts and figures. *Alzheimer's & Dementia* **18**, 700-789 (2022). https://doi.org:https://doi.org/10.1002/alz.12638

2   Eisenberg, D. & Jucker, M. The Amyloid State of Proteins in Human Diseases. *Cell* **148**, 1188-1203 (2012). https://doi.org:https://doi.org/10.1016/j.cell.2012.02.022

3   Hampel, H. *et al.* The Amyloid-β Pathway in Alzheimer's Disease. *Molecular Psychiatry* **26**, 5481-5503 (2021). https://doi.org:10.1038/s41380-021-01249-0

4   Murphy, M. P. & LeVine Iii, H. Alzheimer's Disease and the Amyloid-β Peptide. *Journal of Alzheimer's Disease* **19**, 311-323 (2010). https://doi.org:10.3233/JAD-2010-1221

5   Oltersdorf, T. *et al.* The Alzheimer amyloid precursor protein. Identification of a stable intermediate in the biosynthetic/degradative pathway. *Journal of Biological Chemistry* **265**, 4492-4497 (1990).

6   Selkoe, D. J. Alzheimer's Disease: Genes, Proteins, and Therapy. *Physiological Reviews* **81**, 741-766 (2001). https://doi.org:10.1152/physrev.2001.81.2.741

7   Tomiyama, T. & Shimada, H. APP Osaka Mutation in Familial Alzheimer's Disease—Its Discovery, Phenotypes, and Mechanism of Recessive Inheritance. *International Journal of Molecular Sciences* **21** (2020).

8   Roher, A. E. *et al.* beta-Amyloid-(1-42) is a major component of cerebrovascular amyloid deposits: implications for the pathology of Alzheimer disease. *Proceedings of the National Academy of Sciences* **90**, 10836-10840 (1993). https://doi.org:10.1073/pnas.90.22.10836

9   Nilsberth, C. *et al.* The 'Arctic' APP mutation (E693G) causes Alzheimer's disease by enhanced Abeta protofibril formation.

10   Kamino, K. *et al.* Linkage and mutational analysis of familial Alzheimer disease kindreds for the APP gene region.

11   Bugiani, O. *et al.* Hereditary cerebral hemorrhage with amyloidosis associated with the E693K mutation of APP. *Archives of neurology* **67**, 987-995 (2010).

12   Grabowski, T. J., Cho, H. S., Vonsattel, J. P. G., Rebeck, G. W. & Greenberg, S. M. Novel amyloid precursor protein mutation in an Iowa family with dementia and severe cerebral amyloid angiopathy. *Annals of Neurology: Official Journal of the American Neurological Association and the Child Neurology Society* **49**, 697-705 (2001).

13   Van Broeckhoven, C. *et al.* Amyloid β protein precursor gene and hereditary cerebral hemorrhage with amyloidosis (Dutch). *Science* **248**, 1120-1122 (1990).

14   Schütz, A. K. *et al.* Atomic-Resolution Three-Dimensional Structure of Amyloid β Fibrils Bearing the Osaka Mutation. *Angewandte Chemie International Edition* **54**, 331-335 (2015). https://doi.org:https://doi.org/10.1002/anie.201408598

15   Yang, X. *et al.* On the role of sidechain size and charge in the aggregation of Aβ42 with familial mutations. *Proceedings of the National Academy of Sciences* **115**, E5849-E5858 (2018). https://doi.org:10.1073/pnas.1803539115

16   Elkins, M. R. *et al.* Structural Polymorphism of Alzheimer's β-Amyloid Fibrils as Controlled by an E22 Switch: A Solid-State NMR Study. (2016).

17   Yoo, B. K., Xiao, Y., McElheny, D. & Ishii, Y. E22G Pathogenic Mutation of β-Amyloid (Aβ) Enhances Misfolding of Aβ40 by Unexpected Prion-like Cross Talk between Aβ42 and Aβ40. *Journal of the American Chemical Society* **140**, 2781-2784 (2018). https://doi.org:10.1021/jacs.7b13660

18   Yang, Y. *et al.* Cryo-EM structures of amyloid-β filaments with the Arctic mutation (E22G) from human and mouse brains. (2023).

19   Bennett, A. E., Griffin, R. G. & Vega, S. in *Solid-State NMR IV Methods and Applications of Solid-State NMR*   (ed Bernhard Blümich) 1-77 (Springer Berlin Heidelberg, 1994).

20   Griffin, R. Dipolar recoupling in MAS spectra of biological solids. *Nature Structural Biology* **5**, 508-512 (1998). https://doi.org:10.1038/749

21   Ji, Y., Liang, L., Bao, X. & Hou, G. Recent progress in dipolar recoupling techniques under fast MAS in solid-state NMR spectroscopy. *Solid State Nuclear Magnetic Resonance* **112**, 101711 (2021). https://doi.org:https://doi.org/10.1016/j.ssnmr.2020.101711

22   Su, Y., Andreas, L. & Griffin, R. G. Magic Angle Spinning NMR of Proteins: High-Frequency Dynamic Nuclear Polarization and 1H Detection. *Annual Review of Biochemistry* **84**, 465-497 (2015). https://doi.org:10.1146/annurev-biochem-060614-034206

23   Colvin, M. T. *et al.* Atomic Resolution Structure of Monomorphic Aβ42 Amyloid Fibrils. *Journal of the American Chemical Society* **138**, 9663-9674 (2016). https://doi.org:10.1021/jacs.6b05129

24   Lührs, T. *et al.* 3D structure of Alzheimer's amyloid-β(1–42) fibrils. *Proceedings of the National Academy of Sciences* **102**, 17342-17347 (2005). https://doi.org:10.1073/pnas.0506723102

25   Wälti, M. A. *et al.* Atomic-resolution structure of a disease-relevant Aβ(1–42) amyloid fibril. *Proceedings of the National Academy of Sciences* **113**, E4976-E4984 (2016). https://doi.org:10.1073/pnas.1600749113

26 Xiao, Y. *et al.* Aβ(1–42) fibril structure illuminates self-recognition and replication of amyloid in Alzheimer's disease. *Nature Structural & Molecular Biology* **22**, 499-505 (2015). https://doi.org:10.1038/nsmb.2991

27 Gremer, L. A.-O. *et al.* Fibril structure of amyloid-β(1-42) by cryo-electron microscopy.

28 Kollmer, M. *et al.* Cryo-EM structure and polymorphism of Aβ amyloid fibrils purified from Alzheimer's brain tissue. *Nature Communications* **10**, 4760 (2019). https://doi.org:10.1038/s41467-019-12683-8

29 Le Marchand, T. *et al.* 1H-Detected Biomolecular NMR under Fast Magic-Angle Spinning. *Chemical Reviews* **122**, 9943-10018 (2022). https://doi.org:10.1021/acs.chemrev.1c00918

30 Andreas, L. B. *et al.* Structure of fully protonated proteins by proton-detected magic-angle spinning NMR. *Proceedings of the National Academy of Sciences* **113**, 9187-9192 (2016). https://doi.org:10.1073/pnas.1602248113

31 Loquet, A. *et al.* 3D structure determination of amyloid fibrils using solid-state NMR spectroscopy. *Methods* **138**, 26-38 (2018).

32 Stanek, J. *et al.* NMR spectroscopic assignment of backbone and side-chain protons in fully protonated proteins: microcrystals, sedimented assemblies, and amyloid fibrils. *Angewandte Chemie International Edition* **55**, 15504-15509 (2016).

33 Struppe, J. *et al.* Expanding the horizons for structural analysis of fully protonated protein assemblies by NMR spectroscopy at MAS frequencies above 100 kHz. (2017).

34 Linser, R. *et al.* Proton-Detected Solid-State NMR Spectroscopy of Fibrillar and Membrane Proteins. *Angewandte Chemie International Edition* **50**, 4508-4512 (2011). https://doi.org:https://doi.org/10.1002/anie.201008244

35 Stanek, J. *et al.* NMR Spectroscopic Assignment of Backbone and Side-Chain Protons in Fully Protonated Proteins: Microcrystals, Sedimented Assemblies, and Amyloid Fibrils. *Angewandte Chemie International Edition* **55**, 15504-15509 (2016). https://doi.org:https://doi.org/10.1002/anie.201607084

36 Barbet-Massin, E. *et al.* Rapid Proton-Detected NMR Assignment for Proteins with Fast Magic Angle Spinning. *Journal of the American Chemical Society* **136**, 12489-12497 (2014). https://doi.org:10.1021/ja507382j

37 Agarwal, V. *et al.* De Novo 3D Structure Determination from Sub-milligram Protein Samples by Solid-State 100 kHz MAS NMR Spectroscopy. *Angewandte Chemie International Edition* **53**, 12253-12256 (2014). https://doi.org:https://doi.org/10.1002/anie.201405730

38 Bennett, A. E., Griffin, R. G., Ok, J. H. & Vega, S. Chemical shift correlation spectroscopy in rotating solids: Radio frequency-driven dipolar recoupling and longitudinal exchange. *The Journal of Chemical Physics* **96**, 8624-8627 (1992). https://doi.org:10.1063/1.462267

39 Bennett, A. E. *et al.* Homonuclear radio frequency-driven recoupling in rotating solids. *The Journal of Chemical Physics* **108**, 9463-9479 (1998). https://doi.org:10.1063/1.476420

40   Gullion, T. & Vega, S. A simple magic angle spinning NMR experiment for the dephasing of rotational echoes of dipolar coupled homonuclear spin pairs. *Chemical Physics Letters* **194**, 423-428 (1992). https://doi.org:https://doi.org/10.1016/0009-2614(92)86076-T

41   Eddy, M. T., Yu, T.-Y., Wagner, G. & Griffin, R. G. Structural characterization of the human membrane protein VDAC2 in lipid bilayers by MAS NMR. *Journal of Biomolecular NMR* **73**, 451-460 (2019). https://doi.org:10.1007/s10858-019-00242-8

42   Silvers, R. *et al.* Aggregation and Fibril Structure of AβM01–42 and Aβ1–42. *Biochemistry* **56**, 4850-4859 (2017). https://doi.org:10.1021/acs.biochem.7b00729

43   Andreas, L. B. *et al.* Structure and Mechanism of the Influenza A M218–60 Dimer of Dimers. *Journal of the American Chemical Society* **137**, 14877-14886 (2015). https://doi.org:10.1021/jacs.5b04802

44   Roos, M., Mandala, V. S. & Hong, M. Determination of Long-Range Distances by Fast Magic-Angle-Spinning Radiofrequency-Driven 19F–19F Dipolar Recoupling NMR. *The Journal of Physical Chemistry B* **122**, 9302-9313 (2018). https://doi.org:10.1021/acs.jpcb.8b06878

45   Bayro, M. J., R., R., M., C., T., E. M. & Griffin, R. G. Radio frequency-driven recoupling at high magic-angle spinning frequencies: homonuclear recoupling sans heteronuclear decoupling. (2008).

46   Bahri, S. *et al.* 1H detection and dynamic nuclear polarization–enhanced NMR of Aβ1-42 fibrils. *Proceedings of the National Academy of Sciences* **119**, e2114413119 (2022). https://doi.org:10.1073/pnas.2114413119

47   Wickramasinghe, A. *et al.* Sensitivity-Enhanced Solid-State NMR Detection of Structural Differences and Unique Polymorphs in Pico- to Nanomolar Amounts of Brain-Derived and Synthetic 42-Residue Amyloid-β Fibrils. *Journal of the American Chemical Society* **143**, 11462-11472 (2021). https://doi.org:10.1021/jacs.1c03346

48   Balbirnie, M., Grothe, R. & Eisenberg, D. S. An amyloid-forming peptide from the yeast prion Sup35 reveals a dehydrated β-sheet structure for amyloid. *Proceedings of the National Academy of Sciences* **98**, 2375-2380 (2001). https://doi.org:10.1073/pnas.041617698

49   van der Wel, P. C. A., Lewandowski, J. R. & Griffin, R. G. Solid-State NMR Study of Amyloid Nanocrystals and Fibrils Formed by the Peptide GNNQQNY from Yeast Prion Protein Sup35p. *Journal of the American Chemical Society* **129**, 5117-5130 (2007). https://doi.org:10.1021/ja068633m

50   Kaar, W. *et al.* Refolding of Npro fusion proteins. *Biotechnology and Bioengineering* **104**, 774-784 (2009). https://doi.org:https://doi.org/10.1002/bit.22432

51   Thacker, D. *et al.* The role of fibril structure and surface hydrophobicity in secondary nucleation of amyloid fibrils. *Proceedings of the National Academy of Sciences* **117**, 25272-25283 (2020). https://doi.org:10.1073/pnas.2002956117

52   Linse, S. *et al.* Kinetic fingerprints differentiate the mechanisms of action of anti-Aβ antibodies. *Nature Structural & Molecular Biology* **27**, 1125-1133 (2020). https://doi.org:10.1038/s41594-020-0505-6

53   Lundqvist, M., Rodriguez Camargo, D. C., Bernfur, K., Chia, S. & Linse, S. Expression, purification and characterisation of large quantities of recombinant human IAPP for mechanistic studies. *Biophysical Chemistry* **269**, 106511 (2021). https://doi.org:https://doi.org/10.1016/j.bpc.2020.106511

54   Zhong, X. *et al.* Amyloid Fibril Formation of Arctic Amyloid-β 1–42 Peptide is Efficiently Inhibited by the BRICHOS Domain. *ACS Chemical Biology* **17**, 2201-2211 (2022). https://doi.org:10.1021/acschembio.2c00344

55   Lewandowski, J. R., Sein, J., Blackledge, M. & Emsley, L. Anisotropic Collective Motion Contributes to Nuclear Spin Relaxation in Crystalline Proteins. *Journal of the American Chemical Society* **132**, 1246-1248 (2010). https://doi.org:10.1021/ja907067j

56   Shaka, A. J., Keeler, J., Frenkiel, T. & Freeman, R. An improved sequence for broadband decoupling: WALTZ-16. *Journal of Magnetic Resonance (1969)* **52**, 335-338 (1983). https://doi.org:https://doi.org/10.1016/0022-2364(83)90207-X

57   Zhou, D. H. & Rienstra, C. M. High-performance solvent suppression for proton detected solid-state NMR. *Journal of Magnetic Resonance* **192**, 167-172 (2008). https://doi.org:https://doi.org/10.1016/j.jmr.2008.01.012

58   van der Wel, P. C. A., Hu, K.-N., Lewandowski, J. & Griffin, R. G. Dynamic Nuclear Polarization of Amyloidogenic Peptide Nanocrystals: GNNQQNY, a Core Segment of the Yeast Prion Protein Sup35p. *Journal of the American Chemical Society* **128**, 10840-10846 (2006). https://doi.org:10.1021/ja0626685

59   van der Wel, P. C. A., Lewandowski, J. R. & Griffin, R. G. Structural Characterization of GNNQQNY Amyloid Fibrils by Magic Angle Spinning NMR. *Biochemistry* **49**, 9457-9469 (2010). https://doi.org:10.1021/bi100077x

60   Nelson, R. *et al.* Structure of the cross-beta spine of amyloid-like fibrils. (2005).

61   Sawaya, M. R. *et al.* Atomic structures of amyloid cross-beta spines reveal varied steric zippers. (2007).

62   Ishii, Y. 13C–13C dipolar recoupling under very fast magic angle spinning in solid-state nuclear magnetic resonance: Applications to distance measurements, spectral assignments, and high-throughput secondary-structure determination. *The Journal of Chemical Physics* **114**, 8473-8483 (2001). https://doi.org:10.1063/1.1359445

63   Colvin, M. T. *et al.* High resolution structural characterization of Aβ42 amyloid fibrils by magic angle spinning NMR. *Journal of the American Chemical Society* (2015).

64   Wang, S. *et al.* Nano-Mole Scale Side-Chain Signal Assignment by 1H-Detected Protein Solid-State NMR by Ultra-Fast Magic-Angle Spinning and Stereo-Array Isotope Labeling. *PLOS ONE* **10**, e0122714 (2015). https://doi.org:10.1371/journal.pone.0122714

65   Paluch, P. *et al.* NMR Assignment of Methyl Groups in Immobilized Proteins Using Multiple-Bond (13)C Homonuclear Transfers, Proton Detection, and Very Fast MAS. (2022).

66   Nishiyama, Y., Malon, M., Ishii, Y. & Ramamoorthy, A. 3D ^{15}N/^{15}N/^{1}H chemical shift correlation experiment utilizing an RFDR-based ^{1}H/^{1}H mixing period at 100 kHz MAS. (2014).

67   Baldus, M. & Meier, B. H. Total Correlation Spectroscopy in the Solid State. The Use of Scalar Couplings to Determine the Through-Bond Connectivity. *Journal of Magnetic Resonance, Series A* **121**, 65-69 (1996). https://doi.org:https://doi.org/10.1006/jmra.1996.0137

Chapter 5 : High Aspect Ratio Diamond Nanosecond Laser Machining

Adapted from Golota, N.C[†]. Preiss, D[†]., Fredin, Z.P., Patil, P., Banks, D.P., Bahri, S. Griffin, R.G., Gershenfeld, N. High Aspect Ratio Diamond Nanosecond Laser Machining. *Submitted to Applied Physics A, Materials Science & Processing.* [†]These authors contributed equally.

5.1 Introduction

Diamond is a promising material for next generation quantum devices, micro-electromechanical systems (MEMS), biocompatible microfluidic and spectroscopic devices, and thermally optimized micro and power electronics[1-6]. Its superior material strength, thermal conductivity, high electrical resistivity, and highly transparent optical characteristics make it the ideal material for such applications. Decades of research and development have resulted in cost effective methods of producing synthetic single crystal diamond using either chemical vapor deposition (CVD) or high-pressure high temperature (HPHT) methods [7,8]. However, conventional machining processes are typically ineffective against the extreme hardness of diamond. In contrast, pulsed laser machining methods have become the standard for fabrication of diamond microstructures and devices.

During laser machining of diamond, material removal is achieved through a phase change from diamond to graphite, followed by vaporization and expulsion of carbon-based species from the workpiece. Under nanosecond machining, laser irradiation is absorbed as thermal energy following thermal transfers and equilibration between electrons and the lattice within the laser pulse duration. The absorbed thermal

energy drives the diamond to graphite phase transition, and continued laser irradiation promotes the vaporization of graphite from the machined surface [9-12]. However, the ejection of graphite and other carbon-based vapors interferes with the laser beam, generating a plasma plume that considerably attenuates the incident irradiation, which is particularly detrimental to the energy intensive fabrication of high aspect ratio holes [12]. In contrast, when the pulse length is less than ~ 1 ps, ablation occurs through multi-photon absorption processes at wavelengths above 225 nm, which represents a threshold for the energy of a single photon to exceed the wide bandgap of diamond [9-11,13-15]. This mechanism offers the advantage of reduced heat affected zones and microcracking in the ablated material [13,14]. Although ultrafast lasers offer the potential of reduced laser induced damage in diamond, nanosecond lasers are significantly more accessible with considerably lower cost/watt compared to ultrafast lasers.

While the body of literature supporting nanosecond machining in diamond is extensive, there have been fewer investigations into achieving high aspect ratios in diamond at nanosecond time scales [16-24]. Aspect ratios between 12-15:1 are most commonly reported in diamond, with the highest achieved aspect ratio being 500:1 using a Bessel function focused beam and femtosecond laser [25-28].

This chapter begins by describing the thermal model of laser ablation and gaussian beam propagation principles. A complete description of the achievable aspect ratio via percussion hole drilling and rotary stage assisted drilling follows. We characterize the effect of pulse energy and machining profile on the aspect ratio and taper, and report ~40:1 average aspect ratio holes in diamond. Finally, we characterize the induced strain as a measure of laser induced damage during nanosecond

machining of 10:1 aspect ratio tubes. We observe a reduction in tensile strain following heat treatment at 600°C for 24 hrs. Overall, we present a method of achieving high aspect ratios with a commercially available nanosecond laser machining system. This represents an accessible way of fabricating diamond structures for microelectronics, biomedical sensing, and nuclear magnetic resonance [29,30]

5.2 Pulsed Laser Ablation

At 532 nm the photon energy is 2.33 eV, whereas the bandgap energy of diamond is 5.47 eV. Accordingly, multiphoton absorption is required for direct excitation of electrons within the diamond crystal to drive laser ablation. Under ultrashort laser machining, the photon density is much higher than in nanosecond machining, and multiphoton absorption is the dominant mechanism of ablation. Under nanosecond laser machining, thermally derived ablation is thought to be the dominant mechanism of rapid material removal, given sufficiently high absorption coefficient[31].

The source term can be broken into two fundamental components, where $\vec{S}$ is the Poynting vector describing the energy flux of an electromagnetic field via laser irradiation and $U(z,t)$ effectively describes internal heat sinks due to phase transformations within the material.

$$Q(z,t) = -\nabla\langle\vec{S}\rangle + U(z,t)$$
(5-1)

We now will use electromagnetic principles to determine the energy flux or Poynting vector from an incident laser beam [32]. The Poynting vector describes the energy density times the velocity of the wave and is written in terms of the electric and magnetic fields in (5-2).

$$\langle \vec{S} \rangle = \frac{c \langle \vec{E} \times \vec{H} \rangle}{4\pi} \tag{5-2}$$

We can write the electric and magnetic field expression for a plane wave propagating in the direction as:

$$\vec{E}(z,t) = \widehat{E_0} e^{i(kz - \omega t)}$$

$$\vec{B}(z,t) = \widehat{B_0} e^{i(kz - \omega t)} \tag{5-3}$$

For a transverse wave, $(E_0)_z = (B_0)_z = 0$ since the electric and magnetic fields are perpendicular to the propagation direction. Using Faraday's law, we can write the magnetic field complex amplitude as:

$$\vec{B}_0 = \frac{k}{\omega} (\hat{z} \cdot \widehat{E_0}) \tag{5-4}$$

Since the electric and magnetic fields are in phase and perpendicular, the real amplitude is given by:

$$B_0 = \frac{k}{\omega} E_0 = \frac{1}{c} E_0 \tag{5-5}$$

We can compute the energy density of an electromagnetic plane wave using the relation $B^2 = \frac{1}{c} E^2 = \mu_0 \epsilon_0 E^2$, where μ_0 is the magnetic permeability and ϵ_0 is the electric permittivity.

$$u = \frac{1}{2} \left(\epsilon_0 E^2 + \frac{1}{\mu_0} B^2 \right) = \epsilon_0 E^2 \tag{5-6}$$

For a monochromatic plane wave propagating in the z direction:

$$\vec{S} = cu\hat{z} = c\epsilon_0 E^2 \cos^2(kz - \omega t + \delta)\,\hat{z} \tag{5-7}$$

The average power per unit area transported via an electromagnetic wave propagating in the z direction is given by $\langle \vec{S} \rangle$, and is referred to as the intensity, I and is given by:

$$\langle \vec{S} \rangle = \frac{1}{2} c \epsilon_0 E^2 \hat{z} = I \hat{z}$$

(5-8)

The gradient of the Poynting vector is related to the spatial derivative of the intensity, where α is the absorption coefficient of the material.

$$-\nabla \langle \vec{S} \rangle = \frac{dI(z)}{dz} = -\alpha I(z)$$

(5-9)

For a Gaussian beam, the energy density is described as a function of the laser intensity, $I(t)$, the surface transmission, 1-R, and the material absorption coefficient, α along the direction of propagation in 1 dimension.

$$S = I_0 (1 - R) \alpha e^{-\alpha z}$$

(5-10)

In summary, we have derived the source of energy density that is used to drive thermal effects in laser machining from fundamental electromagnetic principles. We will now use these relations to describe the thermodynamic effects of the incident irradiation. Photon-matter interaction upon incident laser irradiation can be described by the one-dimensional, two temperature diffusion model [53]. In this model, the temperature of the electron subsystem is given by T_e and the temperature of the lattice subsystem is given by T_i. While this argument is generally taken for the ablation of metals, the derivation is instructive for understanding the basis for thermal ablation under nanosecond pulses.

$$C_e \frac{\partial T_e}{\partial t} = -\frac{\partial Q(z)}{\partial z} - \gamma (T_e - T_i) + S$$

(5-11)

Where C_e is the electron subsystem heat capacity, $Q(z)$ is the heat flux in the z direction taken perpendicular to the machining surface, S is the laser source heating term, and γ is the electron-lattice coupling constant.

The interaction between the lattice and electrons can be re-written in terms of the heat capacity of the lattice and the temperature differential between the two subsystems:

$$C_i \frac{\partial T_i}{\partial t} = -\gamma(T_e - T_i) \qquad (5\text{-}12)$$

The heat flux is related to the electron thermal conductivity and electron temperature gradient along the irradiation axis.

$$Q(z) = -k_e \frac{\partial T_e}{\partial z} \qquad (5\text{-}13)$$

The duration of the laser pulse, τ_L, must be considered in relation to the electron cooling time, τ_e, and the lattice heating time τ_i. The electron cooling time is given by C_e/γ, while the lattice heating time is given by C_i/γ. Typically, $\tau_e \ll \tau_i$. In the case of nanosecond pulses, $\tau_L \gg \tau_e$, allowing for equilibration between the electron and lattice subsystems, where $T = T_e = T_i$. Typically, the electronic specific heat capacity is much smaller than that of the lattice and can be neglected. Now we can substitute this equality and substitute equations (5-12) through (5-10) into (5-11) to obtain:

$$C_i \frac{\partial T}{\partial t} = \frac{\partial}{\partial z}\left(\kappa \frac{\partial T}{\partial z}\right) + I_0(1 - R)\alpha e^{-\alpha z} \qquad (5\text{-}14)$$

In (5-14), the change in temperature of the system is dependent on the heat capacity of the lattice, and is equal to the net thermal change within the system, dependent on the lattice thermal conductivity, κ, and thermal energy supplied by the source term.

The thermal diffusivity, D, is given by and is a measure of a materials ability to conduct vs. store thermal energy.

$$D = \frac{\kappa}{\rho C_p}$$
(5-15)

The thermal diffusivity is related to the thermal diffusion length, where τ_L is the pulse length.

$$l_T = 2(D\tau_L)^{1/2}$$
(5-16)

For diamond, using the simplified 1-dimensional heat equation, the thermal diffusivity length is ~ 9.5 µm for a single pulse. The thermal diffusivity of single crystal diamond is on the order of 5-10 cm^2/s [33-35]. This simplified equation applies only for a point source in space and is highly dependent on the boundary conditions of the system, resulting in considerable variation from (5-16). The thermal diffusivity length indicates the importance of multiple pulse effects and thermal conductivity in laser machining.

Following the description of the 1-D heat equation using the source term provided by the laser, we will now turn to examining the effect of phase changes that occur only when the threshold fluence of material is exceeded. In effect, the phase transformations required for ablation represent a thermal sink, requiring additional source energy to be overcome beyond achieving the threshold laser absorption. For a constant pressure thermodynamic process, the relevant quantities are the enthalpies of fusion, ΔH_{fus}, better known as melting, and heat of vaporization, ΔH_v or in the case of direct sublimation, $\Delta H_{sub} = \Delta H_{fus} + \Delta H_v$.

For common laser machining materials (e.g. polymers or metals), the enthalpies of fusion are on the order of 10-50 kJ/mol while the enthalpies of vaporization are considerably higher at 200-450 kJ/mol [31]. In the case of diamond, the high stability of the diamond crystal lattice requires considerably higher enthalpies of fusion, on the order of 120 kJ/mol and even higher enthalpies of vaporization and sublimation, resulting in higher typical threshold fluences and difficulty in machining. High threshold fluences are also influenced by the low absorption coefficient of diamond. The change in internal energy due to phase change, $U(z,t)$, within a volume element, dV, becomes non zero once the ablation threshold is reached via thermal absorption:

$$\Delta U(z, t)dV \approx \vec{v}_{fus}\Delta H_{fus}dF_{fus} + \vec{v}_{vap}\Delta H_{vap}dF_{vap} \tag{5-17}$$

Where $\vec{v}$ and dF are the velocity and surface element of the liquid-solid or liquid-gas interface within dV. We can then compute the total enthalpy of the machining process as:

$$\Delta H(T) \sim \int_{T(\infty)}^{T} \rho(T')C_p(\text{T}')dT' + (T - T_{fus})\Delta H_{fus} + (T - T_{vap})\Delta H_{vap} \tag{5-18}$$

In (5-18) we have made several simplifications to obtain an approximate enthalpy required for diamond laser machining. The first term describes the energy density required to heat the material sufficiently to promote phase change. The second and third terms are zero if $T < T_{fus}$ or $T < T_{vap}$. In the event of temperatures greater than such threshold temperatures, these terms describe the additional energy required for either fusion (e.g. melting) or vaporization.

Under ambient conditions (~21% oxygen in air), the phase transition proceeds via two largely simultaneous events given sufficient incident energy density. The
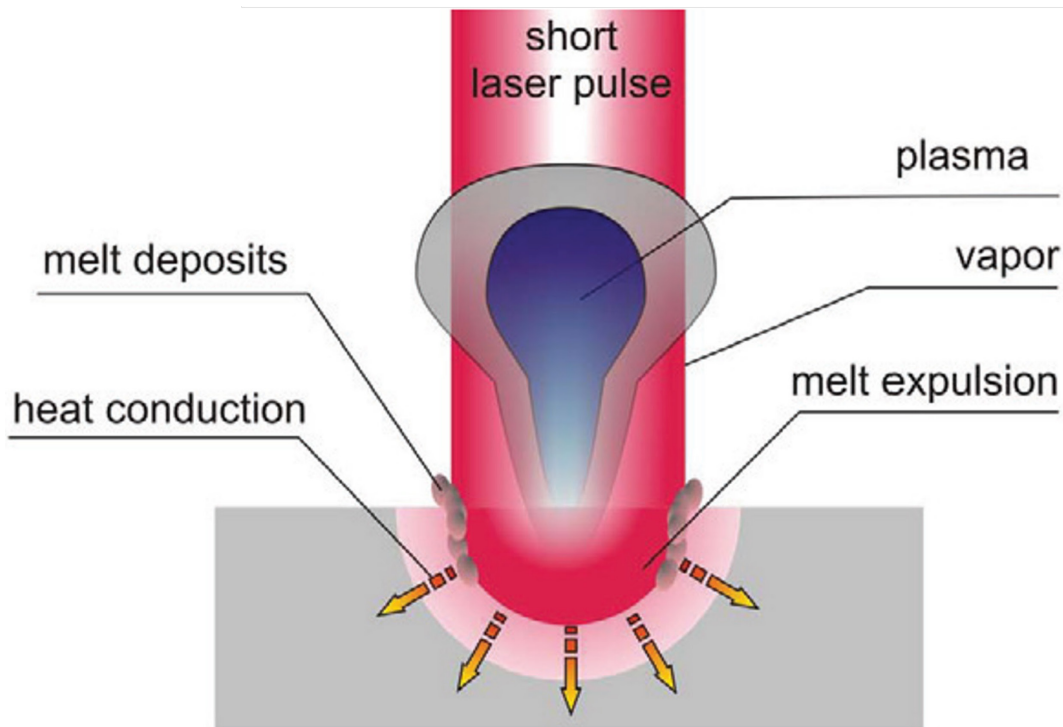
Figure 5.1. Schematic of laser ablation. During laser machining, the incident nanosecond pulsed laser beam results in thermally driven laser ablation. The incident energy is absorbed as heat in the diamond sample and generates melt, vapors and plasma during the phase transformation from diamond to graphite and subsequent vaporization and oxidation of graphite. Figure 5.1 adapted with permission from Chen et. al. Copyright The Authors, some rights reserved; exclusive licensee Light Publishing Group. Distributed under a Creative Commons Attribution License 3.0 (CC BY) https://creativecommons.org/licenses/by/4.0/

transition of the sp^3 diamond can proceed to sp^2 graphite, either crystalline or amorphous, at temperatures above 700°C, but is more prominently observed at temperatures above 1300 °C. The thickness of the graphite layer formed under such conditions has been shown to be proportional to the thermal diffusion length and pulse width, which indicates that graphite formation is driven by thermal effects [55-61].The phase transition and subsequent oxidation of graphite and amorphous carbon is described by (5-19).

$$C(sp^3) \longrightarrow C(sp^2) \quad \Delta H_1$$

$$2C(sp^2) + \frac{3}{2}O_2(g) \longrightarrow CO(g) + CO_2(g) \quad \Delta H_2 \qquad (5\text{-}19)$$
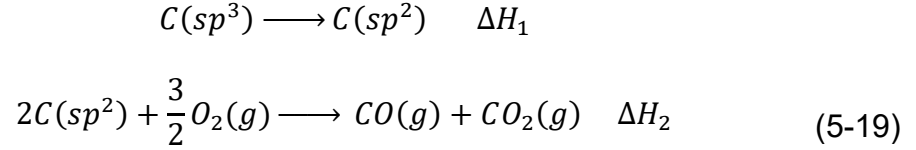
Where $\Delta H_2 \gg \Delta H_1$. We note this is a simplified thermodynamic approach, and rigorous treatment would require involvement of $C_2(g)$ and $C(g)$ species. This is beyond the scope of the present thesis. Overall, nanosecond laser ablation of diamond proceeds by thermal heating, melt formation, boiling, and vaporization of graphite and amorphous carbon species.

5.3 Gaussian Beam Propagation

A laser source with a gaussian output mode can be largely described by the wavelength and the beam waist. The 532 nm DPSS Q-switched Nd:YAG laser used has a Gaussian TEM_{00} mode and the spot size was found to be 14.1±0.8 μm, as described in Section 4.5. Herein, we present the relevant parameters of Gaussian beam propagation including the Rayleigh Length, propagation of the beam waist, wavefront curvature, and Guoy phase.

The Rayleigh length is the distance along the direction of beam propagation at which the beam radius is increased by $\sqrt{2}$. The Rayleigh length is given by (5-20) in terms of the beam waist, w_0, the wavelength, λ, and the refractive index of the propagation medium, n. In free space (n=1), the Rayleigh length of the Oxford laser system is 290 μm.

$$z_R = \frac{\pi w_0^2 n}{\lambda} \qquad (5\text{-}20)$$

The beam waist as a function of propagation distance, *w(z)*, is given by (5-21) and plotted in Figure 1.

$$w(z) = w_0 \sqrt{1 + \left(\frac{z}{z_R}\right)^2} \tag{5-21}$$

The minimum diffraction limited laser beam divergence angle in radians, θ_0, is given by the far-field value in (5-22).

$$\theta_0 = M^2 \frac{\lambda}{\pi \, w_0} \tag{5-22}$$

The divergence angle of the Oxford laser is ~ 1.38°, where M^2 describes the beam quality and is < 1.2 for the laser system used. Overall, a very tightly focused beam diverges more rapidly than a less focused beam containing lower energy density.
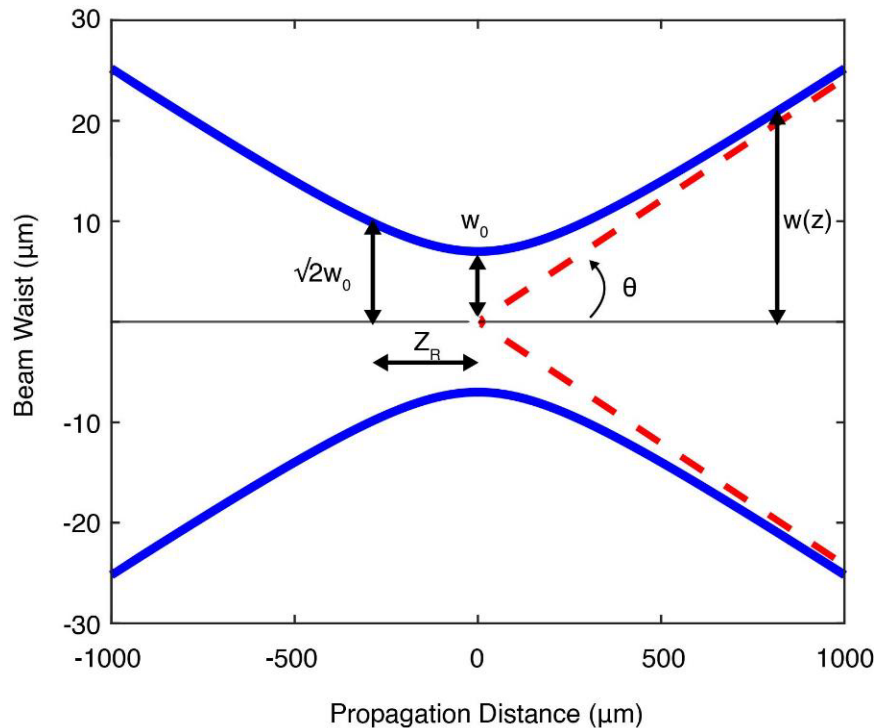
Figure 5.2. Beam width of a propagating Gaussian beam. The spot size is plotted as a function of the beam propagation distance in µm. The beam begins to linearly diverge after 1 Rayleigh length. The divergence angle is shown in dashed red.

The wavefront curvature, *R(z),* is another key parameter of gaussian beam propagation. A wavefront is defined as the surface composed of in phase points of a waveform. The wavefront shape is always spherical in nature and the beam propagates perpendicular to the wavefront. The radius of curvature for a gaussian beam in fundamental TEM mode is given by (5-23).

$$R(z) = z \left[1 + \left(\frac{z_R}{z} \right)^2 \right]$$

(5-23)

Finally, the Gouy phase, *ψ(z)*, describes the phase accumulated by a beam near the focal region of the beam, given in (5-24). This serves as a correction factor representing an increase in the effective wavelength at the focal point.

$$\psi(z) = arctan \left(\frac{z}{z_R} \right)$$

(5-24)

As discussed previously, the intensity of laser irradiation can be computed using fundamental electromagnetic quantities. The electric field amplitude of a Gaussian beam is given by (5-25):

$$E(r,z) = E_0 \frac{w_0}{w(z)} exp \left(- \frac{r^2}{w(z)^2} \right) exp \left(-i \left(kz + k \frac{r^2}{2R(z)} - \psi(z) \right) \right)$$

(5-25)

Where *r* is the radial distance from the center of the beam, *R(z)* is the radius of curvature of the beam, w_0 is minimum beam waist, and *w(z)* is the beam waist at a distance *z*. The beam waist is defined as the radius at which the beam intensity is $1/e^2$ the axial value along the propagation direction. The electric field amplitude at the focus point (*r=0, z=0*) is given by E_0. The Guoy phase is denoted by $\psi(z)$. This relation holds

when the beam is not strongly divergent and $w_0 \gg \lambda/n$. In (5-25), k is used to denote the wavenumber.

The power density or irradiance of a gaussian beam (W/m^2) focused using a thin lens is given by:

$$I(r) = I_0 \exp\left(\frac{-2r}{w}\right)^2 \tag{5-26}$$

The intensity of the beam is plotted as a function of the radial distance and propagation distance. The total power contained in the laser beam is defined as:

$$P = 2\pi \int_0^\infty r\, I_0 \exp\left(-\frac{2r}{w}\right)^2 dr = \frac{\pi w_0^2 I_0}{2} \tag{5-27}$$
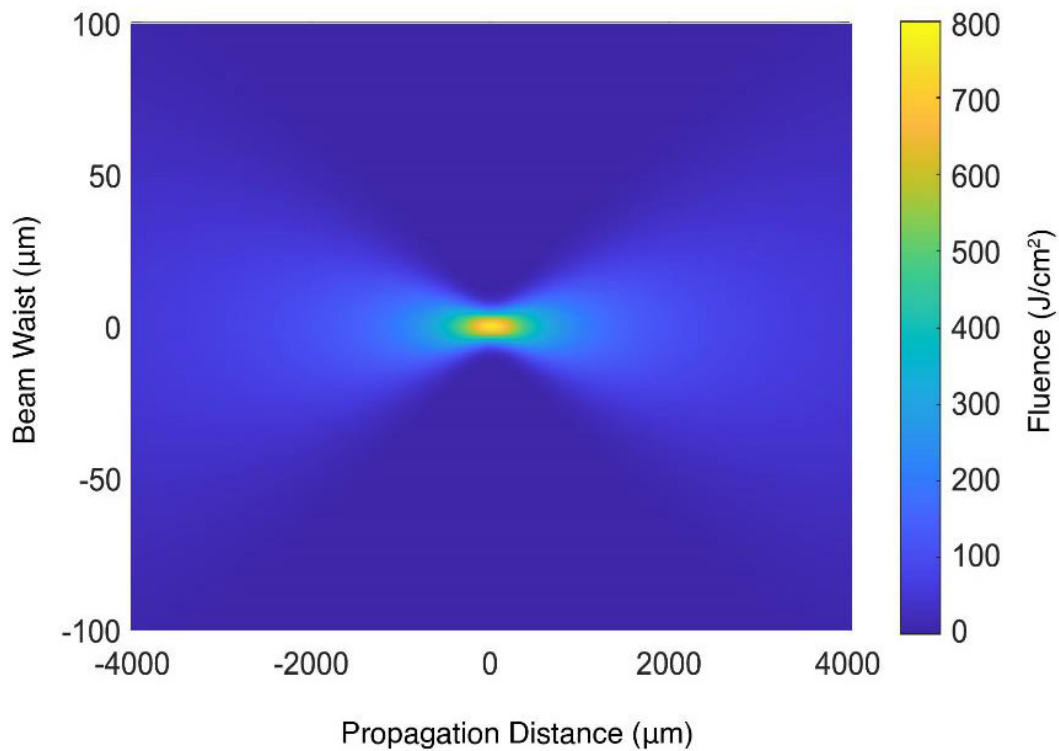
Figure 5.3 Fluence Distribution in the xz plane. The fluence is plotted as a function of propagation distance and resultant beam waist.

202

We can re-write Equation (5-26) using (5-27). The peak power density is given by (5-28) and is maximized when the beam waist is focused at the minimum spot size, occurring when r=0.

$$I(r) = \frac{2P}{\pi w_0^2} \exp\left(\frac{-2r}{w}\right)^2 \tag{5-28}$$

The laser peak power, P, is computed using (5-30), where τ_p is the pulse duration, in this case 20 ns. At 5 kHz repetition rate, f_p, for a 2.97 W average power, the peak power is 29.7 kW.

$$P = \frac{P_{avg}}{f_p \tau_p} \tag{5-29}$$

The single pulse energy of a laser can be calculated below, in units typically of μJ.

$$E_p = \frac{P_{avg}}{f_p} \tag{5-30}$$

Laser ablation will occur when the applied fluence, Φ, is greater than the threshold fluence of the material, Φ_{Th}. The fluence represents an energy density and is computed in J/cm^2 using (5-31).

$$\Phi = \frac{2 E_p}{\pi w_0^2} \tag{5-31}$$

Based on gaussian beam optics, we can determine the propagation length of the beam that has sufficient energy density for laser ablation of diamond to occur. The fluence as a function of the propagation distance and beam waist is shown in Figure 5.3.

We can additionally compute the maximum beam waist that has sufficient energy density for ablation to occur, w_{Th}, at a given single pulse energy. This is computed using (5-21) and (5-31).

$$w_{Th} = \sqrt{\frac{2\,E_p}{\pi\Phi_{Th}}}$$ (5-32)

We can then compute a machining depth with sufficient energy density for laser ablation to occur as

$$z_{th} = \sqrt{z_R^2\left(\left(\frac{w(z)}{w_0}\right)^2 - 1\right)}$$ (5-33)

For the maximum single pulse energy of 592 µJ, the maximum beam waist is 55 µm and the maximum machining depth is ~ 2 mm for a given negative focus depth, not considering the considerable attenuation of the laser beam due to the ejected debris, carbon vapors and plasma.

5.4 Experimental

5.4.1 Diamond Material

Type Ib HPHT diamond with four-point 100 crystal orientation was obtained from Element6 (Didcot, Oxfordshire, UK), crystal orientation is described in Figure 5.4. For the percussion hole drilling the material was 1.1 ×1.1 × 3 mm. For other samples, the material was 1.6 ×1.6 × 4 mm. The absorption coefficient and optical penetration depth of type 1b HPHT was determined using the same material, but with sample dimension of 10 × 10 × 1.1 mm. A 3D-printed sample cuvette was used to hold the sample during
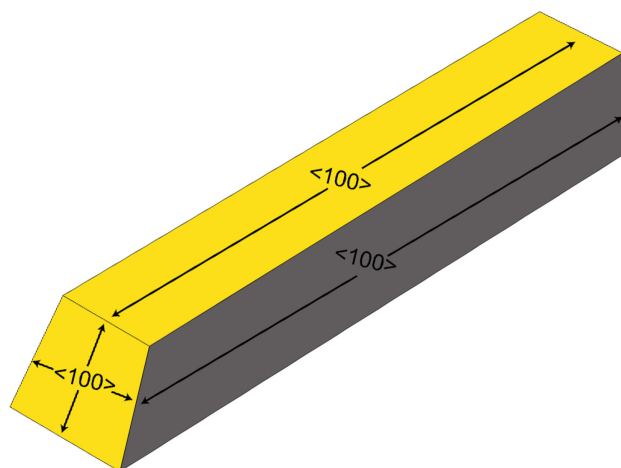
Figure 5.4. Crystal orientation of HPHT material. The starting material used in all samples has <100> four-point orientation on all faces.

UV/VIS/NIR transmission measurement using a Perkin Elmer Lambda 1050 UV/VIS spectrophotometer.

5.4.2 Laser System

Samples were fabricated using an Oxford Lasers (Didcot, Oxfordshire, UK) A-series laser micromachining system equipped with a Q-switched 532 nm diode-pumped Nd:YAG laser with a spot size of 13-14 μm. The pulse duration was ~ 20 ns at a repetition rate of 5 kHz with a maximum average power of 2.97 W. Motion control in X and Y axes is achieved with a linear motor with linear encoding for a resolution of 0.25 μm and accuracy of ±2 μm. Motion control along the beam propagation axis, Z, is achieved with a servomotor drive system that has a resolution of 0.5 μm and accuracy of ±6 μm. Complete description of laser system is given in Figure 5.5.
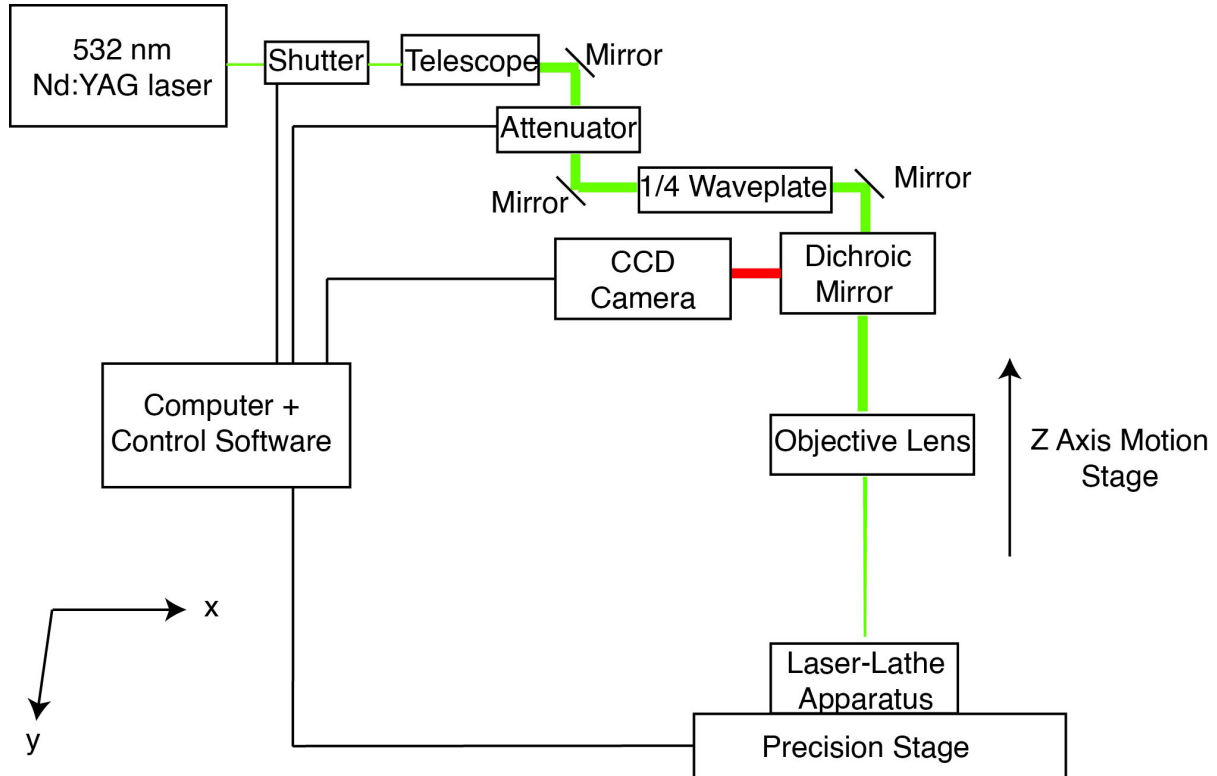
Figure 5.5. Laser system block diagram. A 532 nm Q-switch diode-pumped-solid-state Nd:YAG laser operating at a maximum average power of 3 W with a 5 kHz repetition rate was used. The laser beam is expanded to 10 mm prior to the objective lens which focuses the beam to a 10 μm spot size over a focal length of 100 mm. The focus of the beam incident onto a machining part is controlled through a precision servomotor drive system with a linear motor with resolution of 0.25 μm and accuracy of ±2 μm. The workpiece is fixtured onto a homebuilt laser-lathe and is manipulated in the x,y directions using a high precision stage. Finally, an on-axis CCD camera equipped with a laser-cross hair alignment aid is used to confirm workpiece alignment, laser position and machining progress.

5.4.3 Percussion Holes and Ablation Threshold

Percussion hole drilling was performed with the diamond fixtured as shown in

Figure 5.11 (E,F) with single pulse energies ranging from 6.8 to 594 μm. The diameter

and depth of percussion holes was determined using a Rigaku CT Lab HX130 (Toykyo,

Japan) microCT scanner at 2.1 μm voxel size. Analysis was performed using ImageJ by

compiling 3 adjacent radiographic slices and computing the average projection [36]. Hole diameters were then determined using a plotted profile from ImageJ and analyzed in MATLAB to determine the hole size measured at a constant gray-value to ensure uniformity of measurement.

5.4.4 Holes with Aspect Ratio ~ 40:1

An in-house fabricated precision rotary drilling apparatus was used with a Thorlabs (Newton, NJ, USA) DDR100 direct drive rotary stage to achieve rotational frequency up to 2.76 Hz (166 RPM) during laser drilling, shown in Figure 5.11. Focus, power, inner diameter, and feed rate were modulated using g-code written in Python and executed by Cimita control software. The high-aspect ratio holes were machined using a linear stage added in series with the rotary stage to translate the diamond stock while maintaining laser position relative to the center of rotation of the diamond material. The center of rotation was identified by taking a long exposure coaxial photograph, which allowed accurate positioning of the laser. During machining, initial radial passes at 250 µJ pulse energy traversed from the center of rotation of the diamond stock to the desired target radius at a feed rate of 10 µm /s and were repeated 10 times at both 0 and 250 µm of negative focus for a total of 140,000 equivalent pulses. In this case, negative focus is defined as a translation of the focal plane of the laser beam into the material. This was repeated with finishing passes of 400 µJ pulses, a feed rate of 5 µm/s and 25 µm depth increments of negative focus to a depth of 250 µm for a total of 1,540,000 equivalent pulses. During both machining cycles, the rotation rate was fixed at 66.6 RPM. The number of machining cycles investigated were 1, 2, and 3. Samples

were characterized using a Rigaku CT Lab HX130 (Tokyo, Japan) with voxel sizes of 5.7 µm and a Hitachi FlexSEM1000 SEM (Tokyo, Japan) following sputter coating of 100 nm of gold onto the surface.

5.4.5 Rotary assisted drilling of 10:1 aspect ratio tubes

Diamond rods were first fabricated using a single pulse energy of 296 µJ and a feed rate of 5 µm /s in lathe orientation shown in Figure 5.11 (A, B). This was followed by a finishing pass at a feed rate of 1 µm/s at a single pulse energy of 236 µJ in which roughly 10 µm of material was removed from the diameter achieving average outer diameter of 500 µm with typical combined outer diameter eccentricity and taper of less than 6 µm over the 3 mm rod. Inner diameters were machined by rotating the entire laser lathe apparatus, as shown in Figure 5.11 (C, D) with the laser beam incident upon the top flat surface of the rod. The inner diameter was machined using a roughing cut in which a radial line of 150 µm was machined while the sample was rotating at 166 RPM and repeated 10 times at a feed rate of 50 µm/s with the focus negatively incremented (focus advanced into the sample) by 250 µm at a time to a maximum depth of 4 mm, resulting in application of 224,000 equivalent pulses. This was followed by a finishing pass in which a 50 µm line was traced with the endpoint being aligned with the desired inner diameter, again at a feed rate of 50 µm /s and with focus negatively incremented by 25 µm to a maximum depth of 4 mm for a total of 2.24 M equivalent pulses. The total machining time per inner diameter was ~ 90 minutes. Samples were characterized using a Hitachi FlexSEM1000 SEM (Tokyo, Japan) and taper was analyzed using SEM micrographs in Autodesk Inventor (San Rafael, CA, USA). 3-dimensional images of 10:1

aspect ratio tubes were acquired using a 20x objective on a VK-X250 laser scanning confocal microscope (Osaka, Japan), which was also used for surface roughness calculation. Data analysis of confocal microscope images was performed using the Keyence MultiFileAnalyzer software package. Surface roughness was measured over the entire 3 mm sample length and ~25 µm in width at the vertex of the inner diameter.

5.4.6 Strain Measurement

Internal strain mapping was performed using a WITec alpha300 apryon Confocal Raman spectrometer (Ulm, Germany) at 532 nm using a 50× object with a numerical aperture of 0.8 and irradiation power of 15 mW to avoid surface graphitization upon irradiation. Typical scan resolution was 0.5 µm in width and 1 µm in depth, limited by the specified sampling scheme rather than the optical diffraction limit to reduce acquisition time. The spectral resolution was maximized using an 1800 g/mm grating and the observed spectral stability and resolution of the ~1332 cm^{-1} Raman shift was ±0.01 cm^{-1}. The linear relationship between Raman shift and strain was 360 MPa/cm^{-1}, as previously determined [37,38]. For each strain measurement, 3 locations were profiled, and 300 pixels were accumulated per location with an integration time of 0.2 s. Each reported strain is the average of these 3 locations for a total of 900 pixel accumulations. No significant differences were observed in the Raman spectra as a function of location. Between each sample strain measurement, the Raman shift of the reference diamond corresponding to unmachined surface of the specific sample being studied and was used to account for any spectrometer instabilities. The Raman shift distribution in the sample was determined using a Lorentzian fit in WITec Project

software. Highly ordered pyrolytic graphite (HOPG) ZYB quality was purchased and used without modification from Ted Pella (Redding, CA, USA) as a graphite standard. Samples were then subjected to 24 hours of heat treatment at 600°C in air and atmospheric pressure (~100 kPa) in a tabletop oven. After 24 hours the samples were allowed to cool to room temperature over ~2-4-hour duration. Sample mass was taken before and after heat treatment. The Raman measurements were then repeated as described above.

5.5 Results and Discussion

For a given number of pulses, increasing the pulse energy increased the observed hole depth and diameter, as shown in Figure 5.6(B) for 5,000 laser pulses. The ablation thresholds for multiple pulse numbers were determined by the linear relation in Equation (5-34), where D is the hole diameter, $2w_0$ is the spot size, E_p is the single pulse energy, and E_{TH} is the single pulse ablation threshold energy.

$$D^2 = 2\ \omega_0^2 ln\frac{E_p}{E_{TH}} \tag{5-34}$$

We observed distinct strong and gentle ablation regimes in HPHT diamond, as shown in Figure 5.6(B) and Figure 5.17. While two distinct ablation regimes are most observed during ultrafast machining processes; they have been observed with nanosecond machining, including in diamond [21,39,40]. Gentle ablation proceeds when the single pulse energy is below ~ 125 μJ and in this regime the spot size of the laser was determined to be 14.1± 0.8 μm. The gentle ablation threshold was determined
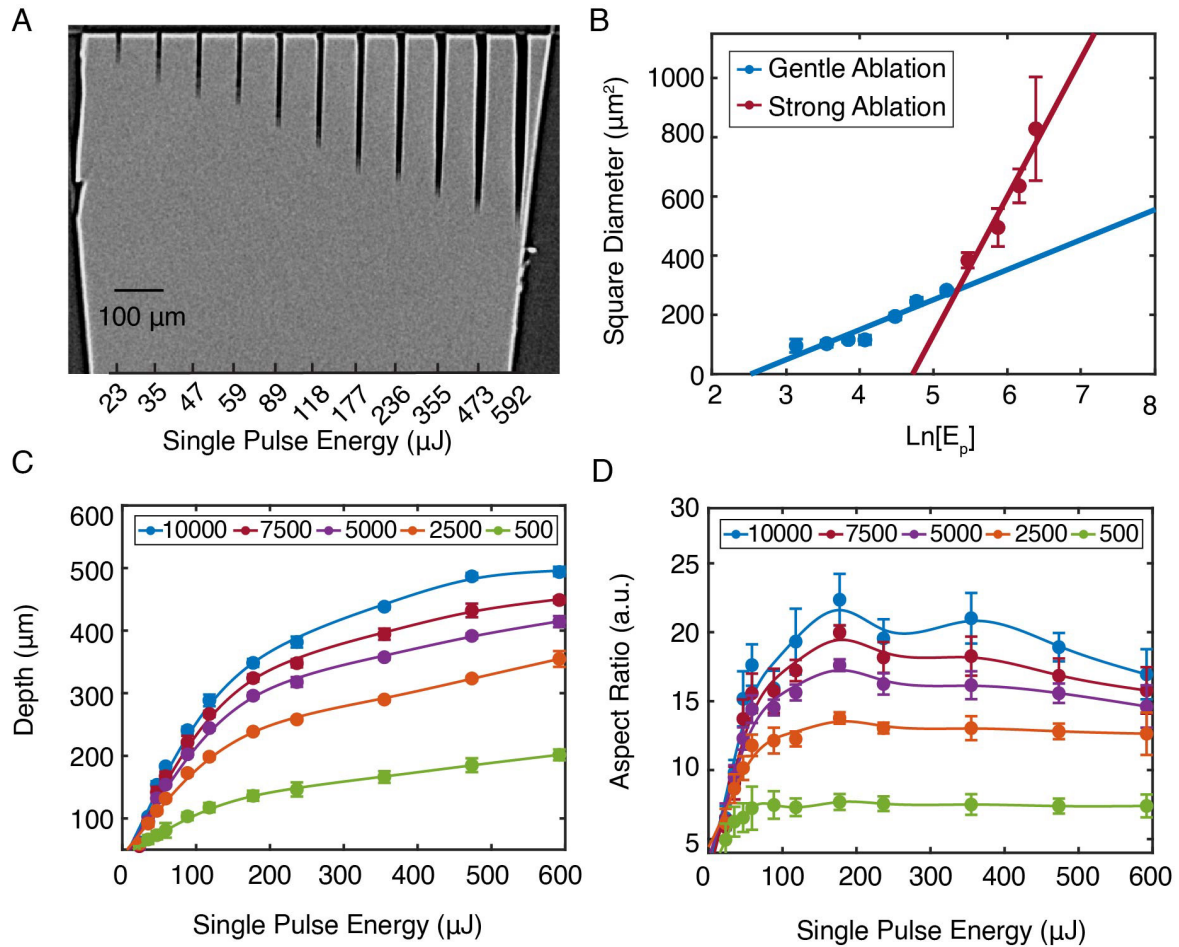
Figure 5.6. Percussion hole drilling. (A). MicroCT radiograph showing the effect of pulse energy on the diameter and depth of the ablated percussion hole. (B). Distinct gentle and strong ablation regimes were observed during percussion hole drilling, shown for 5,000 pulses. (C). The achievable depth as a function of single pulse energy and number of laser pulses. (D). The aspect ratio was calculated using the depth and percussion hole diameter as a function of laser pulses and single pulse energy.

to be subject to incubation effects, with an incubation coefficient of 0.919 ± 0.008 as determined by Equation (5-35), where N is the number of pulses, Φ_N is the multiple pulse ablation threshold, and Φ_1 is the single pulse ablation threshold.

$$\ln[N \cdot \Phi_N] = S \ln[N] + \ln[\Phi_1] \qquad (5\text{-}35)$$

An incubation coefficient < 1 indicates that the ablation threshold decreases with multiple pulses due to accumulation of laser induced damage regions that more strongly absorb laser irradiation. Incubation effects are expected in diamond, given the starting material is largely transparent with initial absorption driven only by crystal inclusions and defects.

Accordingly, for 10,000 pulses the ablation threshold fluence was 12.4 ± 1.4 J/cm^2 which increased to 17 ± 3.3 J/cm^2 for 500 pulses, and a single pulse threshold fluence was determined to be 29.5 ± 1.3 J/cm^2. The multiple pulse ablation thresholds are within literature values for nanosecond machining of single crystal diamond, particularly for HPHT diamond which has a higher ablation threshold than CVD diamond [21,41,42]. The low absorption coefficient of HPHT diamond and thermodynamic stability of diamond contribute to the large threshold fluences.

The strong ablation regime began between 127-162 J/cm^2 and without the observation of incubation effects. In this regime, we observed 3-7 μm eccentricities in hole diameter between the x and y radiograph cross sections, which resulted in variability in average hole size. The decrease in circularity of percussion holes at higher pulse energies has been observed previously [43]. The higher energy pulses may drive a more rapid expulsion of graphite leading to a larger relative increase in hole diameter, evidenced by the steeper observed slope in Figure 5.6(B) and Figure 5.17

The maximum depth of percussion hole drilling achieved was 493.6 ± 6.4 μm using a single pulse energy of 592 μJ and 10,000 laser pulses. Within the gentle

A

79.8 μm   31.6 μm   29.7 μm

77.9 μm   33.4 μm   31.6 μm

79.7 μm   29.7 μm   24.1 μm

1600 μm

B

MIT CBA 20.0kV x750 SE   50.0μm

C

MIT CBA 20.0kV x750 SE   50.0μm
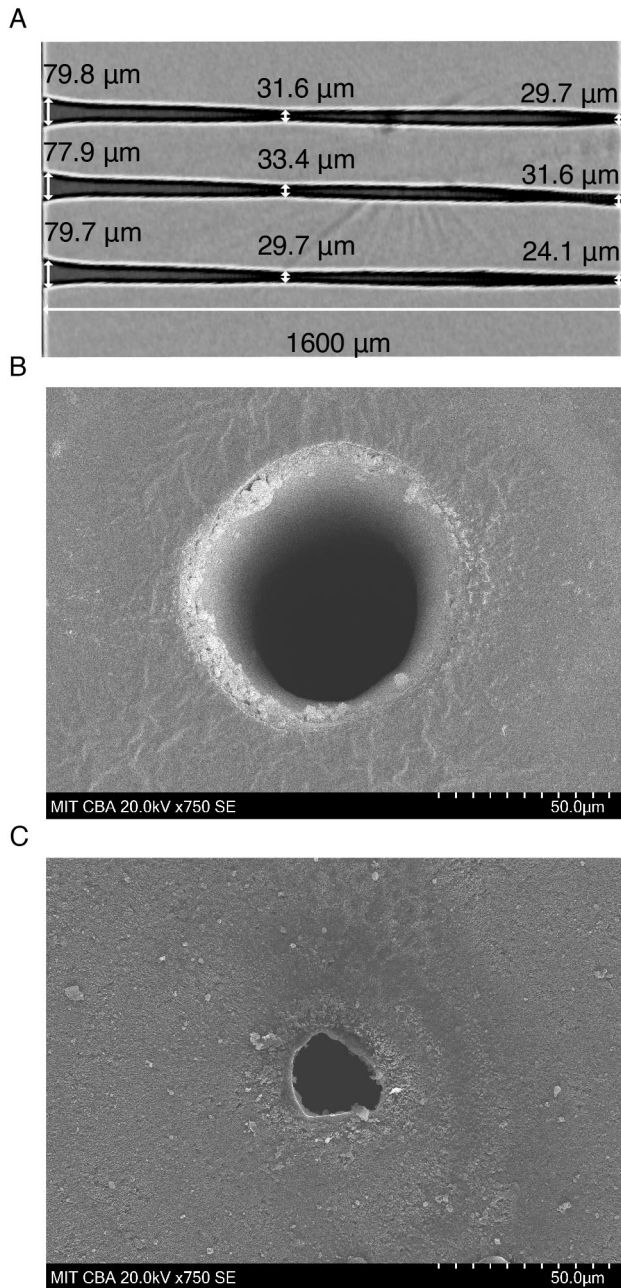
Figure 5.7. Average 40:1 aspect ratio holes in diamond. (A). MicroCT cross section showing three holes fabricated with rotary assisted drilled to a negative focus of 250 μm through 1.6 mm of HPHT diamond. From bottom to top the number of machining cycle repetitions was increased from 1 to 3. (B). The SEM of the entrance hole shows evidence of chamfer at the top of the hole. (C). SEM of exit of the bottom hole, shows the expulsion pattern, reduced circularity, and evidence of internal taper.

ablation regime, the hole depth increased rapidly with single pulse energy for a given number of laser pulses, Figure 5.6(C). However, in the strong ablation regime, the additional depth provided by higher energy pulses was reduced in magnitude relative to the gentle ablation regime.

The maximum achievable aspect ratio was 22.4 ± 1.8 using 10,000 pulses at a single pulse energy of 177 μJ and is shown in Figure 5.6(D). At higher powers, the increase in hole diameter dominated the nominal gain in depth resulting in lower aspect ratios when > 5000 pulses were used. As the pulse number decreased, the aspect ratio plateaued at ~ 12 and 7 for 2,500 and 500 pulses at pulse energies above ~ 75 μJ, respectively. Overall, the results of percussion hole drilling

213

demonstrate distinct gentle and strong ablation regimes. The maximum aspect ratios are obtained below the highest pulse energies applied, while maximum depths are achieved at highest pulse energies and pulse accumulations.

Higher aspect ratios of up to 66:1 were achieved using a rotary assisted drilling while the beam focus was advanced into the workpiece, as shown in Figure 5.11(E, F). In this case, negative focus is defined as a translation of the focal plane of the laser beam into the material. Large equivalent pulse numbers were used to achieve the high aspect ratio holes, with 140,000 and 1,540,000 pulses for rough or finishing machining cycles, respectively. The equivalent pulse number was computed as $2w_0 f / v$, where f is the laser repetition rate and v is the traverse rate. The average aspect ratio achieved was 42.5, 38.6 and 39.3, respectively, where the number of machining cycle repetitions was increased from 1 to 3. The largely unchanging aspect ratio with number of machining cycle repetitions indicates pulse saturation was achieved. The formation of a chamfer feature at the entrance hole resulted in minimum aspect ratios of 20.1, 20.5, and 20.1, with chamfer geometry dependent on negative focus depth, Figure 5.20(A, B). The exit hole was undersized, with corresponding aspect ratios of 66.4, 50.6 and 53.9 for 1 to 3 machining cycle repetitions. The non-uniform hole geometry and reduction in exit hole circularity, shown in Figure 5.7(C), is related to the complex dynamics of material vaporization, melt and debris expulsion. As machining progresses, the absorptive losses increase within vaporized graphite and plasma, reducing the effective energy density and ablation efficiency resulting in the hourglass shape of the hole. Finally, occlusion of the diverging laser beam at depths far exceeding the Rayleigh length of the laser beam results in the formation of chamfer and overall taper of ~ 0.9°.

The far field divergence angle of the gaussian beam is 1.38°. Overall, we demonstrate

use of high accumulated pulse numbers to achieve, to our knowledge, the highest

aspect ratios in diamond using nanosecond laser machining to date.

While aspect ratios up to 66.4:1 were achieved, the inner diameter was non-

uniform, tapered, and with poor circularity. While micro-hole arrays have potential uses

in microfluidics and for thermal management, the fabrication of micro-tubes has
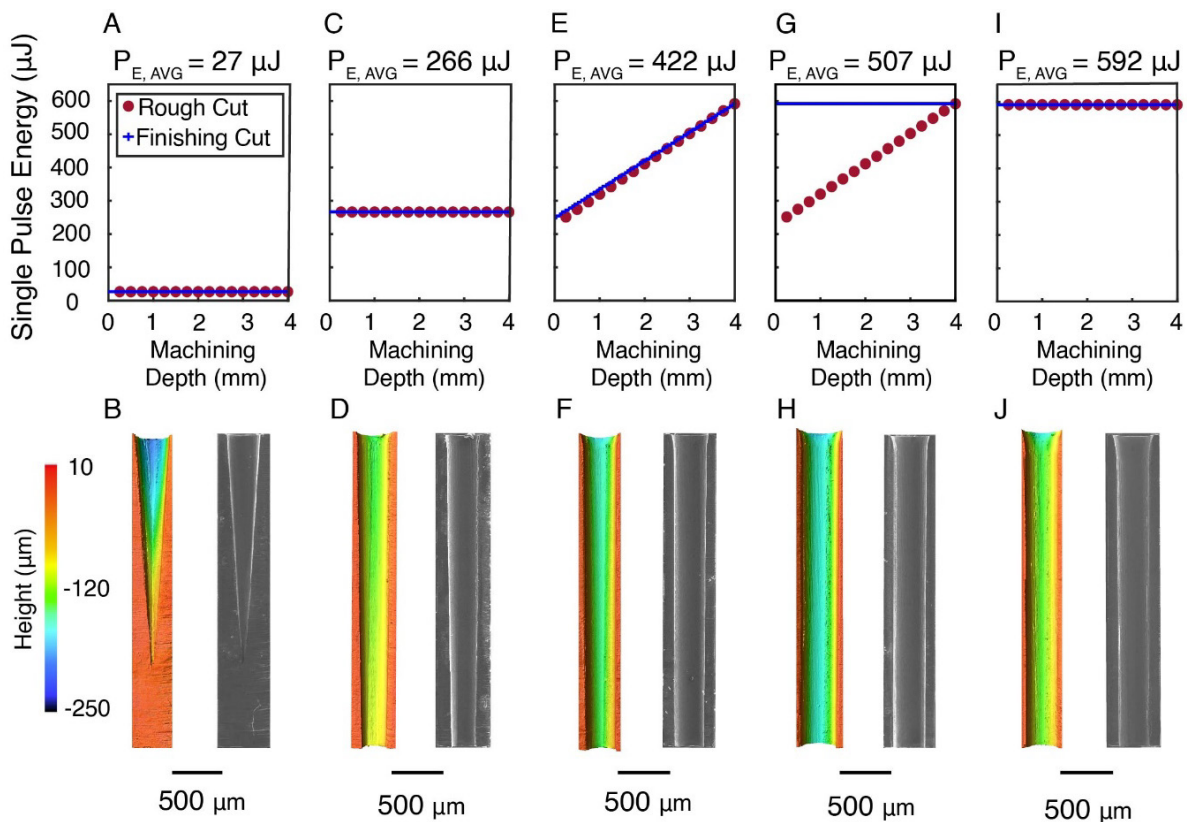
Figure 5.8. 10:1 Aspect Ratio Machining. Top panels show the machining profile used. The single pulse energy was either held constant while the machining focus was negatively incremented down the machining depth (A-C, D) or ramped (E, G) during initial rough cuts or final finishing cuts. The bottom panels show the laser confocal scanning microscope images of the inner surface of a cross section of the 10:1 aspect ratio tube. SEM images are provided to show the entire structure, uncropped images provided in supplementary information.

additional applications in biocompatible devices and for magnetic resonance sample holders, as we demonstrate in a forthcoming publication. For the latter application, diamond sample holding tubes are pneumatically driven to rotational rates exceeding 7 $\times$ 10^6 RPM [29,30] As such, we aimed to minimize internal taper angle by varying the irradiation profile for a constant target aspect ratio of 10:1, as shown in Figure 5.8 and described previously. The impact of the machining profiles on the chamfer angle, overall taper, taper excluding chamfer, and entrance diameter is provided in Figure 5.9. Three samples were machined with a constant single pulse energy (Figure 5.8, A, C, I). A constant single pulse energy of 27 µJ, nearly 3x the gentle ablation threshold, was insufficient to promote thermal ablation throughout the entire 3 mm thick diamond, with a resulting ~4° internal taper along the maximum depth machined of ~2.1 mm, as shown in Figure 5.8 (A, B) and Figure 5.9. At all higher single pulse energies, the inner diameter was machined throughout the entire 3 mm sample. In all samples, the single pulse energy was linearly correlated with the chamfer angle and the entrance diameter. Maximum chamfer angles up to 16.8° and entrance diameters ~100 µm greater than the target diameter were observed with constant, high-energy finishing passes at 592 µJ. The length of the chamfer is roughly 100-200 µm and is formed by the diverging beam's expanded beam waist having sufficient energy to induce ablation. We note, while machining the inner diameter 1 mm beyond the target inner diameter length aids in taper also increases chamfer angle.

While chamfer was positively correlated with pulse energy, minimization of taper angle was generally achieved with high average pulse energies, as shown in Figure 5.9. The lowest overall taper angles of 0.80° and 0.72° were achieved using ramped pulse

energy machining with average pulse energies of 422 or 507 µJ, shown in Figure 5.8

(E, F). However, at a pulse energy of 592 µJ, roughly 5x the strong ablation threshold,

the overall taper increased to 0.95°, comparable to the sample machined with a

constant pulse energy of 226 µJ or that of the 40:1 aspect ratio holes. At such pulse

energy, the constant application of laser irradiation with a beam waist of up to 55 µm

containing sufficient energy density to generate ablation results in the observed chamfer

formation that dominates the overall taper of the hole.

When considering the inner diameter taper angle excluding chamfer, the use of

high pulse energy finishing passes results in taper angles between 0.11 and 0.17°. We

conclude the effect of high pulse energy is on the dynamics of debris and vapor ejection
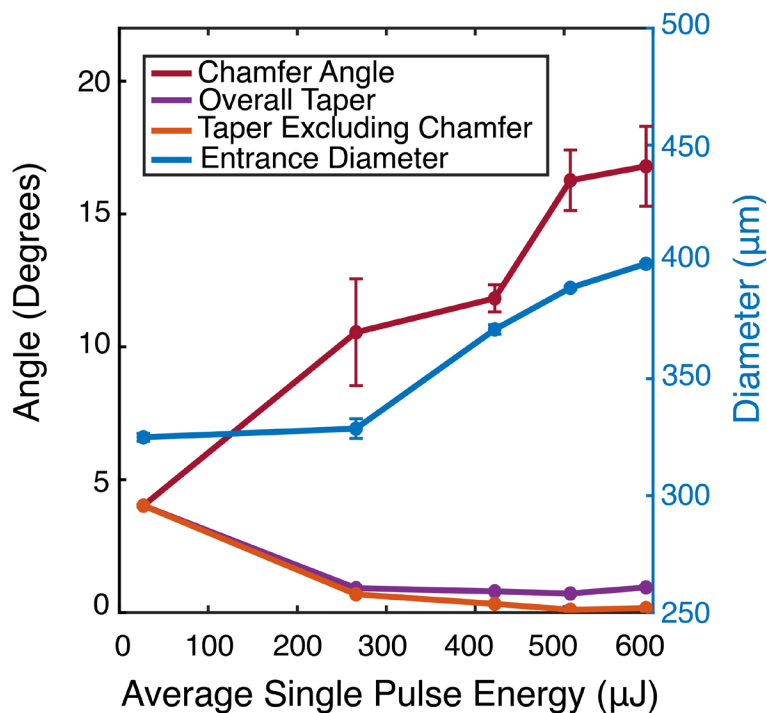
Figure 5.9. Characteristics of 10:1 Aspect ratio structures. The effect of average single pulse energy on the chamfer angle, overall taper, taper excluding chamfer and the entrance diameter is determined. At high average single pulse energies, taper can be reduced, however, up to ~17° of chamfer occurs, corresponding to nearly a 100 µm increase in the entrance hole diameter.

217

from the machined hole. When the energy density is ramped toward higher fluence at the base of the hole, a greater fraction of ablated material is removed from the bottom of the hole and reduces beam attenuation, as reported in the literature [44]. In contrast, at lower pulse energies the upward material removal fraction is dominant, with debris, vapor, and plasma strongly attenuating the incident irradiation. Additionally, the use of high-power pulses may further reduce particulate size, resulting in higher ejection velocities and reduced taper. The development of tunable chamfer may be advantageous for many applications. However, when chamfer is detrimental this region can be removed during processing, leaving a structure with very low internal taper below the beam divergence angle.

While use of high pulse energies aided in the fabrication of low internal taper 10:1 aspect ratio tubes, high energy nanosecond laser machining can result in large heat affected zones with associated laser induced damage. Confocal Raman spectroscopy is an accepted method of mapping the internal strain in CVD diamond, in addition to characterizing the effects of laser machining [12,20,37,38,45-47]. In this study, confocal Raman spectroscopy was applied to characterize the effects of the laser machining process including the formation of graphite and amorphous carbon and generation of laser induced strain. The ablation mechanism was confirmed by the presence of surface localized graphite, in addition to generation of amorphous carbon, shown in Figure 5.24. From Raman images, the surface graphite layer was found to be 1-2 μm thick.

Raman strain mapping was performed on all 10:1 aspect ratio tube cross sections and unmachined reference samples from the corresponding starting material.

The starting material had been previously laser cut into trapezoidal logs, and Raman mapping was performed on the first 15 µm of unmachined surface. The linear relationship between Raman shift and strain was 360 MPa/cm^{-1}, as previously determined [37,38].As shown in Figure 5.10, reference samples without in-house machining had tensile strains ranging from -34 to -51 MPa. In these samples, areas of lowest strain were found within the first 1-2 µm of the surface, depicted in Figure 5.25. Further below the surface, greater magnitudes of tensile strain were observed, but was homogeneously distributed, as indicated in Figure 5.10 and Figure 5.25. The observed tensile strain indicates an increase in effective bond length relative to the ideal diamond crystal lattice. The baseline strain is attributed to two factors: (1) the presence of defects and P1 center inclusions within the stock material and (2) prior exposure to unknown levels of laser irradiation during stock material processing by Element6.

In all machined samples, laser ablation resulted in a broadened strain distribution, particularly within the first 2.5 µm of the surface relative to reference samples. For samples machined with average single pulse energies of 27, 266 and 422 µJ, less than a 5% net increase in strain was observed. This represents an increase in tensile strain of ~ 3 MPa, which is on the order of the stability of the spectrometer across measurements. However, when 592 µJ finishing passes with ~ 2.2 M equivalent laser pulses were used, we observed a resultant 16-36% increase in induced strain. This corresponds to a total tensile strain of 48 and 55.4 MPa. In these two samples, the accumulated exposure to high energy laser irradiation and prolonged thermal treatment resulted in additional elongation of the carbon-carbon bonds in the crystal lattice.
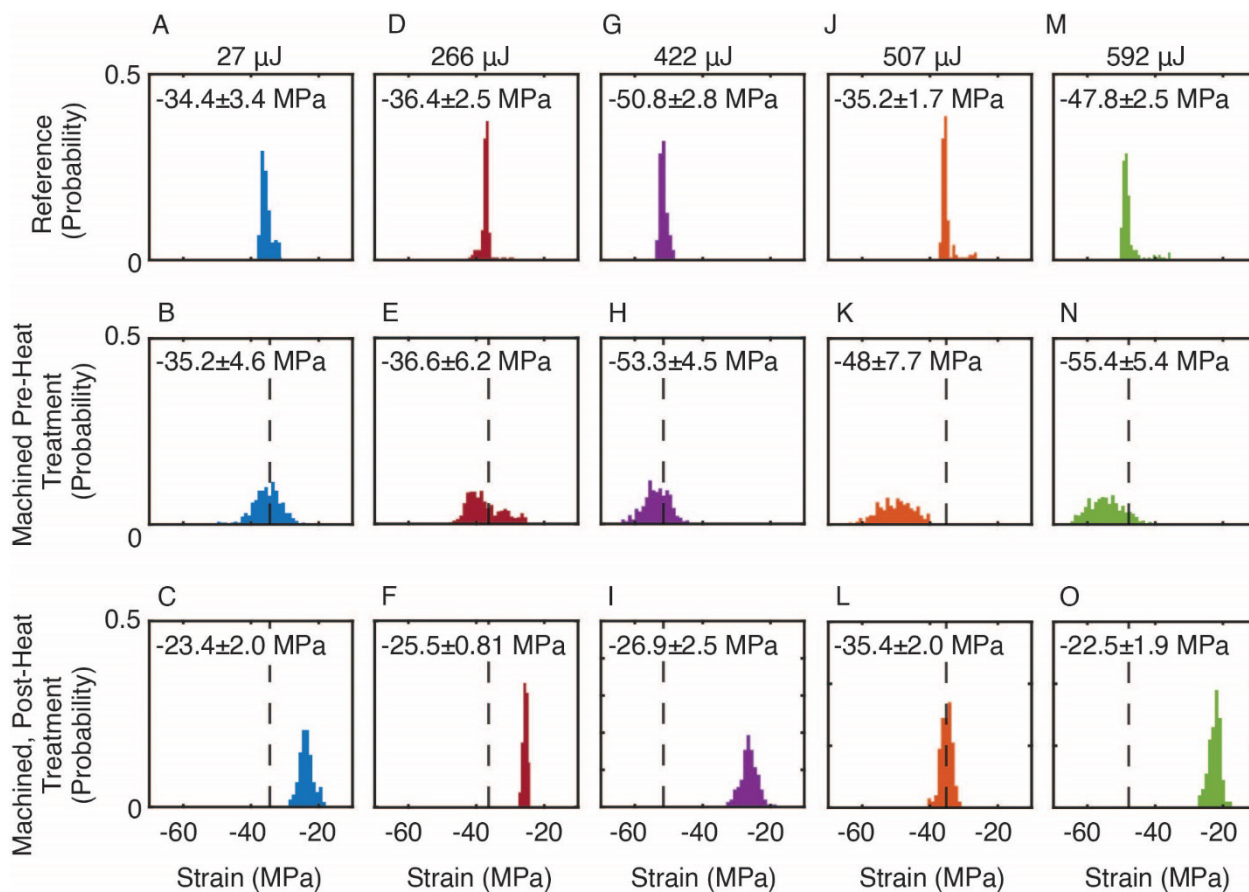
Figure 5.10. Laser machining induced strain in single crystal diamond. The effect of laser machining on internal strain in the diamond crystal was determined using confocal Raman spectroscopy. In the top panel, reference sections from the 10:1 aspect ratio tube and unmachined by the Oxford laser were used as a standard sample. All standard samples showed tensile strains between ~35-51 MPa in magnitude with narrow strain distributions within a sample. In the middle panels, samples were studied through the first 15 µm of material and the distribution of internal strain computed. The dashed line corresponds to the average strain in the reference sample. The bottom panel shows the same machined samples following 24 hours of heat treatment at 600° C. In all cases the strain induced by laser machining is comparable or reduced to that in the reference sample.

Following laser machining, samples were subjected to oxidative heat treatment at atmospheric pressure for 24 hours to remove graphite from the surface of the material. At temperatures above 700°C and ambient pressure, diamond can begin to burn and form graphite, as such, the temperature was maintained at 600°C [48-50]. Representative samples were weighed before and after heat treatment with typical

mass changes on the order of ±2%. Raman spectroscopy was repeated and in all cases a reduction in total strain was observed, including in reference samples. Typical reduction in strain for reference samples following heat treatment was ~ 32%. A 26-59% percent reduction of strain in machined samples following heat treatment was uncorrelated with the machining power applied. The laser induced broadened strain distributions was observed to be reversible, as evidenced by the comparable standard deviation in strain measurement for all samples following heat treatment, provided in Figure 5.10 and Table 5.5. For additional Raman images and detailed strain changes in all samples, we refer the reader to the supporting information.

High temperature (> 1700 °C) annealing using either high pressure (> 50 kBar) or low pressures (< 0.4 Bar) in diamond has been previously found to reduce strain and modify defects such as nitrogen vacancy centers in diamond [51-55]. In these cases, strain was relieved via vacancy diffusion and crystal lattice defect rearrangement that reduces non equilibrium bond distances within the lattice. In the case of heat treatment up to 800° C in nanodiamonds, strain release has been observed, however, this was concurrent with crystal volume loss and surface graphitization via surface etching [56]. A twofold mechanism was proposed in which the strained, surface exposed crystal was graphitized, and the interior lattice structure was homogenized by defect annihilation. In a recent study, low temperature annealing up to 500°C reported reduction in radiation stains of natural diamond via reduction in interstitial carbon vacancy complexes at lower activation energies than nitrogen vacancies [57].

In the present study, we did not observe heat treatment induced graphitization of any samples or crystal volume loss. We hypothesize the thermal energy supplied was

sufficient to aid in the dispersal of unstable impurities, such as metal catalyst inclusions, that led to more homogeneous and slightly decreased strains, of low initial magnitude. In HPHT/LPHT annealing, changes in strain are often on the order of a few gigapascals, indicating much larger changes to the diamond crystal lattice. While Raman spectra show no evidence of graphitization, we cannot fully exclude graphitization of the surface and thermal etching as the mechanism of strain reduction. Further study should also include electron paramagnetic resonance (EPR) studies to determine if charge transfer or transformation of defect states derived from P1 center (C-center) substitutions has occurred.

5.6 Conclusion

In conclusion, we have characterized the effect of pulse energy, pulse accumulation, machining depth, and drilling method on nanosecond laser machining of diamond. We observed two distinct machining regimes in HPHT diamond, dictated by the thermal diffusivity of the diamond in relation to accumulated thermal energy within the lattice. The achievable aspect ratio is dictated by the pulse energy and number, with a required balance between excessive chamfer formation at high pulse energy and machining depth. At maximum, 66:1 aspect ratio was obtained, with the average aspect ratio of ~40:1 being achieved following saturation of multiple pulse (> 10^6) effects in diamond. While low internal taper is achieved with high pulse energy, the concurrent formation of chamfer must be carefully controlled. A minimum 0.11° internal taper angle was achieved over ~ 3 mm lengths at an aspect ratio of 10:1, representing an important step toward high precision, low taper structures in diamond. Finally, the nanosecond

diamond laser machining process was profiled using confocal Raman spectroscopy and formation of surface localized amorphous carbon and graphite was confirmed. All samples had between -30 to -55 MPa of tensile strain, which was increased by ~ 36% upon application of high energy laser irradiation. In all cases, the distribution of internal tensile strains was broadened particularly within the first 2.5 μm of diamond following laser irradiation. However, these effects were reduced following heat treatment at 600°C. Overall, the results presented here demonstrate the utility of nanosecond machining in the fabrication of high aspect ratio diamond structures and a method of mitigating nanosecond laser induced changes in diamond.

5.7 Supporting Information
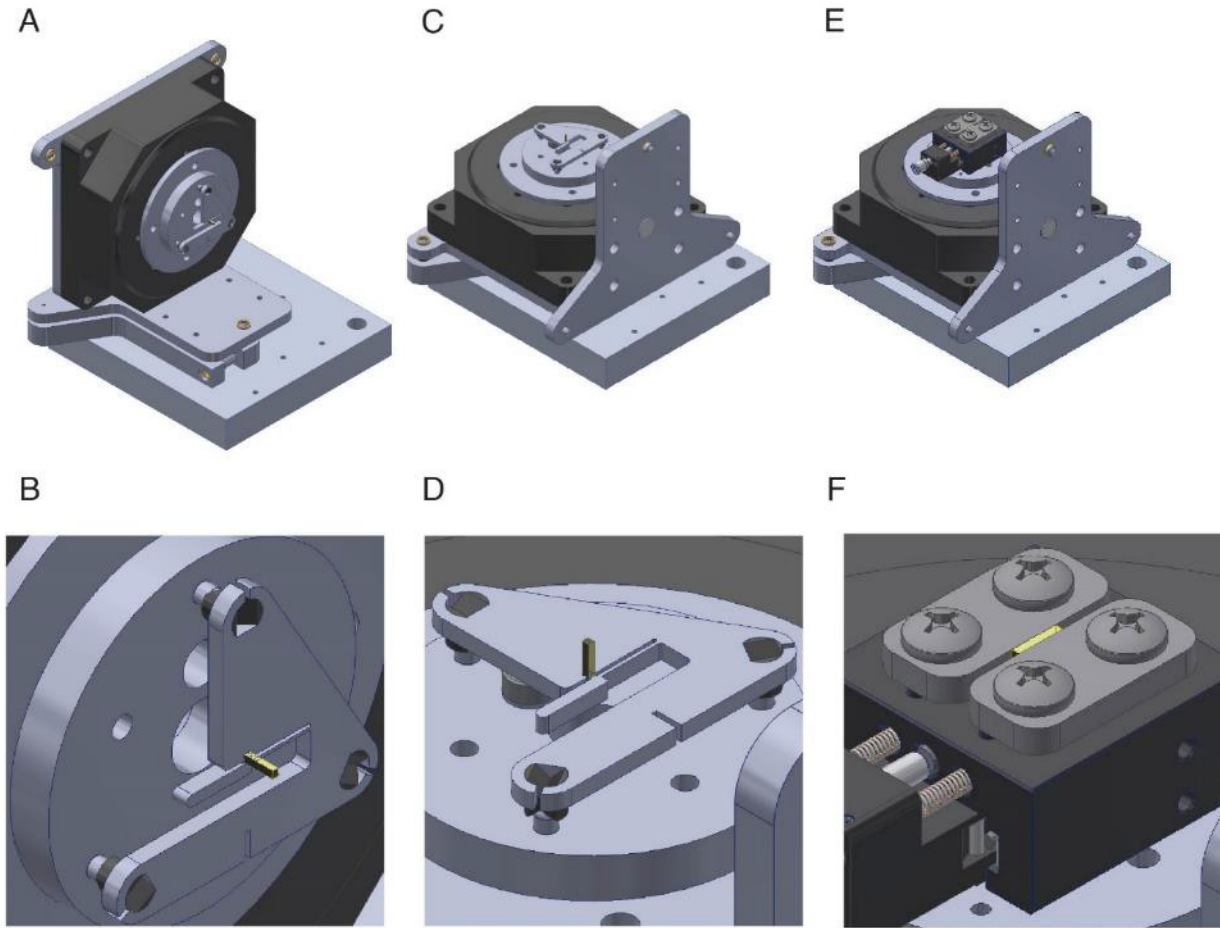
Figure 5.11.Homebuilt laser-lathe apparatus. In all configurations, the laser beam is incident from the top of the image. Baseplates of laser lathe allow for adjustment of pitch and yaw in addition to kinematic couplings for reliable re-orientation between machining schemes. The rotary stage provides 1000 degrees/s rotational speeds used during machining inner and outer diameters of high aspect ratio holes. (A,B). Laser lathe orientation for outer diameter machining, used to turn the 10:1 aspect ratio tubes. (C,D). Orientation used for machining the inner diameter of 10:1 aspect ratio tubes. (E,F). Fixture used to machine ~40:1 aspect ratio tubes.
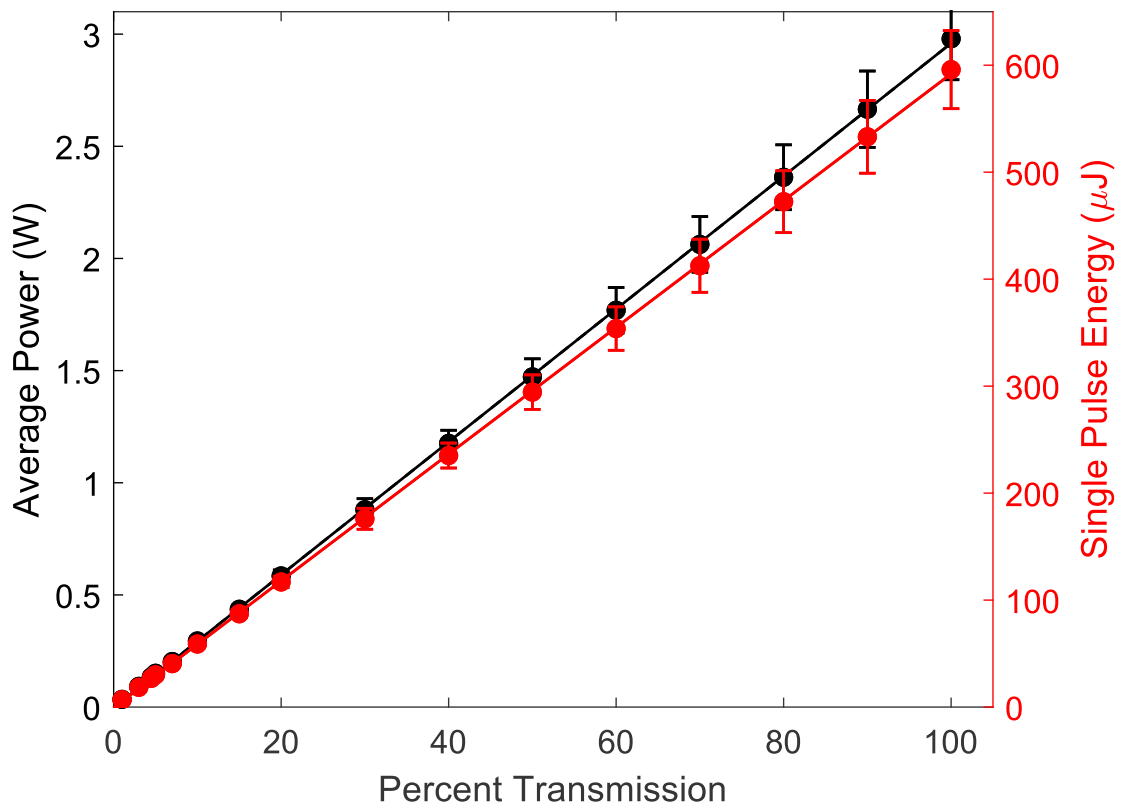
Figure 5.12. Laser power output. The measured average laser power as a function of percent transmission was measured using the built in power meter. A linear relation is maintained between the transmitted laser power and pulse energy across the powers used in this study.
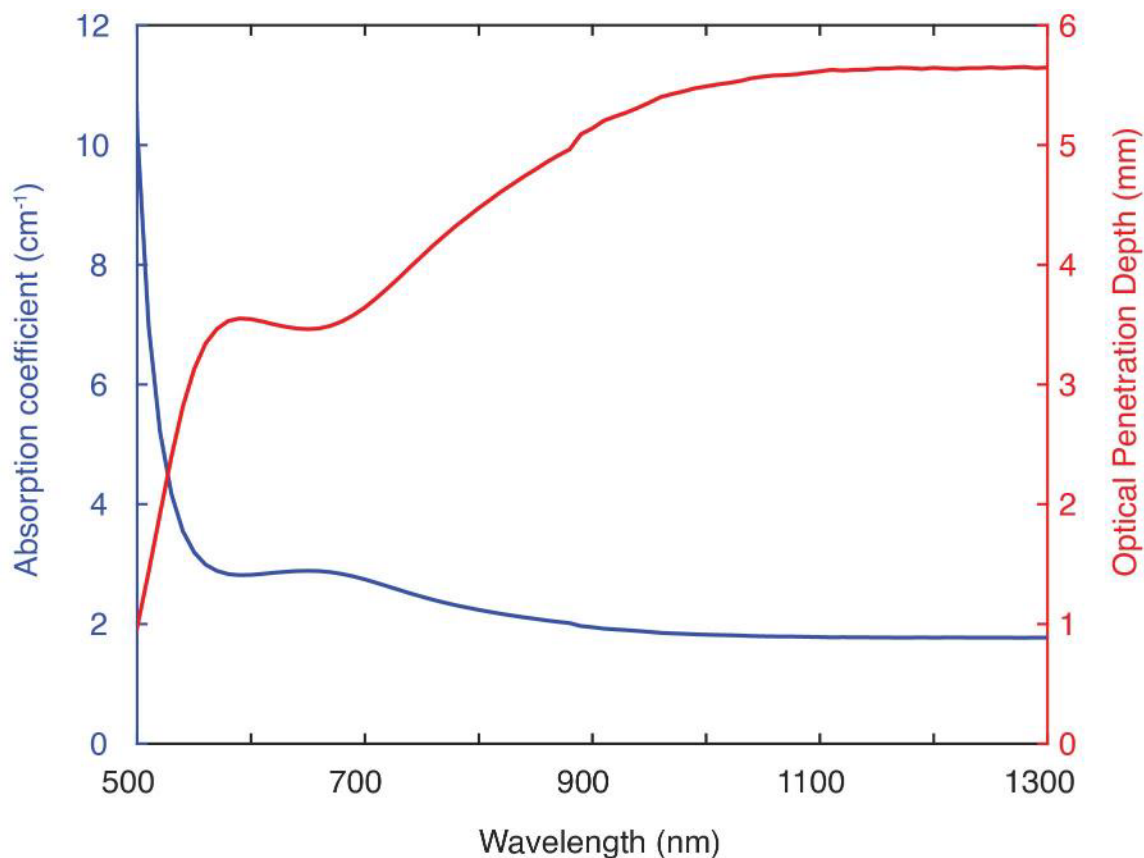
Figure 5.13. Optical properties of Type Ⅰb HPHT Diamond. Absorption coefficient and optical penetration depth for type Ⅰb HPHT diamond. Measured was performed using a Perkin Elmer Lambda 1050 UV/VIS spectrophotometer on a 1.1 mm thick diamond sample. At 532 nm, the absorption coefficient was found to be 4.19 ± 0.002 cm^{-1}. The optical penetration depth was calculated to be 2.39 ± 0.13 mm at 532 nm.
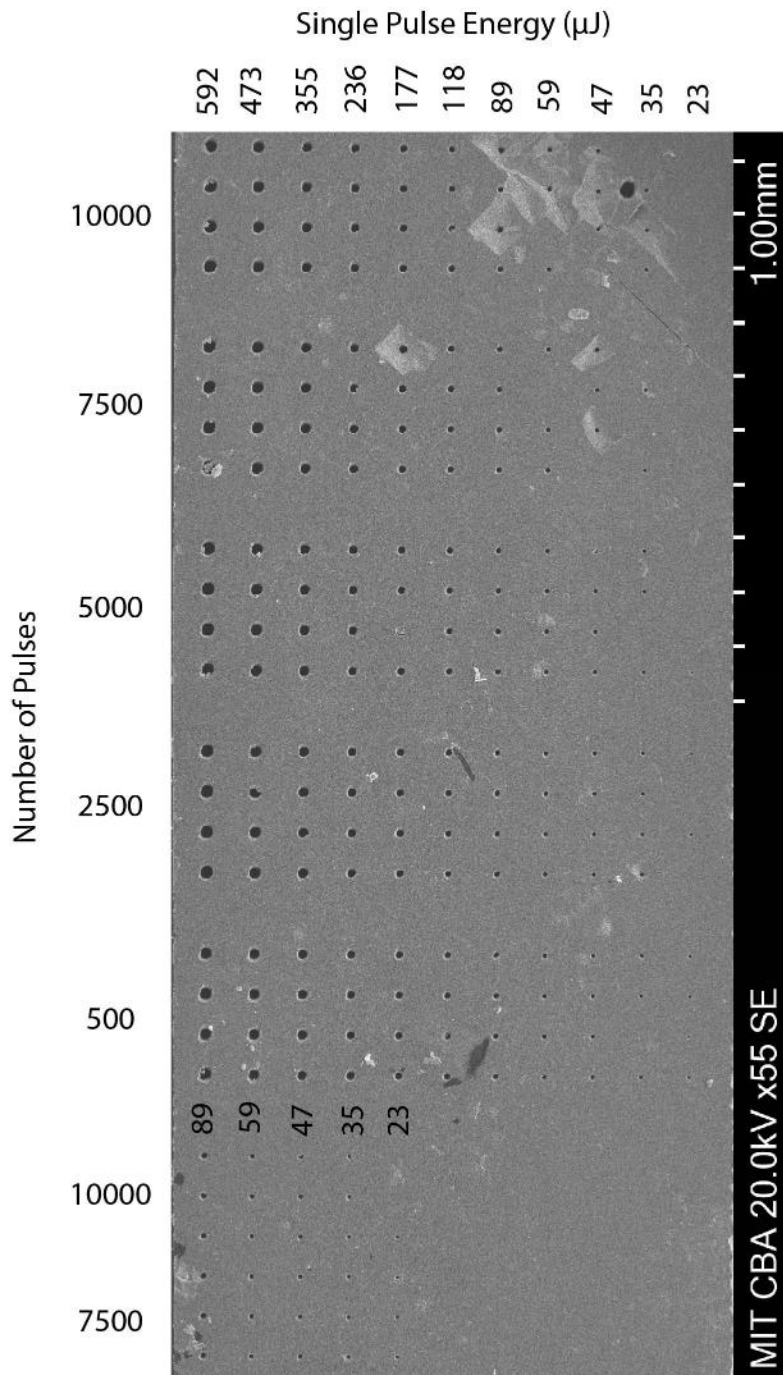
Figure 5.14. SEM of percussion holes. SEM of percussion holes used to determine ablation threshold. Extensive cracking was observed at the 5 lowest powers for 7500 and 10000 pulses. These tests were repeated and provided in the left most section of the figure. Holes were repeated four times.
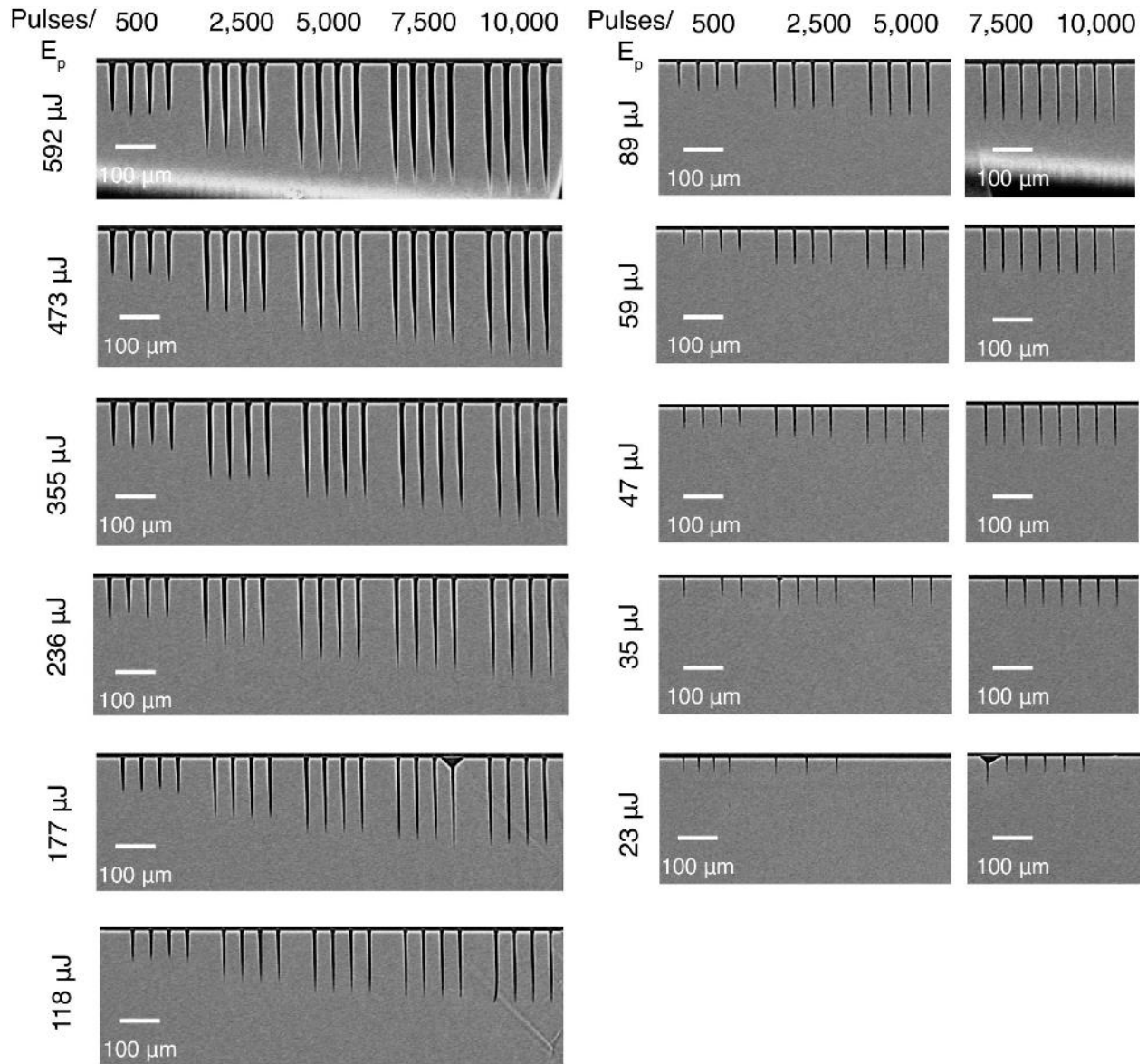
Figure 5.15. MicroCT Cross section views of percussion holes in the y-direction. CT scans were acquired with 2.1 µm voxel resolution. Each image is an average of 3 adjacent slices to ensure the center of the hole is captured for each sample.
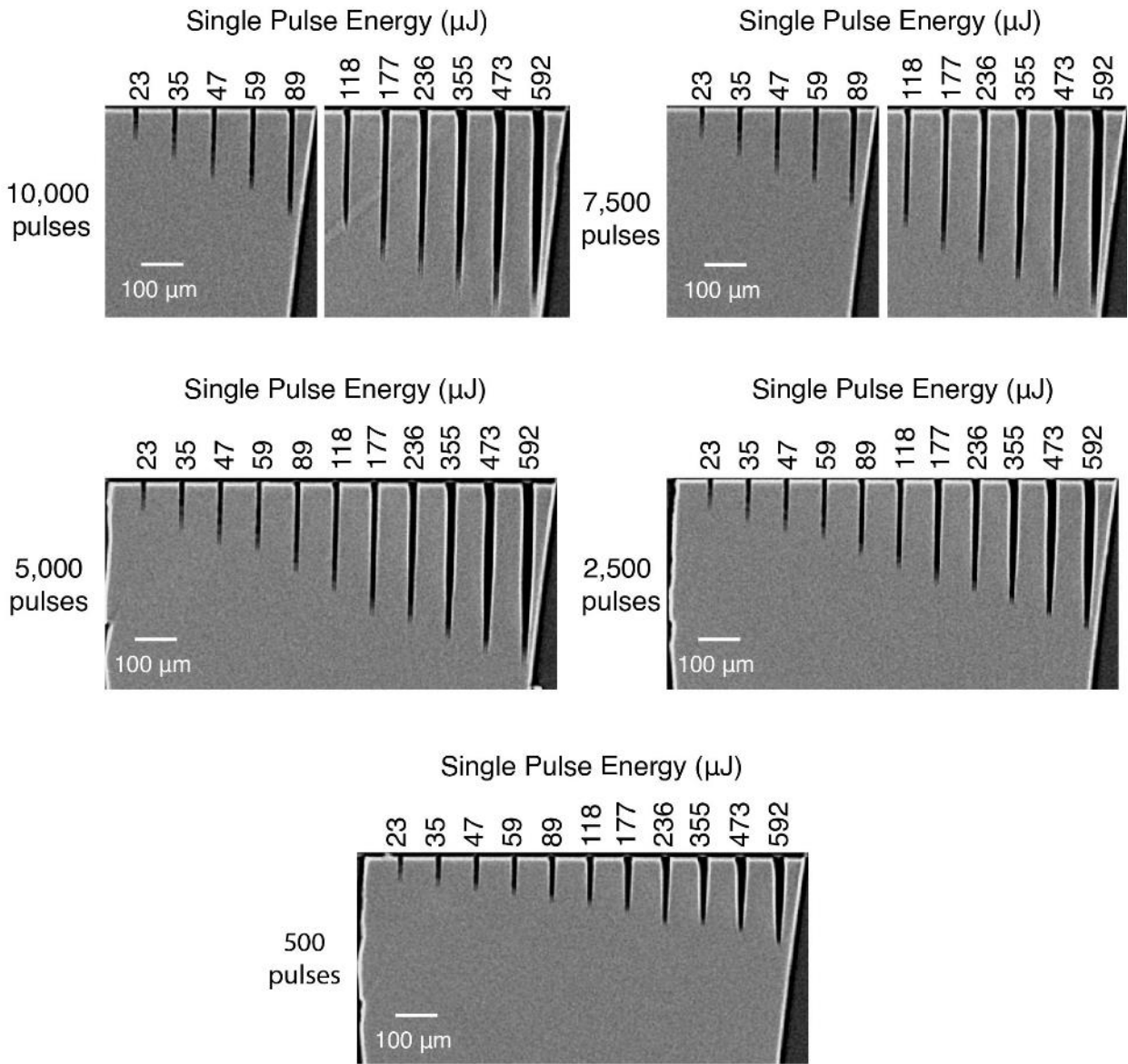
Figure 5.16. MicroCT cross section views of percussion holes in the x-direction.
CT scans were acquired with 2.1 μm voxel resolution. Each image is an average of 3
adjacent slices to ensure the center of the hole is captured for each sample.

Pulse Number	Spot Size	Gentle Ablation single pulse energy threshold (µJ)	Gentle Ablation threshold fluence (J/cm^2)	Strong Ablation single pulse energy threshold (µJ)	Strong Ablation threshold fluence (J/cm^2)
10,000	12.9 ± 1.1	9.6 ± 0.5	12.4 ± 1.4	124.7 ± 13.7	161.6 ± 22.4
7,500	13.7 ± 0.2	11.5 ± 2.8	14.9 ± 3.5	120.7 ± 18.9	156.4 ± 26.5
5,000	14.3 ± 0.3	12.6 ± 2.5	16.4 ± 3.2	109.1 ± 22.1	141.4 ± 28.7
2,500	14.7 ± 0.2	13.3 ± 1.8	17.2 ± 2.6	102.5 ± 26.6	132.7 ± 32.9
500	14.8 ± 0.1	13.2 ± 2.5	17.0 ± 3.3	97.9 ± 24.5	126.9 ± 30.5

Table 5.1. Ablation threshold of HPHT diamond. The ablation threshold in gentle and strong regimes are provided as a function of pulse number. For all fluences, the peak fluence was computed.
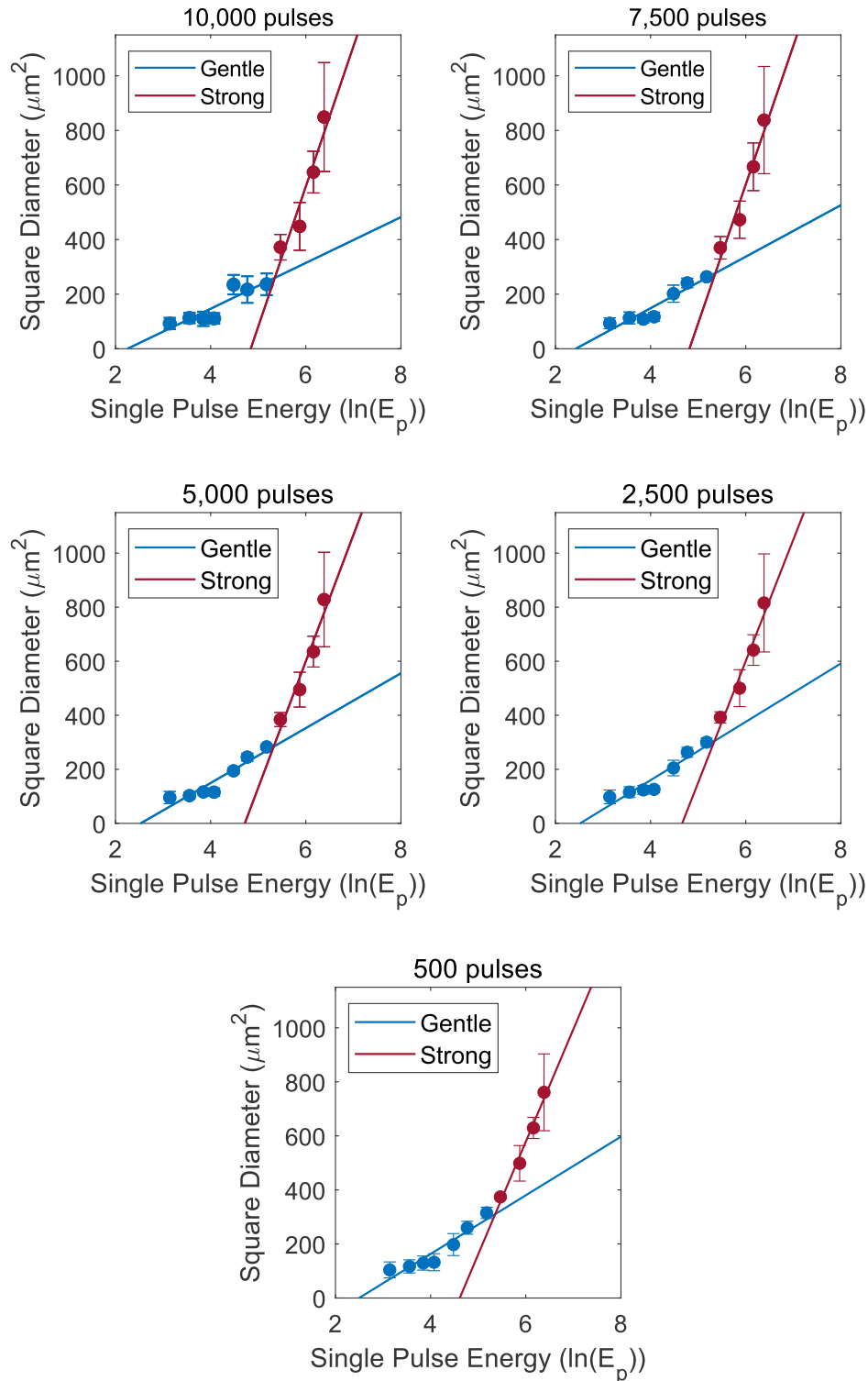
Figure 5.17. Determination of multiple pulse ablation threshold. The effect of multiple pulses on the square of the hole diameter as a function of single pulse energy. The red plot indicates the strong ablation regime, while the blue plot is for the gentle ablation regime.
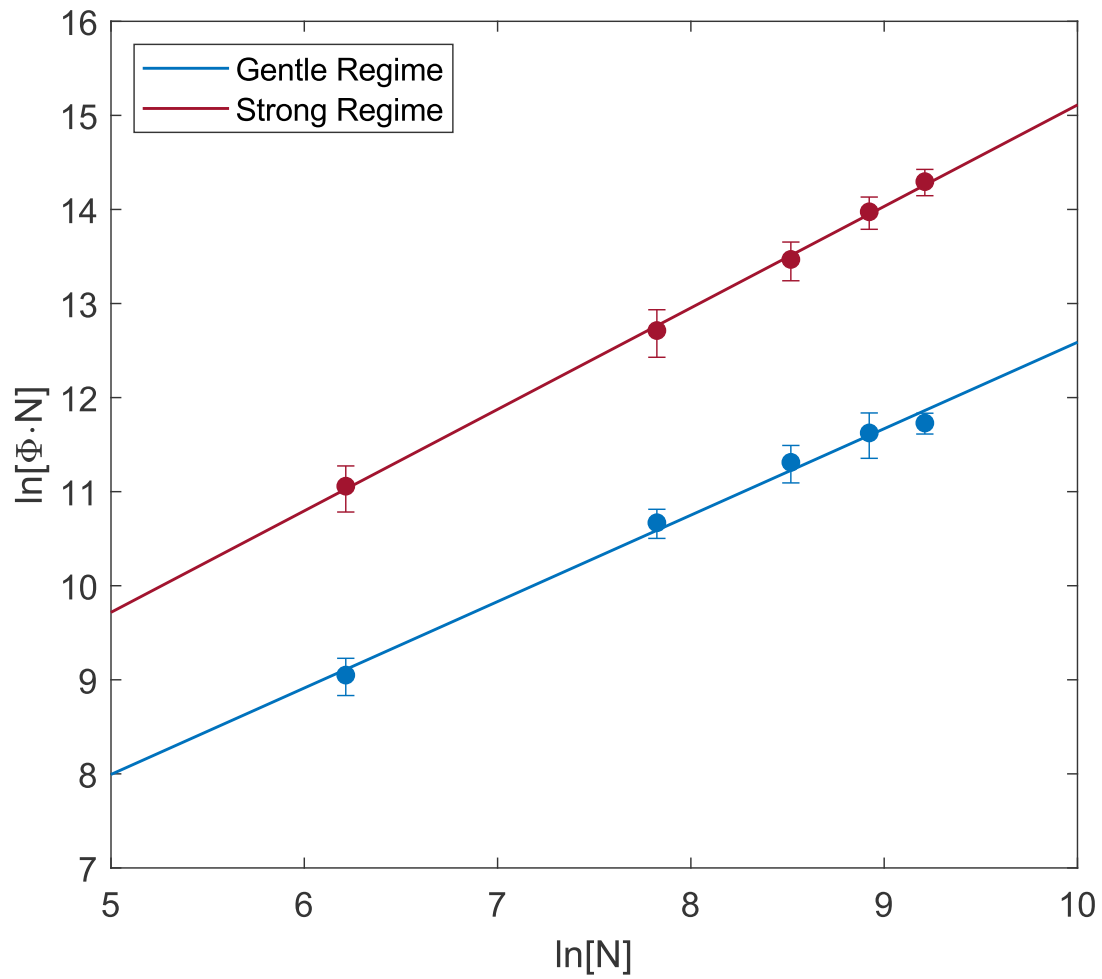
Figure 5.18. Single pulse ablation threshold. The single pulse ablation threshold is determined from the plot of the natural log of the pulse number vs. the natural log of the product of the N-pulse ablation threshold, and the number of pulses, N.
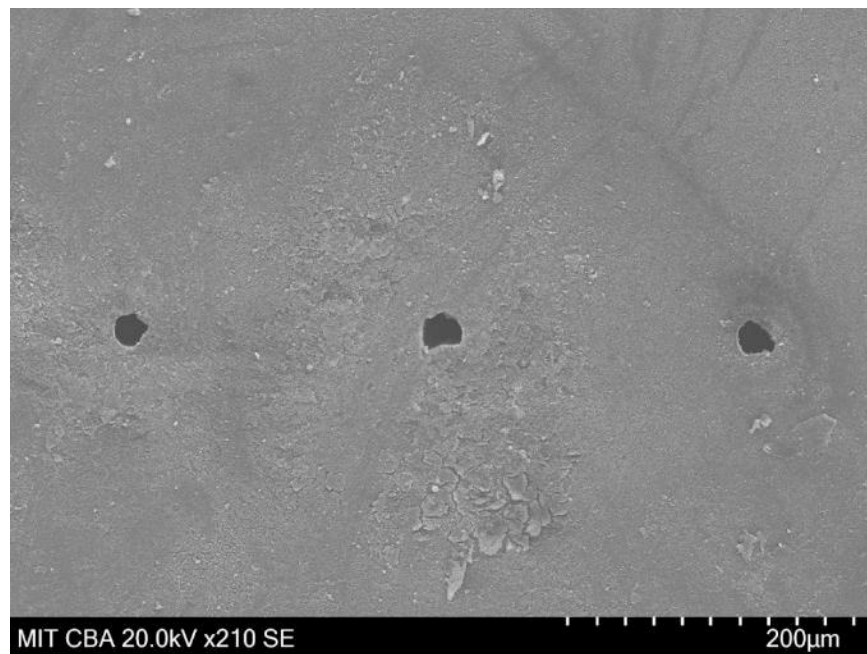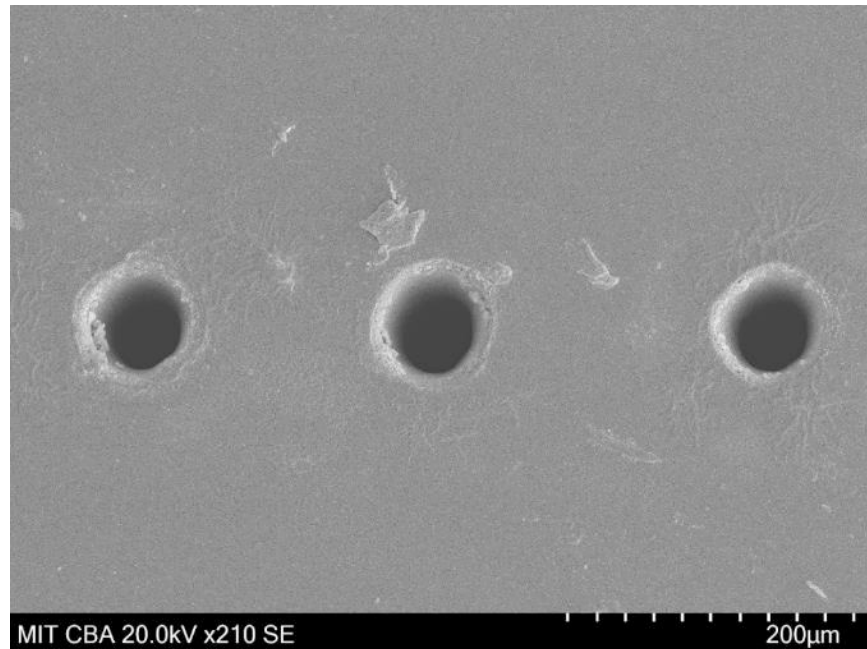
Figure 5.19. Entrance and Exit holes of ultra-high aspect ratio holes. SEM of the entrance and exit hole sides of holes 1 through 3. Diamond sample was sputter coated with 100 nm of gold prior to SEM.

Position (mm)	0	0.4	0.67	1.3	1.6	Average
Diameter hole 1 (µm)	79.7	46.4	29.7	42.6	24.1	44.5
Diameter hole 2 (µm)	77.9	46.3	33.4	40.8	31.6	46.0
Diameter hole 3 (µm)	79.8	46.4	31.6	42.7	29.7	46.0

Table 5.2 Inner diameters of 40:1 aspect ratio holes. Hole inner diameter (µm) as a function of position down the depth of the hole for each of the three holes shown in Figure 5.7. A position of 0 mm corresponds to the surface of the entrance of the laser machined hole, while a position of 1.6 mm corresponds to the bottom surface of the exit hole.

Position (mm)	0	0.4	0.67	1.3	1.6	Average
Aspect ratio hole 1	20.1	34.5	53.9	37.6	66.4	42.5
Aspect ratio hole 2	20.5	34.6	47.9	39.2	50.6	38.6
Aspect ratio hole 3	20.1	34.5	50.6	37.5	53.9	39.3

Table 5.3. Aspect Ratio as a function of position. Aspect ratio as a function of position down the depth of the hole for each of the three holes in Figure 5.7.
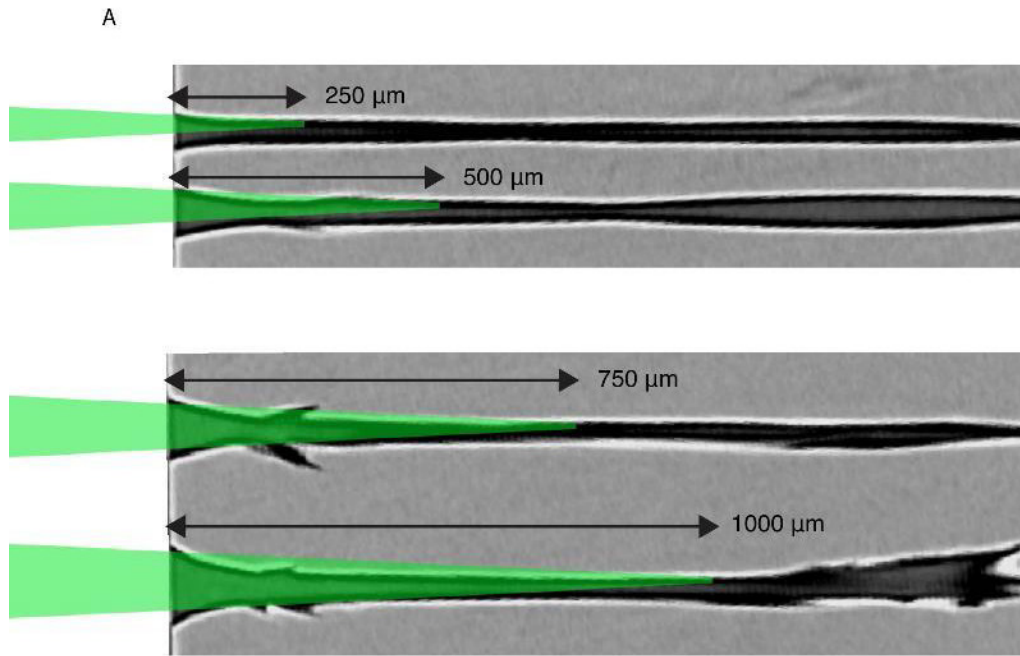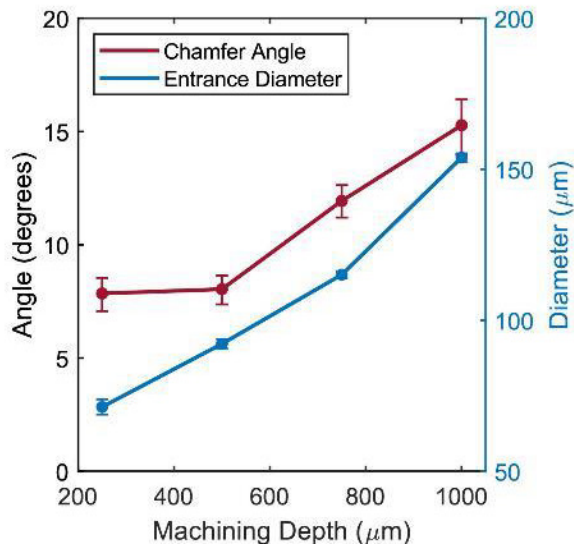
Figure 5.20. Chamfer as a function of machining depth. The fabrication of ~40:1 high aspect ratio holes resulted in considerable observed chamfer near the top ~150 μm of the entrance hole. The laser beam profile is overlaid onto the hole in green and centered 10 μm from the center of rotation of the part, representing the 20 μm nominal hole diameter tool pathed. The observed chamfer increases linearly to the machining depth. The machining depth is defined as the distance the z-axis is stepped down to maintain optical focus into the material during machining.

27 µJ Average Pulse Energy
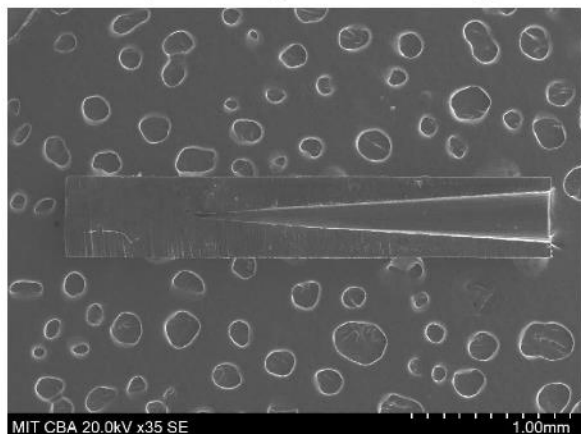
226 µJ Average Pulse Energy
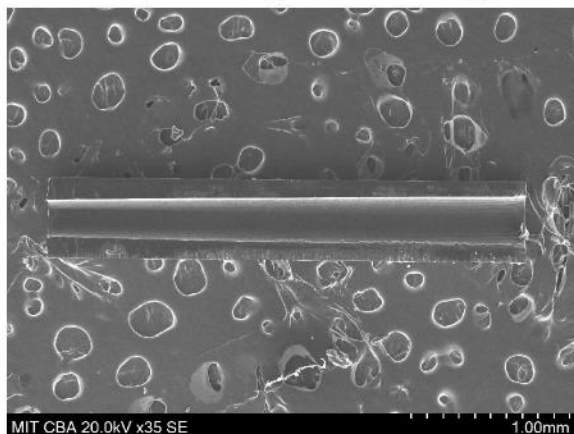
422 µJ Average Pulse Energy
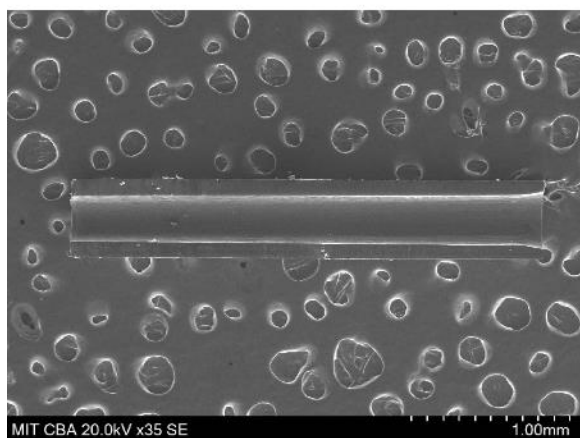
507 µJ Average Pulse Energy
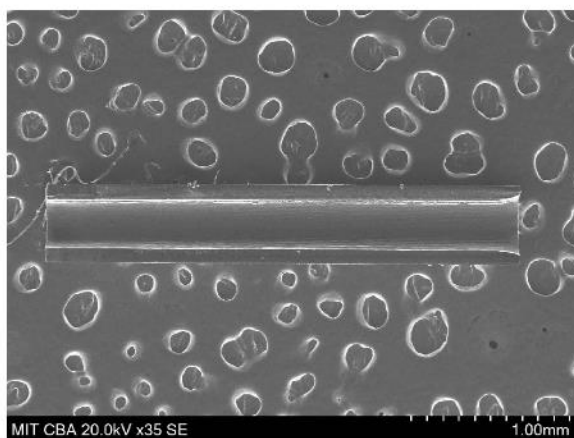
592 µJ Average Pulse Energy
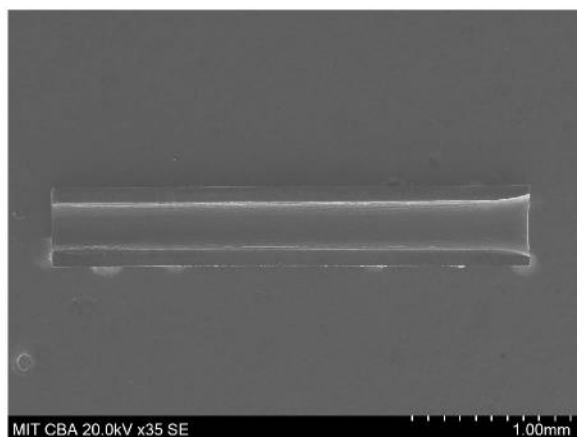
Figure 5.21. Uncropped SEMs of 10:1 Aspect Ratio holes. Uncropped images of the 10:1 aspect ratio tubes in Figure 5.8.
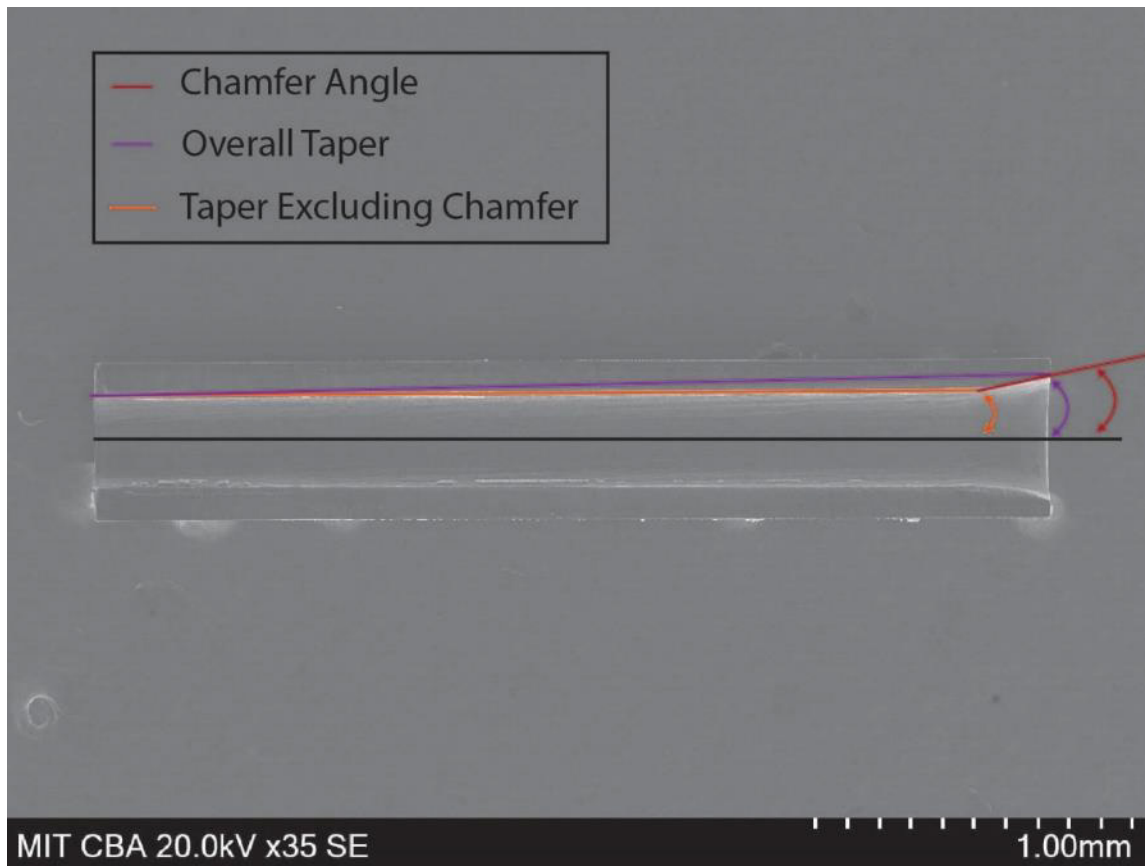
Figure 5.22. Definition of chamfer and taper angles. Chamfer and taper angles were determined by analyzing SEM data using Autodesk Inventor CAD software.

Average Single Pulse Energy (µJ)	Chamfer Angle (Degrees)	Overall Taper (Degrees)	Taper Excluding Chamfer (Degrees)	Entrance Diameter (µm)
27	4.03 ± 0.04	4.03 ± 0.04	4.03 ± 0.04	325.0 ± 1.7
226	10.55 ± 2.01	0.92 ± 0.05	0.69 ± 0.05	328.7 ± 4.2
422	11.83 ± 0.51	0.80 ± 0.02	0.33 ± 0.04	371.2 ± 2.0
507	16.27 ± 1.14	0.72 ± 0.04	0.11 ± 0.05	388.9 ± 0.8
592	16.80 ± 1.50	0.95 ± 0.06	0.17 ± 0.05	399.2 ± 0.8

Table 5.4. Chamfer, taper, and diameter of 10:1 aspect ratio holes.
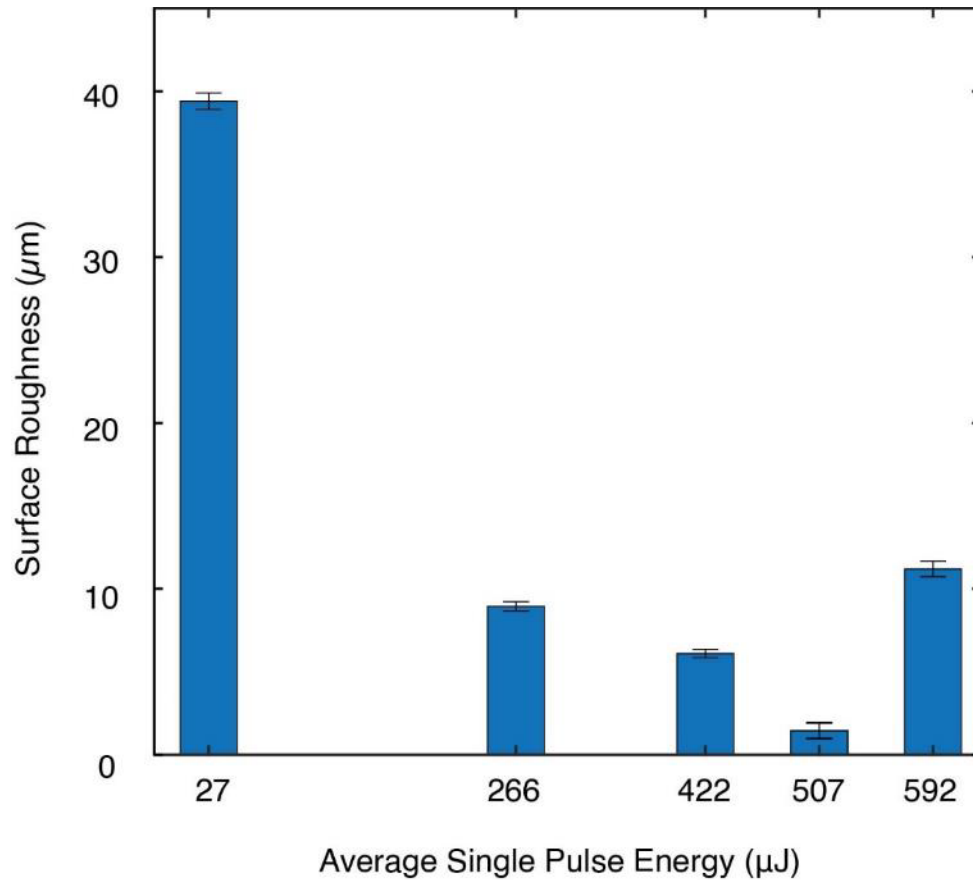
Figure 5.23. Surface finish of 10:1 Aspect Ratio Tubes. The surface roughness, R_a was determined for an 3 mm long, ~ 25 μm section down the center of rotation of the 10:1 aspect ratio tube using a Keyence VK-X250 laser scanning confocal microscope at 20x magnification. The optimal machining regime for surface finish was found to be using an average single pulse energy of 507 μJ. This corresponds to a ramped roughing cut procedure from pulse energy of 266 μJ to 592 μJ, followed by a finishing pass at 592 μJ.
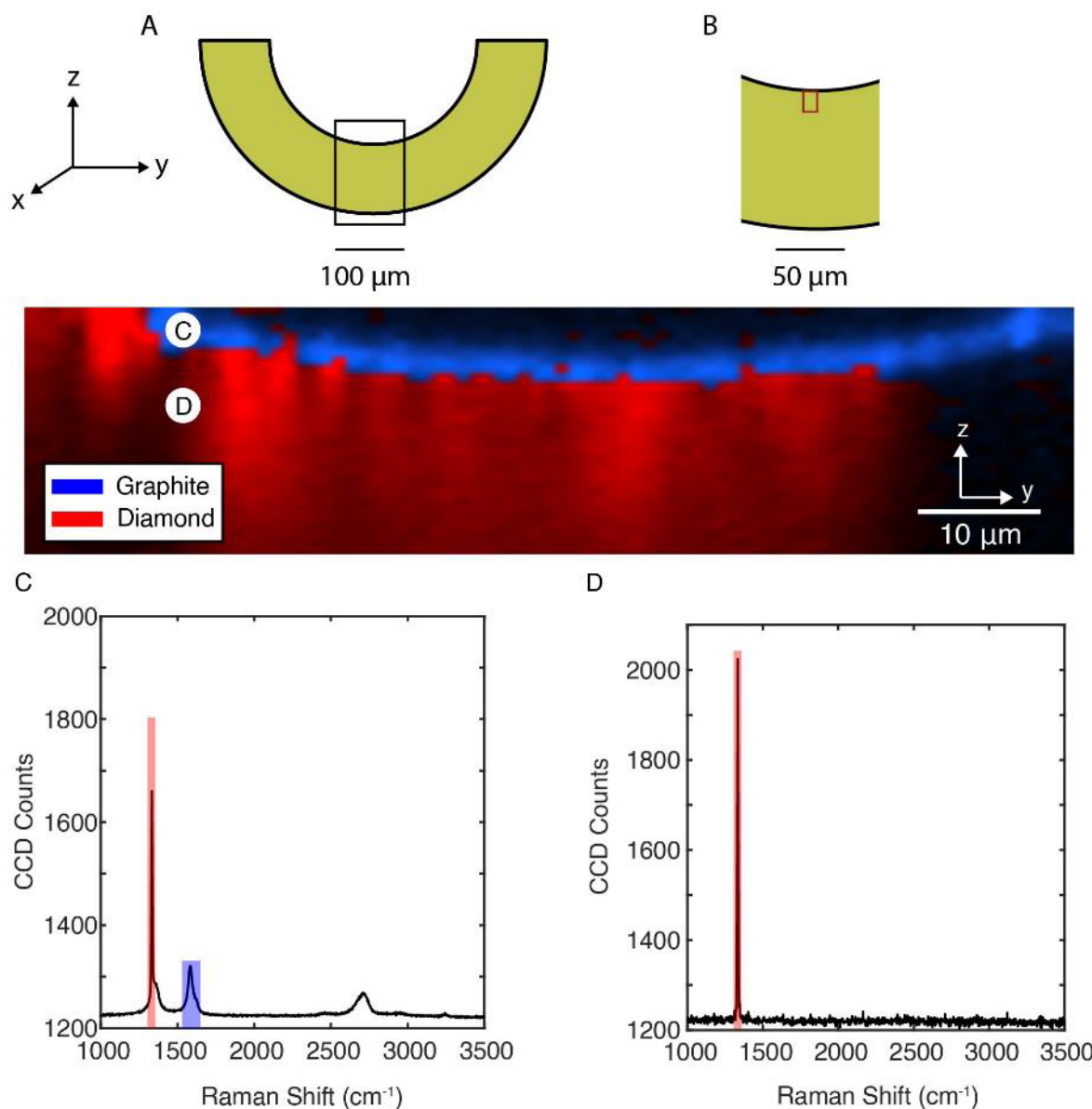
Figure 5.24. Surface Graphitization during ns laser machining. Under nanosecond laser machining of diamond, laser absorption drives a phase transition from diamond to graphite. While most graphite is vaporized during machining, a thin layer, ~ 2 μm, remains on the machined inner surface. In the figure, the graphite signal is colored blue and corresponds to the sum of signals originating from the Raman shift of 1594 ± 60 cm^{-1}. The diamond signal is colored red and corresponds to the sum of signals originating from the Raman shift of 1332 ± 25 cm^{-1}.
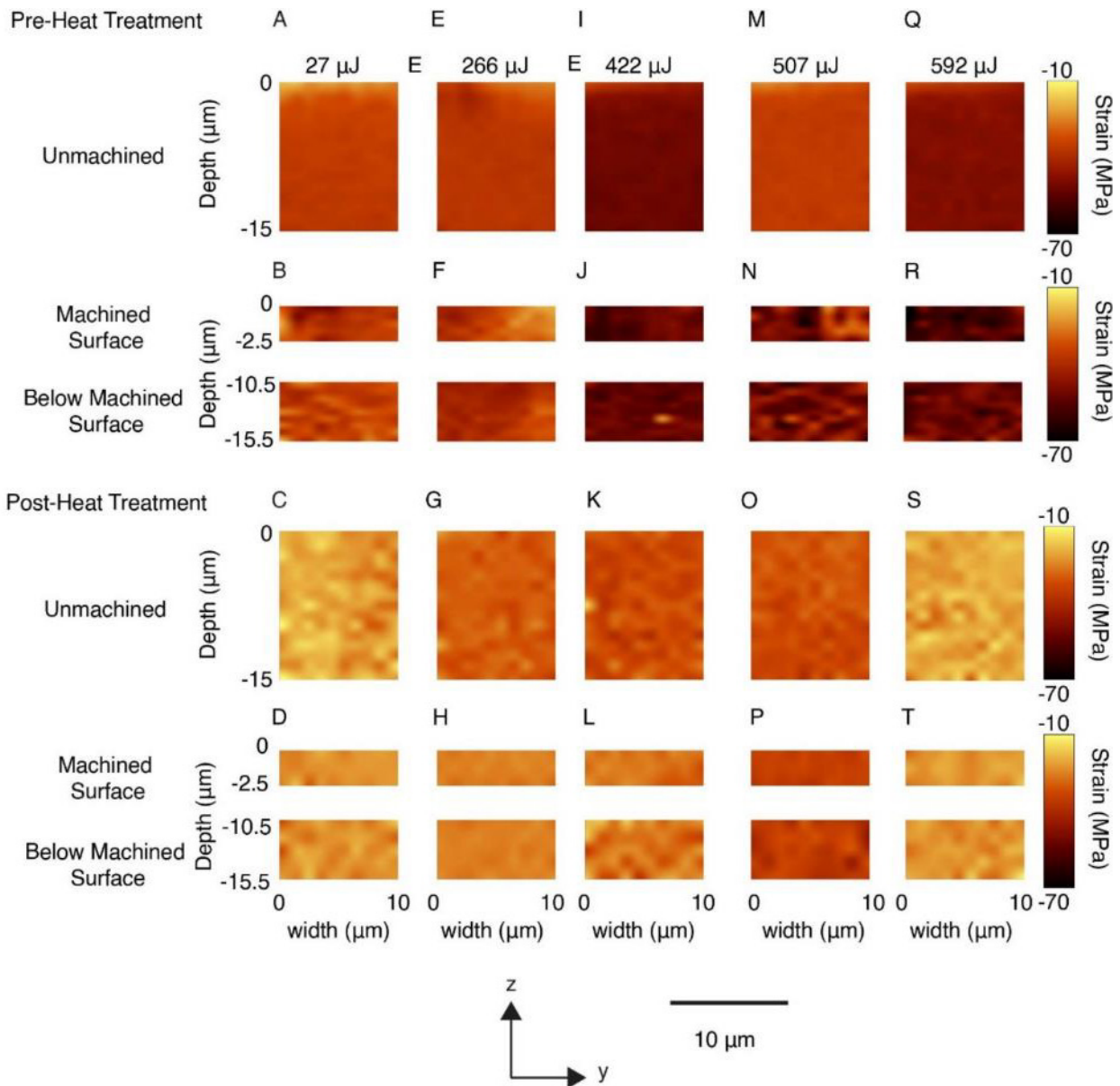
Figure 5.25. Raman images of 10:1 aspect ratio tube cross sectional samples. Each image is 10 μm wide and the result of 900 accumulations averaged across three locations on the sample at 250 μm, 1250 μm, and 2750 μm down the tube length. No significant changes were observed as a function of location along the tube. For the unmachined reference samples, a depth of 15 μm was profiled from the top of the sample. For surface strain measurements, a depth of -1 ± 2 μm was profiled, while for the below surface strain measurements a depth of -13 ± 2 μm was profiled.

Average Single Pulse Energy	Reference, Pre-Heat Treatment Strain (MPa)	Reference, Post Heat Treatment Strain (MPa)	Reference, Heat Treatment	Machined Sample, Pre-Heat Treatment Strain (MPa)	Induced Strain Laser Machining	Machined Sample, Post Heat Treatment Strain (MPa)	Sample, change in strain heat treatment
27	-34.4±3.4	-20.9±3.2	-39%	-35.2±4.6	2%	-23.4±2.0	-34%
266	-36.4±2.5	-29.9±1.8	-18%	-36.6±6.2	0.5%	-25.5±0.81	-30%
422	-50.8±2.8	-32.6±2.4	-36%	-53.3±4.5	5%	-26.9±2.6	-50%
507	-35.2±1.7	-31.7±2.0	-10%	-48.0±7.7	36%	-35.4±2.0	-26%
592	-47.8±2.5	-20.4±2.7	-57%	-55.4±5.0	16%	-22.5±1.9	-59%

Table 5.5. Measured strain values from confocal Raman spectroscopy. The reference sample strain measurements are provided before and after heat treatment, all samples show at least a ~10% reduction in strain and up to 57% reduction. The net laser induced strain as a percent increase is provided prior to heat treatment. Following heat treatment, the strain was re-measured in the machined samples and the percent reduction in strain is provided, relative to the machined sample prior to heat treatment.
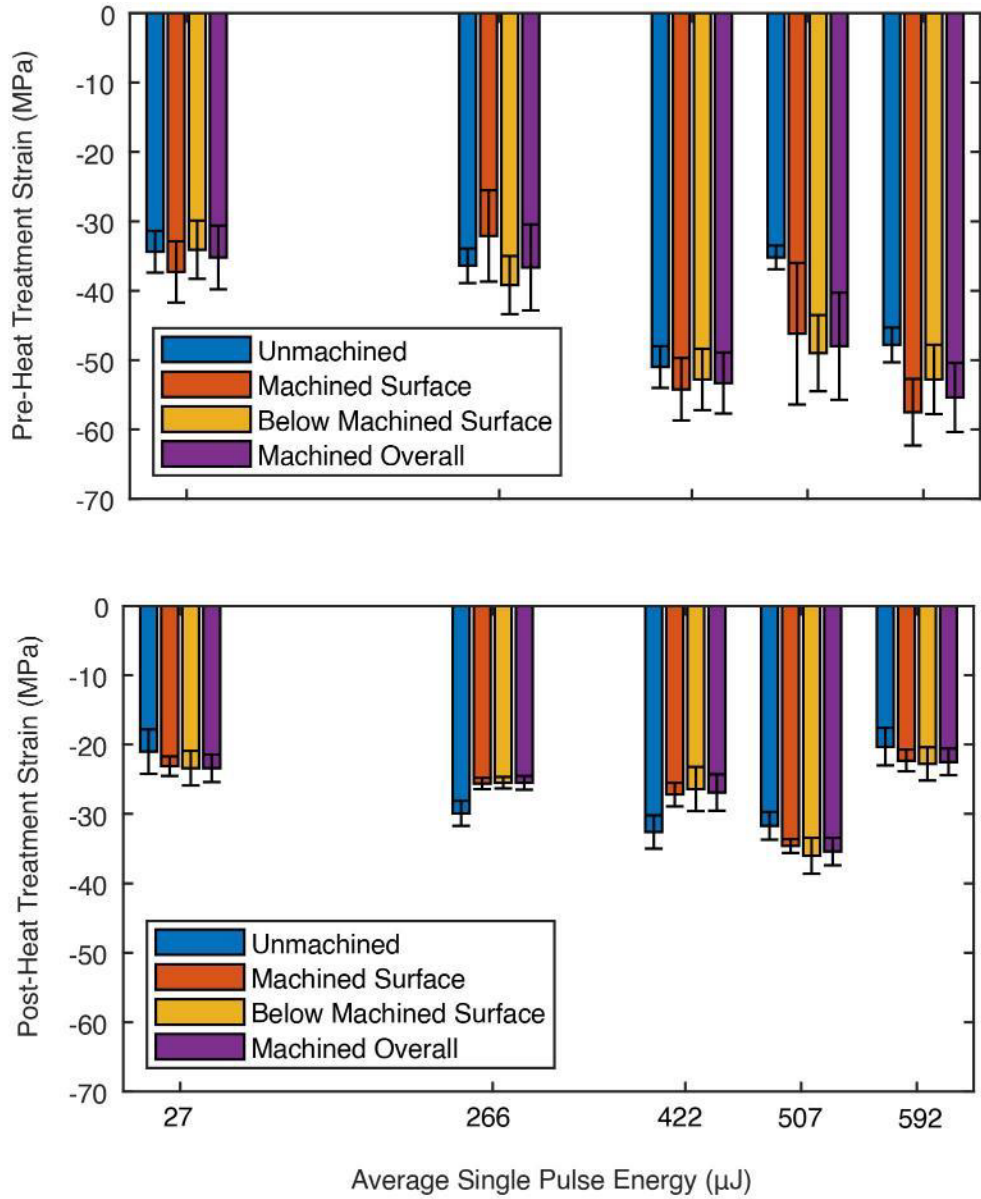
Figure 5.26. Pre and Post Heat Treatment Strain. Observed strain in the diamond crystal as a function of machining power before and after heat treatment at 600° C for 24 hours. In all cases, high temperature treatment reduces the observed internal strain in HPHT diamond. This step importantly mitigates any strain introduced during the machining process.

5.8 Acknowledgements

5.9 References

1   Abobeih, M. H. *et al.* Fault-tolerant operation of a logical qubit in a diamond quantum processor. *Nature* **606**, 884-889 (2022). https://doi.org:10.1038/s41586-022-04819-6

2   Araujo, D., Suzuki, M., Lloret, F., Alba, G. & Villar, P. Diamond for Electronics: Materials, Processing and Devices. *Materials* **14**, 7081 (2021).

3   Bhaumik, A., Sachan, R. & Narayan, J. Tunable charge states of nitrogen-vacancy centers in diamond for ultrafast quantum devices. *Carbon* **142**, 662-672 (2019). https://doi.org:https://doi.org/10.1016/j.carbon.2018.10.084

4   Joseph, M. B. *et al.* Fabrication Route for the Production of Coplanar, Diamond Insulated, Boron Doped Diamond Macro- and Microelectrodes of any Geometry. *Analytical Chemistry* **86**, 5238-5244 (2014). https://doi.org:10.1021/ac501092y

5   Liao, M. Progress in semiconductor diamond photodetectors and MEMS sensors. *Functional Diamond* **1**, 29-46 (2021). https://doi.org:10.1080/26941112.2021.1877019

6   Wu, Y., Jelezko, F., Plenio, M. B. & Weil, T. Diamond Quantum Devices in Biology. *Angewandte Chemie International Edition* **55**, 6586-6598 (2016). https://doi.org:https://doi.org/10.1002/anie.201506556

7   Bundy, F. P., Hall, H. T., Strong, H. M. & Wentorfjun, R. H. Man-Made Diamonds. *Nature* **176**, 51-55 (1955). https://doi.org:10.1038/176051a0

8   Spitsyn, B. V., Bouilov, L. L. & Derjaguin, B. V. Vapor growth of diamond on diamond and other surfaces. *Journal of Crystal Growth* **52**, 219-226 (1981). https://doi.org:https://doi.org/10.1016/0022-0248(81)90197-4

9   Apostolova, T., Kurylo, V. & Gnilitskyi, I. Ultrafast Laser Processing of Diamond Materials: A Review. *Frontiers in Physics* **9** (2021). https://doi.org:10.3389/fphy.2021.650280

10   Boerner, P., Hajri, M., Ackerl, N. & Wegener, K. Experimental and theoretical investigation of ultrashort pulsed laser ablation of diamond. *Journal of Laser Applications* **31**, 022202 (2019). https://doi.org:10.2351/1.5096088

11   Leitz, K.-H., Redlingshöfer, B., Reg, Y., Otto, A. & Schmidt, M. Metal Ablation with Short and Ultrashort Laser Pulses. *Physics Procedia* **12**, 230-238 (2011).

12   Windholz, R. & Molian, P. A. Nanosecond pulsed excimer laser machining of chemical vapour deposited diamond and highly oriented pyrolytic graphite: Part I An experimental investigation. *Journal of Materials Science* **32**, 4295-4301 (1997). https://doi.org:10.1023/A:1018611604403

13   Schaeffer, R. *Fundamentals of Laser Micromachining*. (CRC Press, 2012).

14   Shirk, M. D., Molian, P. A. & Malshe, A. P. Ultrashort pulsed laser ablation of diamond. *Journal of Laser Applications* **10**, 64-70 (1998). https://doi.org:10.2351/1.521822

15   Sundaram, S. K. & Mazur, E. Inducing and probing non-thermal transitions in semiconductors using femtosecond laser pulses. *Nature Materials* **1**, 217-224 (2002). https://doi.org:10.1038/nmat767

16   Hermani, J., Emonts, M. & Brecher, C. in *Proceedings of the Lasers in Manufacturing Conference, Munich, Germany.* 22-25.

17   Li, Z., Chen, N., Li, L., Wu, Y. & He, N. Influence of the grain size of CVD diamond on the thermal conductivity, material removal depth and surface roughness in nanosecond laser machining. *Ceramics International* **46**, 20510-20520 (2020). https://doi.org:https://doi.org/10.1016/j.ceramint.2020.05.157

18   Mouhamadali, F. *et al.* Nanosecond pulsed laser-processing of CVD diamond. *Optics and Lasers in Engineering* **126**, 105917 (2020). https://doi.org:https://doi.org/10.1016/j.optlaseng.2019.105917

19   Okuchi, T. *et al.* Micromachining and surface processing of the super-hard nano-polycrystalline diamond by three types of pulsed lasers. *Applied Physics A* **96**, 833-842 (2009). https://doi.org:10.1007/s00339-009-5326-8

20   Ullah, N. *et al.* Ablation Threshold Measurement and Chemical Modification of UV Nanosecond Laser Micromachining of Polycrystalline Diamond. *physica status solidi (a)* **218**, 2100450 (2021). https://doi.org:https://doi.org/10.1002/pssa.202100450

21   Wang, H. *et al.* Ablation characteristics and material removal mechanisms of a single-crystal diamond processed by nanosecond or picosecond lasers. *Opt. Express* **29**, 22714-22731 (2021). https://doi.org:10.1364/OE.430354

22   Windholz, R. & Molian, P. A. Nanosecond pulsed excimer laser machining of chemically vapour-deposited diamond and graphite: Part II Analysis and modelling. *Journal of Materials Science* **33**, 523-528 (1998). https://doi.org:10.1023/A:1004308921860

23   Wu, M. *et al.* The influence of the focus position on laser machining and laser micro-structuring monocrystalline diamond surface. *Optics and Lasers in Engineering* **105**, 60-67 (2018). https://doi.org:https://doi.org/10.1016/j.optlaseng.2018.01.002

24 Xing, Y. *et al.* Micro-channels machining on polycrystalline diamond by nanosecond laser. *Optics & Laser Technology* **108**, 333-345 (2018). https://doi.org:https://doi.org/10.1016/j.optlastec.2018.07.024

25 Brian, K. C., Alexander, T., Lino, C. & Lloyd, M. D. in *Proc.SPIE.* 111730D.

26 Jeong, B. *et al.* Drilling of sub-100 μm hourglass-shaped holes in diamond with femtosecond laser pulses. *Quantum Electronics* **50**, 201 (2020). https://doi.org:10.1070/QEL17097

27 Martin, A. A. *et al.* Ultra-high aspect ratio pores milled in diamond via laser, ion and electron beam mediated processes. *Diamond and Related Materials* **105**, 107806 (2020). https://doi.org:https://doi.org/10.1016/j.diamond.2020.107806

28 Tianlun, S. *et al.* Structural changes during femtosecond laser percussion drilling of high-aspect-ratio diamond microholes. *Optical Engineering* **61**, 016103 (2022). https://doi.org:10.1117/1.OE.61.1.016103

29 Golota, N., Zach Fredin, Daniel Banks, Prashant Patil, David Preiss, Robert Griffin, Neil Gershenfeld. Two-sided laser micromachinig for MAS NMR diamond rotors. (2022).

30 Prashant Patil, D. B., Salima Bahri, William Langford, Camron Blackburn, Zach Fredin, Robert Griffin, Neil Gershenfeld. Diamond Rotors for MAS-NMR. (2020).

31 Chen, N. *et al.* Investigation of metal-coating-assisted IR nanosecond pulsed laser ablation of CVD diamond. *Journal of Materials Research and Technology* **18**, 4114-4129 (2022). https://doi.org:https://doi.org/10.1016/j.jmrt.2022.04.072

32 Griffiths, D. J. *Introduction to electrodynamics*. (Fourth edition. Boston : Pearson, [2013] ©2013, 2013).

33 Chattopadhyay, S., Chien, S. C., Chen, L. C., Chen, K. H. & Lee, H. Y. Thermal diffusivity in diamond, SiCxNy and BCxNy. *Diamond and Related Materials* **11**, 708-713 (2002). https://doi.org:https://doi.org/10.1016/S0925-9635(01)00606-9

34 ElementSix. (ed De Beers Group) (2020).

35 Tokmakoff, A., Banholzer, W. F. & Fayer, M. D. Thermal diffusivity measurements of natural and isotopically enriched diamond by picosecond infrared transient grating experiments. *Applied Physics A* **56**, 87-90 (1993). https://doi.org:10.1007/BF00351908

36 Schneider, C. A., Rasband, W. S. & Eliceiri, K. W. NIH Image to ImageJ: 25 years of image analysis. *Nature Methods* **9**, 671-675 (2012). https://doi.org:10.1038/nmeth.2089

37 Alexander, W. B., Holloway, P. H., Simmons, J. & Ochoa, R. Increased precision in strain measurement of diamond by microRaman spectroscopy. *Journal of Vacuum Science & Technology A* **12**, 2943-2945 (1994). https://doi.org:10.1116/1.578973

38 Sharma, S. K., Mao, H. K., Bell, P. M. & Xu, J. A. Measurement of stress in diamond anvils with micro-Raman spectroscopy. *Journal of Raman Spectroscopy* **16**, 350-352 (1985). https://doi.org:https://doi.org/10.1002/jrs.1250160513

39 Borowiec, A. & Haugen, H. K. Femtosecond laser micromachining of grooves in indium phosphide. *Applied Physics A* **79**, 521-529 (2004). https://doi.org:10.1007/s00339-003-2377-0

40 Lim, F. S., Wang, X., Yaacob, K. A., Soh, A. K. & Chang, W. S. Effect of indirect irradiation on surface morphology of Au film by nanosecond laser. *Applied Physics A* **123**, 664 (2017). https://doi.org:10.1007/s00339-017-1277-7

41 Komlenok, M. S., Kononenko, V. V., Ralchenko, V. G., Pimenov, S. M. & Konov, V. I. Laser Induced Nanoablation of Diamond Materials. *Physics Procedia* **12**, 37-45 (2011). https://doi.org:https://doi.org/10.1016/j.phpro.2011.03.103

42 Takayama, N. & Yan, J. Laser Irradiation Responses of a Single-Crystal Diamond Produced by Different Crystal Growth Methods. *Applied Sciences* **7**, 815 (2017).

43 Ghoreishi, M., Low, D. K. Y. & Li, L. Effects of processing parameters on hole circularity in laser percussion drilling – A statistical model. *International Congress on Applications of Lasers & Electro-Optics* **2001**, 326-333 (2001). https://doi.org:10.2351/1.5059880

44 Low, D. K. Y., Li, L. & Byrd, P. J. The influence of temporal pulse train modulation during laser percussion drilling. *Optics and Lasers in Engineering* **35**, 149-164 (2001). https://doi.org:https://doi.org/10.1016/S0143-8166(01)00008-2

45 Gheeraert, E., Deneuville, A., Bonnot, A. M. & Abello, L. Defects and stress analysis of the Raman spectrum of diamond films. *Diamond and Related Materials* **1**, 525-528 (1992). https://doi.org:https://doi.org/10.1016/0925-9635(92)90157-J

46 Liscia, E. J. D. *et al.* Stress Analysis on Single-Crystal Diamonds by Raman Spectroscopy 3D Mapping. *Materials Sciences and Applications* **Vol.04No.03**, 7 (2013). https://doi.org:10.4236/msa.2013.43023

47 Sudheer, S. K., Pillai, V. P. M. & Nayar, V. U. Characterization of laser processing of single-crystal natural diamonds using micro-Raman spectroscopic investigations. *Journal of Raman Spectroscopy* **38**, 427-435 (2007). https://doi.org:https://doi.org/10.1002/jrs.1663

48 Cobb, S. J. *et al.* Assessment of acid and thermal oxidation treatments for removing sp2 bonded carbon from the surface of boron doped diamond. *Carbon* **167**, 1-10 (2020).

49 Paci, J. T., Minton, T. K. & Schatz, G. C. Hyperthermal Oxidation of Graphite and Diamond. *Accounts of Chemical Research* **45**, 1973-1981 (2012). https://doi.org:10.1021/ar200317y

50 Zhu, W., Wang, X. H., Pickrell, D. J., Badzian, A. R. & Messier, R. The oxidation of CVD diamond films. *Carbon* **28**, 796 (1990). https://doi.org:https://doi.org/10.1016/0008-6223(90)90302-F

51 DeVries, R. C. Plastic deformation and "work-hardening" of diamond. *Materials Research Bulletin* **10**, 1193-1199 (1975). https://doi.org:https://doi.org/10.1016/0025-5408(75)90026-4

52 Jackson, W. E. & Webb, S. W. Synthetic Diamond Strength Enhancement Through High Pressure/High Temperature Annealing. *MRS Online Proceedings Library* **383**, 267-272 (1995). https://doi.org:10.1557/PROC-383-267

53 Meng, Y. F. *et al.* Enhanced optical properties of chemical vapor deposited single crystal diamond by low-pressure/high-temperature annealing. (2008).

54   Torelli, M. D. *et al.* High Temperature Treatment of Diamond Particles Toward Enhancement of Their Quantum Properties. *Frontiers in Physics* **8** (2020).

55   Webb, S. W. & Jackson, W. E. Synthetic diamond crystal strength enhancement through annealing at 50 kbar and 1500 °C. *Journal of Materials Research* **10**, 1700-1709 (1995). https://doi.org:10.1557/JMR.1995.1700

56   Hruszkewycz, S. O. *et al.* In situ study of annealing-induced strain relaxation in diamond nanoparticles using Bragg coherent diffraction imaging. *APL Materials* **5**, 026105 (2017). https://doi.org:10.1063/1.4974865

57   Eaton-Magaña, S., Breeding, C. M. & Bassoo, R. Low-temperature annealing and kinetics of radiation stains in natural diamond. *Diamond and Related Materials* **132**, 109649 (2023). https://doi.org:https://doi.org/10.1016/j.diamond.2022.109649

Chapter 6 : Diamond Rotors

6.1 Introduction

Magic angle spinning (MAS) nuclear magnetic resonance (NMR) is one of the only spectroscopic techniques that can determine molecular structures at atomic resolution while probing molecular dynamics in insoluble, non-crystalline biomolecules and materials[1,2]. Accordingly, over the past two decades, MAS, together with dipole recoupling experiments [3], has evolved into a critical tool for structural biology research in systems such as amyloid fibrils [4-8], membrane proteins [9-11], macromolecular viral assemblies [12,13], and in a variety of materials science problems [14-16]. Despite these successful studies, many of the most pressing and complex biomedical and materials science challenges remain inaccessible due to limited resolution, inherently poor sensitivity, and the requirements for copious isotopically enriched samples.

To address these limitations in solids, several decades of development have led to the advent of sophisticated MAS stators and rotors, and a progressively miniaturized series of yttria-stabilized zirconia (YSZ) cylindrical and more recently spherical rotors [17-21]. While MAS rotors have been fabricated using a variety of materials -- silicon nitride, sapphire, Delrin® and MACOR® -- only YSZ has been employed to date in the fabrication of commercially available rotors less than 3 mm in outer diameter. With commercially available 0.7 mm YSZ rotors and N_2 gas as the driving fluid, MAS frequencies up to 111 kHz are routinely achieved. More recently prototype 0.4 mm and

0.5 mm YSZ rotors were reported to spin at $\omega_r/2\pi$=150 to 200 kHz MAS [22,23], again

using N_2. At present the spinning frequencies are limited by the speed of sound in N_2.

However, the improved resolution and sensitivity from spinning frequencies greater than

100 kHz have enabled important insights into the study of samples ranging from

amyloid fibrils to membrane proteins [24-26]. Despite these significant advances, the

achievable proton resolution under MAS restricts ubiquitous adoption of proton

detection in the solid-state, as is performed in solution NMR. Recognizing this limitation,

several groups have calculated the theoretical MAS frequency required to yield solution

like linewidths and coherence lifetimes in solids to be ~300 kHz and in many cases up

to 1 MHz (18-60 × 10^6 RPM) [27-29].

In addition to proton-detected MAS methods, dynamic nuclear polarization (DNP)

can be used to enhance the sensitivity of solid-state NMR. DNP uses microwave

irradiation to transfer the high spin polarization of electrons to nuclear spins at cryogenic

temperatures (typically ~100 K), offering a theoretical maximum enhancement of ~660

relative to conventional NMR [30,31]. This has stimulated significant developments with

gyrotron microwave sources and low temperature MAS probes that have enabled DNP

on biomolecules in frozen solution with enhancements routinely yielding ~50-100 [32-

34]. However, at the high magnetic fields (>16.4 T) required for improved spectral

resolution, typical CW DNP mechanisms become less efficient. Consequently, the

continued development of high field DNP methods is focused on improving (a)

polarizing agent efficiency, (b) microwave coupling efficiency into the rotor, (c) the

achievable sample temperature, with lower temperatures yielding higher enhancements,

(d) instrumentation for time domain DNP experiments and (e) the achievable MAS frequency at 100 K [35-44].

The continued expansion of MAS NMR to the most biomedically relevant systems likely requires realizing spinning frequencies greater than 300 kHz coupled with improved efficiency during DNP experiments. Current MAS NMR rotor technology has relied solely on decreasing the rotor diameter to achieve higher spinning frequencies, with a resulting decrease in sample volume up to the cube of the rotor radius. However, rotor diameters and associated spinning components are approaching fabrication limitations while the MAS frequency remains insufficient. Thus, without introducing new rotor materials used to fabricate MAS rotors, the required higher MAS frequencies are increasingly difficult to achieve.

The study of currently inaccessible ex-vivo protein samples using MAS NMR motivated our development of novel laser micromachining methods. These applications require the combination of high spinning frequencies, $\omega_r/2\pi > 100$ kHz, with large sensitivity enhancements from DNP at high magnetic fields. In particular, it is critical to employ a new rotor material and associated fabrication methodology that will enable MAS in the 150-300 kHz regime. The desirable properties of the material should include high strength, high thermal conductivity, and low THz absorption material, and, as illustrated in Figure 6.1 the ideal material to simultaneously satisfy these three criteria is single crystal diamond. Additional data relevant to this point is available in the Supporting Information, Figure 6.8. Diamond's cubic crystal structure provides exceptionally high atomic bond strengths, making it one of the strongest materials available. However, the high strength of diamond also prohibits application of traditional mechanical drilling or

abrasive grinding methods. While laser machining is utilized to fabricate diamond micro-structures, the required ~10:1 aspect ratio (referring to the ratio between the length and inner diameter of the rotor), micron tolerances and near zero internal taper of MAS rotors were thought to be unattainable using available laser machining strategies. As such, there were no commercially available methods of fabricating diamond rotors.

Herein we describe a novel laser micromachining strategy using dual-sided axial ablation to fabricate diamond rotors with less than 0.05° of internal taper while maintaining micron tolerances. We quantify spinning stability at $\omega_r/2\pi$ =111 kHz with a standard deviation in spinning frequency of <4 Hz (0.004%), further demonstrating the success of the machining strategy. Finally, we present the initial ^{1}H detected MAS NMR spectra
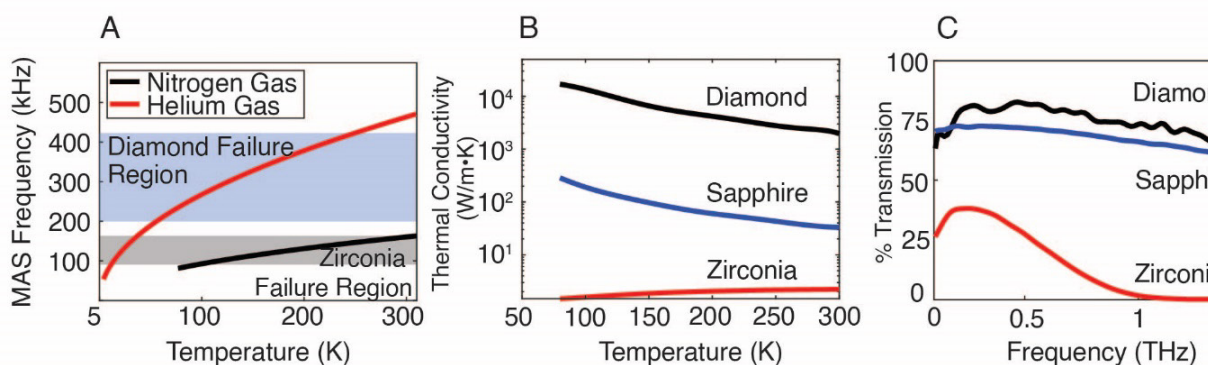
Figure 6.1. Advantages of Diamond Rotors. The diamond mechanical failure region is estimated to be a factor of 1.5-2.5 times higher than that of conventional YSZ rotors. Over the range of required temperatures for DNP NMR, using diamond will allow for MAS frequency increase by taking advantage of helium gas's high speed of sound. Speed of sound data for both helium and nitrogen gases as a function of temperature obtained from Ref [45]. **(B).** The improved thermal conductivity of single crystal diamond relative to sapphire or zirconia offers rapid sample temperature equilibration and efficient heat dissipation induced during fast MAS and microwave irradiation under DNP. Thermal conductivity data obtained from Ref [46-48]. **(C).** THz field transmission measurement for diamond, sapphire ('C-cut' orientation), and zirconia.

obtained using diamond rotors. These results highlight the feasibility and potential dramatic change that continued development of such technology can bring to the field of solid-state NMR.

6.2 Experimental

6.2.1 Rotor Fabrication

Rotors were fabricated using an Oxford Lasers (Didcot, Oxfordshire, UK) A-series laser micromachining system equipped with a Q-switched 532 nm diode-pumped Nd:YAG laser with a spot size of 13-14 µm. The pulse duration was ~ 20 ns at a repetition rate of 5 kHz. Single crystal high pressure high temperature (HPHT) type Ⅰb diamond was purchased from Element6 (Didcot, Oxfordshire, UK) for ~ $20/mm^3. All machining operations were aligned to the 100 (4 point) crystal axis to avoid the (111) diamond cleavage plane. A lab-fabricated precision lathe apparatus was used for all machining operations and relied upon a Thorlabs (Newton, NJ, USA) DDR100 direct drive rotary stage to achieve rotational frequency of 2.76 Hz (166 RPM) during both inner and outer diameter machining steps. The diamond was secured using a flexural clamp fabricated from 17-4 stainless steel and was mechanically flipped for a second axial machining step to reduce inner diameter taper. Alignment was maintained in this process through use of a fabricated Kelvin-style magnetic kinematic coupling system (Figure 6.9). Typical fluences used ranged from 300 J/cm^2 to 770 J/cm^2. A complete description of the fabrication process is given in Figure 6.10. Following fabrication, the rotors were subjected to 24 hours of heat treatment at 600°C in air to remove graphite and amorphous carbon formed during machining using a tabletop oven.

6.2.2 Rotor Characterization

Immediately following machining, graphite coated machined surfaces were characterized using a Hitachi FlexSEM1000 SEM (Tokyo, Japan). Inner diameter tapers were measured using a Nikon Metrology XT H 160 MicroCT (Tring, UK) at 3 μm voxel resolution. CT reconstruction was performed using CT Pro3D XT 5.4 software (Nikon Metrology, Tring, UK) and visualized using VGStudio by Volume Graphics Inc. (Charlotte, NC, USA). Rotor inner and outer diameters were characterized using a Keyence (Osaka, Japan) TM-X5006 telecentric measurement system with ±0.2 μm measurement positional accuracy. A detailed description of rotor measurements is given in the supporting information.

6.2.3 Raman Analysis

Single crystal HPHT diamond was analyzed without modification, in addition to machined samples pre- and post-heat treatment. Highly ordered pyrolytic graphite (HOPG) ZYB quality was purchased and used without modification from Ted Pella (Redding, CA, USA) as a graphite standard. Raman analysis was performed using a Renishaw Invia Reflex spectrometer equipped with a confocal microscope. Raman excitation was performed using a 532 nm laser. Raman shifts were calibrated against a silicon standard and data was processed using Renishaw's WiRE™ software.

6.2.4 THz Transmission Measurements

Terahertz transmission spectra were collected using a standard terahertz time-domain spectroscopy (THz-TDS) [45]. Broadband THz radiation was generated by optical rectification in a 1 mm thick ZnTe crystal using the 1 mJ, 100 fs output of an

Astrella Ti:Sapphire regenerative amplifier (Coherent Inc, Santa Clara, CA USA) operating at a repetition rate of 1 kHz and with a center wavelength of 800 nm. The THz beam was focused onto the sample (beam waist ~ 2 mm) at normal incidence, and then collected and refocused onto a 2 mm thick ZnTe crystal for electro-optical detection using three paraboloid mirrors after sample transmission. Sample thicknesses were 1.93 mm, 1.17 mm, and 6.37 mm for zirconia, diamond, and sapphire, respectively. 10% of the amplified laser output was split off prior to THz generation, time-delayed, and recombined with the THz beam at the detection crystal. Time-domain traces of the THz electric field were obtained by time delaying the THz and 800 nm probe pulses with respect to each other in a stepwise fashion. In this process, the instantaneous THz electric field at each time-step is encoded onto the polarization state of the probe pulse, which is then read out using a typical balanced detection scheme. THz transmission spectra were then obtained by computing the fast Fourier transform of the time-domain THz traces collected with and without the sample in place. The refractive index, surface reflections, and absorption coefficient were used to compute the absorption and reflection coefficients, A and R, Figure 6.8. These were then used to compute the percent transmission for a 1 mm sample thickness of each material using the equation T= 1-A-R.

6.2.5 MAS Stability Testing

Diamond rotors were fitted with Bruker BioSpin (Billerica, MA, USA) Vespel® drive tips and end caps. For MAS stability testing rotors were packed with potassium bromide powder (KBr) purchased from Millipore-Sigma (Burlington, MA). MAS control

was achieved using dry nitrogen spinning gas, a MAS 3 Controller (Bruker BioSpin, Billerica MA, USA), and a 0.7 mm test stand system (Bruker BioSpin, Billerica, MA USA) (Figure 6.16). MAS frequency was recorded at 1 s intervals using a Rigol oscilloscope (Suzhou, China) DS1104Z oscilloscope and logged using a Python script. The spinning frequency data was analyzed using Matlab (Mathworks, Natick MA). A 0.7 mm YSZ rotor was used as a standard in MAS stability measurement and was purchased from Bruker BioSpin. 1.3 mm YSZ rotors used in failure testing were purchased from O'Keefe Ceramics (Woodland Park, CO USA), packed with KBr, and fitted with end caps and drive tips were purchased from Bruker BioSpin.

6.2.6 NMR Spectroscopy

A diamond rotor was packed with a 1:1 mixture of U-^{13}C, ^{15}N N-Formyl-methionyl-leucyl-phenylalanine-OH previously packed into a larger MAS rotor and zirconia powder (Sigma Aldrich, St. Louis MO). All spectra were acquired at a static field of 18.8 T (800 MHz ^{1}H) with a three channel (HCN) 0.7 mm Bruker MAS probe. The sample was spun at 111 kHz using a MAS 3 controller. The 90° pulse durations were 1.875 µs, 3 µs, and 3 µs for ^{1}H, ^{13}C, and ^{15}N, respectively. Dipolar based CP-HSQC spectra were recorded using the pulse sequence previously described [46]. ^{1}H-^{13}C forward cross polarization (CP) was achieved with a contact time of 2 ms while the ^{1}H RF-field amplitude was ramped from 142 kHz to 158 kHz and the carbon RF field was constant at 36 kHz. ^{13}C-^{1}H back CP was achieved using a contact time of 1.2 ms while the proton RF field amplitude was ramped from 158 kHz to 142 kHz while the ^{13}C RF amplitude was constant at 45 kHz. ^{1}H-^{15}N forward CP was achieved with a contact time

of 1.5 ms while the proton RF amplitude was ramped from 140 kHz to 156 kHz and the ^{15}N RF amplitude was constant at 28 kHz. The ^{15}N-^{1}H back CP was achieved with a 1.2 ms contact time during which the ^{1}H RF field was ramped from 156 kHz to 140 kHz while the ^{15}N RF amplitude was constant at 40 kHz. During both CP-HSQC experiments, swept-low power TPPM at an RF field amplitude of 22.6 kHz was used for proton decoupling during t_1 and WALTZ-16 was applied to ^{13}C or ^{15}N at RF field strength of 10 kHz [47,48] . Water suppression was achieved through the MISSISSIPPI pulse sequence without homospoil gradients [49], using a 23 kHz RF field and 200 ms pulse duration. Spectra were apodised using 60° shifted squared sine bells and zero filled to at least twice the number of points in the indirect dimension. Additional acquisition parameters are given in Table 6.2.

6.3 Results and Discussion

To address current limits in MAS instrumentation, and thus applications of MAS NMR, we developed laser micromachining methods to realize diamond rotors. Prior to this work, it was predicted that the combined high aspect ratio, micron tolerances and near zero required
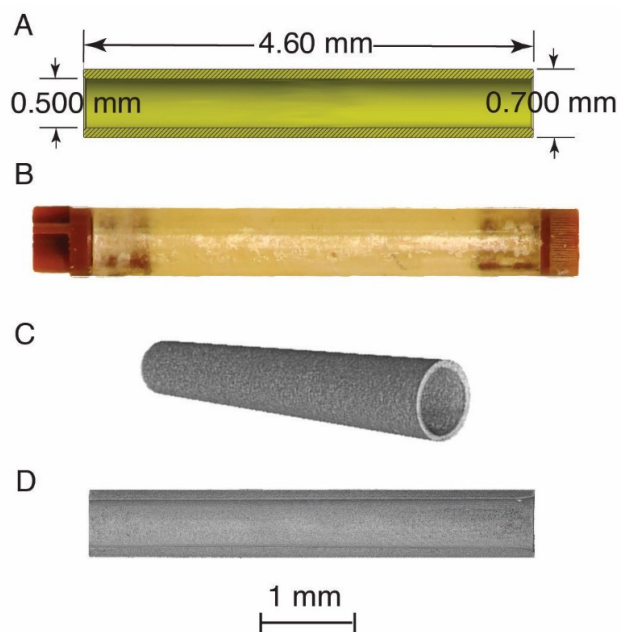
Figure 6.2. Diamond rotors. (A). CAD model of 0.7 mm rotor and associated dimensions. (B). Photograph of assembled diamond rotor including drive tip and end cap. (C). Isometric view of diamond rotor from microCT scan. (D). Cross section view of microCT scan of a diamond rotor.

256

internal taper angle could not be achieved in diamond. However, we demonstrated a dual-sided axial machining strategy that enabled fabrication of diamond rotors. During nanosecond laser machining of diamond, thermal energy is absorbed by imperfections in the diamond crystal lattice, resulting in a phase transformation from diamond to graphite. At radiation levels beyond the threshold fluence of diamond, graphite is largely vaporized and expelled from the inner diameter of the hole. However, during this process, the laser beam becomes partially attenuated by the formation of a plasma, effectively reducing the depth of hole that can be obtained in

Figure 6.3. SEM of diamond rotor. (A). Diamond rotor side 1 (entrance hole) with annotated wall thickness. (B). Diamond rotor side 2 (exit hole).

diamond. Fluences at least twenty-five times the ablation threshold for diamond combined with dual-sided axial machining allowed sufficient radiation incident to the diamond, enabling the fabrication of ~ 5 mm deep holes in diamond with ~0.5 mm diameters.

To quantify the geometric dimensions and tolerances achieved during laser micromachining, we employed a variety of methods including SEM, microCT and optical telecentric measurement. The dimensions for several commercial zirconia rotors and diamond NMR rotors fabricated in-house are given in the supporting information, (Table 6.1). Typical measured outer diameters and rotor-to-rotor tolerances are 695 ± 5 µm, as determined using a non-contact optical telecentric measurement system with a published accuracy of ± 0.2 µm. With this method, we were able to achieve typical internal tapers of less than ~ 0.05° over 4.6 mm, as determined by analysis of SEM data (Figure 6.3) and verified by microCT (Figure 6.2). The resulting rotors produced using mechanical re-orientation (Figure 6.9) demonstrated an inner and outer diameter concentricity error of less than 13 µm for all rotors, as shown in the SEM measurements.

The total fabrication time per rotor, which is mostly automated, is currently ~ 6-10 hours, with the potential for optimization to further reduce the fabrication time. The reproducibility of the fabrication scheme used to date is highly dependent on the structural integrity of the flexural clamping mechanism used to hold the rotor during fabrication, shown in the supplemental information, along with operator technique and careful alignment of the machining apparatus. These shortcomings can be further improved by changing the machining methodology to reduce the need for manual manipulation of partially machined rotors. Despite this, our current strategy for fabricating diamond rotors is uniquely suited to continued miniaturization of MAS components, whereas conventional ceramic drilling technologies are already
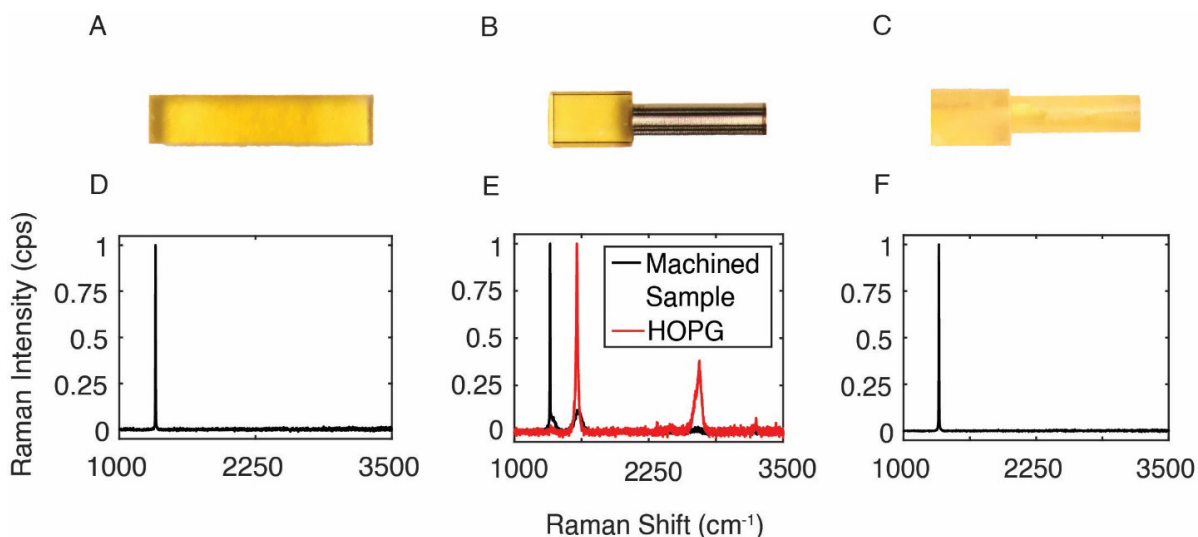
Figure 6.4. Raman analysis of diamond rotor fabrication. (A, D). In the starting material only diamond is detected. (B). Photograph of machined diamond material without heat treatment; graphite layer is visually contrasted with unmachined yellow diamond. (C). After heat treatment the graphite is observed to be removed. (E). Raman spectroscopy of HOPG graphite Raman spectra (red) used as a standard sample used to confirm presence of graphite on machined sample (black). (F). Following 24-hour heat treatment, graphite is removed from the machined sample.

approaching feasibility limitations. For further details on the machining process, we refer the reader to the supplementary information.

Raman spectroscopy was used to confirm the laser ablation mechanism previously presented in the literature [49-53]. We confirmed the presence of the single, narrow resonance associated with single crystal diamond in the starting, un-machined material at 1333 cm^{-1} (Figure 6.4 D), in accordance with literature values [54]. Following laser ablation, a resonance at ~1585 cm^{-1} was observed, characteristic of the G band of graphite [55]. In the machined sample, we observed this band had broadened relative to a highly orientated pyrolytic graphite (HOPG) standard sample (Figure 6.4 E). Therefore, we conclude amorphous carbon species are formed as indicated by the broadening of both resonances in addition to graphite formation. Finally, we note the

reduced intensity of the graphite signal relative to the diamond signal in the machined

sample. This supports optical telecentric measurements taken before and after heat

treatment indicating the layer of graphite formed is on the order of 1-2 μm thick.

For use in NMR and DNP applications, the electrically conductive graphite

species must be entirely removed from the rotor prior to use in experiments. The

surface graphite could prohibit efficient transmission of microwaves into the rotor for

DNP and serve as a potential source of electrical arcing to the transmit and receive coil.

To remove the accumulated graphite, a high temperature oxidative step was employed

at 600 °C for 24 hours [56,57]. Following heat treatment, the Raman analysis was
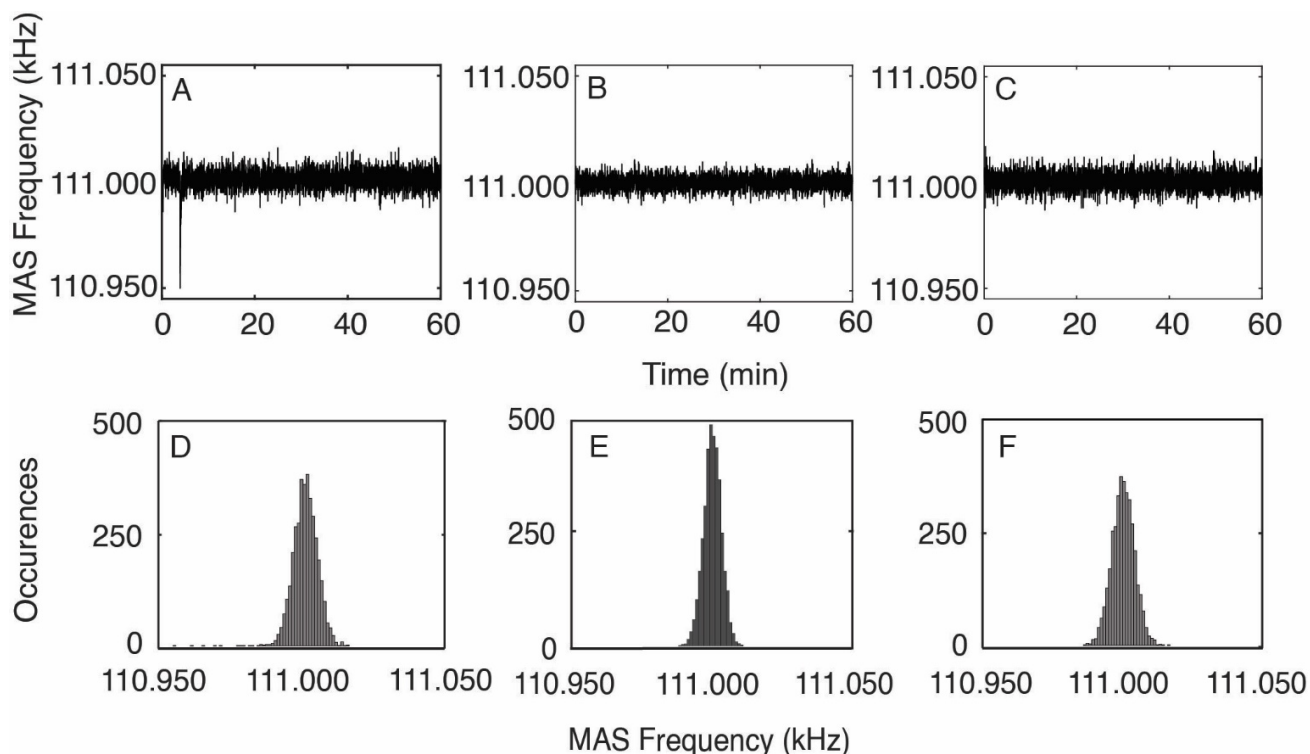
Figure 6.5. MAS stability measurements. Top Row shows time dependent traces of (A) YSZ rotor, (B). Diamond rotor 1, and (C). Diamond rotor 2. Bottom row shows histogram plot at a mean spinning frequency of 111.001 kHz. (D). YSZ rotor, standard deviation of 4.43 Hz. (E). Diamond rotor 1, standard deviation of 3.13 Hz. (F). Diamond rotor 2, standard deviation of 4.04 Hz.
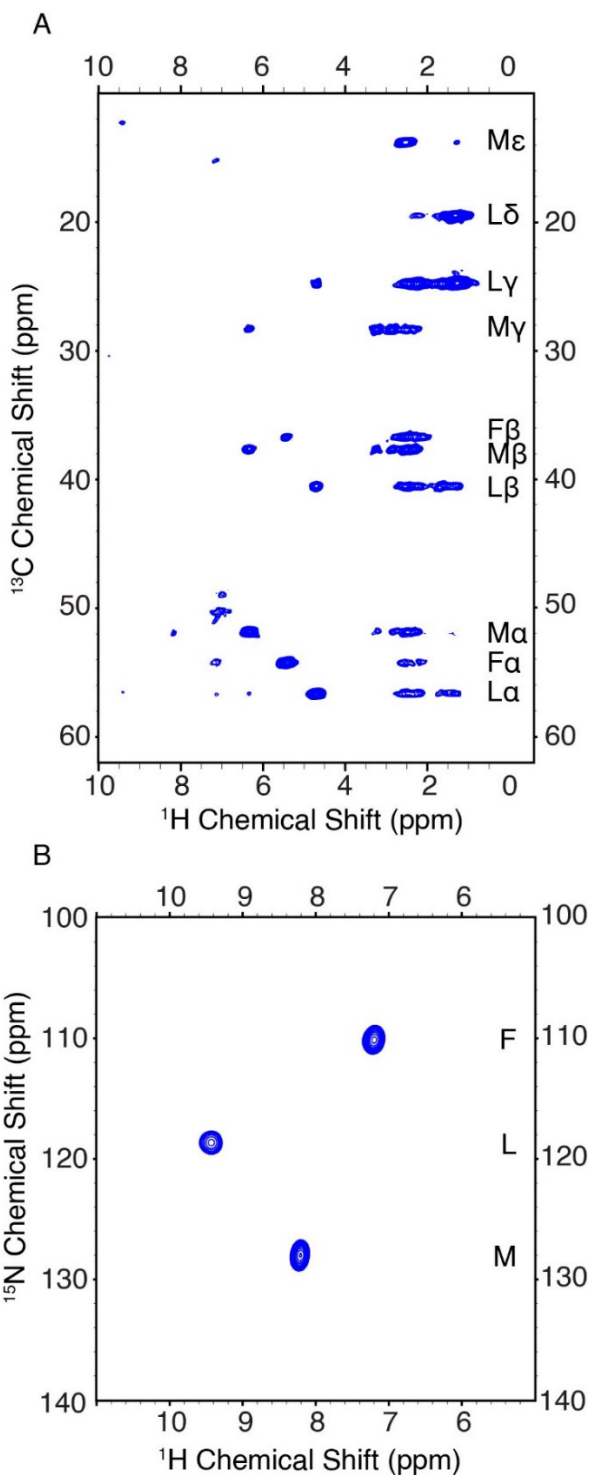
Figure 6.6.[1]H detected spectra of U-^{15}N,[13]C-N-*f*-MLF-OH. Spectra recorded using a diamond rotor. (A). (H)CH correlation spectrum. (B). (H)NH correlation spectrum.

repeated, and signal from graphite or other sp[2] carbon species was absent (Figure 6.4 F). Overall, Raman spectroscopy confirmed the ablation mechanism and importantly verified the absence of graphite at the end of rotor processing.

All 0.7 mm rotors were packed with potassium bromide ($\rho_{KBr} = 2.75 \ g/cm^3$) and spun to 111 kHz manually using a test stand with MAS 3 controller supplied by Bruker. The standard deviation in spinning stability over the course of one hour at 111 kHz was determined to be 3.13 Hz and 4.04 Hz for each of the two diamond rotors we tested, as shown in Figure 6.5.

The standard deviation in spinning stability over one hour was also measured for a zirconia rotor at 111 kHz and was determined to be 4.43 Hz (Figure 6.5. A, D). We note

here the spinning stability is impacted by both the rotor-bearing interaction that is modulated by rotor mass imbalance in addition to the stability of the drive and bearing gas regulation. The measured stability of the MAS 3 controller used for these experiments was 2696 ± 2.14 mBar and 4112 ± 5.35 mBar, for bearing and drive gas, respectively. Importantly, using diamond rotors results in a decrease in the force exerted on the rotor by ~40%, afforded by the reduction in rotor density when using diamond (3.5 g/cm^3) relative to YSZ (~6.0 g/cm^3).

In Figure 6.6, we show ^{1}H-detected ^{13}C and ^{15}N MAS NMR spectra of n-formyl-methionine-leucine-phenylalanine-OH (N-*f*-MLF-OH) recorded using a diamond rotor for a proof of concept set of experiments at 111 kHz. Likely due to the minor remaining concentricity errors discussed previously, the spin up profile of the diamond rotors is non-linear (Figure 6.18); we attribute this behavior to excitation of translational and whirl resonance conditions between 2-20 kHz [58]. To reduce risk to the NMR probe during rotor spin up, the N-*f*-MLF-OH powder was mixed in a 1:1 ratio with YSZ powder, which reduced the effective concentricity error, lowering the translational and whirl resonance conditions. This improved the linearity of response to drive gas and ensured the NMR probe was not damaged during these initial experiments. However, the rotors are sufficiently concentric and balanced to achieve highly stable rotation at greater than 111 kHz (6.6 × 10^6 RPM) with lower density samples. The dipolar based (H)NH and (H)CH heteronuclear correlation experiments were recorded without electric arcing, confirming the absence of electrically conductive graphite. Additionally, the spectra obtained were free of any ^{13}C background signal from the diamond rotor itself. This is afforded by the expected long relaxation rates of the highly ordered carbon species in ^{13}C natural

abundance single crystal diamond. In addition, the use of cross polarization transfer steps insured excitation of only ^{15}N or ^{13}C near ^1H, preventing detection of ^{13}C from the diamond rotor itself. The acquisition of proton-detected heteronuclear correlation experiments demonstrates the utility of diamond rotors for use in NMR and their compatibility with standard, commercially available instrumentation.

Resolution in MAS NMR experiments remains limited by the accessible spinning frequency. To date, rotor outer diameters have been continuously decreased to access higher MAS frequencies using YSZ. Despite these efforts, the current maximum MAS frequency achievable is 200 kHz, only 20% of the upper bound of the theoretically required MAS frequency to achieve solution-like resolution in complex, solid state biomolecules. At present, the highest MAS frequencies can be achieved using 0.4 mm rotors, which approach the practical limit of conventional ceramic machining practices.

The maximum achievable MAS frequency is ultimately determined by three factors:(1) the speed of sound of the gas used in the air bearings and gas turbine, (2) the structural integrity of the rotor material used, and (3) the efficiency of the turbine and air bearings. Significant rotor turbulence and reduced drive efficiency is expected as the circumferential frequency of the rotor approaches the speed of sound for a given spinning gas [59]. The maximum MAS frequency of a rotating cylinder is given by the rotor's circumferential frequency of $v/2\pi r$, where v is speed of sound of the gas used and r is the rotor outer diameter. For a 0.7 mm diameter rotor and nitrogen gas, the maximum circumferential frequency is 161 kHz or a surface speed of 354 m/s. In practice, MAS rotors typically operate at a maximum ~80% of the speed of sound in N_2 or air due to frictional losses in the air bearings [59]. Using nitrogen gas, we achieved

maximum MAS frequencies of 120 kHz, which has a corresponding surface speed of 264 m/s, or roughly 75% the speed of sound. 0.7 mm YSZ rotors are rated to 111 kHz, or 68% the speed of sound.

To exceed these frequencies, helium gas can be used to access a ~ 3 times improvement in spinning frequency afforded by a ~3 times increase in the speed of sound of helium gas relative to nitrogen, (Figure 6.1 A) [60]. To date, helium has mainly been used in solid-state NMR to realize low temperature experiments for improved sensitivity under DNP, notably without observation of electrical arcing [17,60-66]. However, the use of helium to achieve faster MAS at room temperature has been restricted to use with large rotors due to challenges with the stability of current air bearing designs which are not sized for use with helium lubricant [20,67]. Recently, significant efforts in the optimization of air bearings for use with helium gas and 0.4 mm zirconia rotors only resulted in a maximum spinning frequency of 18 kHz, compared to 110 kHz in air [67]. The maximum MAS frequency we achieved with a 0.7 mm rotor and 100% helium gas was 80 kHz. When tested, the rotor stability was extremely poor and changes in drive or bearing pressures by < 10-20 millibar could result in fluctuations in the MAS frequency of several kHz or lead to rotor crash. With a 70:30 volumetric mixture of helium: nitrogen gas, diamond rotors were spun to 124 kHz but could not be increased past this point (Figure 6.17). At 124 kHz the significant rotor instability led to a diamond rotor crash, however, the rotor was recovered intact and without damage. The same rotor was spun to ~123 kHz with nitrogen gas and did not display this instability, in agreement with past observations using helium gas. As shown in Figure 6.19, we found the initiation of MAS is nontrivial and was found to be generally unreproducible with 0.7

mm rotors spun with helium. 1.3 mm YSZ rotors achieved 88-89 kHz using 100% helium gas when packed with KBr, however, this required considerable optimization of the bearing and drive pressures.

The non-trivial application of helium gas to rotors < 1.3 mm in diameter is likely due to insufficient bearing stiffness when helium gas is used in bearings design for air or nitrogen. Thus, access to higher MAS frequencies using helium requires fabricating bearings designed for helium gas by varying both the radial air gap and nozzle diameter to increase radial bearing stiffness. Overall, our result of $\omega_r/2\pi$ =124 kHz using a mixture of He and N_2 represents to our knowledge the highest MAS frequency achieved with helium. Prior to the fabrication of diamond rotors, the insufficient material strength of YSZ did not make the considerable investment into helium optimized bearings worthwhile. However, with the demonstration of diamond rotor technology and in-house diamond machining capabilities, helium optimized bearings have become a necessary and realistic research objective.

As the failure point of diamond rotors could not be obtained experimentally, we evaluated three models associated with rotor failure. Previous literature describing rotor failure is based on the tensile strength or the elastic modulus in determining hoop stress and bending mode limited frequencies, respectively [20,68,69]. In practice, failure of MAS rotors fabricated from brittle materials is more likely due to surface defects (flaws and cracks) serving as a stress concentration point from which failure is initiated [70,71]. These defects reduce the effective toughness of the material below its theoretical maximum with corresponding underperformance in MAS. In general, given comparable surface defect concentrations, a material with a higher fracture toughness resists crack

propagation and performs more closely to its theoretical strength and toughness than a

material with a low fracture toughness. The relative performance of MAS rotor materials

is properly predicted using basic fracture mechanics, given in terms of relative angular

frequency to that of YSZ in Figure 6.7 and considers the fracture toughness, density,

and Poisson's ratio for each material [72]. For further details on this calculation, we refer

the reader to the supporting information. The fracture toughness of YSZ can vary as a

function of mol % yttria stabilization with typical values between 3-8 MPa·m$^{1/2}$ [73-75].

For the 1.3 mm YSZ rotors stabilized with 5 mol% yttria the fracture toughness is 7

MPa·m$^{1/2}$. We note that specially engineered zirconia has reached fracture toughness

up to 15 MPa· m$^{1/2}$ [76]. For further comparison, we included silicon nitride which has

been used in larger MAS rotors and typically achieve higher MAS frequencies than YSZ
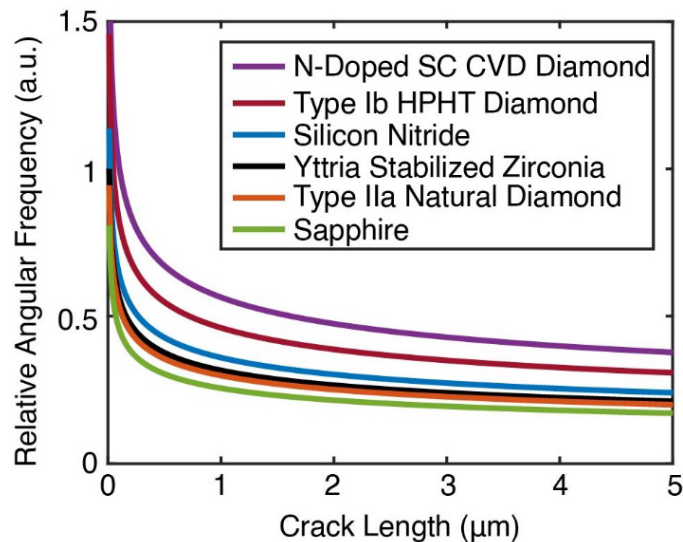
Figure 6.7. Fracture mechanics derived relative angular frequencies. Basic fracture
mechanics were applied to determine the theoretical performance of nitrogen doped single
crystal chemical vapor deposition (CVD) diamond, type Ib HPHT diamond (used in this
work), silicon nitride, type IIa natural diamond, and sapphire all relative to yttria stabilized
zirconia. The relative angular frequency is related to the density, fracture toughness and
Poisson's ratio of the material under consideration. For further details we refer the reader to
the supplemental information.

rotors. The fracture toughness is comparable to YSZ, but the reduced density accounts for improved performance over YSZ. Finally, fracture mechanics properly predicts that sapphire has the lowest anticipated MAS performance due to its low fracture toughness.

Diamond offers the advantage of improved fracture toughness and reduced density relative to YSZ. HPHT type Ⅰb diamond has a fracture toughness in the range of 10 ± 2 MPa·m$^{1/2}$, while nitrogen and/or boron doping of CVD diamond can increase the fracture toughness beyond 34 MPa·m$^{1/2}$ [77,78]. Type Ⅱa natural diamond has a lower fracture toughness between 4-5 MPa·m$^{1/2}$, but the reduced density results in comparable predicted performance to YSZ using fracture mechanics. A forthcoming publication demonstrates that nanosecond laser machining of diamond does not significantly alter the crystal lattice or introduce strain that would serve as surface defects leading to reduced performance in MAS. Finally, on the basis of hoop stress and bending mode failure regimes, the high tensile strength of diamond and high elastic modulus offer superior performance over other MAS rotor materials, as described in the supplemental information. Across the three analyses, we estimate an increase in achievable MAS frequency by ~1.5-2.5 times with diamond rotors.

We emphasize the approximate nature of these calculations, rotor failure can occur below the estimated frequencies due to the role of surface defects, sample packing, turbine imperfections, gas delivery failures and user error. For a precise model of rotor failure, complex fracture mechanics based finite element analysis or machine learning may be employed considering surface defects, fracture toughness, and yield strength [70,79]. Finally, efforts into measuring these parameters of MAS rotors could be worthwhile, though previously non-trivial given the small sample sizes [80].

Ultimately, the only way to determine the failure regime of diamond rotors is through extensive failure testing with helium gas.

Beyond the improvement in accessible MAS frequency, diamond rotors offer significant advantages for both ambient MAS NMR and DNP NMR. The higher thermal conductivity and improved microwave transmission properties are expected to result in larger DNP enhancements compared to traditional zirconia rotors. The improved thermal conductivity of diamond is expected to dissipate heat resulting more efficiently from microwave irradiation or frictional heating at fast MAS. More rapid and effective dissipation of heat reduces cooling demands for MAS NMR of biological samples at room temperature, in addition to DNP conditions. A potentially lower sample temperature afforded by diamond rotors with more effective sample cooling under DNP is expected to result in increased enhancements for the same microwave irradiation power in a zirconia rotor. As shown in Figure 6.1 (C), the THz transmission spectra of diamond and sapphire are relatively comparable, with diamond having a slight advantage. However, as shown in the supplementary material, diamond has lower surface reflection afforded by the low refractive index. In contrast, sapphire has a relatively high transmission across the THz regime, but the increased refractive index results in higher surface reflections. Overall, zirconia offers poor THz transmission in addition to high surface reflections. The high transparency of diamond coupled with low surface reflections makes diamond an optimal material for MAS DNP rotors at high fields. The experimental validation of diamond rotors under DNP is the subject of future work.

6.4 Conclusion

Diamond rotors offer the most promising technology to achieve solution-like resolution and coherence lifetimes in the solid-state. We have presented a new and novel laser machining method using dual-sided axial ablation to fabricate 0.7 mm diamond rotors, spun the rotors to $\omega_r/2\pi$=123 kHz using N_2 gas, and used the rotors to record ^{1}H detected MAS spectra at 18.8 T. Importantly, future developments and applications of this work can enable improved resolution and sensitivity in NMR and DNP enhanced NMR. In particular, diamond rotors, in addition to drive tips and end caps fabricated from diamond and helium bearings optimized for diamond rotors, should offer the ability to reach higher MAS frequencies. Along with improved microwave transmission and thermal conductivity diamond rotors offer a route toward performing high resolution ^{1}H detected DNP for unprecedented sensitivity and resolution of currently inaccessible biomolecules.

6.5 Supporting Information
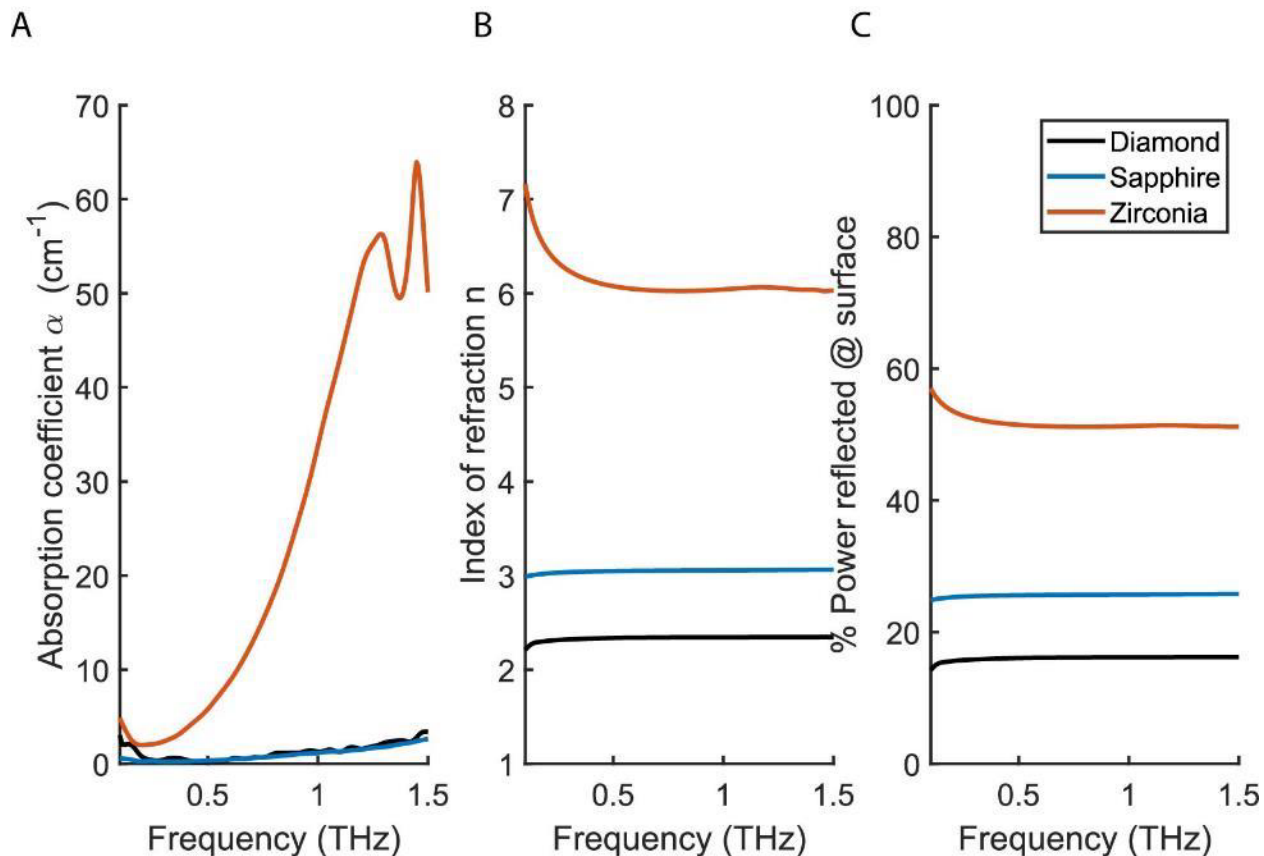
Figure 6.8 THz Spectroscopy. (A). The absorption coefficient of diamond, sapphire, and zirconia was determined across the THz spectral region. (B). Refractive indices of all materials agree with known values. (C). The percent of reflected power at the surface was measured. The surface reflections were found to be 16.1%, 25.6% and 51.5% for diamond, sapphire and zirconia at 0.5 THz and normal incidence, respectively.
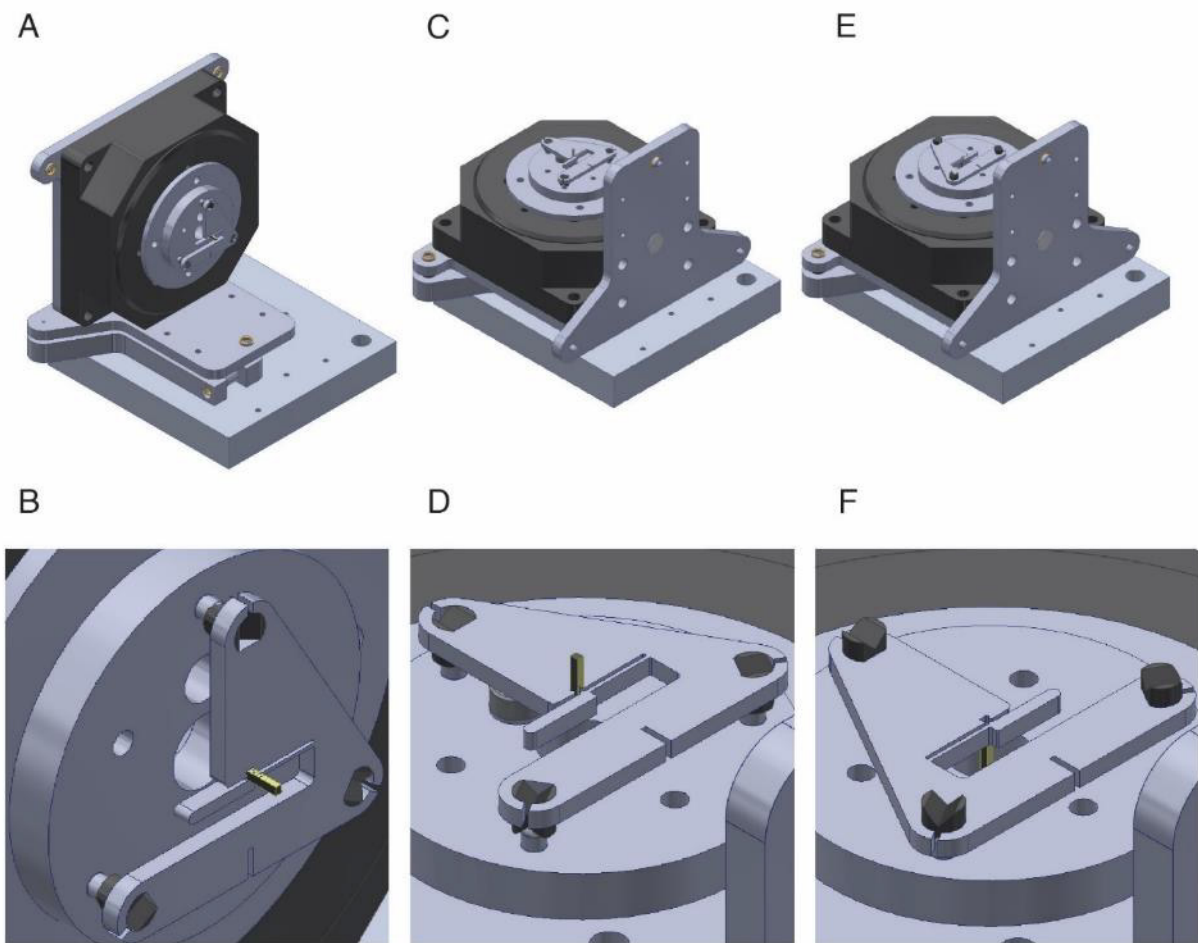
Figure 6.9. Lathe Apparatus. In all schemes, laser beam is incident from top of image. (A, B). Laser lathe scheme for outer diameter machining. This orientation is also used for final parting of the diamond rotor from remaining stock material at the end of machining. (C, D). Scheme for inner diameter machining with laser incident upon side 1. (E, F). Scheme for inner diameter machining with laser incident upon side. Mechanical reorientation is achieved through use of Kelvin-style kinematic coupling and has a known concentricity error of ~ 8 um.

1	Fixture starting diamond stock material (typical 1mmx1mmx5mm) log into flexural clamp and rotary stage. Optically obtain the stock material's center of rotation to align all machining operations to.
2	Use the pulsed-laser micromachining lathe to turn down the outer diameter using rough cuts with depth of 50 microns and traverse rate of 0.005 mm/s. Use telecentric measurement system to confirm diameter. End rough cuts when outer diameter is ~1.3 x the desired final diameter.
3	Use pulsed-laser micromachining lathe to turn down the outer diameter using cuts with depth of less than 10 microns, at higher fluences than in preceeding step, and 5x reduced laser traversing speed. Use telecentric measurement system to confirm desired outer diameter, continue finishing cuts until that diameter is achieved with 5% at maximum.
4	Re-orient lathe apparatus to align the laser incident axially to the top surface of the first side of the diamond rod. Machine using depth of cut of 500 microns and a width of the desired inner radius with rotary stage at frequency of ~3 Hz. Follow with finishing passes with depth of cut of 25 microns at fluence of 400-500 J/cm^2.
5	Perform mechanical flip to align the laser incident axially to the top surface of the second side of the diamond. Begin machining depth of cut of 500 microns and a width of the desired inner radius with rotary stage at frequency of ~ 3 Hz. Follow with finishing passes with depth of cut of 25 microns at fluence of 400-500 J/cm^2 to a depth of approximately half the length of the rotor.
6	Re-orient the lathe apparatus into starting lathe orientation. Using the laser traverse a line perpendicular to the outer diameter to cut a straight edge on the starting end of the rotor. Traverse across the outer surface of the rotor by the desired rotor length and cut a straight line perpendicular to the outer diameter to part the fabricated rotor from the excess stock material.
7	Perform metrology analyses using tools such as SEM, microCT and telecentric measurement systems.
8	Subject rotor to 600 °C heat treatment for 24 hours in air to remove graphite on the surface of the rotor.

Figure 6.10. Rotor Fabrication Process. Flow chart describing fabrication process used to produce diamond rotors in this publication. The outer diameter is machined in steps 2 and 3 with the lathe apparatus as shown in Figure 6.9 (A, B). Side 1 inner diameter is machined as in step 4 using the lathe apparatus as shown in Figure 6.9 (C, D). Side 2 inner diameter is machined in step 5 using the lathe apparatus as shown in Figure 6.9 (E, F).

Rotor Metrology

The rotor outer diameter was measured in multiple locations along the length of rotor and measured at 0° and 90° incident to the Keyence optical telecentric measurement device to capture any potential taper or runout in the measured outer diameter. The concentricity error on side 1 and side 2 of several diamond rotors are provided using the wall thickness measured using SEM, representative micrographs of these measurements are provided in Figure 6.12 and Figure 6.13. The reported concentricity is calculated for each side using (6-1) where C_x or C_y is the difference in wall thickness in the x or y direction measurements.

$$C = \sqrt{C_x^2 + C_y^2}$$

(6-1)

The inner diameter of each side was calculated taking the average wall thickness in both x and y directions. The inner taper angle, defined as the half angle, was computed as (6-2), represented in Figure 6.11.

$$\theta = \frac{1}{2}\tan^{-1}\left(\frac{ID_1 - ID_2}{L}\right)$$

(6-2)

Overall, concentricity error for side 1 represents the concentricity error associated with manually positioning the laser at the center of rotation of the diamond with use of built-in optical microscope on the Oxford laser machining system. Concentricity error for side 2 represents the concentricity error associated with the mechanical reorientation for the second axial machining step. Diamond rotors 1 and 2 correspond to the rotors described in the text and used in spinning stability measurements. The concentricity error in side 1 of rotor 2, and associated taper angle is

subject to ± 10 um error due to contaminant on the SEM micrograph of side 1 obscuring a clear view of the rotor wall thickness for one measurement in the x direction. Rotors 3 and 4 were fabricated while the flexural clamp began degrading but was not initially observed by the user. Nevertheless, rotor 3 was spun to ~ 80 kHz standard spinning stability on the order of ± 5 Hz. After 80 kHz the spinning instability began to increase, and the rotor was not spun to higher frequencies to avoid costly damage to the test stand apparatus. The undersized average outer diameter of rotor 3 was due to user error in the calibration of the z focus for the specific machining operation. Rotor 4 was not spun.

Due to the high cost of YSZ rotors, we were unable to collect high quality SEM micrographs of the electrically insulating YSZ rotors. As such, concentricity error and inner taper angle are not available for these rotors. Notably, the deviation in the outer diameter for YSZ rotors is comparable to that for diamond rotors.
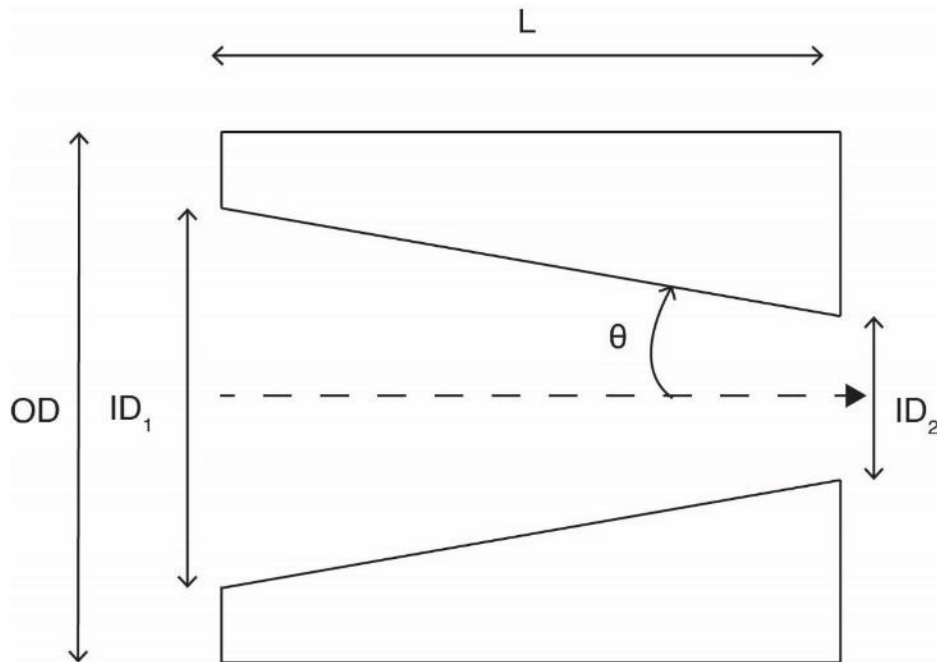
Figure 6.11. Diagram showing internal taper angle.

Rotor	Outer Diameter (µm)	Deviation (µm)	Concentricity error side 1 (µm)	Concentricity error side 2 (µm)	Length (mm)	Inner Diameter Taper angle
Diamond Rotor 1	697.2	± 3.15	3.2	8.1	4.592	0.04
Diamond Rotor 2	697.6	± 3.05	8.5*	9.5	4.591	0.02
Diamond Rotor 3	690.6	± 0.55	3.5	12.6	4.601	0.09
Diamond Rotor 4	699.8	± 2.7	10.1	12.2	4.586	0.02
YSZ Rotor 1	701.5	± 1.95	-	-	4.60	-
YSZ Rotor 2	695.2	± 3.7	-	-	4.61	-
YSZ Rotor 3	699.7	± 0.2	-	-	-	-

Table 6.1. Diamond and YSZ Rotor Measurements.
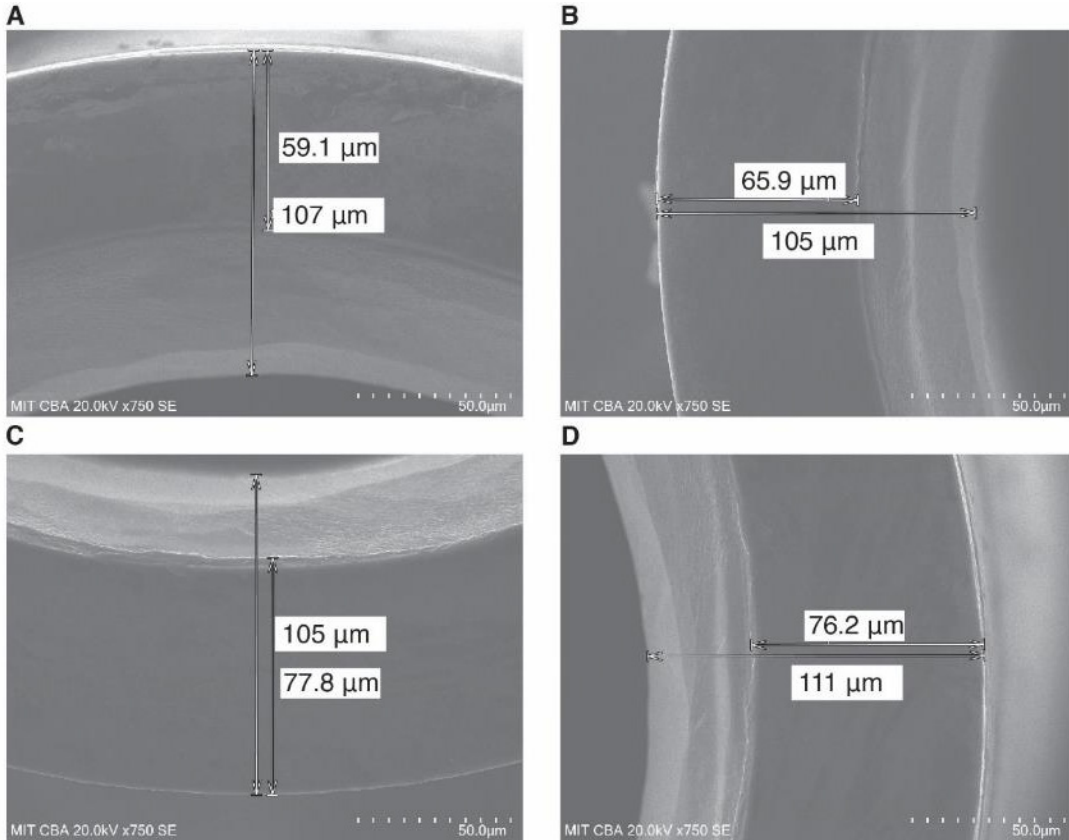
Figure 6.12.SEM micrographs of Side 1 of diamond rotor 1. Wall thickness measurement used to determine concentricity errors in x (B, D) and y (A, C). Arrows showing measurements were added during SEM analysis using FlexSEM1000 software package and used to generate the printed wall thicknesses. For reader clarity the font size of the measured wall thickness of the chamfered section and total wall thickness were enlarged using Adobe Illustrator.
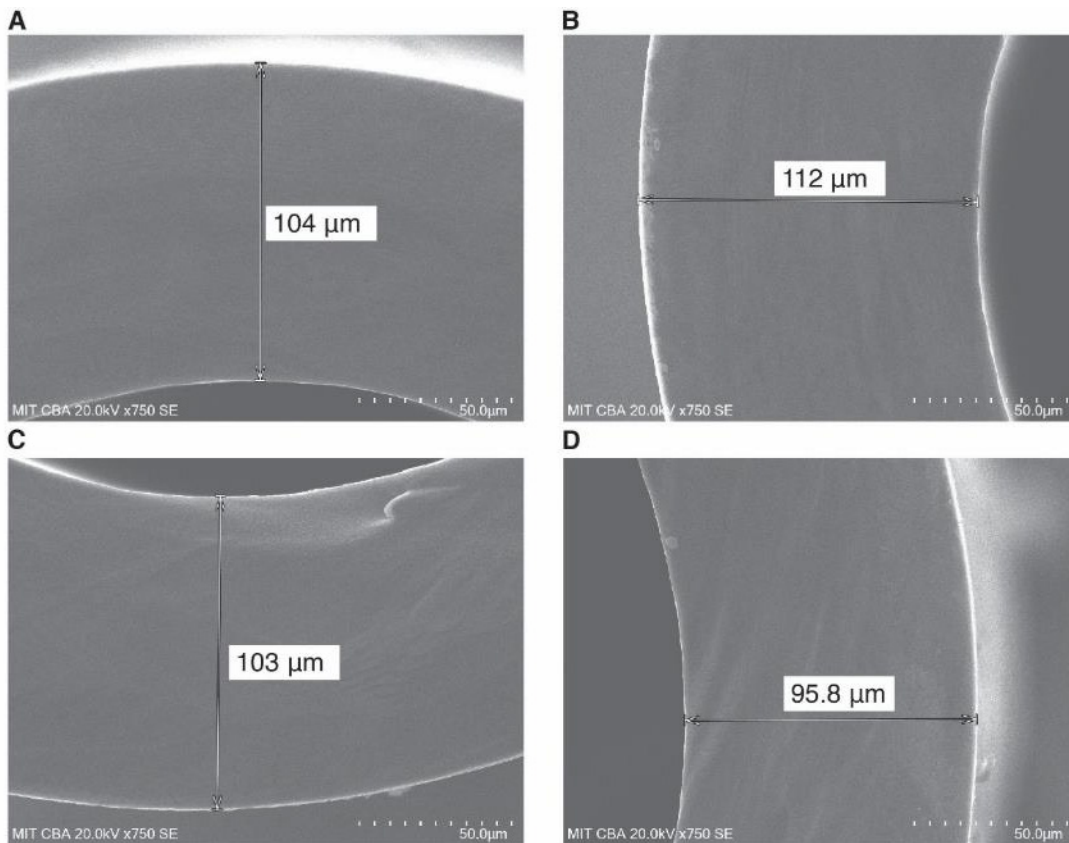
Figure 6.13. SEM micrographs of Side 2 of diamond rotor 1. Wall thickness measurement used to determine concentricity errors in x (B, D) and y (A, C). Arrows showing measurements were added during SEM analysis using FlexSEM1000 software package and used to generate the printed wall thicknesses. For reader clarity the font size of the measured wall thickness of the was enlarged using Adobe Illustrator.
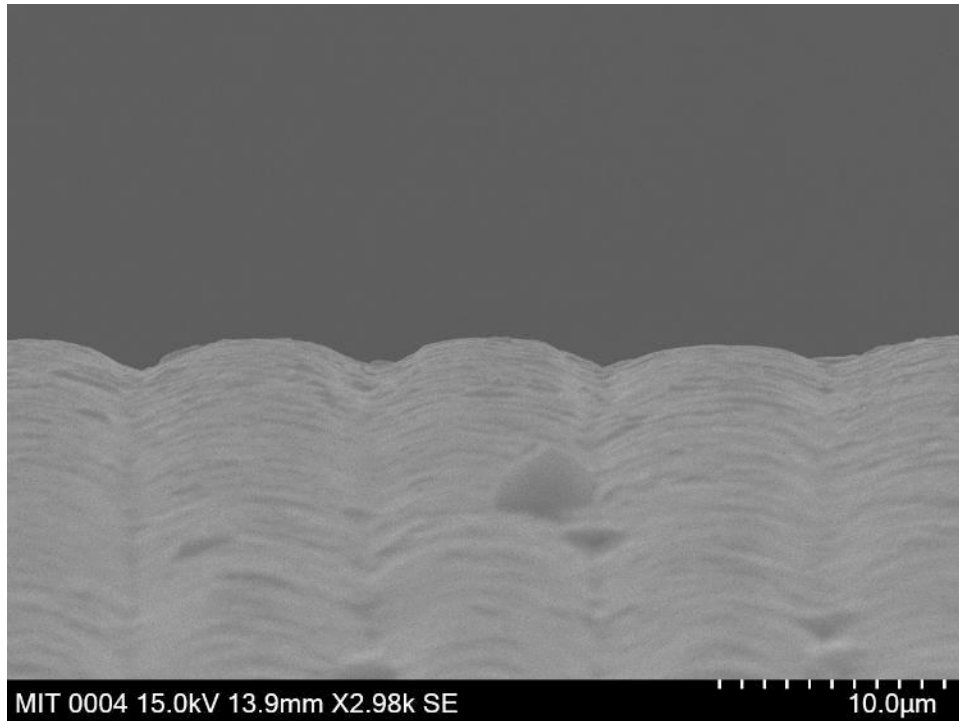
Figure 6.14. Surface finish of diamond rotor. SEM micrograph showing the surface finish along the outer diameter of the rotor. The surface finish is currently a result of the feed rate and rotary stage frequency given the 13 µm spot size. To date, we have not performed any laser polishing steps following outer diameter machining.
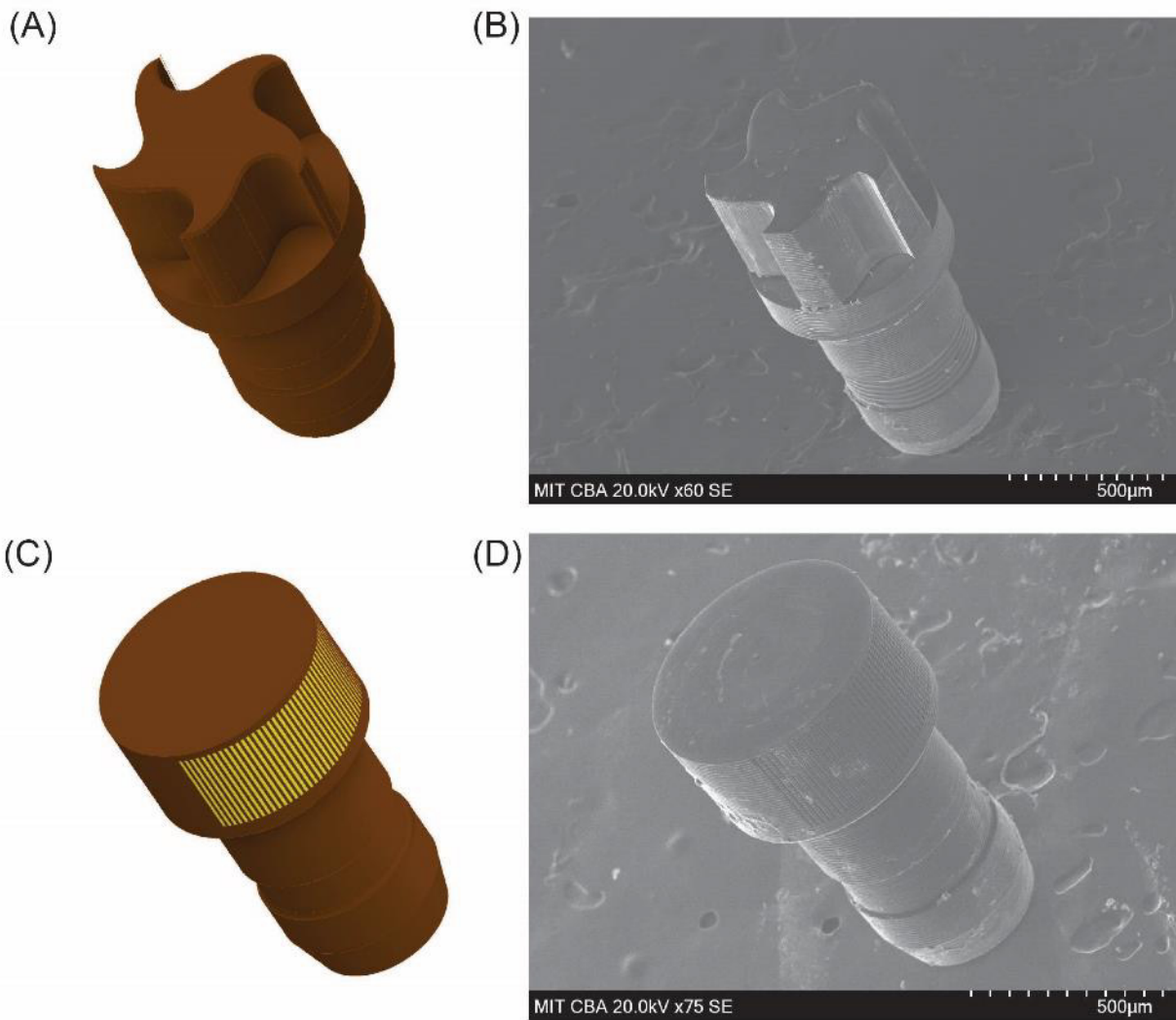
Figure 6.15. Diamond Drive Tip and End Cap. (A). CAD model of 0.7 mm drive tip (design courtesy of Bruker BioSpin). (B). SEM of fabricated diamond drive tip. (C). CAD model of 0.7 mm end cap. (D). Fabricated diamond end cap.
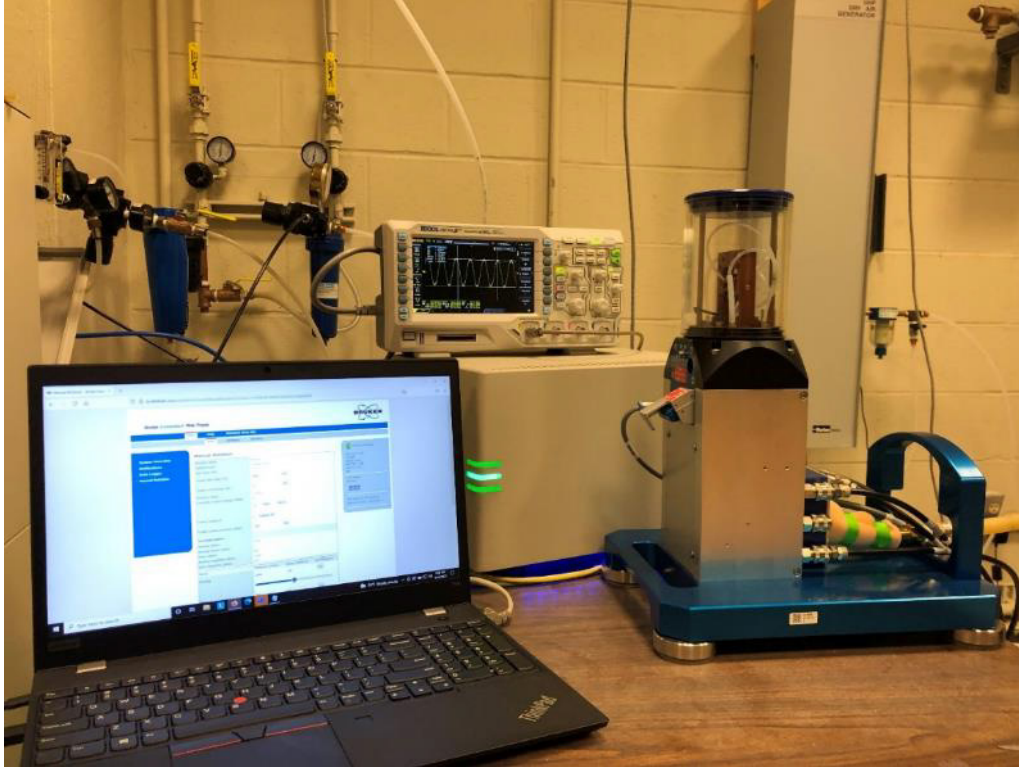
Figure 6.16. Test stand station for rotor stability measurements.
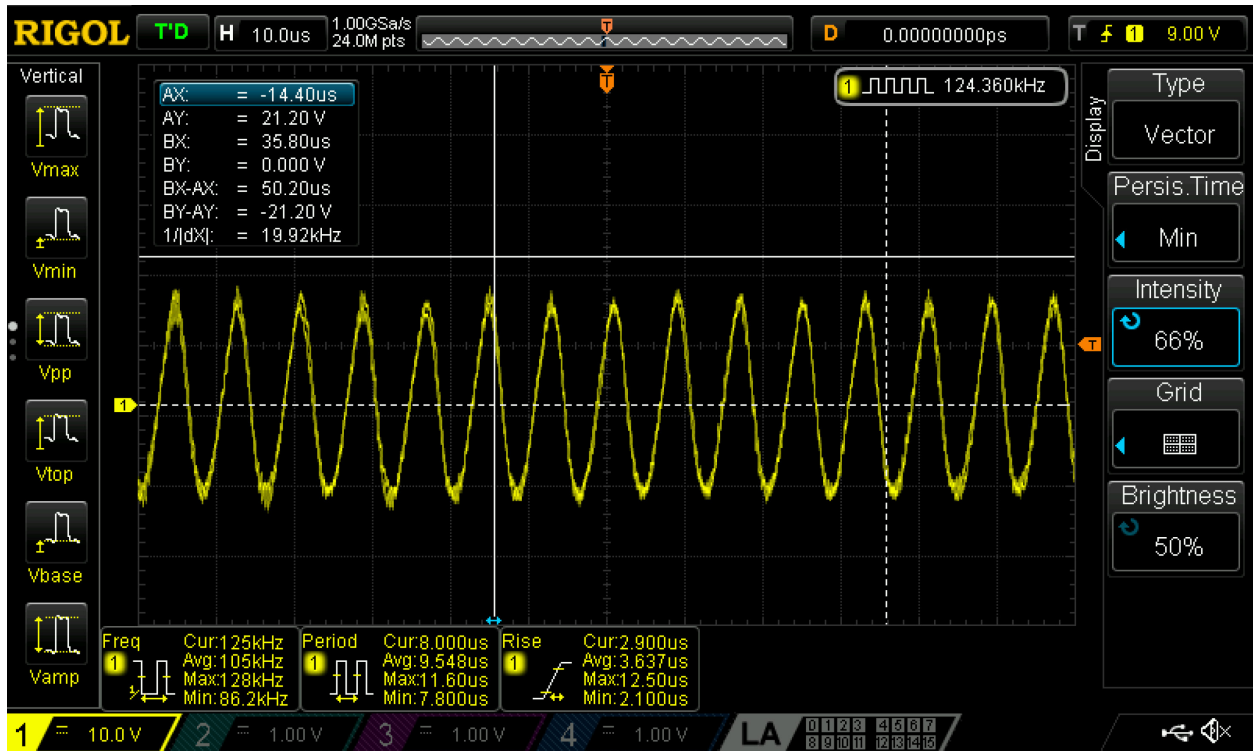
Figure 6.17. Oscilloscope trace during diamond rotor operation at 124 kHz. Rotor was spun using a 70:30 by volume mix of helium and nitrogen gas.
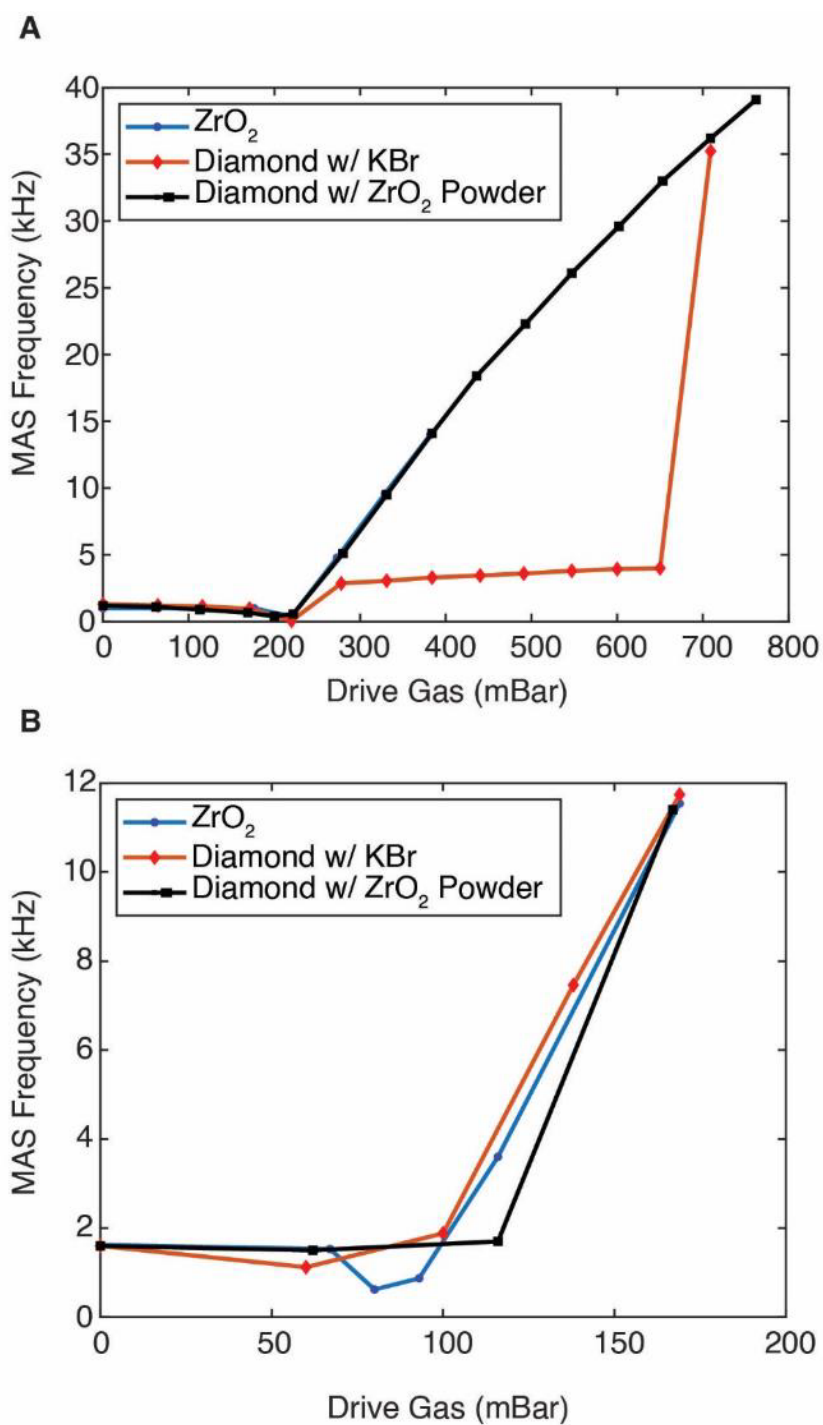
Figure 6.18. Response of rotor to drive gas as a function of bearing gas. (A). At high bearing pressure, typical of auto spinning procedure, zirconia powder (ZrO_2) packed into diamond rotor improves linearity of frequency response to drive gas. The heavy powder redistributes at low spinning frequency to reduce effects of concentricity errors. (B). At low bearing pressure where resonance mode excitation frequency is reduced, diamond rotors spin up linearly as a function of drive gas.
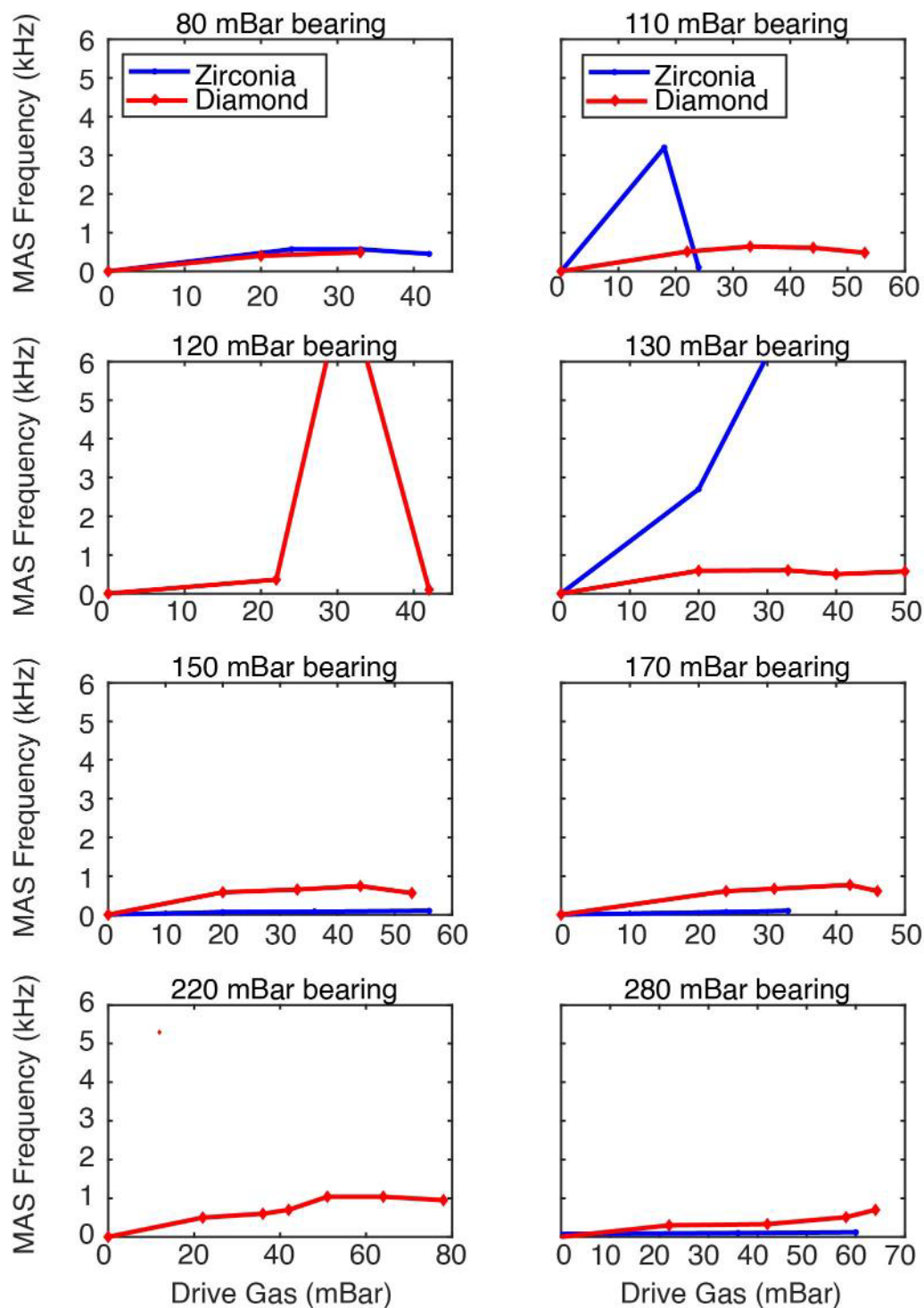
Figure 6.19. Helium MAS with 0.7 mm rotors. Spin up profiles using 100% helium gas for both drive and bearing for yttria stabilized zirconia and diamond 0.7 mm rotors. Overall, achieving MAS with helium and 0.7 mm has limited success and once MAS is intiated rotors are very unstable. Bearing pressures up to 2 bar were tried without success.

Spectrum	Max Evolution Time (ms)		Number of complex points		Spectral Width (Hz/ppm)		Scans per point	Interscan delay (s)	Experiment time
	ω_1	ω_2	t_1	t_2	ω_1	ω_2			
(H)NH	13.2	10.2	128	2048	4860/60	100,000/125	8	1.5	30 min
(H)CH	14.3	12.5	460	2048	16069/80	81521/102	8	1.5	1 hr 46 min

Table 6.2. Acquisition for parameters for (H)NH and (H)CH spectra.

This section provides three methods of evaluating a material's suitability for MAS. Inherent in all 3 models is variability in the material properties and surface defects in each sample. In all cases, the treatment is a simplified approximation and rotor failure can occur at any point due to external factors such as rotor packing, turbine failure, gas regulation failure, and user error or more significant surface defects or material strain than expected.

1. Crack induced failure

Property	Yttria Stabilized Zirconia	Single Crystal Diamond	Sapphire	Silicon Nitride
Tensile Strength (MPa)	550-690[a] (600)	180-5190 (2000)[b]	190-400 (300)	550
Young's Modulus (GPa)	200-220 (210)	1050	340-440 (360)	270-300
Fracture Toughness (MPa·m$^{1/2}$)	3-15 (7)[c]	4-34 (10±2)[d]	1.4-4.4 (3)	4-7 (6)
Density (g/cm^3)	5.85-6.10 (6)	3.52	3.98	3.17-3.25
Poisson's Ratio	0.31	0.1[e]	0.28	0.23

Table 6.3. MAS Rotor Material Properties. . For values given as a range, parenthesis indicate the value used in calculations described in the text. Values for YSZ found in [73,75,81], values for diamond are found in [20,77,78,82-84], and values for sapphire found in [85].

[a] Typical tensile strength is found in the range of 550-650 MPa, however, continued development of higher strength YSZ has yielded tensile strengths of 1690 recently in nanometric YSZ.

[b] The material properties of diamond vary considerably with natural, CVD and HPHT diamond.

[c] Continued development of YSZ and mol % of yttria dopant greatly affects the fracture toughness. The reported fracture toughness for the 1.3 mm YSZ rotors used in this work was 7 MPa·m$^{1/2}$, values up to 15 MPa·m$^{1/2}$ have been reported.

[d] The fracture toughness of diamond is highly dependent on synthesis and chemical dopants. For Type II a natural diamond, fracture toughness of 4.2$-$5.6 MPa·m$^{1/2}$ are reported. Type I b HPHT diamond, used in this work, has typical values of 10±2 MPa·m$^{1/2}$. The co-doping of boron and nitrogen into SC-CVD diamond has resulted in fracture toughness of 22-34 MPa·m$^{1/2}$. SC-CVD diamond with nitrogen dopants has resulted in fracture toughness of 15.2±4.8MPa·m$^{1/2}$. For further information, the reader is referred to [77]

[e] Poisson's ratio of diamond is orientation dependent with ranges of 0.07-0.2.

It has been described in the literature that in centrifugal loading conditions, brittle failure is dominant and determined by the fracture toughness [72,75]. The fracture toughness represents the critical value at which crack growth occurs, and in the case of MAS leads to rotor failure. The critical angular frequency for a material described by the fracture toughness, K_{IC}, the density of the material, ρ, the outer radius, R, Poisson's ratio, υ, and the crack length, l is described by (6-3).

$$\omega_C = \frac{2}{R}\sqrt{\frac{2K_{IC}}{\rho(3+v)\sqrt{\pi\,l/2}}} \tag{6-3}$$

This relation can be used to semi-quantitatively compare brittle materials resistance to crack propagation, and for a given length crack, the ability to withstand a higher angular frequency. This relation is solely dependent on the characterized density, fracture toughness and Poisson's ratio of the material. Moving beyond a solid rod, as described above, requires numerical simulation of scenario specific geometries and crack propagation mechanisms. For a simplistic comparison of common MAS NMR materials in the same standard geometry, we can compare the computed angular frequencies, relative to YSZ. As shown in Figure 6.7, this model accurately describes the known performance of silicon nitride, zirconia and sapphire. Type Ⅰb HPHTor nitrogen doped CVD diamond can offer improved fracture toughness relative to silicon nitride and YSZ, in addition to reduced density relative to YSZ may enable higher angular frequencies.

2.   Hoop Stress Analysis

Following the treatment of [20], we have used the tensile strength to calculate the hoop stress limited MAS frequencies. This describes the resistance against pressure generated at the internal surface of the rotor against the inner wall of the rotor, where the generated pressures due to MAS are at a maximum. We caution that the effective resistance against such pressure is dependent on the surface defects present and the fracture toughness of the material. We have shown this represents a lower bound frequency, particularly in the case of sapphire with a low fracture toughness. To describe the pressure to rupture a MAS rotor due to the centripetal force and pressure under MAS the force can be described by (6-4), with a mass, m, angular frequency, ω, rotor radius, r, rotor length, L, and rotor density, ρ.

$$F_c = m\omega^2 r = \pi r^3 L \rho \omega^2 \tag{6-4}$$

The hoop stress, θ_θ, on the inner surface of a thick-walled cylinder can be derived using Lame's equation, given in Equation (6-5) when evaluated at the inner radius, r_{ID}. The internal pressure is given by P_{int}, the external pressure by P_{ext} and the outer radius, r_{OD}. We take the external pressure acting on the MAS rotor to be the inlet pressure of the radial bearing gas, 2-3 Bar. The wall thickness of a typical MAS rotor is typically 0.125-0.156 times the outer diameter. We note that to apply the thin-walled cylinder approximation, the wall thickness should be less than 0.05 times the outer diameter.

$$\theta_\theta = \frac{P_{int} r_{ID}^2 - P_{ext} r_{OD}^2}{r_{OD}^2 - r_{ID}^2} + \frac{r_{ID}^2 r_{OD}^2 (P_{int} - P_{ext})}{(r_{OD}^2 - r_{ID}^2) r_{ID}^2} \tag{6-5}$$

We can re-arrange (6-5) to determine the maximum allowable internal pressure for a MAS rotor and setting the maximum hoop stress, θ_θ, to 70% of the tensile strength

of the material. For brittle glasses and ceramic materials, a safety factor of 70% of the maximum frequency has been used historically due to the potential for slow crack formation at high MAS frequencies [20,84].

For MAS frequency strictly limited by the tensile strength of the material, we would expect long-term failure to occur when the hoop stress exceeds the tensile strength. We denote this frequency f_θ, and can be numerical solved for using (6-6), where the sample density is denoted, ρ_s, the rotor wall material has a density of ρ_r, and a wall thickness of w.

$$f_\theta = \frac{1}{2\pi} \sqrt{\frac{2\,P_{int}}{\rho_s r_{ID}^2 + 2\rho_r r_{OD} w}} \tag{6-6}$$

For a sample density of 2.75 g/cm^3, typical of potassium bromide used in MAS stability measurements in this work, the results of the hoop stress limited MAS frequency are provided in Table 6.4. The hoop stress limited calculation approximately predicts the rated MAS frequency for both YSZ and sapphire MAS rotors using 600 MPa and 200 MPa tensile strengths, respectively, particularly in the case of larger diameter rotors. Given the experimental results of 0.7 mm diamond rotor spinning at 111-124 kHz, we can estimate that the tensile strength of the Type 1b HPHT diamond is at least ~ 650-750 MPa, making it at least comparable to zirconia. However, as rotor failure was not achieved, this is a lower threshold. This also suggests the diamond rotors fabricated do not contain severe surface defects or surface strains that would result in failure far below 111 kHz. The stator incompatibility remains the limiting factor on achieving high enough MAS frequencies to determine the failure regime of diamond rotors. In the case

of rotors < 2.5 mm the hoop stress limited MAS frequency is unable to accurately

predict the rated MAS frequency. While a higher tensile strength could be used, there

are several sources in the literature describing, particularly when the outer diameter is

small, that the tensile limited value may not represent the upper bound of the spinning

frequency [68,69].

3.   Bending Mode Failure Analysis

Bending mode failure occurs as the rotor natural frequency is approached and

the first vibrational mode is excited. Ideally, a MAS rotor will have a very high natural

frequency afforded by a high elastic modulus, as in the case of diamond. However, the

elastic modulus and associated bending mode analysis does not consider the role of

surface defects and crack propagation in brittle materials and can overestimate the

achievable MAS frequency. This is clearly the case for sapphire where the material has

insufficient toughness to approach bending mode failure.

Rotor OD (mm)	Rated MAS Frequency YSZ (kHz)	f_θ Yttria Stabilized Zirconia (kHz)	f_θ Diamond (kHz)	Rated MAS frequency Sapphire (kHz)	f_θ Sapphire (kHz)
4	15	15	32	10	10
3.2	24	20	45	15	14
2.5	35	28	63	N/A	19
1.9	42	30	63	N/A	19
1.3	67	50	109	N/A	33
0.7	111	90	196	N/A	60
0.4	160-200	152	324	N/A	99

Table 6.4. Hoop stress limited MAS frequencies. Hoop stress limited MAS frequency, f_θ, for common MAS rotor materials and sizes considering typical 70% safety factor. Sapphire MAS rotors are only commercially available and rated for use in 4 and 3.2 mm rotors.

To determine the upper bound of the rotor failure region, we calculate the rotor natural frequency of the first vibrational state of the bending mode resonance [68]. The natural vibrational frequency for the bending resonance of a tube is given by (6-7):

$$f_E = \frac{\lambda^2}{2\pi L^2} \sqrt{\frac{EI}{A\rho}} \tag{6-7}$$

Where E is the longitudinal elastic modulus, I is the moment of inertia, L is the length, λ is the first vibrational factor having a numerical value of 4.730, A is the cross sectional area and ρ is the density of the rotor, taking into account both the rotor and the sample. Equation (6-7) can be rewritten incorporating a numerical corrective factor of B, as recommended in [68] with numerical values provided for a range of L/D ratios, where D is the outer diameter. For the specific rotor sizes of interest, the value of B was numerically interpolated by fitting values from [68], provided in Table 6.5.

$$f_E = \frac{\lambda^2}{2\pi L^2} \sqrt{\frac{E(D^2 + d^2)}{16\rho}} B \tag{6-8}$$

A 70% safety factor is also applied to the rotor natural frequency calculation to determine the practical upper bound in MAS frequency, with values provided in Table 6.6. We have simplified the calculation to neglect the density of the rotor drive tip and end caps and consider a rotor entirely filled with sample of 2.75 g/cm^3. We note the end caps and drive tips are typically made of Vespel® with a density of 1.4 g/cm^3, comparable to the canonical density of a protein (1.35 g/cm^3).

In the case of YSZ rotors, we are typically unable with any level of statistical certainty obtain the exact failure mode of the rotor. However, from conventional

operation, it appears the practical MAS frequency is bounded between the hoop stress

and bending mode limited MAS frequencies, with the location within these bounds

dependent on the rotor diameter. For a 1.3 mm YSZ rotor packed with KBr (density 2.75

g/cm^3), operated with helium gas in a conventional stator we could repeatably achieve

failure at 89 kHz. Rotor instability was observed as well as a decreased effect of

additional drive gas before each failure. Whether failure was due to insufficient rotor

strength or the unoptimized bearings with helium gas is unknown. We emphasize the

approximate and semi-quantitative nature of these simplified approaches and

recommend the use of fracture mechanics simulations in the future.

Rotor Size	L/D	B
4	4.500	0.865
3.2	4.813	0.881
2.5	4.800	0.880
1.9	5.789	0.906
1.3	5.923	0.909
0.7	6.571	0.921
0.4	6.75	0.925

Table 6.5. Interpolated values of B. Numerical values of L/D provided in [80] were used to determine B for specific rotor sizes of interest and applied as a scaling factor in (6-8).

Rotor OD (mm)	Rated MAS Frequency YSZ (kHz)	f_E Yttria Stabilized Zirconia (kHz)	f_E Diamond (kHz)	Rated MAS frequency Sapphire (kHz)	f_E Sapphire (kHz)
4	15	59	153	10	85
3.2	24	62	164	15	91
2.5	35	73	200	N/A	110
1.9	42	82	210	N/A	117
1.3	67	104	276	N/A	152
0.7	111	162	428	N/A	237
0.4	160-200	280	729	N/A	405

Table 6.6. Rotor natural frequency. Values based on Young's modulus for common MAS rotor sizes with typical 70% safety factor.

6.6 Acknowledgements

6.7 References

1   Berruyer, P., Emsley, L. & Lesage, A. in *eMagRes*   93-104 (2018).
2   Bonaccorsi, M., Le Marchand, T. & Pintacuda, G. Protein structural dynamics by Magic-Angle Spinning NMR. *Current Opinion in Structural Biology* **70**, 34-43 (2021). https://doi.org:https://doi.org/10.1016/j.sbi.2021.02.008
3   Bennett, A. E., Griffin, R. G. & Vega, S. in *Solid-State NMR IV Methods and Applications of Solid-State NMR*   (ed Bernhard Blümich) 1-77 (Springer Berlin Heidelberg, 1994).
4   Colvin, M. T. *et al.* Atomic Resolution Structure of Monomorphic Aβ42 Amyloid Fibrils. *Journal of the American Chemical Society* **138**, 9663-9674 (2016). https://doi.org:10.1021/jacs.6b05129
5   Lu, J. X. *et al.* Molecular structure of β-amyloid fibrils in Alzheimer's disease brain tissue. *Cell* (2013).
6   Reif, B., Ashbrook, S. E., Emsley, L. & Hong, M. Solid-state NMR spectroscopy. *Nature Reviews Methods Primers* **1**, 2 (2021). https://doi.org:10.1038/s43586-020-00002-1
7   Schütz, A. K. *et al.* Atomic-Resolution Three-Dimensional Structure of Amyloid β Fibrils Bearing the Osaka Mutation. *Angewandte Chemie International Edition* **54**, 331-335 (2015). https://doi.org:https://doi.org/10.1002/anie.201408598
8   Wälti, M. A. *et al.* Atomic-resolution structure of a disease-relevant Aβ(1–42) amyloid fibril. *Proceedings of the National Academy of Sciences* **113**, E4976-E4984 (2016). https://doi.org:10.1073/pnas.1600749113

9   Eddy, M. T., Yu, T.-Y., Wagner, G. & Griffin, R. G. Structural characterization of the human membrane protein VDAC2 in lipid bilayers by MAS NMR. *Journal of Biomolecular NMR* **73**, 451-460 (2019). https://doi.org:10.1007/s10858-019-00242-8

10   Mandala, V. S., Williams, J. K. & Hong, M. Structure and Dynamics of Membrane Proteins from Solid-State NMR. *Annual Review of Biophysics* **47**, 201-222 (2018). https://doi.org:10.1146/annurev-biophys-070816-033712

11   Wang, S. & Ladizhansky, V. Recent advances in magic angle spinning solid state NMR of membrane proteins. *Progress in Nuclear Magnetic Resonance Spectroscopy* **82**, 1-26 (2014). https://doi.org:https://doi.org/10.1016/j.pnmrs.2014.07.001

12   Lecoq, L., Fogeron, M.-L., Meier, B. H., Nassal, M. & Böckmann, A. Solid-State NMR for Studying the Structure and Dynamics of Viral Assemblies. *Viruses* **12**, 1069 (2020).

13   Porat-Dahlerbruch, G., Goldbourt, A. & Polenova, T. Virus Structures and Dynamics by Magic-Angle Spinning NMR. *Annual Review of Virology* **8**, 219-237 (2021). https://doi.org:10.1146/annurev-virology-011921-064653

14   Berruyer, P. *et al.* Three-Dimensional Structure Determination of Surface Sites. *Journal of the American Chemical Society* **139**, 849-855 (2017). https://doi.org:10.1021/jacs.6b10894

15   Kong, X. *et al.* Mapping of Functional Groups in Metal-Organic Frameworks. *Science* **341**, 882-885 (2013). https://doi.org:10.1126/science.1238339

16   Pecher, O., Carretero-González, J., Griffith, K. J. & Grey, C. P. Materials' Methods: NMR in Battery Research. *Chemistry of Materials* **29**, 213-242 (2017). https://doi.org:10.1021/acs.chemmater.6b03183

17   Andrew, E. R., Farnell, L. F., Firth, M., Gledhill, T. D. & Roberts, I. High-speed rotors for nuclear magnetic resonance studies on solids. *Journal of Magnetic Resonance (1969)* **1**, 27-34 (1969). https://doi.org:https://doi.org/10.1016/0022-2364(69)90004-3

18   Beams, J. W. An apparatus for obtaining high speeds of rotation. *Review of Scientific Instruments* **1**, 667-671 (1930). https://doi.org:10.1063/1.1748654

19   Chen, P. *et al.* Magic angle spinning spheres. *Science Advances* **4**, eaau1540 (2018). https://doi.org:10.1126/sciadv.aau1540

20   Doty, F. D. & Ellis, P. D. Design of high speed cylindrical NMR sample spinners. *Review of Scientific Instruments* **52**, 1868-1875 (1981). https://doi.org:10.1063/1.1136530

21   Schledorn, M. *et al.* Protein NMR Spectroscopy at 150 kHz Magic-Angle Spinning Continues To Improve Resolution and Mass Sensitivity. *ChemBioChem* **21**, 2540-2548 (2020). https://doi.org:https://doi.org/10.1002/cbic.202000341

22   BioSpin, B. in *International Conference on Magnetic Resonance in Biological Systems.*

23   Samoson, A. in *Experimental Nuclear Magnetic Resonance Conference.*

24   Andreas Loren, B. *et al.* Structure of fully protonated proteins by proton-detected magic-angle spinning NMR. *Proceedings of the National Academy of Sciences* **113**, 9187-9192 (2016). https://doi.org:10.1073/pnas.1602248113

25   Bahri, S. *et al.* 1H detection and dynamic nuclear polarization–enhanced NMR of Aβ1-42 fibrils. *Proceedings of the National Academy of Sciences* **119**, e2114413119 (2022). https://doi.org:10.1073/pnas.2114413119

26   Struppe, J. *et al.* Expanding the horizons for structural analysis of fully protonated protein assemblies by NMR spectroscopy at MAS frequencies above 100 kHz. *Solid State Nucl Magn Reson* **87**, 117-125 (2017). https://doi.org:10.1016/j.ssnmr.2017.07.001

27   Böckmann, A., Ernst, M. & Meier, B. H. Spinning proteins, the faster, the better? *Journal of Magnetic Resonance* **253**, 71-79 (2015). https://doi.org:https://doi.org/10.1016/j.jmr.2015.01.012

28   Penzel, S. *et al.* Spinning faster: protein NMR at MAS frequencies up to 126 kHz. *Journal of Biomolecular NMR* **73**, 19-29 (2019). https://doi.org:10.1007/s10858-018-0219-9

29   Xue, K. *et al.* Magic-Angle Spinning Frequencies beyond 300 kHz Are Necessary To Yield Maximum Sensitivity in Selectively Methyl Protonated Protein Samples in Solid-State NMR. *The Journal of Physical Chemistry C* **122**, 16437-16442 (2018). https://doi.org:10.1021/acs.jpcc.8b05600

30   Abragam, A. & Goldman, M. Principles of Dynamic Nuclear Polarization. *Reports on Progress in Physics* **41**, 395-467 (1978). https://doi.org:10.1088/0034-4885/41/3/002

31   Overhauser, A. W. Polarization of Nuclei in Metals. *Physical Review* **92**, 411-415 (1953). https://doi.org:10.1103/PhysRev.92.411

32   Becerra, L. R., Gerfen, G. J., Temkin, R. J., Singel, D. J. & Griffin, R. G. Dynamic nuclear polarization with a cyclotron resonance maser at 5 T. *Physical Review Letters* **71**, 3561-3564 (1993). https://doi.org:10.1103/PhysRevLett.71.3561

33   Hall, D. A. *et al.* Polarization-Enhanced NMR Spectroscopy of Biomolecules in Frozen Solution. *Science* **276**, 930-932 (1997). https://doi.org:10.1126/science.276.5314.930

34   Jaudzems, K. *et al.* Dynamic Nuclear Polarization-Enhanced Biomolecular NMR Spectroscopy at High Magnetic Field with Fast Magic-Angle Spinning. *Angewandte Chemie International Edition* **57**, 7458-7462 (2018). https://doi.org:https://doi.org/10.1002/anie.201801016

35   Berruyer, P. *et al.* Dynamic Nuclear Polarization Enhancement of 200 at 21.15 T Enabled by 65 kHz Magic Angle Spinning. *The Journal of Physical Chemistry Letters* **11**, 8386-8391 (2020). https://doi.org:10.1021/acs.jpclett.0c02493

36   Judge, P. T. *et al.* Sensitivity analysis of magic angle spinning dynamic nuclear polarization below 6 K. *Journal of Magnetic Resonance* **305**, 51-57 (2019). https://doi.org:https://doi.org/10.1016/j.jmr.2019.05.011

37   Mathies, G. *et al.* Efficient Dynamic Nuclear Polarization at 800 MHz/527 GHz with Trityl-Nitroxide Biradicals. *Angewandte Chemie International Edition* **54**, 11770-11774 (2015). https://doi.org:https://doi.org/10.1002/anie.201504292

38   Nanni, E. A. *et al.* Microwave field distribution in a magic angle spinning dynamic nuclear polarization NMR probe. *Journal of Magnetic Resonance* **210**, 16-23 (2011). https://doi.org:https://doi.org/10.1016/j.jmr.2011.02.001

39   Purea, A. *et al.* Improved waveguide coupling for 1.3 mm MAS DNP probes at 263 GHz. *Journal of Magnetic Resonance* **302**, 43-49 (2019). https://doi.org:https://doi.org/10.1016/j.jmr.2019.03.009

40   Rosay, M. *et al.* Solid-state dynamic nuclear polarization at 263 GHz: spectrometer design and experimental results. *Physical Chemistry Chemical Physics* **12**, 5850-5860 (2010). https://doi.org:10.1039/C003685B

41   Thurber, K. & Tycko, R. Low-temperature dynamic nuclear polarization with helium-cooled samples and nitrogen-driven magic-angle spinning. *Journal of Magnetic Resonance* **264**, 99-106 (2016).

42   Can, T. V. *et al.* Frequency-Swept Integrated and Stretched Solid Effect Dynamic Nuclear Polarization. *The Journal of Physical Chemistry Letters* **9**, 3187-3192 (2018). https://doi.org:10.1021/acs.jpclett.8b01002

43   Can, T. V., Tan, K. O., Yang, C., Weber, R. T. & Griffin, R. G. Time domain DNP at 1.2 T. *Journal of Magnetic Resonance* **329**, 107012 (2021). https://doi.org:https://doi.org/10.1016/j.jmr.2021.107012

44   Tan, K. O., Weber, R. T., Can, T. V. & Griffin, R. G. Adiabatic Solid Effect. *The Journal of Physical Chemistry Letters* **11**, 3416-3421 (2020). https://doi.org:10.1021/acs.jpclett.0c00654

45   Naftaly, M. & Miles, R. E. Terahertz Time-Domain Spectroscopy for Material Characterization. *Proceedings of the IEEE* **95**, 1658-1665 (2007). https://doi.org:10.1109/JPROC.2007.898835

46   Barbet-Massin, E. *et al.* Rapid Proton-Detected NMR Assignment for Proteins with Fast Magic Angle Spinning. *Journal of the American Chemical Society* **136**, 12489-12497 (2014). https://doi.org:10.1021/ja507382j

47   Lewandowski, J. R., Sein, J., Blackledge, M. & Emsley, L. Anisotropic Collective Motion Contributes to Nuclear Spin Relaxation in Crystalline Proteins. *Journal of the American Chemical Society* **132**, 1246-1248 (2010). https://doi.org:10.1021/ja907067j

48   Shaka, A. J., Keeler, J., Frenkiel, T. & Freeman, R. An improved sequence for broadband decoupling: WALTZ-16. *Journal of Magnetic Resonance (1969)* **52**, 335-338 (1983). https://doi.org:https://doi.org/10.1016/0022-2364(83)90207-X

49   Zhou, D. H. & Rienstra, C. M. High-performance solvent suppression for proton detected solid-state NMR. *Journal of Magnetic Resonance* **192**, 167-172 (2008). https://doi.org:https://doi.org/10.1016/j.jmr.2008.01.012

50   Hermani, J., Emonts, M. & Brecher, C. in *Proceedings of the Lasers in Manufacturing Conference, Munich, Germany.* 22-25.

51   Konov, V. I. Laser in micro and nanoprocessing of diamond materials. *Laser & Photonics Reviews* **6**, 739-766 (2012). https://doi.org:https://doi.org/10.1002/lpor.201100030

52   Mouhamadali, F. *et al.* Nanosecond pulsed laser-processing of CVD diamond. *Optics and Lasers in Engineering* **126**, 105917 (2020). https://doi.org:https://doi.org/10.1016/j.optlaseng.2019.105917

53   Patil, P. *Laser direct-write fabrication of MEMS*, Massachusetts Institute of Technology, (2019).

54 Ramaswamy, C. Raman Effect in Diamond. *Nature* **125**, 704-704 (1930). https://doi.org:10.1038/125704b0

55 Nemanich, R. J. & Solin, S. A. First- and second-order Raman scattering from finite-size crystals of graphite. *Physical Review B* **20**, 392-401 (1979). https://doi.org:10.1103/PhysRevB.20.392

56 Howe, J. Y. *The oxidation of diamond*, Alfred University, (2001).

57 Paci, J. T., Minton, T. K. & Schatz, G. C. Hyperthermal Oxidation of Graphite and Diamond. *Accounts of Chemical Research* **45**, 1973-1981 (2012). https://doi.org:10.1021/ar200317y

58 Samoson, A. H-MAS. *Journal of Magnetic Resonance* **306**, 167-172 (2019). https://doi.org:https://doi.org/10.1016/j.jmr.2019.07.010

59 Wilhelm, D., Purea, A. & Engelke, F. Fluid flow dynamics in MAS systems. *Journal of Magnetic Resonance* **257**, 51-63 (2015). https://doi.org:https://doi.org/10.1016/j.jmr.2015.05.006

60 Jensen, J. E., Tuttle, W. A., Stewart, R. B., Brechna, H. & Prodell, A. G. Brookhaven National Laboratory selected cryogenic data notebook: Volume 1, Sections 1-9. (United States, 1980).

61 Bouleau, E., Lee, D., Saint-Bonnet, P., Hediger, S. & De Paëpe, G. Ultra-Low Temperature Nuclear Magnetic Resonance. *IOP Conference Series: Materials Science and Engineering* **171**, 012142 (2017). https://doi.org:10.1088/1757-899X/171/1/012142

62 Herzog, N. *et al.* Ultra Low Temperature Microturbine for Magic Angle Spinning System. *Journal of Fluids Engineering* **144** (2022). https://doi.org:10.1115/1.4053746

63 Matsuki, Y., Nakamura, S., Fukui, S., Suematsu, H. & Fujiwara, T. Closed-cycle cold helium magic-angle spinning for sensitivity-enhanced multi-dimensional solid-state NMR. *Journal of Magnetic Resonance* **259**, 76-81 (2015). https://doi.org:https://doi.org/10.1016/j.jmr.2015.08.003

64 Myhre, P. C., Webb, G. G. & Yannoni, C. S. Magic angle spinning nuclear magnetic resonance near liquid-helium temperatures. Variable-temperature CPMAS studies of C4H7+ to 5 K. *Journal of the American Chemical Society* **112**, 8992-8994 (1990). https://doi.org:10.1021/ja00180a061

65 Sesti, E. L. *et al.* Magic angle spinning NMR below 6 K with a computational fluid dynamics analysis of fluid flow and temperature gradients. *Journal of Magnetic Resonance* **286**, 1-9 (2018). https://doi.org:https://doi.org/10.1016/j.jmr.2017.11.002

66 Thurber, K. R. & Tycko, R. Biomolecular solid state NMR with magic-angle spinning at 25K. *J Magn Reson* **195**, 179-186 (2008). https://doi.org:10.1016/j.jmr.2008.09.015

67 Deb, R., Hunkeler, A., Wilhelm, D., Jenny, P. & Meier, B. H. Numerical modeling and design decisions for aerostatic bearings with relatively large nozzle sizes in Magic-Angle Spinning (MAS) systems. *Tribology International* **175**, 107855 (2022). https://doi.org:https://doi.org/10.1016/j.triboint.2022.107855

68 Endo, Y., Hioka, K. & Yamauchi, K. Sample Tube and Measurement Method for Solid State NMR. United States patent (2011).

69   Genta, G. *Dynamics of Rotating Systems*. 201-213 (Springer, 2005).

70   Liu, X., Athanasiou, C. E., Padture, N. P., Sheldon, B. W. & Gao, H. A machine learning approach to fracture mechanics problems. *Acta Materialia* **190**, 105-112 (2020). https://doi.org:https://doi.org/10.1016/j.actamat.2020.03.016

71   Pike, K. J. *et al.* A spectrometer designed for 6.7 and 14.1T DNP-enhanced solid-state MAS NMR using quasi-optical microwave transmission. *Journal of Magnetic Resonance* **215**, 1-9 (2012). https://doi.org:https://doi.org/10.1016/j.jmr.2011.12.006

72   Blauel, J. G., Beinert, J. & Wenk, M. Fracture-mechanics investigations of cracks in rotating disks. *Experimental Mechanics* **17**, 106-112 (1977). https://doi.org:10.1007/BF02324247

73   Kulyk, V. *et al.* The Effect of Yttria Content on Microstructure, Strength, and Fracture Behavior of Yttria-Stabilized Zirconia. *Materials* **15** (2022).

74   Marinis, A. *et al.* Fracture toughness of yttria-stabilized zirconia sintered in conventional and microwave ovens. *The Journal of Prosthetic Dentistry* **109**, 165-171 (2013). https://doi.org:https://doi.org/10.1016/S0022-3913(13)60037-2

75   Roitero, E. *et al.* Ultra-fine Yttria-Stabilized Zirconia for dental applications: A step forward in the quest towards strong, translucent and aging resistant dental restorations. *Journal of the European Ceramic Society* **43**, 2852-2863 (2023). https://doi.org:https://doi.org/10.1016/j.jeurceramsoc.2022.11.048

76   ZIRPRO, S. G.   (2020).

77   Liang, Q. *et al.* Enhancing the mechanical properties of single-crystal CVD diamond. *Journal of Physics: Condensed Matter* **21**, 364215 (2009). https://doi.org:10.1088/0953-8984/21/36/364215

78   Liang, Q. *et al.* Recent advances in high-growth rate single-crystal CVD diamond. *Diamond and Related Materials* **18**, 698-703 (2009). https://doi.org:https://doi.org/10.1016/j.diamond.2008.12.002

79   Athanasiou, C. E. *et al.* Integrated simulation, machine learning, and experimental approach to characterizing fracture instability in indentation pillar-splitting of materials. *Journal of the Mechanics and Physics of Solids* **170**, 105092 (2023). https://doi.org:https://doi.org/10.1016/j.jmps.2022.105092

80   Athanasiou, C.-E. & Bellouard, Y. A Monolithic Micro-Tensile Tester for Investigating Silicon Dioxide Polymorph Micromechanics, Fabricated and Operated Using a Femtosecond Laser. *Micromachines* **6**, 1365-1386 (2015).

81   Kondoh, J., Shiota, H., Kawachi, K. & Nakatani, T. Yttria concentration dependence of tensile strength in yttria-stabilized zirconia. *Journal of Alloys and Compounds* **365**, 253-258 (2004). https://doi.org:https://doi.org/10.1016/S0925-8388(03)00640-6

82   Drory, M. D., Dauskardt, R. H., Kant, A. & Ritchie, R. O. Fracture of synthetic diamond. *Journal of Applied Physics* **78**, 3083-3088 (1995). https://doi.org:10.1063/1.360060

83   Hess, P. The mechanical properties of various chemical vapor deposition diamond structures compared to the ideal single crystal. *Journal of Applied Physics* **111**, 051101 (2012). https://doi.org:10.1063/1.3683544

84   Olson, D. S. *et al.* Tensile strength of synthetic chemical‐vapor‐deposited diamond. *Journal of Applied Physics* **78**, 5177-5179 (1995). https://doi.org:10.1063/1.359752

85   Kurlov, V. N. in *Encyclopedia of Materials: Science and Technology* (eds K. H. Jürgen Buschow *et al.*) 8259-8264 (Elsevier, 2001).

Chapter 7 : Applications and Challenges of 3D printing for Molecular and Atomic Scale Analytical Techniques

Adapted and reproduced with permission from: Golota, N., Banks, D., Michael, B. & Griffin, R. G. in *3D Printing : Fundamentals to Emerging Applications* (ed Ram Gupta) (Routledge, 2023).

7.1 Introduction

Over the past one hundred years, fundamental discoveries in the field of physical chemistry enabled the development and adoption of molecular spectroscopies based on the exposure to and subsequent absorption of electromagnetic radiation. The absorption of photons across the electromagnetic spectrum results in light– matter interactions which are then detected as a function of the frequency of irradiation. Different elements and molecules have distinct spectral signatures, enabling the identification and quantification of sample analytes ranging from small molecules to large macromolecular assemblies. These techniques have evolved to become critical, ubiquitous tools central to the development of modern science and medicine. They have enabled countless discoveries in various fields, including medicine, materials science, and chemistry.

Initially, access to spectroscopic devices was limited as spectrometers were research objectives in themselves and typically found only in research and development laboratories. However, between the 1950s and 1990s, there was rapid commercialization of scientific equipment through the founding of many large- scale scientific device manufacturers. This improved accessibility to spectroscopy and increased the rate of scientific discovery profoundly.

While the design of many spectrometers will be detailed further in the chapter, their fabrication has previously been dependent on traditional subtractive manufacturing methods requiring extensive infrastructure to support. As commercial equipment began entering laboratories, machine shop facilities became less widespread and the number of laboratories developing their customized spectrometers has decreased over time. As a result, while access to spectroscopy has increased, the ability to rapidly tailor instrumentation to experimental needs has decreased over time.

While this trend continued into the early 2000s, the commercialization and cost reduction of 3D printers has made them a standard and necessary resource in many scientific laboratories today. Technologies such as fused deposition model (FDM) and stereolithography (SLA) printers are most common in laboratories, however, 2- photon 3D printing has rapidly become a viable strategy uniquely suited for the miniaturization of scientific devices. Rapid, low- cost, and often in- house fabrication strategies using 3D printing have resulted in a rapid resurgence of customized instrumentation demonstrated by hundreds of publications each year incorporating 3D- printed components. Importantly, most published work contains open- access CAD models which further improve the accessibility of innovative instrumentation. Overall, 3D printing has not only furthered the customization of instrumentation but has also led to improved democratization of scientific equipment. For many labs, upgrades to spectrometers has become a cost-prohibitive step, however, when using 3D printing the cost is near zero, particularly when considering the availability of 3D printers on most university campuses.

Within this chapter, we discuss a small selection of the numerous creative and innovative uses of 3D printing for molecular scale analyses. Herein we focus on the application of printing to ultraviolet and visible spectrophotometry, infrared and Raman spectroscopy, mass spectrometry, and nuclear magnetic resonance.

7.2 UV/VIS Spectrophotometry

Ultra- violet and visible (UV/ VIS) spectrophotometry is used to determine analyte compositions and concentrations of samples ranging from biomolecules to materials. UV/ VIS measures the absorption or transmission of UV and visible light through the sample. The absorption of photons in this range of the electromagnetic spectrum can then be used to determine concentrations of the analyte of interest. This versatile technique is widely used in academic labs, industry, and clinical settings. Additionally, it is a foundational technique used to introduce chemistry and biology students to spectroscopic methods.

Typical spectrometers for UV/ VIS in research settings cost between several hundred to several thousands of dollars and can take up a large footprint in the laboratory. All UV/ VIS spectrometers use a UV/ VIS light source which is then sent through a diffraction grating or monochromator to achieve spectral resolution in the UV/ VIS electromagnetic region. The sample is typically contained in quartz, optical glass, or disposable plastic cuvette. The transmitted light is then recorded on a CCD detector and sample absorbance is used to determine analyte concentrations. While these simple components can become more sophisticated in high- quality research- grade

equipment, the overall simplicity of the spectrometer makes it highly amenable to customization using 3D printing technology.

3D printing has accelerated the customization of UV/ VIS spectrometers enabling researchers to increase the utility of these devices while decreasing the cost of consumables. A wide variety of printing technologies have been applied to overcome challenges related to printing air and watertight components, the use of highly transparent resins, and improved chemical resistance of printing resins. Moreover, 3D printing has accommodated the required flexibility of researchers interested in the integration of electrochemistry during UV/ VIS, the study of samples in the gaseous phase or solid phases, under flow- cell conditions, and variable temperatures. While commercial suppliers have developed limited add- on components to their spectrometers to address these and other user needs, the associated high costs of such devices limit widespread adoption.

To this end, low- cost, variable volume and path length cuvettes with integrated temperature control have been fabricated primarily using FDM printing techniques. Pisaruka et al. expanded the commercially available spectrometer functionality to include an integrated water bath heating chamber surrounding the sample chamber, enabling variable temperature measurements on decreased sample volumes of amphiphile micelle concentrations to probe phospholipid aggregation properties [1]. These sample chambers were fabricated from acrylonitrile butadiene styrene (ABS) and polylactic acid (PLA) filaments via FDM printing using a MakerBot Replicator 2X printer. This was followed by a post- printing processing step in which PLA or ABS cuvettes

were immersed in either chloroform or acetone to fuse layer defects and improve watertight properties.

Universal cuvette adapters have also been 3D-printed to accommodate a variety of commercial spectrometers in addition to enabling the use of common laboratory containers to serve as cuvettes directly. The development by Whitehead et al. uses a standard glass or quartz microscope slide integrated into a 3D- printed support piece, for an estimated cost of $1 or $14, respectively [2]. Furthermore, the authors demonstrate a universal adapter that can house gas- tight commercially available vials, in addition to supporting solid samples that would otherwise be difficult to study with existing devices. A total of 24 designs were printed in less than two hours each using a LulzBot Mini Printer with Black PLA filament.

Flow capabilities have been integrated into optically transparent cuvettes using a Dreamer Sygnis New Technologies printer and NinjaFlex Midnight Black Filament to fabricate rubber-like components that housed small tubing for flow studies [3]. The flow cell maintained a volume of only 50 µL and the reported total cost was ~$1.3 which the authors state as being hundred times less expensive than a commercially available flow cell. The authors validated their design with use over 20 hours on two model analytes, bromothymol blue and fluorescein.

While the previous examples used FDM printed sample chambers incorporating optical glass, Sirjani et al. used optically transparent filaments- transparent PLA (MakerBot), HD glass (Formfutura), and T-Glase (Taulman3D) to directly fabricate the entire sample cuvette [4] . Significant light scattering effects due to layer spacing in the FDM printing process were overcome using XTC-3D ®, a

finishing coating for 3D-printed parts that are used to fill in print striations and imperfections to create a smooth and high gloss finish. The authors extended their application from a simple cuvette to the fabrication of a 3D-printed, optically transparent device containing three reaction chambers with embedded neodymium magnets used to immobilize enzymes conjugated to magnetic Dynabeads™. Two and three-step lactose assays were performed to validate the enzyme immobilization assay. This work represented an important step toward the rapid fabrication of optic- ally transparent, custom reaction chambers for biosensing applications without chemical compatibility issues.

Beyond fabrication of the sample chamber, several groups have developed multiple components for UV/VIS spectroscopy which further extend its utility and applications. This includes the functionalization of printed components to serve as electrodes for combined spectro-electrochemistry applications by Vaněčková et al. [5]. This enables the study of electron transfer mechanisms and detection of electrochemical reaction products. The electrochemical electrodes were printed from PLA-carbon nanotubes (CNT) using a Prusa I3 MK3 printer followed by electrochemical activation and integration into a quartz cuvette. Importantly, the electrode design included an optical window integrated into the 3D-printed structure. The authors validated their electrodes using a standard sample and printed components behaved similarly to conventional electrodes.

3D printing has enabled the fabrication of accessible and portable spectrometers that couple inexpensive optical elements to smartphones serving as the detector. 3D-printed housings allow the integration of all components of the spectrometer. Grasse et
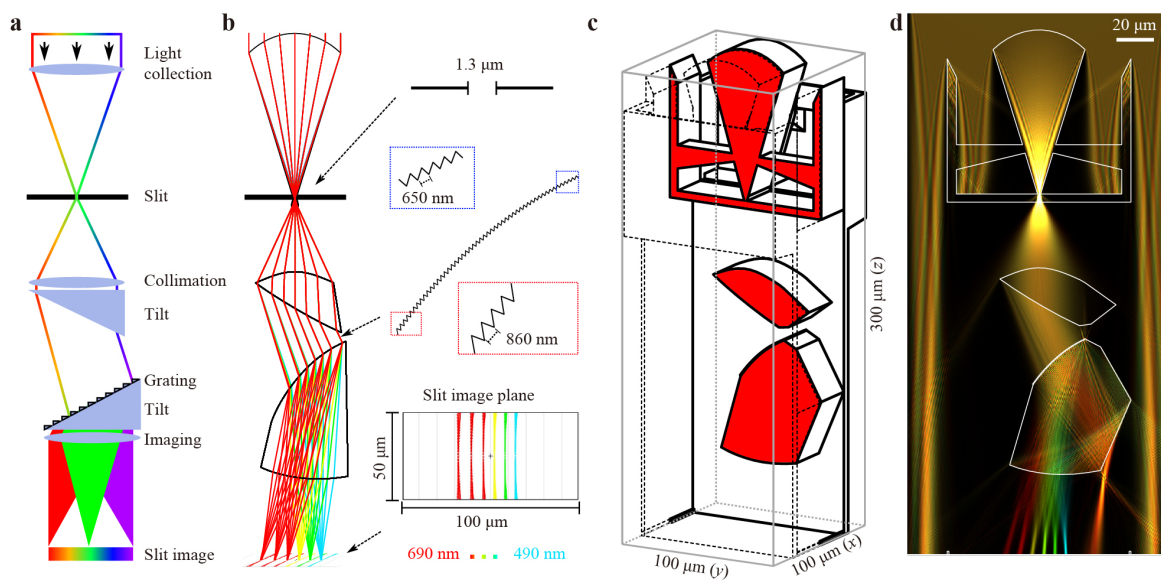
Figure 7.1. Optical design and simulation of the miniature spectrometer. (A) Design principle. (B) Optical design and ray-tracing simulation. Slit width, blazed grating, topography, and footprint spot diagram are highlighted for the indicated surfaces. (C) Cut view of the 3D-printed volume model. Lenses, grating, slit, and mounts are printed in one step and fit in a volume of only 100 × 100 × 300 µm3. (D) Two-dimensional wave-optical simulation (WPM) of the plane highlighted in red in (C). Around the slit a perfectly absorbing material is assumed. Simulation wavelengths are in the visible range from 490 nm to 690 nm in 40 nm steps. Figure 7.1 adapted with permission from Ref [7] Copyright The Authors, some rights reserved; exclusive licensee Light Publishing Group. Distributed under a Creative Commons Attribution License 4.0 (CC BY) https://creativecommons.org/licenses/by/4.0/

al. offered a procedure for translating pixels from smartphone-detected images into conventional UV/VIS absorption spectra and validated their methodologies by determining Kool-Aid concentrations [6].

3D printing has also enabled the miniaturization of UV/VIS spectrometers with a total volume of only 100 µm × 100 µm × 300 µm using two-photon direct laser writing

3D printing technology, while the diffraction slit of the spectrometer was fabricated using super-fine inkjet process [7].

This is one of the first instances of micro-optics being fabricated using 3D-printing technology and represents a large potential opportunity for a variety of sensing and spectroscopic applications. The printed device is shown in Figure 7.1 and details the optical design and 3D-printed volume including micro-optics. The authors compared the spectrum collected with the 3D-printed miniaturized spectrometer to a commercial spectrometer and found sufficient agreement between the results, despite the footprint of the miniaturized device is eight orders of magnitude less than the commercial spectrometer.

The primary remaining challenges toward widespread adoption of 3D printing for UV/VIS spectroscopy lie in the chemical compatibility of resins and filaments used that are in contact with analyte solutions. Moreover, ensuring leak-tight characteristics of sample cuvettes and integrating optically transparent resins and filaments into designs will continue to be a challenge to researchers. However, as demonstrated by the previously mentioned studies, several authors have been able to overcome these challenges and 3D printing represents a viable method of fabricating and upgrading UV/VIS spectrometers.

7.3 Fourier Transform Infrared and Raman Spectroscopy

Fourier transform infrared (FTIR) spectroscopy and Raman spectroscopy are analytical techniques that probe the vibrational modes of molecules. These measurements provide rich information about the chemical bonds present in a sample

of interest. The frequencies associated with vibrational transitions within molecules generally fall within the infrared region of the electromagnetic spectrum. FTIR measures the absorption of infrared radiation which will occur only at specific frequencies associated with particular vibrations within a sample. Raman measurements on the other hand are based on inelastic scattering. Samples are irradiated with a laser and scattered light is collected and measured. The dominant scattering effect is elastic Rayleigh scattering which preserves the frequency of the light. There are also inelastic Raman scattering effects that cause the frequency of the light to shift up or down by the frequency of vibrational transitions present in the sample.

Since FTIR is an absorption measurement it requires an infrared light source and detector that function across the entire spectral region of interest. Typically, the light source is a heated silicon carbide element or a tungsten-halogen lamp. Rather than using a monochromator or diffraction grating to produce spectral resolution (as is common practice when working with visible or ultra- violet light) FTIR employs an interferometer. The light is split into two parts that are directed to the detector via separate paths. Depending on the frequency of the light and the difference in the lengths of the two paths the two beams can positively or negatively interfere with one another. By varying the length of one of the two beam paths an interferogram can be produced that encodes the frequency and intensity of the light. This signal can then be converted into a spectrum via a Fourier transform.

Raman spectroscopy requires a more complex arrangement of optics. A laser, typically in the visible or near-infrared, is focused on a sample using a microscope objective. That same objective lens is used to collect light scattered from the sample.

Great pains must be taken to avoid fluorescence which can also emit light that would be collected by the objective. Scattered light at the same frequency as the laser is produced by Rayleigh scattering and must be filtered out before detection. As the light in a Raman microscope is at higher frequencies than that in an FTIR spectrometer it generally is spectrally resolved using a monochromator or a grating paired with a CCD detector.

Most FTIR and Raman instruments that chemists and material scientists in academic and industrial labs have access to are commercial devices that are not intended to be significantly altered by the user. Constructing homebuilt instruments or modifying existing commercial instruments is generally difficult and expensive but can offer a crucial path to new and innovative spectroscopic methodologies. 3D-printing approaches have significantly lowered the barrier to experimenting with novel apparatuses needed for studying challenging samples and overcoming practical barriers that previously prevented some types of measurements.

In the most common case, FTIR measurements are performed by passing a beam of infrared light through a sample and then into an interferometer for detection. This arrangement is effective but has significant limitations. Such transmission mode measurements usually require that the sample be in the solid state and be very thin to avoid excessive attenuation of the beam. Attenuated total reflection (ATR) is a popular alternative method in which the sample is placed directly on a crystal with a high refractive index. The beam travels through the crystal and hits the interface with the sample at an oblique angle such that total internal reflection occurs, and the beam effectively bounces off the interface. A small portion of the beam, known as an

evanescent wave, extends a short distance beyond the interface and interacts with the sample allowing absorption to occur. ATR attachments are available for many commercial FTIR spectrometers, but they are expensive and inflexible. 3D printing has been used to produce low-cost ATR modules that allow for variation of many aspects of the measurements, such as the type of ATR crystal [8]. By creating custom ATR modules researchers could alter the number of times the beam bounces off the interface, a parameter that generally cannot be adjusted using commercial equipment, to optimize the sensitivity of measurements of proteins in dilute solution. Additionally, because the 3D-printed modules could be made overnight at a relatively low cost, they could be used in a disposable fashion to reduce cross-contamination and study otherwise inaccessible biological samples.

3D printing has also been applied to great effect in Raman spectroscopy. Due to their increased complexity and cost, Raman instruments are often less accessible than FTIR spectrometers, especially in teaching labs. By integrating 3D-printed parts with off-the-shelf optical components, a functional Raman spectrometer was developed that cost less than $4000, even including $3000 for a 3D printer [9]. Such an approach can make it significantly cheaper to provide students with hands-on experience of Raman spectroscopy.

3D printing has also been used to build experimental apparatuses aimed at overcoming the low sensitivity of Raman measurements. One method for enhancing the signal of Raman spectroscopy makes use of a liquid core waveguide, in which the sample is placed in a Teflon-amorphous fluoro- polymer (AF) tube to provide a longer path length and help capture the scattered light [10]. A major issue encountered in this
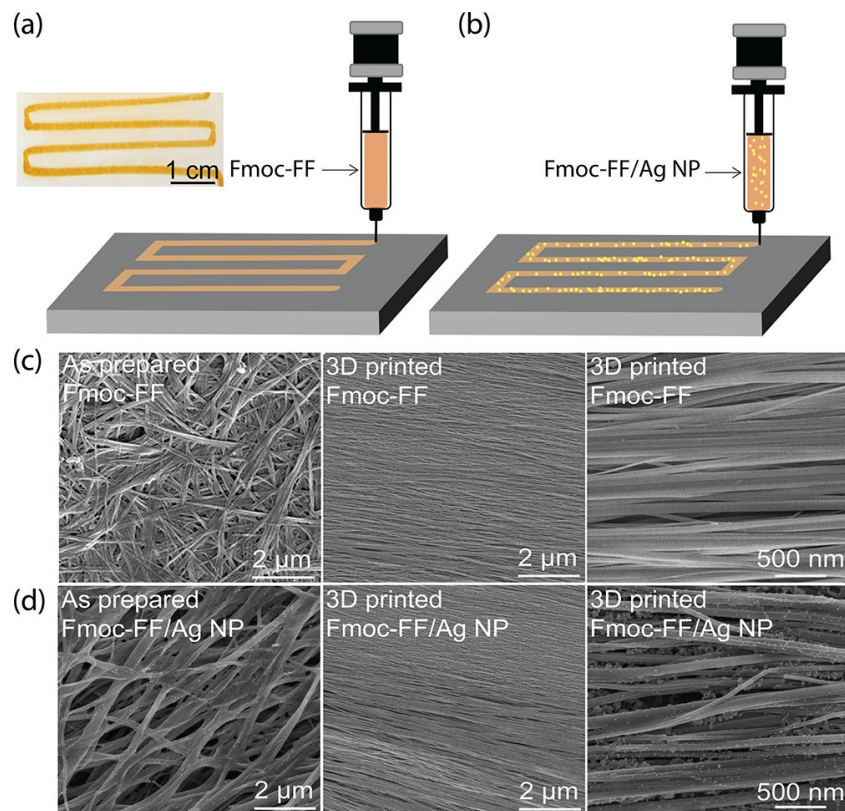
Figure 7.2. Schematic representation of the 3D-printed hydrogel. (A) without and (C) with NPs. The inset in a is an optical image of the hydrogel (mixed with 0.06 g of orange food dye (U8-OSL0-PS8Q, Preema, UK)) printed on glass. (C) SEM images of the as prepared and 3D-printed Fmoc-FF. (d) SEM images of the as prepared and 3D-printed Fmoc-FF with Ag NPs. Reprinted (adapted) with permission from [12]. Copyright (2019) American Chemical Society.

approach is the difficulty of preventing bubbles in the sample. A 3D- printed negative pressure module was developed for easy removal of bubbles allowing for fast and reproducible analytical measurements.

Another commonly employed method is surface-enhanced Raman spectroscopy (SERS) in which samples adsorbed to rough metal surfaces or plasmonic nanomaterials exhibit significantly stronger Raman signals. SERS samples are frequently prepared via drop casting, by depositing a solution on a surface and allowing the solvent to evaporate. This process often produces inhomogeneous samples where the

concentration of the target molecules varies with the distance from the center of deposition. 3D printing has been used to develop a set of alignment tools to precise position a pipette tip used to deposit a sample and the focal point of a Raman microscope relative to one another [11]. These simple 3D-printed parts allowed for reproducible sampling at controlled distances from the center of a drop on a gold-coated substrate. 3D printing can also offer methods to control plasmonic nanomaterials, such as silver nanoparticles suspended in a hydrogel (Figure 7.2) [12]. Extrusion- based 3D printing can alter the structure of hydrogels by causing the shear-induced alignment of nanofibers. The aligned 3D-printed hydrogel gives a significant signal enhancement compared to a hydrogel that had not gone through the printing process.

Pairing Raman spectroscopy with other modalities, such as electrochemistry can provide insight that cannot be obtained from either technique operating independently. Conducting these sorts of tandem experiments requires the development of new experimental apparatuses, which are often not commercially available, that allow electrochemical cells and electrodes to be mounted to a Raman spectrometer. The low cost and rapid iteration permitted by 3D printing have enabled the development of cheap and versatile electrochemical cells allowing in situ Raman measurements of electro- chemical film deposition while avoiding expensive components such as quartz plates and platinum rings used in previously reported devices [13,14]. These experiments were able to use Raman spectroscopy to probe the chemical changes that occurred as a function of the potential of the electrode. 3D-printed electrochemical cells have also been used to pair voltammetry of immobilized particles with Raman spectroscopy. The formation of new compounds at precise locations on the electrode

surface could be directly monitored almost simultaneously by Raman providing detailed insight into the effects of the electrochemical process.

One of the major limitations of the 3D printing-based approaches discussed here is the chemical compatibility of 3D-printed parts. FTIR and Raman spectroscopy are widely applied techniques that researchers use to investigate a variety of biological, organic, and inorganic systems. If the polymers commonly used in 3D printing are incompatible with the target molecules or the solvents they are stable in, then 3D-printed parts cannot be employed. Further development of new 3D-printed materials with a variety of chemical properties could help broaden the applicability of the types of innovations described here.

7.4 Mass Spectrometry

Mass spectrometry (MS) is one of the oldest and most powerful spectroscopic techniques used to analyze molecular compounds and mixtures by measuring the mass-to-charge (m/z) ratio of a molecule and its fragments. Such ratios can be used to elucidate numerous chemical properties of a com- pound, including its elemental composition, chemical structure, and isotopic ratios. The detection limit of modern mass spectrometers routinely allows studies on femtomole quantities of samples, making MS one of the most sensitive analytical techniques available. The information that can be obtained from MS in conjunction with the broad availability of commercial mass spectrometers makes MS one of the most used analytical techniques for studying chemical systems. As a result, MS has had a profound impact in fields ranging from materials science to biotechnology.

The type of equipment found in a mass spectrometer can differ based on the type of sample being analyzed and the information desired to be obtained. However, in general, all mass spectrometers consist of a few essential components. First, an inlet system is required to introduce the sample of interest to the spectrometer so that it can be analyzed. Next, an ion source is used to ionize the molecules in the sample. Ion sources can be categorized as hard or soft sources based on the degree of molecular fragmentation that takes place. Depending on the initial sample phase and type of spectrometer, conversion of the sample to a gaseous phase, which is required for analysis, is accomplished either by the inlet system or the ionization source.

After ionization, the molecular ions are accelerated via an electric field through a mass analyzer, typically consisting of a magnetic or electric field, which separates the different molecular ions based on their m/z ratio. An ion detector is then used to count the number of molecular ion fragments with a given m/z ratio. The ion source, mass analyzer, and ion detector are all kept under a high vacuum to prolong the lifetime of the molecular ions as they travel through the spectrometer. Finally, a computer is used to translate the data collected via the detector into an interpretable spectrum.

To date, most MS components developed with 3D printing have focused on modifications to the inlet system and ion source. Because 3D printing allows for rapid prototyping of components for mass spectrometers, its application greatly expands the types of analysis and experiments that can be performed. When choosing materials for 3D printing numerous material properties should be considered, including heat resistance, chemical compatibility, and resistance to outgassing. Here we highlight recent MS hardware developments using 3D printing. For a more comprehensive

literature review of 3D printing related to MS, the reader is referred to additional sources [15].

With respect to the inlet system, 3D printing has allowed for unique customization of both online and offline sample preparation methods. Online sample preparation methods involve direct integration with the inlet system of the spectrometer, while offline sample preparation methods prepare the sample in a separate station before interfacing with the spectrometer. An example of improvement offered by 3D-printed devices for online sample preparation is the ability to monitor chemical reactions in real-time. In one case, a 3D-printed polypropylene fluidic device allowed live reaction monitoring of the formation of a metal-salt complex using electrospray ionization MS (ESI-MS) [16]. The stoichiometry of the reaction was controlled by varying the flow rates of each reactant at the individual inlets of the 3D-printed device. In another example, 3D printing allowed for the fabrication of a polypropylene reactor with an internal magnetic stir bar and nanospray ion emitter [17]. The magnetic stir bar was incorporated into the reaction device via insertion during the FDM print, with the remainder of the housing built around the stir bar following the insertion, something not possible with traditional subtractive manufacturing methods. An image of this reactor can be seen in Figure 7.3. One of the fastest growing areas of MS is the development of ambient ionization (AI) methods that allow the MS sample to be prepared at atmospheric pressure with minimal sample prep. One promising method of AI is paper spray ionization (PSI), which involves soaking a sheet of paper with a solvent of interest and then applying a high voltage source to ionize the sample and introduce it to the mass spectrometer. One of the disadvantages of the PSI method is the rapid depletion of the solvent,
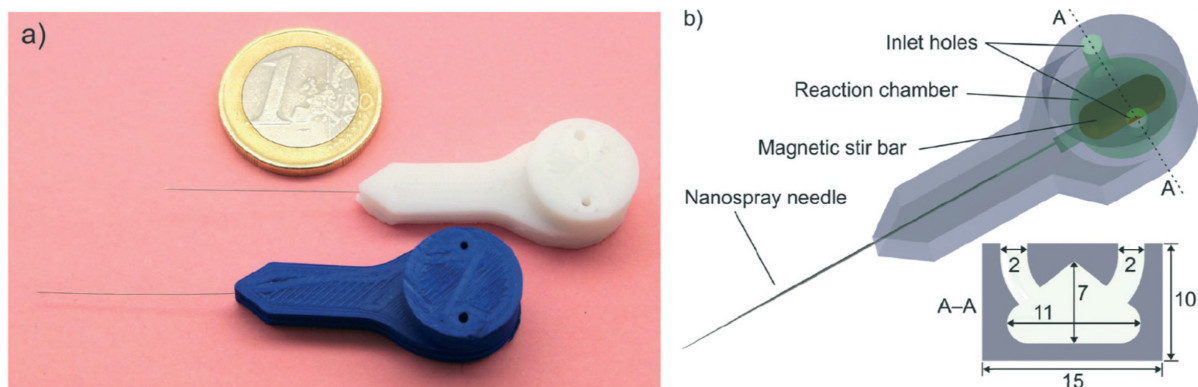
Figure 7.3. 3D Printed polypropylene reactor for mass spectrometry. (A) Image of polypropylene reactor. (B) Transparent image of polypropylene reactor with individual components highlighted. A cross section of the reaction are can be seen where the given dimensions are in mm. Figure 7.3 adapted with permission from [17]. Copyright The Authors, some rights reserved; exclusive licensee Royal Society of Chemistry. Distributed under a Creative Commons Attribution License 3.0 (CC BY) https://creativecommons.org/licenses/by/3.0/

which limits analysis time. However, recent developments in 3D printing have allowed this analysis to be extended via the integration of polylactic acid (PLA) sample reservoirs. In one example, employing a PLA cartridge with a paper tip and dual hydrophilic wicks extended the sample spray to tens of minutes [18]. The design of this reservoir allowed fast wetting of the paper via one wick placed near the surface of the reservoir, while a second wick placed deeper in the reservoir allowed for an extended supply of solvent to the paper through slow capillary action. In the case of the fast-wetting wick, it was found that diffusion of the solvent through the paper occurred faster between the paper-PLA interface rather than direct wetting of the paper.

Another AI technique that has benefited from the application of 3D printing is electrospray ionization (ESI). ESI can be challenging under ambient conditions as the number of analyzable ions is greatly reduced due to the expansion of the spray before even entering the vacuum region of the spectrometer for analysis. However,

this challenge of spray expansion was recently overcome through the employment of 3D-printed electrodes capable of focusing the ion beam before it enters the spectrometer [19]. The electrodes were fabricated using an FDM printer and polyethylene terephthalate glycol printing material doped with conductive CNT.

A final AI method ripe for the application of 3D printing is low-temperature plasma (LTP) ionization. In this method a plasma, often generated from helium gas, is used to generate molecular ions. The low power consumption and simplistic design of LTP probes are attractive advantages, and the customized nature of the probes (to date the majority of LTP probes have been home built) makes them well suited for production via 3D printing. In one study, an LTP probe 3D-printed from PLA and ABS was used to successfully obtain MS spectra of small molecule organic compounds [20].

One of the greatest benefits of 3D printing for MS applications is that many of the designs mentioned in this section are open source and available to researchers free of charge. However, despite these benefits, several challenges remain that impede the integration of 3D printing into MS. For example, many 3D-printing resins are soluble in organic solvents, which can limit the types of solvents that can be used in 3D-printed reaction vessels.

7.5 Nuclear Magnetic Resonance Spectroscopy

Nuclear magnetic resonance (NMR) is an extremely powerful and versatile spectroscopic technique for the study of chemicals ranging from biomolecules to materials. NMR is a non-destructive spectroscopic method that is capable of probing individual atomic sites within a molecule at atomic resolution. Over the last few decades,

317

NMR has proven to be an indispensable tool for the structural determination of organic compounds and biomolecules such as proteins and has found additional applications in emerging technological fields such as battery applications, among others.

NMR is most used to study chemical systems in a liquid or solid state. Generally, the type of equipment used is similar regardless of physical state. First, a superconducting magnet (typically in the range of 9–28 tesla) is used to generate an energy level splitting between the nuclear spin states in a sample. The sample itself is housed within a chamber with an RF coil surrounding it. The purpose of this coil is two-fold: it transmits RF radiation to the sample where it is absorbed and acts as a receiver to detect the corresponding RF radiation that is emitted from the sample. The RF coil and sample chamber are part of the NMR probe which sits within the bore of the superconducting magnet.

In solution state NMR the sample is typically placed in a glass NMR tube while in solid-state NMR the sample is typically placed into a ceramic NMR rotor and fitted with a microturbine cap. In the latter case, this rotor is placed into a stator and the sample is pneumatically rotated at a fixed angle (54.74°) at frequencies that can exceed 7 million RPM. This technique is referred to as magic angle spinning (MAS) and is used to substantially improve the resolution of NMR experiments on solid-state samples. Finally, the spectrometer itself is used to generate the necessary RF pulses for exciting the nuclear transitions. The spectrometer typically consists of RF transmitters, high-power amplifiers, and a receiver unit that translates the analog RF signal into a digital format that can be processed by a computer.

Over the last several years there has been a substantial increase in the application of 3D-printed materials to enhance the performance of NMR equipment. This has been driven by a need for low- cost, open-source equipment that can be rapidly customized and produced. In this section, we highlight a few of the most prominent examples of 3D printing related to NMR. For a more extensive review, the reader is referred to other literature [21].

One of the first examples of 3D printing components for NMR spectroscopy is the fabrication of 3D-printed sample exchangers for dynamic nuclear polarization (DNP) NMR [22]. DNP is a powerful technique that significantly improves the sensitivity of an NMR experiment by transferring the abundant spin polarization of electrons to the nuclei of interest via microwave irradiation. DNP experiments are most efficient when performed at low temperatures, typically <-173°C. Furthermore, because the sample must be rapidly cooled, the NMR rotor must be inserted into the probe at a low temperature. Despite these challenging temperature requirements, 3D-printed eject pipes were fabricated that allowed for seamless insertion and ejection of MAS rotors at temperatures of -173°C. The eject pipes were not only able to handle the extreme temperatures necessary for DNP experiments, but also the extreme thermal cycling that occurs between different probe cooldown cycles.

While most NMR coils in MAS NMR consist of a uniform pitch solenoid coil, non-uniform pitch coils offer improved RF homogeneity and microwave access for DNP experiments. One example of using 3D printing to create non-uniform pitch coils involves the fabrication of dissolvable coil inserts [23]. In this example, CAD software allowed the straightforward design of templates on which coils were wound with

variable pitch. The coil templates were 3D printed from ABS material on an FDM printer.

After winding the coil around a template, the template was then dissolved in acetone,

leaving behind just the coil with the given template geometry. This approach allows

easy, rapid, and reproducible prototyping of coil designs.

Stators used for MAS NMR experiments are capable of spinning rotors at extremely

high rotation frequencies, currently up to ~7 million RPM. However, to accomplish this,

the individual components of the stator must be fabricated to very tight tolerances,

sometimes on the order of a few microns. As such, it is often difficult to manufacture

these MAS stators with traditional additive manufacturing methods. However, recent

work has shown that it is possible to fabricate many stator components using a

combination of ceramic and plastic SLA printing, thus greatly reducing the overall

fabrication cost of the stator [24]. Additionally, it was shown that the cost of certain

consumables such as MAS drive caps, which function as microturbines and enable

sample rotation, could be greatly reduced as well. Using the Protolabs proprietary resin

microfine green, researchers were able to fabricate 3.2 mm drive caps capable of

reproducibly spinning at frequencies of 1.2 million RPM for periods of weeks at a time

with comparable performance to commercially machined drive caps. An image of the

3D-printed stator mounted to a spinning test station and NMR probe can be seen in

Figure 7.4

  While most MAS stators are designed to spin cylindrical rotors, a recent

development in MAS NMR is the implementation of spherical rotors [25]. Initial tests

with 9.5 mm diameter spherical rotors found that they were able to spin to 636,000

RPM using helium gas in a 3D-printed stator. The stator design requirements for
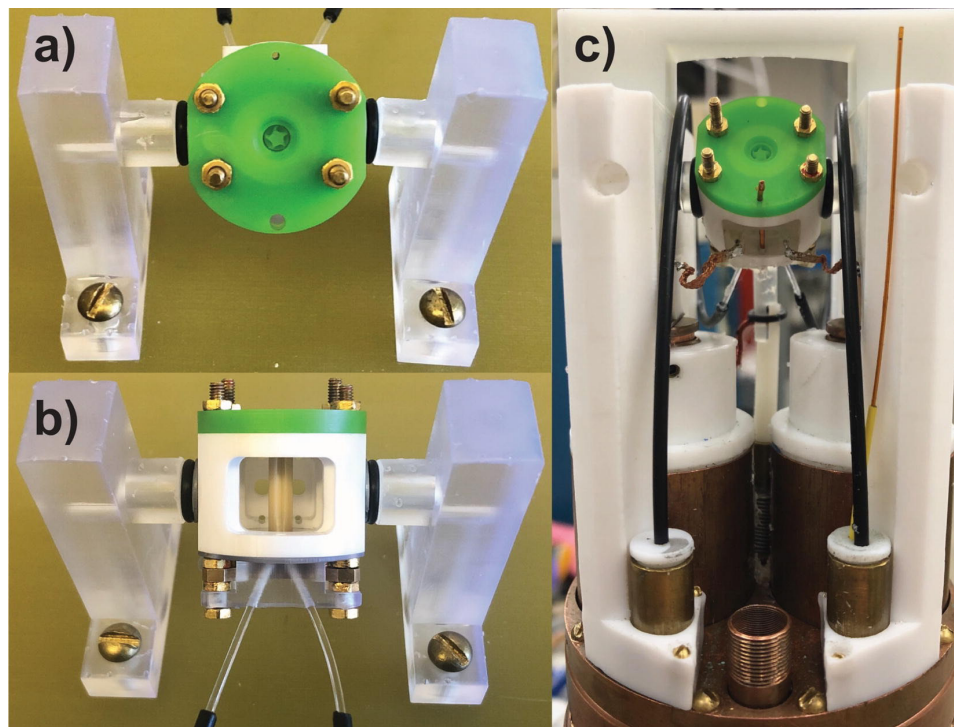
Figure 7.4. 3D printed MAS stator. (A) Top and (B) front view of 3D printed stator assembly mounted on 3D printed spinning test station. (C) 3D printed stator mounted on triple-resonance NMR probe. Reprinted from [24], with permission from Elsevier.

spherical rotors are significantly different than that of stators for cylindrical rotors.

Therefore, when designing initial prototypes of the stator it was highly convenient to use 3D printing to rapidly iterate through stator designs with minor modifications. As the size of spherical rotors began to shrink it was found that further modifications need to be made to the stator design [26]. For 2 mm MAS spheres, the aperture for the bearing gas had to be reduced to 0.4 mm, a significant challenge for most commercial 3D printers. It was also discovered that smaller spherical rotors had difficulty remaining in the stator and would tend to eject during spinning. The issue was eliminated by 3D printing a 'cage' as part of the stator design, thus keeping the sphere in place. Using these design modifications the 3D-printed stators were capable of spinning 2 mm spherical rotors to > 4 million RPM using helium gas.

3D printing has also been used extensively to fabricate non-MAS NMR components. One example of this is using 3D printing to make custom NMR probe heads [27]. The authors utilized both FDM and SLA printing methods followed by a liquid metal injection step to fabricate high complexity, custom radio frequency coils, as shown in Figure 7.5. These inductor designs were optimized for improved sensitivity over previous designs that were limited by conventional fabrication methods. This work represents important progress toward low-cost magnetic resonance imaging (MRI) coils in addition to in situ-reaction monitoring.

In another example, researchers were able to 3D print a low-cost, easy-to-use autosampler for a benchtop NMR system [28]. The autosampler could store 30 samples at a time for solution NMR analysis, significantly increasing the throughput of the system which had previously required manual insertion of the sample. Both the CAD designs and software for controlling the autosampler are open-source and readily available to the research community.

Continued miniaturization of RF transmit and receive coils is critical for magnetic resonance devices, and recently enabled using two-photon polymerization 3D printing. This printing strategy was used to fabricate sub-nanoliter (sub-nL) microfluidic channels on a single chip NMR probe with a resolution better than 1 μm^3 [29]. The high-resolution printing method enabled the printing of the detection coil 10 μm from the sample, which allowed the detection of low concentrations (6×10^{-12} moles) of intact biomolecules at 0.1 parts per million spectral resolution. Despite the immense progress
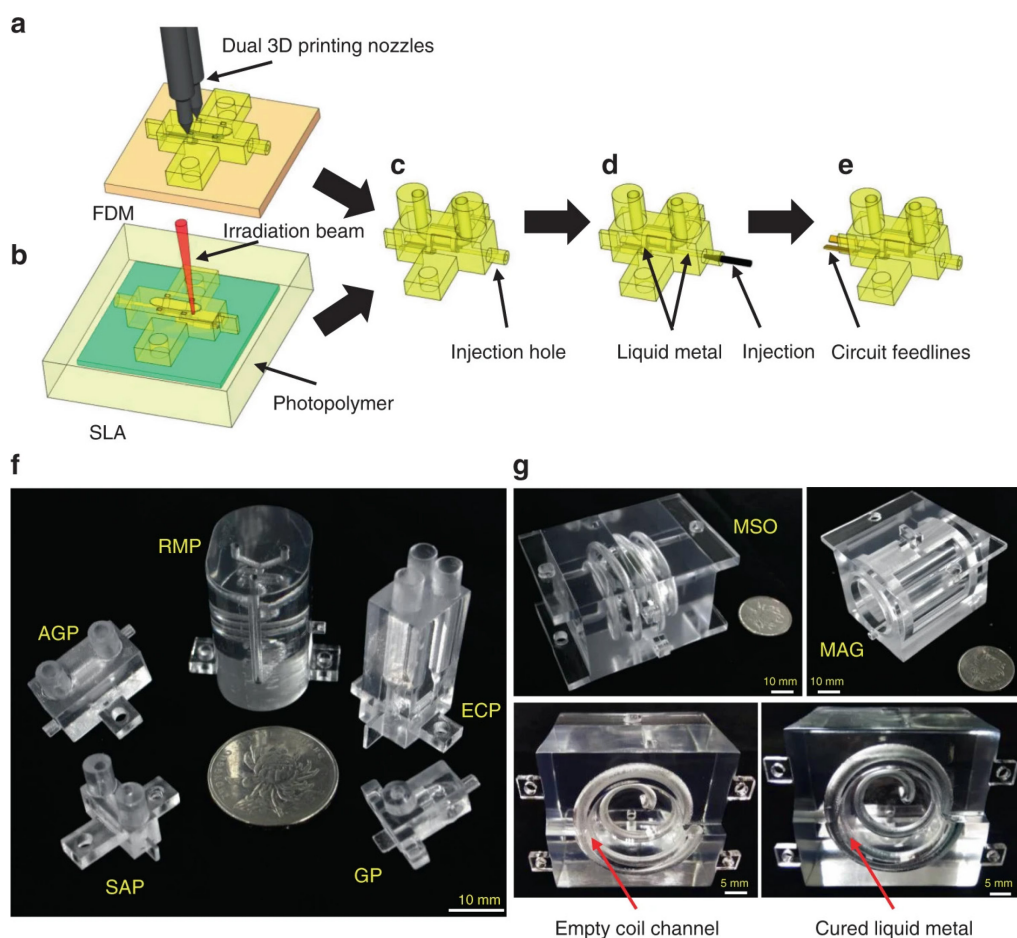
Figure 7.5. SLA and FDM fabrication of NMR probehead. Both **(A)** fused deposition modeling (FDM) and **(B)** stereo lithography appearance (SLA) techniques are utilized to fabricate a complete probehead (**C**) layer by layer according to the simulation design. **(D)** Liquid metal is perfused into the model through the injection hole to form an RF coil. **(E)** The RF coil is connected to the matching circuit by two copper strips to form a complete probe. The entrance and exit of the liquid metal channel are completely sealed with silver paste. Various 3D-printed probeheads suitable for MR applications can be fabricated and utilized, including **(F)** U-tube saddle probehead (SAP), U-tube Alderman-Grant probehead (AGP), reaction monitoring probehead (RMP), electrochemical reaction monitoring probehead (ECP), gradient probehead (GP) for MR, and **(G)** modified solenoid imaging probehead (MSO), modified Alderman-Grant imaging probehead (MAG) for MRI. The coil channel of MSO probehead, before and after the liquid metal perfusion, are also shown. Figure 7.5 adapted with permission from [27] Copyright The Authors, some rights reserved; exclusive licensee Nature Publishing Group. Distributed under a Creative Commons Attribution License 4.0 (CC BY) https://creativecommons.org/licenses/by/4.0/

that has been made with respect to additive manufacturing in NMR, several challenges remain. One challenge is that NMR equipment often consists of small parts with tight tolerances. As of now, most commercial 3D printers for use in labs still offer tolerances in the range of one hundred microns, limiting the type of equipment that can be manufactured for NMR. Additionally, many NMR applications, particularly in MAS NMR, require airtight parts. This can often be difficult to achieve with certain printing processes such as FDM. Another challenge to consider is the chemical composition of the printing material. Most 3D-printing materials are made of organic compounds abundant in carbon and hydrogen, so care must be taken to ensure that these materials do not produce background signals in NMR spectra.

7.6 Conclusion

We have herein reviewed several notable applications of 3D-printing technologies that have enabled advances in molecular and atomic spectroscopies. From applications in UV/VIS, FTIR, Raman, MS, and NMR, 3D printing has allowed researchers to perform innovative experiments that would be otherwise expensive or not readily accessible due to limitations with existing commercial technology. Across spectroscopic methods, the wide range of chemically compatible resins and material properties supporting a variety of experimental conditions illustrates the robust performance and capabilities of 3D printing. Moreover, in many applications reviewed, sub-micron tolerances were achieved using 3D printing. Continued miniaturization of spectroscopic devices is of primary interest to researchers in academia and industry alike. In the future, we anticipate additive manufacturing will continue to become a

primary fabrication method in both research and commercially available spectroscopic devices. As the resolution and material properties available under 3D printing continue to evolve and advance so too will the complexity of the components fabricated.

7.7 References

1   Pisaruka, J. & Dymond, M. K. A low volume 3D-printed temperature-controllable cuvette for UV visible spectroscopy. *Analytical Biochemistry* **510**, 52-55 (2016). https://doi.org:https://doi.org/10.1016/j.ab.2016.07.019

2   Whitehead, H. D., Waldman, J. V., Wirth, D. M. & LeBlanc, G. 3D Printed UV–Visible Cuvette Adapter for Low-Cost and Versatile Spectroscopic Experiments. *ACS Omega* **2**, 6118-6122 (2017). https://doi.org:10.1021/acsomega.7b01310

3   Michalec, M. & Tymecki, Ł. 3D printed flow-through cuvette insert for UV–Vis spectrophotometric and fluorescence measurements. *Talanta* **190**, 423-428 (2018). https://doi.org:https://doi.org/10.1016/j.talanta.2018.08.026

4   Sirjani, E., Migas, M., Cragg, P. J. & Dymond, M. K. 3D printed UV/VIS detection systems constructed from transparent filaments and immobilised enzymes. *Additive Manufacturing* **33**, 101094 (2020). https://doi.org:https://doi.org/10.1016/j.addma.2020.101094

5   Vaněčková, E. *et al.* UV/VIS spectroelectrochemistry with 3D printed electrodes. *Journal of Electroanalytical Chemistry* **857**, 113760 (2020). https://doi.org:https://doi.org/10.1016/j.jelechem.2019.113760

6   Grasse, E. K., Torcasio, M. H. & Smith, A. W. Teaching UV–Vis Spectroscopy with a 3D-Printable Smartphone Spectrophotometer. *Journal of Chemical Education* **93**, 146-151 (2016). https://doi.org:10.1021/acs.jchemed.5b00654

7   Andrea, T., Johannes, D., Simon, T., Harald, G. & Alois, H. 3D-printed miniature spectrometer for the visible range with a 100 × 100 µm^2 footprint. *Light: Advanced Manufacturing* **2**, 20-30 (2021). https://doi.org:10.37188/lam.2021.002

8   Baumgartner, B., Freitag, S. & Lendl, B. 3D Printing for Low-Cost and Versatile Attenuated Total Reflection Infrared Spectroscopy. *Analytical Chemistry* **92**, 4736-4741 (2020). https://doi.org:10.1021/acs.analchem.9b04043

9   Aydogan, O. & Tasal, E. Designing and building a 3D printed low cost modular Raman spectrometer. *CERN IdeaSquare Journal of Experimental Innovation* **2**, 3-14 (2018). https://doi.org:10.23726/cij.2017.799

10   Zhou, J. *et al.* A novel 3D printed negative pressure small sampling system for bubble-free liquid core waveguide enhanced Raman spectroscopy. *Talanta* **216**, 120942 (2020). https://doi.org:https://doi.org/10.1016/j.talanta.2020.120942

11   Karawdeniya, B. I., Chevalier, R. B., Bandara, Y. M. N. D. Y. & Dwyer, J. R. Targeting improved reproducibility in surface-enhanced Raman spectroscopy with planar substrates using 3D printed alignment holders. *Review of Scientific Instruments* **92**, 043102 (2021). https://doi.org:10.1063/5.0039946

12   Almohammed, S. *et al.* 3D-Printed Peptide-Hydrogel Nanoparticle Composites for Surface-Enhanced Raman Spectroscopy Sensing. *ACS Applied Nano Materials* **2**, 5029-5034 (2019). https://doi.org:10.1021/acsanm.9b00940

13   da Silveira, G. D. *et al.* Ready-to-use 3D-printed electrochemical cell for in situ voltammetry of immobilized microparticles and Raman spectroscopy. *Analytica Chimica Acta* **1141**, 57-62 (2021). https://doi.org:https://doi.org/10.1016/j.aca.2020.10.023

14   dos Santos, M. F. *et al.* 3D-Printed Low-Cost Spectroelectrochemical Cell for In Situ Raman Measurements. *Analytical Chemistry* **91**, 10386-10389 (2019). https://doi.org:10.1021/acs.analchem.9b01518

15   Grajewski, M., Hermann, M., Oleschuk, R. D., Verpoorte, E. & Salentijn, G. I. Leveraging 3D printing to enhance mass spectrometry: A review. *Analytica Chimica Acta* **1166**, 338332 (2021). https://doi.org:https://doi.org/10.1016/j.aca.2021.338332

16   Mathieson, J. S., Rosnes, M. H., Sans, V., Kitson, P. J. & Cronin, L. Continuous parallel ESI-MS analysis of reactions carried out in a bespoke 3D printed device. *Beilstein Journal of Nanotechnology* **4**, 285-291 (2013). https://doi.org:10.3762/bjnano.4.31

17   Scotti, G. *et al.* A miniaturised 3D printed polypropylene reactor for online reaction analysis by mass spectrometry. *Reaction Chemistry & Engineering* **2**, 299-303 (2017). https://doi.org:10.1039/C7RE00015D

18   Salentijn, G. I. J., Permentier, H. P. & Verpoorte, E. 3D-Printed Paper Spray Ionization Cartridge with Fast Wetting and Continuous Solvent Supply Features. *Analytical Chemistry* **86**, 11657-11665 (2014). https://doi.org:10.1021/ac502785j

19   Iyer, K. *et al.* Ion Manipulation in Open Air Using 3D-Printed Electrodes. *Journal of the American Society for Mass Spectrometry* **30**, 2584-2593 (2019). https://doi.org:10.1007/s13361-019-02307-2

20   Martínez-Jarquín, S., Moreno-Pedraza, A., Guillén-Alonso, H. & Winkler, R. Template for 3D Printing a Low-Temperature Plasma Probe. *Analytical Chemistry* **88**, 6976-6980 (2016). https://doi.org:10.1021/acs.analchem.6b01019

21   Kelz, J. I., Uribe, J. L. & Martin, R. W. Reimagining magnetic resonance instrumentation using open maker tools and hardware as protocol. *Journal of Magnetic Resonance Open* **6-7**, 100011 (2021). https://doi.org:https://doi.org/10.1016/j.jmro.2021.100011

22   Barnes, A. B. *et al.* Cryogenic sample exchange NMR probe for magic angle spinning dynamic nuclear polarization. *Journal of Magnetic Resonance* **198**, 261-270 (2009). https://doi.org:https://doi.org/10.1016/j.jmr.2009.03.003

23   Kelz, J. I., Kelly, J. E. & Martin, R. W. 3D-printed dissolvable inserts for efficient and customizable fabrication of NMR transceiver coils. *Journal of Magnetic Resonance* (2019).

24   Banks, D., Michael, B., Golota, N. & Griffin, R. G. 3D-printed stators & drive caps for magic-angle spinning NMR. *Journal of Magnetic Resonance* **335**, 107126 (2022). https://doi.org:https://doi.org/10.1016/j.jmr.2021.107126

25   Chen, P. *et al.* Magic angle spinning spheres. *Science Advances* **4**, eaau1540 (2018). https://doi.org:10.1126/sciadv.aau1540

26   Chen, P.-H. *et al.* Two millimeter diameter spherical rotors spinning at 68 kHz for MAS NMR. *Journal of Magnetic Resonance Open* **8-9**, 100015 (2021). https://doi.org:https://doi.org/10.1016/j.jmro.2021.100015

27   Xie, J. *et al.* 3D-printed integrative probeheads for magnetic resonance. *Nature Communications* **11**, 5793 (2020). https://doi.org:10.1038/s41467-020-19711-y

28   Dyga, M., Oppel, C. & Gooßen, L. J. RotoMate: An open-source, 3D printed autosampler for use with benchtop nuclear magnetic resonance spectrometers.

HardwareX **10**, e00211 (2021).
https://doi.org:https://doi.org/10.1016/j.ohx.2021.e00211

29   Montinaro, E. *et al.* 3D printed microchannels for sub-nL NMR spectroscopy.
PLOS ONE **13**, e0192780 (2018). https://doi.org:10.1371/journal.pone.0192780